Mechanical and tribological characterization of NiTinol 60 parts manufactured by different powder metallurgy processes

by

Khashayar Khanlari

A thesis

Submitted in partial fulfilment of the requirements for the degree of Doctor of Philosophy

Department of Mechanical Engineering

Auckland University of Technology

Auckland, New Zealand

2018

Abstract

NiTinol 60 (60NiTi) is a Ni-rich NiTi alloy comprising approximately ~60 wt.% (55 at.%) Ni and ~40 wt.% (45 at.%) Ti. 60NiTi, when employed in a hardened state, displays outstanding properties. It exhibits excellent corrosion resistance and a high level of hardness, has a low elastic modulus and an extensive elastic range that imparts high mechanical contact load resilience. It is dimensionally stable, has good bio-compatibility, can be machined into precision components and is non-magnetic. This unique set of characteristics make the intermetallic 60NiTi suitable for a wide variety of applications in the marine, medical, aerospace and food processing industries. As an example, this alloy has recently been employed as a rolling element bearing material that is highly corrosion resistant and endures high levels of shock loads before experiencing any permanent deformation.

This work investigates the possibility of using hardened 60NiTi in two other distinct areas of interest. For the first area of interest, the sliding wear performance of 60NiTi is compared to 440C steel. This type of steel has high tensile strength and Rockwell C hardness similar to 60NiTi and is conventionally considered as a wear resistant alloy for applications such as gears where contacting materials slide over each other. This research, apart from defining the conditions under which the responses of these alloys differ and answers questions which arise from testing, helps to understand the conditions under which 60NiTi is a suitable alloy as a wear resistant material in sliding conditions. Results obtained in this research, in addition to introducing 60NiTi as a material for load bearing applications other than rolling, will help the engineering community to properly apply this intermetallic in situations where materials slide over each other. Furthermore, findings obtained in this research give an insight into main wear mechanisms and mechanical properties and clarify the mechanisms that at a microscopic level cause damage in 60NiTi and generally NiTi alloys.

In addition, recent studies showed that the addition of hafnium, even in low concentrations, provides benefits in terms of hardening treatment and phase stability in 60NiTi. These findings have led to consider NiTi-Hf alloy (~58 wt.% Ni-~39 wt.% Ti-~3 wt.% Hf) as a substitute or alternative for 60NiTi alloy. The exact composition by weight percent is 57.6 % Ni-39.2 % Ti-3.2 % Hf (54 at.% Ni- 45 at.%Ti-1 at.% Hf) and is designated as 58Ni39Ti-3Hf. Despite the positive interest in this alloy, direct comparisons of the sliding behavior of 58Ni-39Ti-3Hf and the forerunner 60NiTi alloy

have not been made. This research evaluates and compares the sliding performance of 58Ni39Ti-3Hf with baseline 60NiTi to investigate the effect of Hf-addition and define the conditions under which 58Ni-39Ti-3Hf can be considered as an alternative to 60NiTi for sliding applications. Moreover, reasons behind the observed differences are investigated and discussed through different mechanical and microstructural experimentations. Results obtained from these tests help to understand the effects that Hf-addition has on the mechanical properties of baseline 60NiTi.

The second area of interest focuses on processing 60NiTi to a porous structure suitable for general bone replacements. Implants that are intended for use in general bone replacements such as spinal or cranial inserts are expected to have a porous structure. In such cases, other than good biocompatibility and dimensional integrity and fulfilling the mechanical prerequisite for biomedical applications, final parts should contain interconnected and open pores of 30-80 Vol.% and pore sizes in the range of 100-600 μm. In this research, elemental Ni and Ti powders are used to process and manufacture 60NiTi parts by a conventional press-and-sinter method. This study, while working toward evaluating the possibility of obtaining the mentioned 60NiTi structure through a conventional press-and-sinter method, investigates the effects of different processing factors such as sintering temperature, heating rate and sintering holding time on the microstructure and mechanical properties of these parts. In addition, a series of heat-treatment methods are developed to homogenize and harden porous 60NiTi in a cost-effective way. Outcomes of these heat-treatment methods with regards to obtained microstructures and mechanical properties are discussed and analyzed.

Statement of authentication

Attestation of authorship

I hereby declare that the work presented in this doctoral thesis is my original work, containing primary data collected by me. This doctoral thesis includes seven papers written by me and co-authors, seven previously published in journals. These papers of this doctoral thesis contain no material which has been submitted for any other degree at any other university or academic institution of higher learning.

Co-Authored Works

This is a pathway 2 thesis by publication. Therefore, the thesis includes seven papers, six published and one under review, that were my own work with the joint authorship from my supervisors at Auckland University of Technology (AUT) and University of Auckland (UoA) in New Zealand. The following papers relate to the work undertaken for the thesis:

1- **Khanlari K,** Ramezani M, Kelly P. 60NiTi: A review of Recent Research Findings, Potential for Structural and Mechanical Applications, and Areas of Continued Investigations. *Transactions of Indian Institute of Metals,* 2017; **71**: 781-799.

2- **Khanlari K**, Ramezani M, Kelly P, Cao P, Neitzert T. Reciprocating sliding wear behavior of 60NiTi as compared to 440C steel under lubricated and unlubricated conditions. *Tribology Transactions,* 2018; https://doi.org/10.1080/10402004.2018.1460434

3- **Khanlari K**, Ramezani M, Kelly P, Cao P, Neitzert T. An investigation on reasons causing inferiority in unlubricated sliding wear performance of 60NiTi as compared to 440C steel. *Tribology Transactions,* 2018. (Under review)

4- **Khanlari K,** Ramezani M, Kelly P, Cao P, Neitzert T. Comparison of the reciprocating sliding wear of 58Ni39Ti-3Hf alloy and baseline 60NiTi. *Wear,* 2018; **408-409**: 120-130.

5- **Khanlari K,** Ramezani M, Kelly P, Cao P, Neitzert T. Synthesis of as-sintered 60NiTi parts with a high open porosity level. *Materials Research,* 2018*;* **21**.

6- **Khanlari K,** Ramezani M, Kelly P, Hayat MD, Cao P, Neitzert T. An Investigation on Microstructural and Mechanical Properties of Porous 60NiTi Parts Solutionized by Different Cost-Effective Methods. *Metallography, Microstructure and Analysis,* 2018; **7**: 334-346.

7- **Khanlari K,** Ramezani M, Kelly P, Cao P, Neitzert T. Mechanical and microstructural characteristics of as-sintered and solutionized porous 60NiTi. *Intermetallics,* 2018; **100**: 32-43.

I hereby declare that in all seven papers I was the principal author. I was responsible for the literature review, research design, data collection, data analysis, and writing full papers. The name of supervisors advising me on the project were added as co-authors. In one specific paper (paper 6), the name of a postdoctoral researcher, working at UoA, who assisted me in running some instruments was added as a co-author to the manuscript.

Candidate contributions to co-authored papers

Chapter 1- Paper 1 **Khanlari K,** Ramezani M, Kelly P. 60NiTi: A review of Recent Research Findings, Potential for Structural and Mechanical Applications, and Areas of Continued Investigations. *Transactions of Indian Institute of Metals*, 2017; **71**: 781-799.	Khanlari 80% Ramezani 10% Kelly 10%
Chapter 2- Paper 2 **Khanlari K,** Ramezani M, Kelly P, Cao P, Neitzert T. Reciprocating sliding wear behavior of 60NiTi as compared to 440C steel under lubricated and unlubricated conditions. *Tribology Transactions*, 2018; https://doi.org/10.1080/10402004.2018.1460434	Khanlari 80% Ramezani 5% Kelly 5% Cao 5% Neitzert 5%
Chapter 3- Paper 3 **Khanlari K,** Ramezani M, Kelly P, Cao P, Neitzert T. An investigation on reasons causing inferiority in unlubricated sliding wear performance of 60NiTi as compared to 440C steel. *Tribology Transactions*, 2018.	Khanlari 80% Ramezani 5% Kelly 5% Cao 5% Neitzert 5%
Chapter 4- Paper 4 **Khanlari K,** Ramezani M, Kelly P, Cao P, Neitzert T. Comparison of the reciprocating sliding wear of 58Ni39Ti-3Hf alloy and baseline 60NiTi. *Wear*, 2018; **408-409**: 120-130.	Khanlari 80% Ramezani 5% Kelly 5% Cao 5% Neitzert 5%
Chapter 5- Paper 5 **Khanlari K,** Ramezani M, Kelly P, Cao P, Neitzert T. Synthesis of as-sintered 60NiTi parts with a high open porosity level. *Materials Research*, 2018; **21**.	Khanlari 80% Ramezani 5% Kelly 5% Cao 5% Neitzert 5%
Chapter 6- Paper 6 **Khanlari K,** Ramezani M, Kelly P, Hayat MD, Cao P, Neitzert T. An Investigation on Microstructural and Mechanical Properties of Porous 60NiTi Parts Solutionized by Different Cost-Effective Methods.	Khanlari 80% Ramezani 5% Kelly 5% Hayat 2.5%

Metallography, Microstructure and Analysis, 2018; **7**: 334-346.	Cao 5% Neitzert 2.5 %
Chapter 7- Paper 7 **Khanlari K,** Ramezani M, Kelly P, Cao P, Neitzert T. Mechanical and microstructural characteristics of as-sintered and solutionized porous 60NiTi. *Intermetallics*, 2018; **100**: 32-43.	Khanlari 80% Ramezani 5% Kelly 5% Cao 5% Neitzert 5%

Maziar Ramezani 14/6/2018

Piaras Kelly 14/6/18

Thomas Neitzert 18/6/2018

Peng Cao 25/6/2018

Muhammad Dilawer Hayat 25/06/2018

Dedication

This dissertation is dedicated to true liberal people who are free from the shackles of life imposed by the society and culture. These people fly fearlessly and carelessly beyond the extreme boundaries of mundane life tasting the pleasure of freedom.

Acknowledgments

I would like to take this opportunity to acknowledge all the people who had a role in facilitating and supporting this research project.

I express my sincere thanks to my supervisor, Associate Professor Piaras Kelly, Department of Engineering Science, The University of Auckland (UoA) for the extensive amount of time that he invested in supervising me. Dr. Kelly is a true gentleman who, other than science, I learned manner and professionalism from. I will also surely miss the coffee times we had discussing politics.

Carrying out this project was a great pleasure as it gave me the opportunity to collaborate with and use the first-hand knowledge and experience of the leader of the field of 60NiTi, Dr. Christopher DellaCorte National Aeronautics and Space Administration (NASA), Glenn Research Center, Cleveland, Ohio. I can surely grant him the credit for introducing me to the world of science and technology in the early days of my professional carrier. I truly acknowledge the great amount of time that he spent patiently answering my daily emails, questions, providing novel ideas for my research, teaching me wear mechanisms and guiding me through the challenges that I encountered during the project. I have promised myself to be an academic possessing similar attitudes, passion and professionalism as he has in the future. Unfortunately, I have not yet met him in person but I am certain this would come true in the near future.

Professor Thomas Neitzert is commended because of the support that he gave me to participate in a conference in Xi'an, China. Apart from the conference, I truly enjoyed the evenings spent in exploring the city and a pleasant walk at the Xi'an city wall. I thank Dr. Peng Cao for authorizing me to do experiments in the laboratories of the Department of Chemical and Materials, UoA.

I would like to appreciate Peter McArthur, the director of Titanox Developments Ltd, for all the supports that he has given me to start and develop my career in New Zealand.

In addition, I would like to thank Dr. Michael Alan Hodgson, Dr. Alec Asadov, Patrick Conor, Dr. Matthew Sidford, David Cotton and Ross Jamieson for assisting me in running the experiments and preparing the samples.

The most beautiful days of my life in New Zealand were spent with my ex-girlfriend Ariane Casadebaig. I am thankful to her for being an understanding partner and also an

honest and caring friend. I am thankful to my friend Mehdi Saeidi as he has been a very intelligent and amazing friend. I wish Tino Hermann the best for his future career and thank him for being a welcoming and honest friend. Memories of my friends, Davide Fantozzi, Bruno Di Buo, Marco D'Ignazio, Lucio Azzari, Andrea Milanti, Nemat Dehghanian and Amir Farughian, in Finland during my M.Sc. studies are still alive in my mind. Remembering the good times and true friendship we had together made me feel happy during my Ph.D. journey in New Zealand. I am confident that I would see them once again in Europe.

I believe, good rest is essential for a researcher to refresh the mind needed to focus on the research and overcome the concomitant challenges. I acknowledge all the people who I socialized with and had good times with during the weekends doing recreational activities.

Lastly, special thanks to my parents and siblings for their sincere dedication and support throughout this program.

Khashayar Khanlari

28th May 2018

Contents

List of abbreviations and symbols

A_f	Austenite finish temperature
A_G	The cross-sectional area of the groove
A_P	The cross-sectional area of the lateral pile-up
A_s	Austenite start temperature
at.%	Atomic Percent
BE	Blended elemental
BSE	Back Scattered Electron
CoF	Coefficient of Friction
DSC	Differential Scanning Calorimetry
EDS	Energy Dispersive Spectroscopy
EDM	Electro Discharge Machining
Hf	Hafnium
HIP	Hot Isostatic Pressing
M_f	Martensite finish temperature
M_s	Martensite start temperature
NASA	National Aeronautics and Space Administration
Ni	Nickel
NiTi	NiTinol
NiTinol	Nickel-Titanium Naval Ordnance Laboratory
NOL	Naval Ordnance Laboratory
PAO	poly alpha olefin

PM	Powder metallurgy
P&S	Press-and-sinter
RCF	Rolling Contact Fatigue
RMS	Root mean square
S_D	Scratch depth
SEM	Scanning Electron Microscope
SME	Shape Memory Effect
S_W	Scratch width
Ti	Titanium
TEM	Transmission Electron Microscope
wt.%	Weight Percent
XRD	X-Ray Diffraction

List of Figures

List of Tables

Chapter 1 Introduction[1]

[1]**Khanlari K**, Ramezani M, Kelly P. 60NiTi: A review of Recent Research Findings, Potential for Structural and Mechanical Applications, and Areas of Continued Investigations. *Transactions of Indian Institute of Metals*, 2017; **71**: 781-799.

1.1 Background

Binary Ni-Ti alloys are widely exploited in different applications. The emergence and development of binary Ni-Ti alloys is the result of the investigations and efforts of William J. Buehler and his colleagues in the late 1950s at the Naval Ordnance Laboratory (NOL). Ni-Ti binary alloys were amongst their candidate alloys under research, aiming to find a suitable material for ballistic re-entry vehicular applications. These intensive attempts resulted in identification of two alloys NiTinol 55 and NiTinol 60, which respectively contain about 55 and 60 weight percent (wt.%) Ni. General properties of these alloys were revealed as an outcome of these researches. It is interesting to note that the designation NiTinol often used for these alloys is an abbreviation for Ni-Ti Naval Ordnance Laboratory [1-5].

NiTinol 55 or equiatomic NiTinol is well known for its unique superelastic and shape memory effects (SME) [5, 6]. The occurrence of superelasticity and SME is due to the existence of NiTi phase in this alloy. NiTi generally exists in two different structures, austenite and martensite. NiTi when cooled from the austenitic parent phase below the martensite start temperature (M_s), exhibits a thermoelastic phase change to highly twinned martensite by a first-order diffusionless shear mechanism. This transformation is completed when cooling is continued to below martensite finish temperature (M_f). The parent austenite phase has an ordered B2 (CsCl) structure and the martensitic phase has a monoclinic structure of B-19 type. If a sample of this alloy is deformed below M_f then it can be restored to its original shape by being heated up to the austenite finish temperature ($A_{f,}$) where the austenite phase is stable; this phenomenon is called shape memory effect (figure 1-1).

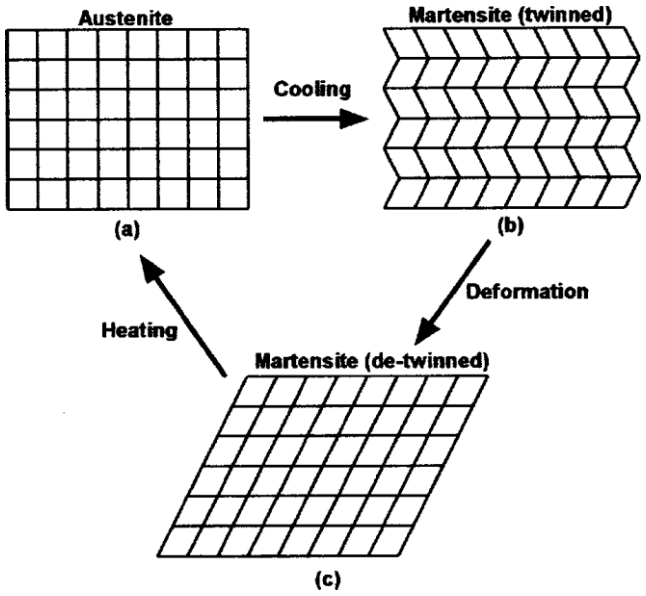

Figure 1-1: Schematic of SME after deformation [7].

This martensitic transformation can also be induced by applying stress while the material is in its austenitic phase. This intermetallic exhibits high strain (more than 3%) through mechanical reversible martenitic transformation between the parent austenite phase and the martensitic phase. The high strain achieved during this transformation, called superelasticity, is due to detwinning of the martensite phase. After unloading, the martensite phase is no longer stable and transforms back to the austenite phase; along a hysteresis curve, resulting in recovery of strain (figure 1-2) [4, 6, 8-16].

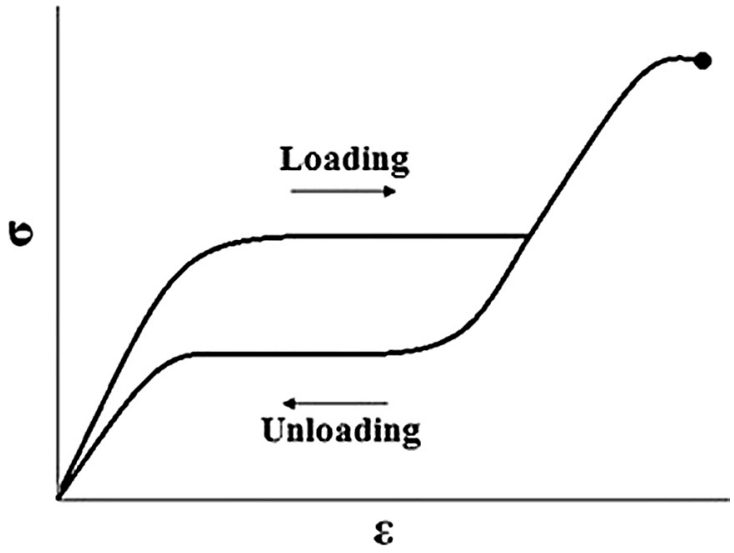

Figure 1-2: Schematic showing superelasticity effect in NiTinol alloy [17].

This alloy is in widespread usage for applications such as actuators, stents and orthodontic arch wires, where superlasticity and shape memory effects are considered a virtue [4, 5, 18]. Despite these advantages, NiTinol 55 is soft and lacks proper dimensional and microstructural stability due to its shape memory property [4, 5, 19]. Because of these reasons, this alloy cannot be considered as a structural alloy suitable for precision mechanical assemblies or load bearing applications [4].

NiTinol 60, containing ~60 wt.% (55 at.%) Ni-~40 wt.% (45 at.%) Ti, or 60NiTi is a Ni-rich version of the equiatomic NiTinol [20]. As can be seen from the binary phase diagram of the Ni-Ti system (figure 1-3), the stoichiometric NiTi alloy can solve an increasing amount of Ni in NiTi phase with increasing temperature above ~625°C [18]. Heating above ~1050°C results in a solutionized 60NiTi with single NiTi phase. Upon cooling from this temperature, precipitation of thermodynamic equilibrium Ni_3Ti and/or metastable Ni_4Ti_3 and/or metastable Ni_3Ti_2 is expected [18].

Increasing Ni in the composition of NiTi phase results in a concomitant drop of austenite to marteniste transformation temperature in binary Ni-Ti alloys [18, 21]. This results in superior dimensional stability of Ni-Ti alloys containing Ni-rich NiTi phases compared to the ones consisting of less Ni-rich NiTi phases [22, 23]. Hardened single phase 60NiTi, which can be achieved by proper heat treatment, does not exhibit the martensitic transformation until at least -100°C. This results in excellent microstructural and dimensional stability of 60NiTi [1, 5].

Hardened 60NiTi is an ordered intermetallic with the CsCl-type B2 cubic crystal structure matrix. In this structure, eight Ni atoms occupy the corners of a cubic unit cell and surround the Ti atom sitting in the centre of the cube (Figure 1-4) [24]. This alloy behaves like an intermetallic, neither a metal nor ceramic in terms of atomic bonding, with intrinsic brittleness. This can be attributed to the high degree of atomic ordering and rigidity of bonding in 60NiTi [24]. In fact, 60NiTi being less covalent than ceramics, is expected to show more toughness compared to ceramics like TiC. But compared to metallic alloys such as Ti-6AL-4, 60NiTi is expected to have higher strength because of its highly directional and strong bonding between Ni and Ti [5, 9].

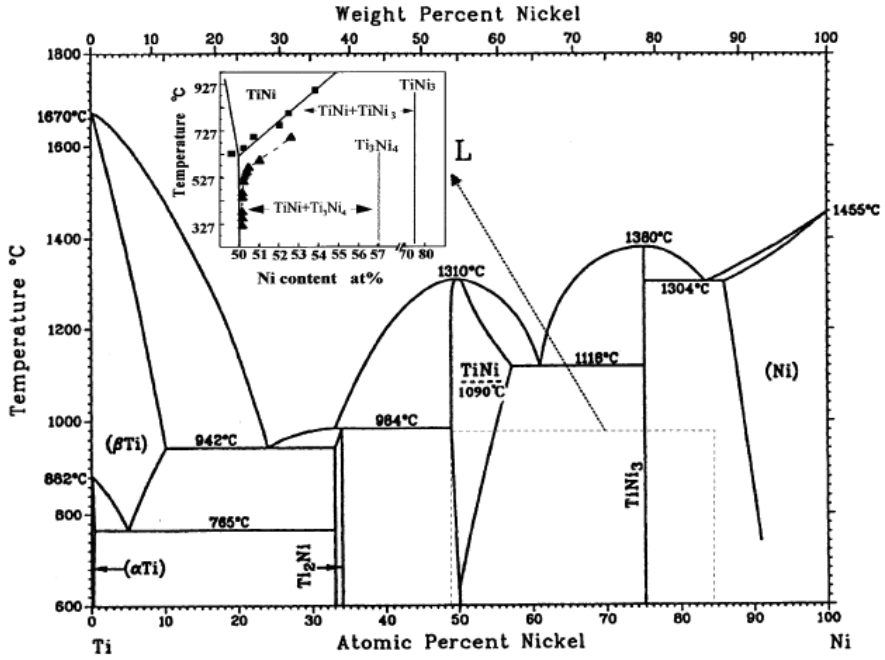

Figure 1-3: Binary Ni-Ti phase diagram [18].

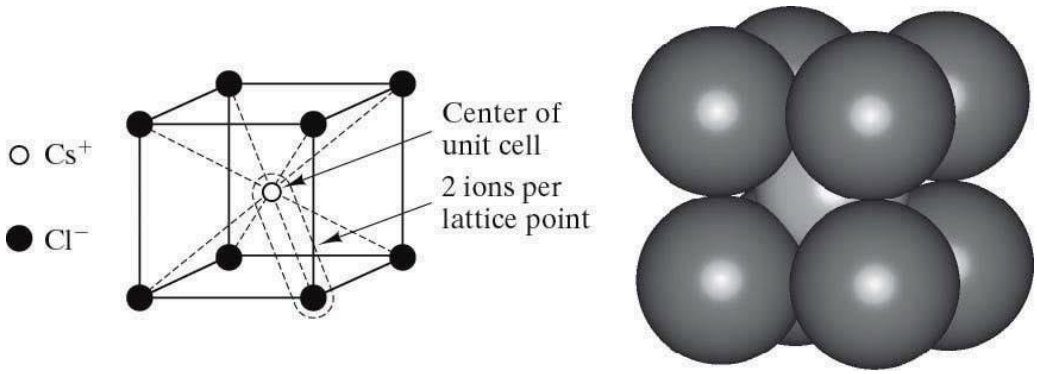

Figure 1-4: B2 NiTi unit cell showing (a) Atomic arrangement, and (b) Relative size of atoms in the unit cell [24].

Hardened 60NiTi combines a unique sets of properties, which make it a promising alloy for consideration as an attractive candidate for structural applications. It possesses high hardness between 58 Rockwell C (RC) to 62 RC, high compressive strength (~2500 MPa), exhibits low elastic modulus of around 100GPa and large recoverable strain range of over 5%. In addition, this alloy can be readily machined prior to final heat treatment and has a moderate density of 6.71 g/cc, which is about 15% less than steel [2, 4, 19, 25, 26]. Hardened 60NiTi is intrinsically highly corrosion resistant, which makes it a suitable material to be employed in common corrosive agents. Moreover, because it does not contain any iron, it is protected against atmospheric rusting [9, 27]. Other than these key material properties, 60NiTi has some other

properties, which can be considered as advantages. This alloy is electrically conductive, non-magnetic with magnetic permeability of less than or equal to 1.002 and has a thermal expansion coefficient which matches closely with that of conventional structural materials. Furthermore, 60NiTi can be ground, polished and lapped to precise final dimensions and an extremely smooth surface finish of less than 0.02 micrometer RMS. [1, 9, 28, 29].

With this desirable combination of properties, 60NiTi has tremendous potential for use in the aerospace, marine, automotive and medical industries for different applications such as gears, bearings, valves, tribological components, medical tools and etc.

1.2 Manufacturing and processing methods

Hardened 60NiTi is indeed a material with desirable properties for use in the manufacture of useful products. Despite this, little effort has been so far allocated in making components out of this alloy [9, 30]. Literally, 60NiTi is known to be a material which is brittle, hard to machine and difficult to work with [19, 21, 31]. For example, high temperature workability of 60NiTi is not favourable due to the presence of substantial amounts of intermetallics [8, 31]. Machining of 60NiTi is, if not impossible, very difficult and is limited to so many restrictions such as using sharp carbide tooling, light feeds and slow speeds [8].

Recently, the application of more advanced manufacturing and processing methods for 60NiTi are emerging, namely powder metallurgy, ceramic cutting tools and electrical discharge machining (EDM). Using such methods, the fabrication of complex and high precision parts from 60NiTi are now possible [3].

Casting and powder metallurgy are the main methods that have been explored to manufacture high-performance 60NiTi objects [32]. Julien [9] invented methods to manufacture different parts from molten 60NiTi by applying friable mold casting and die casting. In this invention, Julien defined the temperatures suitable for successful deformation and hot working of this material. In another invention, Julien [30] described efficient processing methods, including casting, for manufacturing 60NiTi bearing races and balls. In another research, Dehghani and Khamei [3, 31] studied the hot deformation behavior of 60NiTi. According to them, the high temperature workability of 60NiTi can be enhanced and assisted by a dynamic recrystallization (DRX) mechanism activated in high deformation temperatures.

It is hard to avoid contamination, inclusions and voids in objects produced by the casting process (figure 1-5); these contaminants and flaws will act as stress raisers and will reduce the load needed for crack propagation, making the machining of cast products very difficult [8, 19, 20, 27]. 60NiTi is intrinsically brittle in tension and the presence of these flaws degrades the mechanical properties of 60NiTi samples by reducing the energy required for fracture initiation or crack propagation [27, 33, 34]. In a research carried out by Stanford et al. [20], it was found that contamination of casting parts with zirconia (ZrO_2) which was sourced from the crucible liner resulted in quench cracking of the parts during heat treatment above 1000°C. Despite all these disadvantages, results obtained from current research shows that the addition of other elements such as Hf and Zr will improve the microstructural homogeneity in casting produced parts, since they act as "getters", leading to enhanced mechanical properties [34].

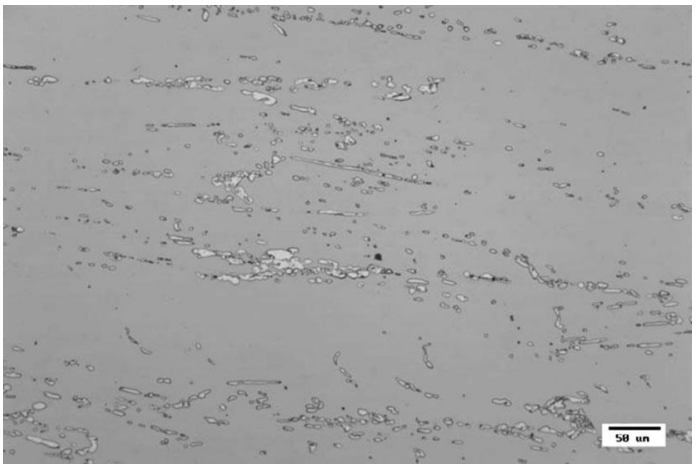

Figure 1-5: Cross-sectional optical micrograph of a cast and rolled 60NiTi rod showing voids and second-phase precipitates [34].

Powder metallurgy processing is another method for fabrication of 60NiTi parts. This process has some advantages compared to casting. By powder metallurgy, near net shape components can be synthesized. This reduces the amount of machining needed to obtain the final geometry [3]. Moreover, random orientation of the powder particles lead to random orientation of the grains in powder metallurgy manufactured samples. This results in samples with more isotropic mechanical properties than ones produced by casting [32]. In addition, chemical segregation, grain growth, voids and contamination are reduced under this process compared to casting [19, 32, 34]. Furthermore, pores produced in powder metallurgy components have less tendency to be spherical than in the casting process. This is another advantage for powder metallurgy by considering the fact that it is very hard to remove spherical porosities [20].

A method for manufacturing bearings from 60NiTi is patented by DellaCorte and Glennon [35]. In this method, powders are produced by an atomization technique and then atomized powders are used to manufacture bearings by applying hot isostatic pressing (HIP); the typical HIP process is shown in figure 1-6. Stanford [32] explored the effects of varying time, temperature and pressure during consolidation of particles in HIP and defined the optimum parameters to achieve the highest hardness and proper microstructure. 60NiTi parts processed by HIP can be readily machined to near final size before the final hardening heat treatment by EDM and/or carbide tool based machining. Grinding, polishing and lapping are done to obtain parts with smooth finishes after conducting the final hardening heat treatment [25].

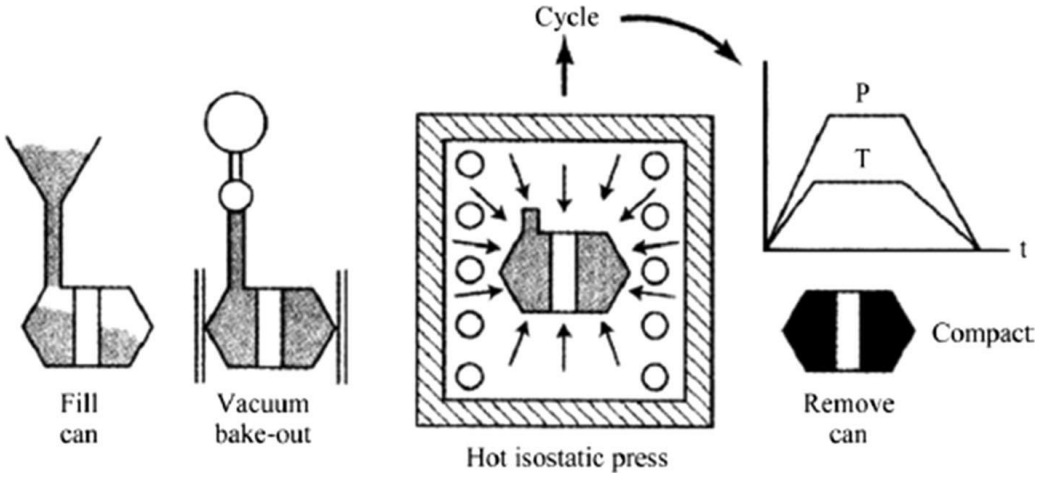

Figure 1-6: Typical hot isostatic pressing (HIP) process [34].

Cost is a major disadvantage of the HIP process [32]. In addition, surface oxidation of powder particles due to the high reactivity of Ti with oxygen is a common issue in this process [33, 34]. These oxide films on the surface of the powders prevent the consolidation of the particles in parts produced by HIP (figure 1-7.a) [19, 32]. Contamination of the molten 60NiTi during the powder processing is another issue in this process. In research done by DellaCorte et al. [36], it was observed that molten 60NiTi picks up ceramic inclusions due to its contact with the ceramic crucible and nozzle during the powder atomization process.

Using high quality powders with minimum amounts of oxidation on the surface and inclusions inside is beneficial. These oxide films and inclusions will affect the mechanical properties by providing brittle fracture propagation paths and/or acting as stress risers [32, 36]. To achieve high quality powders, which can enhance the final mechanical properties, it is necessary to use high quality clean elements and modern processing equipment. Such processing equipment is

made mainly of Ti so that the contamination of the powders with undesirable particles and elements is avoided (figure 1-7.b) [24, 34].

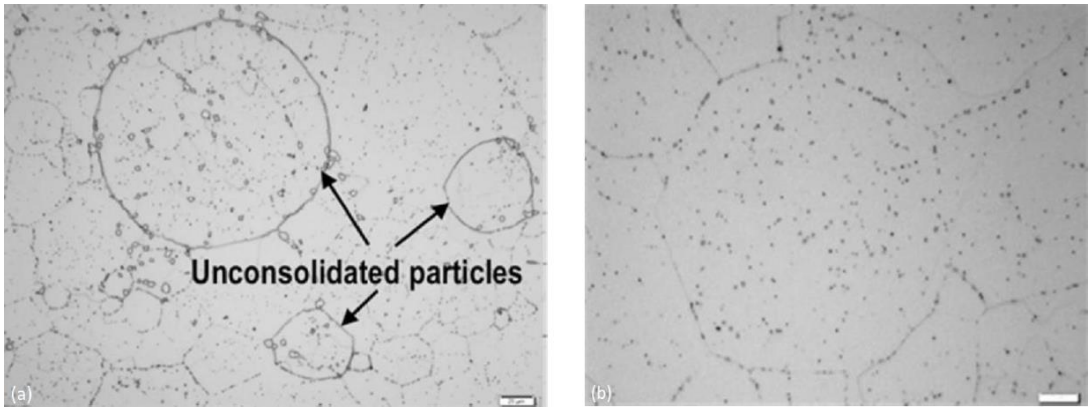

Figure 1-7: Cross-sectional optical micrograph of powder metallurgy processed 60NiTi rods, (a) Microstructure showing unconsolidated particle flaw, (b) Microstructure showing properly consolidated particles [34].

1.3 Hardening mechanism

As explained already, the stoichiometric NiTi alloy can solve increasing amounts of Ni with increasing temperature above ~625°C and form single B2 NiTi phase (figure 1-3) [18]. Ni-rich Ni-Ti alloys of over 50.6 at.% Ni, depending on the rate of cooling applied, exhibit different microstructures and hardness when cooled from the single B2 NiTi matrix phase to room temperature. This is in contrast to equiatomic NiTinol alloy which is relatively unaffected by cooling rate (figure 1-8) [8, 37]. Cooling Ni-Ti alloys of over 50.6 at% Ni, with low cooling rate from B2 single phase zone, results in the precipitation of thermodynamic equilibrium Ni_3Ti and/or metastable Ni_4Ti_3 and/or metastable Ni_3Ti_2 [18, 21, 37]. Conducting high cooling rate heat treatments on these Ni-Ti alloys, from the B2 single phase zone, suppresses precipitation of Ni-rich stable Ni_3Ti and metastable Ni_3Ti_2 phases from the parent NiTi phase [20, 21, 34]. However, nucleation of Ni_4Ti_3 from the NiTi matrix phase occurs in milliseconds rendering the precipitation of this Ni-rich phase inevitable [18, 21, 38].

Based on the results obtained from the molecular dynamic (MD) simulations, both B2 NiTi and Ni_4Ti_3 have high generalized stacking fault energy (GSFE), indicating that slip in both phases will be difficult. Moreover, Ni_4Ti_3 is a phase with rhombohedral crystal structure and as a result has less symmetry compared to cubic B2 NiTi phase. The combination of these facts leads one to conclude that both B2 NiTi and Ni_4Ti_3 are hard, with Ni_4Ti_3 expected to be harder than B2 NiTi [18, 21]. On the other hand, metastable Ni_3Ti_2 and thermodynamically stable

Ni_3Ti are incoherent phases, which are believed to result in brittleness and a decrease in hardness [18, 21, 28, 34, 39]. As a result, applying fast cooling rates on binary Ni-Ti alloys, containing the single phase B2 NiTi, results in parts with a higher hardness than the alloys which are cooled at a slow rate from the single phase B2 NiTi phase.

Knowing the characteristics of the phases and the role of cooling rate, the next step is determining the composition and percentage of Ni, which results in the maximum hardness. A series of binary Ni-Ti alloys with composition varying from 50 at.% to 58 at.% Ni were fabricated by Hornbuckle et al. [18], solutionized at 1050°C to matrix B2 NiTi phase and then quenched. In each of these samples, hardening treatment resulted in the nucleation of the nanoscale Ni_4Ti_3. The highest hardness of ~644 HV, equivalent to 57-58 RC, was achieved for the alloys containing about 55 to 56 at.% Ni corresponding to ~60 wt.% Ni or 60NiTi (figure 1-8).

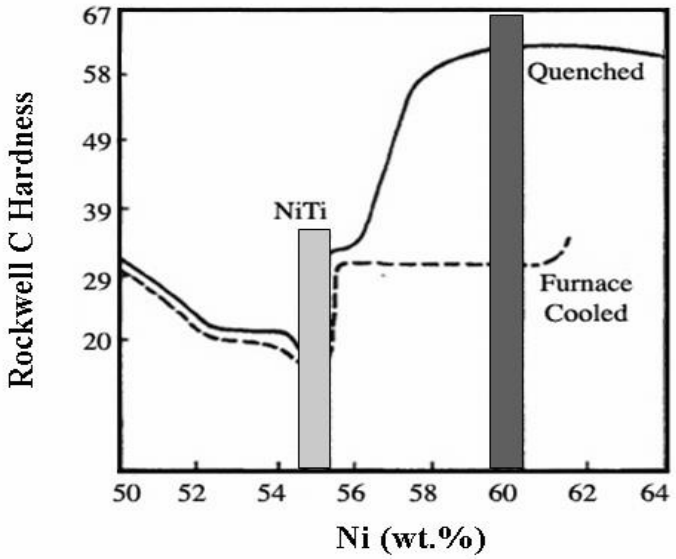

Figure 1-8**:** Variation of hardness (Rockwell C) in Ni-Ti alloys as a function of Ni composition and cooling rates. WQ stands for water quenching (high cooling rate) and FC stands for furnace cooling (slow cooling rate) [40].

At higher Ni contents of 57 at.% and 58 at.% , Ni_3Ti and Ni_3Ti_2 Ni-rich soft phases were found. This is because 1050°C is not adequate to completely solve the Ni-rich phases inside the B2 NiTi matrix phase. Furthermore, applying a higher temperature for solutionizing is not practical as it may cause liquid generation. As a result, Ni-rich Ni-Ti alloys with Ni contents over 57 at.% exhibit a lower hardness than Ni-Ti with about 55 to 56 at.% Ni. Instead, the higher hardness of Ni-Ti alloy containing 55 at.% Ni compared to less Ni-rich alloys is attributed to the formation of the high volume fraction of nanoscale (~67 nm) Ni_4Ti_3 phase [18, 38].

Increasing Ni-content leads to the increased volume fraction of hard coherent Ni_4Ti_3. A simple lever rule calculation, by considering Ni_4Ti_3 and NiTi as line compounds (figure 1-3), approximates to ~71% Ni_4Ti_3 to precipitate after cooling 60NiTi to ambient temperature. This theoretically determined phase volume fraction was in near consistency with the experimental observations. This high volume fraction of Ni_4Ti_3 precipitate results in the formation of narrow B2 NiTi matrix channels between the hard nanoscale Ni_4Ti_3 precipitates (figure 1-9). This structure is ideal to enhance the hardness by activating the Orowan strengthening mechanism [18, 39]. Furthermore, these coherent nanoscale precipitates promote a considerable amount of stress in the microstructure and increases hardness by a strain hardening mechanism [39]. As a result, Ni-Ti alloy containing 55 at.% Ni corresponding to 60 wt.% Ni or 60NiTi is the Ni-rich alloy with the maximum amount of hardness in the binary Ni-Ti family suitable for structural applications.

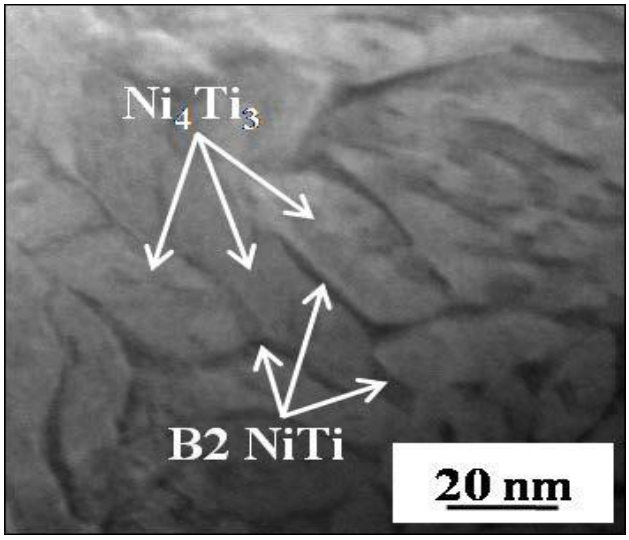

Figure 1-9**:** STEM-HAADF image of hardened 60NiTi revealing two-phase (Ni_4Ti_3 precipitates in a NiTi matrix) structure [18].

A typical hardening treatment for 60NiTi consists of heating the parts to above the solvus temperature of ~1050°C (in a furnace with vacuum or inert gas atmosphere) and then quenching the parts in a quenchant [21, 25]. As explained, this procedure solves the Ni_3Ti and Ni_3Ti_2 phases in B2 NiTi but results in precipitation of hard nanoscale Ni_4Ti_3 precipitates in B2 NiTi matrix [18]. Ni_4Ti_3 precipitates formed due to this procedure are in nanoscale size and cannot be observed by scanning electron microscopy (SEM) (figure 1-10.b) [18]. The average hardness for the hardened specimens had the value of 664±19 HV and the furnace-cooled parts had an average hardness value of 324±39 HV [33]. The lower average hardness of the furnace-

cooled samples is attributed to the decomposition of hard Ni_4Ti_3 to the soft incoherent metastable Ni_3Ti_2 and stable Ni_3Ti phases (figure 1-10.a). Thomas [41] investigated the effect of different quenchants such as room temperature water, shop air, boiling water, ice bath, oil, glycol and liquid nitrogen on the obtained hardness and microstructure of hardened 60NiTi parts. He concluded that all the parts regardless of the type of the studied quenchants achieved high hardness of 58 to 61 RC. The standard Jominy end-quench test, which is designed to check how deep into the core of a given quenched object is hardened, was employed for 60NiTi. Results proved that 60NiTi possesses a high hardenability [8].

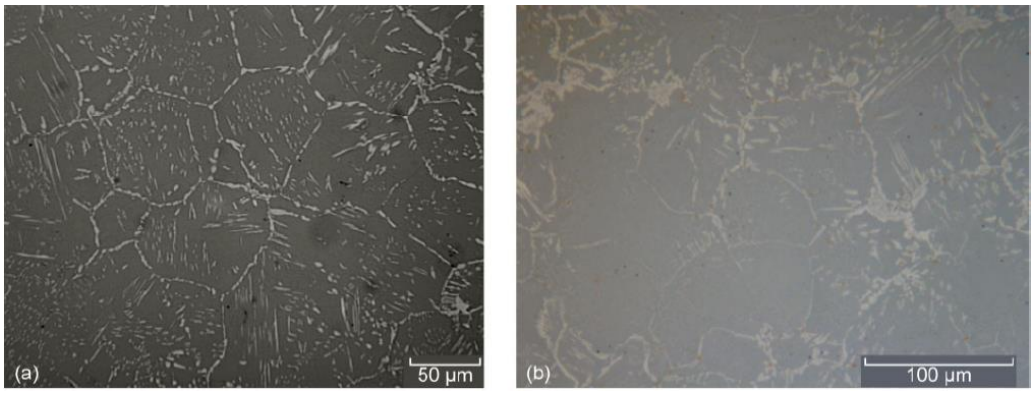

Figure 1-10**:** Microstructure of 60NiTi (a) before and (b) after solutionizing heat treatment [25].

A further consideration in any thermally hardened material is aging; aging treatment allows some residual stress relaxation in heat-treated and quenched specimens [33]. Results show that hardened 60NiTi can sustain its hardness up to ~100 hr of aging at 400°C [18]. Longer aging times result in coarsening of the Ni_4Ti_3 phase or formation of Ni_3Ti_2 and/or Ni_3Ti phases leading to softening of the parts [8, 18, 42]. Hornbuckle et al. [18] explained that in this condition, Ni_4Ti_3 phase provides the heterogeneous nucleate site and Ni-reservoir for the precipitation of the Ni_3Ti_2 and/or Ni_3Ti phases. In another study, Adharapurapu et al. [37] investigated the effect of aging heat-treatments on the precipitation sequence of Ni-rich phases in 60NiTi and developed a time-temperature-transformation chart. In this research, the effect of aging on the hardness variation was also studied.

Quenching from high temperatures with a high cooling rate results in the generation of residual stresses. These may cause dimensional distortion and even quench cracking, especially in parts containing sharp, hard contaminations and voids [20, 21, 34]. Recent researches indicate that the addition of other elements such as Hf, Zr and Ta will decrease the temperature needed to achieve single phase B2 NiTi. This will decrease the quenching rate and consequently the

generated residual stresses in the quenched parts and will reduce the cost and time of the heat treatment [34, 43]. Stanford [21] conducted a systematic research on the hardness and microstructure of binary and ternary Ni-Ti alloys. He compared the hardness and microstructure of each ternary alloy with solutionized and water-quenched 60NiTi, 55 at.% Ni-45 at.% Ti. Heat treatment procedure consisted of solutionizing at 900°C for 2hr, followed by water quenching. The value of hardness achieved for 60NiTi in this condition was 620 HV. Results of this research suggest that hardness of ternary alloys with compositions (ratios in atomic percentage) of 54Ni-45Ti-1Hf, 55Ni-44Ti-1Hf, 54Ni-43Ti-3Hf, 54Ni-43Ti-3Ta, 54Ni-43Ti-3Zr and 54Ni-41Ti-5Hf, were greater than hardness of 60NiTi. Furthermore, ternary alloys with compositions (ratios in atomic percentage) 54Ni-43Ti-3Hf, 54Ni-43Ti-3Zr, 54Ni-41Ti-5Hf and 55Ni-40Ti-5Hf could exceed the 620 HV hardness even if they were heated to only 800 °C.

In another research, Hornbuckle et al. [22, 39] investigated the effect of Hf micro-alloying addition on the microstructure and hardness of some binary and ternary alloys with compositions (ratios in atomic percentage) of 54Ni-46Ti, 54Ni-45Ti-1Hf, 54Ni-44Ti-2Hf, 55Ni-45Ti, 55Ni-44Ti-1Hf, 56Ni-44Ti and 54Ni-40Ti-4H. It was observed that the addition of 2 at.% or greater amounts of Hf was beneficial in terms of achieving harder parts after solutionizing treatments. Amongst all these binary and ternary alloys, 54Ni-40Ti-4H exhibited the highest hardness of ~670 HV and could preserve this hardness up to 300h after aging at 400°C. These observations were attributed to beneficiary aspects of Hf addition in Ni-Ti alloy systems. Hf and Ti are both group IVB transition metals. It is expected that low concentrations of added Hf in Ni-Ti alloy systems would reside in the Ti sub-lattice, boosting the final hardness via a solid-solution strengthening mechanism. Moreover, slower diffusivity of Hf in NiTi phase, compared to Ni and titanium, reduces the kinetics of Ni_4Ti_3 coarsening and prevents its decomposition during aging. Furthermore, aging of ternary Ni-Ti leads to precipitation of complex H-phase. Precipitation of H-phase is assumed to be advantageous in terms of post-aging hardness stability. H-phase formation, which itself can result in increased hardness, will deplete the available Ni that leads to the formation of the higher Ni-content phases, and as a result prevents the decomposition of Ni_4Ti_3 phase.

1.4 Mechanical properties

Hardened 60NiTi is an ordered intermetallic with tendency to brittleness and notch sensitivity in tensile mode [2, 44]. In tension, the alloy can withstand a high stress of ~1.5 GPa and in

compression ~2.5 GPa, exhibiting tension-compression asymmetry common in intermetallic materials [44]. High toughness of 60NiTi under compression is another indicator of tension-compression asymmetric behavior in this alloy [44]. 60NiTi belongs to the family of superelastic materials and exhibits large recoverable elastic strain in compression. Figure 1-11 shows the compression test results for six repeated stress cycles on hardened 60NiTi [4]. During the very first compression cycle, at more than 5% strain and 2.5 GPa load, a permanent deformation offset of about 1 percent occurs. Under the subsequent loading and unloading cycles, the sample did not show any further permanent deformation and, as DellaCorte explains, an "elastic-like" recoverable strain response was exhibited. The hysteresis observed is related to the internal material damping which has roots in reversible austenite-martensite phase transformation [4, 19].

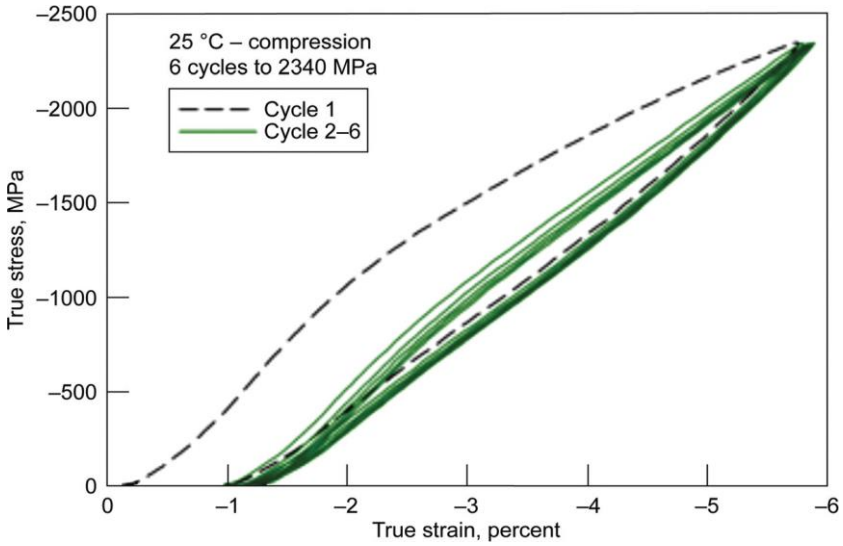

Figure 1-11**:** Compression behavior of hardened 60NiTi. Note: The maximum stress level is limited by the test fixtures [4].

The load applied in this test was higher than the contact load limit of the fixture, so it is expected that hardened 60NiTi can tolerate higher stresses. This level of strength is greater than the strength of Ti alloys and bearing steels such as 440C stainless steel and REX 20 [4, 19]. The elastic range is at least an order of magnitude higher than steel and ceramic [45]. Another feature of 60NiTi is its relatively low elastic stiffness. Its Young's modulus is less than half of that of steels and one-third of that of ceramic silicon nitride [2].

Pre-stressing to the loads and stresses beyond the expected use conditions is a technique used for superelastic materials to assure the maximum degree of elastic behavior [19, 46]. This

technique can certainly be used for hardened 60NiTi so the occurrence of the ~1% permanent deformation after applying the first cycle is avoided in real applications [19].

The effect of aging on compression and tension stress-strain behavior was investgated by Adharapurapu et al. [44]. They showed that typical mechanical properties of 60NiTi such as strength and fracture elongation in both tension and compression mode can be optimized and altered by aging treatment. As expected, the highest strength was obtained from the hardened 60NiTi specimen. In another research, Adharapurapu et al. [37] performed high strain rate dynamic compression tests. Results of these tests were promising and confirmed the potential of 60NiTi in exhibiting high dynamic compressive strength and toughness. Based on the results obtained in high temperature compression tests done by Dehghani et al. [31], the yield stress of hardened 60NiTi decreases with increasing deformation temperature and decrease of strain rate. In addition, dynamic recrystallization was observed for this alloy during the hot compression testing, assisting the hot deformation of this alloy.

Benafan et al. [38, 47] performed cyclic compression and tension tests on hardened 60NiTi. Based on the results obtained from their research, Ni_3Ti phase was formed in tension and coarsening of Ni_4Ti_3 occurred in both tension and compression. These phenomena were attributed to the effect of external stress on the local strain field between the Ni_4Ti_3 and Ni_3Ti phases, leading to selective variant growth of Ni_4Ti_3 phase and formation of other thermodynamically stable phases. It was noted that, although coarsening of Ni_4Ti_3 and the formation of Ni_3Ti occurred in low fractions in one cycle, this phenomenon would definitely be a concern for cyclic mode applications. In fact, coarsening of Ni_4Ti_3 and precipitation of Ni_3Ti are not desirable because they will decrease the strength, become a source of fatigue, and act as preferential corrosion sites.

The dependence of the superelasticity effect in 60NiTi on the loading rate is another important issue that needs attention. In order to investigate this, Neupane et al. [10] performed nano-indentation tests under different loading rates. They observed a drop in superelasticity effect as the loading rate applied by the indenter was increased. This 5%-10% drop in superelasticity, although mild, leads to the generation of more plastic deformation. Neupane et al. [10] attributed this effect to retardation of stress-induced martensite transformation. This can be considered to be a concern for gear and other applications where, for example sliding occurs at high frequencies.

It is essential to consider the inherent brittleness of 60NiTi when it is used under conditions where tensile stress is produced. Inherent brittleness of this alloy is due to the lack of available slip systems and rigid arrangement of atoms in B2 crystal structure. Impact loading is one of the conditions that results in the generation of tensile stress [20, 33]. Stanford [33] performed systematic Charpy impact tests to identify the failure mechanisms of this alloy in various heat treatments and processing methods. This material, regardless of the processing method, exhibits brittle intergranular and intragranular fracture and has relatively low impact resistance. The furnace cooled specimens had an average impact energy of 0.89 to 1.18 J and hardened specimens had average impact energies of 0.33 to 0.49 J.

These impact energies in both water quenched and furnace cooled conditions are low compared to structural alloys such as 410 stainless steel or M50. That said, 60NiTi even in notched conditions exhibits higher impact energies compared to unnotched engineering ceramics (Table 1-1) [33].

Table 1-1: 60NiTi impact test results compared to other engineering materials [33].

Material	**Impact Energy, J**
L2 tool Steel	26
410 stainless steel	34
Cast 60NiTi: Furnace cooled Water-quenched Aged	 1.0 (notched) 0.4 (notched) 0.5 (notched)
Partially stabilized ZrO_2	0.9 (unnotched)
Cold isostatically pressed and sintered Al_2O_3	0.1 (unnotched)
Sintered SiC	0.1 (untouched)
Sintered and HIPped Si_3N_4	0.08 (unnotched) 0.01 (notched)

Aging treatment could not improve much the impact resistance of hardened samples and resulted in impact energies of 0.43±0.08 J, just a minor energy enhancement compared to 0.39±0.08 J for the hardened parts processed by casting [33].

Processing routes can affect the impact resistance and brittleness of 60NiTi parts. Surface oxidation of powder particles prevent the consolidation of the particles in parts produced by HIP, this issue amplifies the brittleness of 60NiTi parts and reduces its impact resistance [20, 32, 33]. Contamination of casting parts with sharp or hard inclusions or the existence of voids has the same effect on their impact resistance. As a result, cleanliness of the objects is very important for the applications where tensile stress is produced [20, 33].

Consideration of rolling contact fatigue (RCF) behavior of hardened 60NiTi is essential for applications such as balls and races in bearings. DellaCorte et al. [36] evaluated RCF of 60NiTi by 3-ball-on-rod fatigue tests complying with the ASTM STP 771 standard. Tests were undertaken at three different stresses of 1.7, 2.5 and 3.6 GPa with test length goal of 800h. Results indicated that the quality of the specimens plays a critical role on the RCF stress of 60NiTi [4, 36]. Samples containing flaws such as oxidation, contaminations and voids failed at low stress levels of 1.7 GPa. These flaws act as stress risers or provide brittle fracture propagation routes and in these ways degrade the mechanical properties [20, 32]. Substituting these samples with high quality 60NiTi parts, like casting specimens devoid of inclusions, stringers and pores or powder metallurgy specimens without unconsolidated particles, improves the results. Using modern powder metallurgy techniques to avoid oxidation of powders and achieving microstructures lacking unconsolidated particles, is an effective strategy to obtain high quality samples. These high quality samples could pass the low stress levels of 1.7 GPa and rarely fail under moderate stresses of 2.5 GPa [34, 36].

The addition of small amounts of other elements such as Hf, which result in microstructural homogeneity, in casting products is another recent strategy to produce high quality parts (figure 1-12). RCF tests were applied on 58Ni39Ti-3Hf (ratios in weight percent) parts manufactured by vacuum induction casting. Results of RCF tests on these specimens were comparable and even in some cases superior to those of high quality samples made by modern powder metallurgy techniques [34]. This ternary compound, designated as 58Ni39Ti-3Hf, containing 57.6 % Ni-39.2 % Ti-3.2 % Hf (54 at.% Ni- 45 at.%Ti-1 at.% Hf), has recently been considered as a substitute or alternative for 60NiTi alloy for applications such as bearings and gears and is under development at NASA [34, 48].

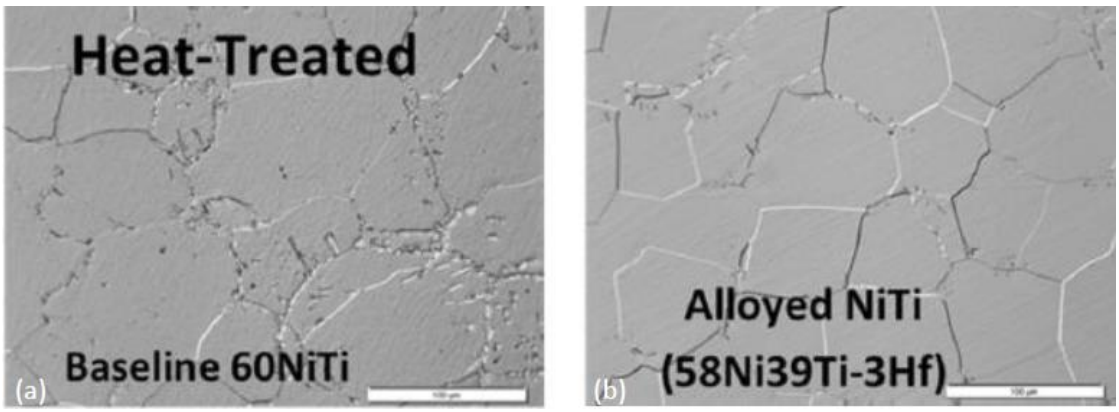

Figure 1-12**:** Comparison of microstructures of (a) 60NiTi, containing contaminations, and (b) 58Ni39Ti3Hf devoid of contamination [34].

Despite this, none of these high quality samples could tolerate high stresses of 3.6 GPa and all rapidly failed. Close-up surface view by SEM revealed that 60NiTi parts, regardless of their quality and manufacturing route, show brittle intergranular and intragranular fracture after RCF tests. This RCF stress limit of 60NiTi is relatively low compared to conventional bearing steels such as 440C steel (~3.5GPa) or high performance bearing steels (~5.5 GPa) [34, 36].

1.5 Resilience

The ability of a material to recover its shape upon removal of force is called resilience. High resilience of a material results in the ability to endure relatively high local stresses without any permanent damage. Hardened 60NiTi exhibits extraordinary resilience in compression mode [25].

High hardness (~60 Rc), relatively low elastic modulus (~100 GPa) and superelasticity of hardened 60NiTi are three main factors that cause its extraordinary resilience [19, 29, 36, 45]. High hardness and strength of this intermetallic means that large applied loads are required to cause permanent deformations in this alloy. A relatively low elastic modulus in 60NiTi means that upon applying a specific load, this material will immediately undergo a high degree of elastic strain [4, 19, 29]. In addition, 60NiTi belongs to the family of superelastic materials. As mentioned, superelasticity effects in 60NiTi cause this alloy to undergo large recoverable elastic deformations of above 5% (figure 1-11) [4, 19, 29, 45]. Furthermore, as DellaCorte et al. [4] described, the superelasticity effect results in a non-linear elastic modulus causing 60NiTi to have an even smaller “effective modulus”. This high degree of elastic strain due to relatively low elastic modulus and superelasticity of 60NiTi results in an expanded contact area under a concentrated applied load and a consequent reduced peak Hertz stress avoiding permanent deformation [4, 19, 25, 29].

A relative comparison between the hardness and recoverable deformation of hardened 60NiTi and bearing steels will effectively demonstrate the potential of 60NiTi to show high resilience. Hardness of hardened 60NiTi is in the same range as hardened bearing steels [4]. On the other hand, the elastic modulus of 60NiTi is similar to that of Ti and Al and is about half of that for steels [29, 45]. While 60NiTi, upon tolerating over 5% strain, will experience just a minor amount of plastic deformation (figure 1-11), typical hardened bearing steels will show permanent plastic damage after going through just 1% strain [4, 19, 29, 36]. DellaCorte et al. [19, 29, 45] performed static indentation tests using a 12.7 mm diameter Si_3N_4 indenter ball on plates of 60NiTi and other typical bearing steels, and plotted their dent load thresholds. They

concluded that a combination of the factors discussed above leads to a 2 to 4 times increase in threshold load in 60NiTi, before experiencing permanent damage, as compared to typical bearing steels such as REX20 and 440C steel (figure 1-13).

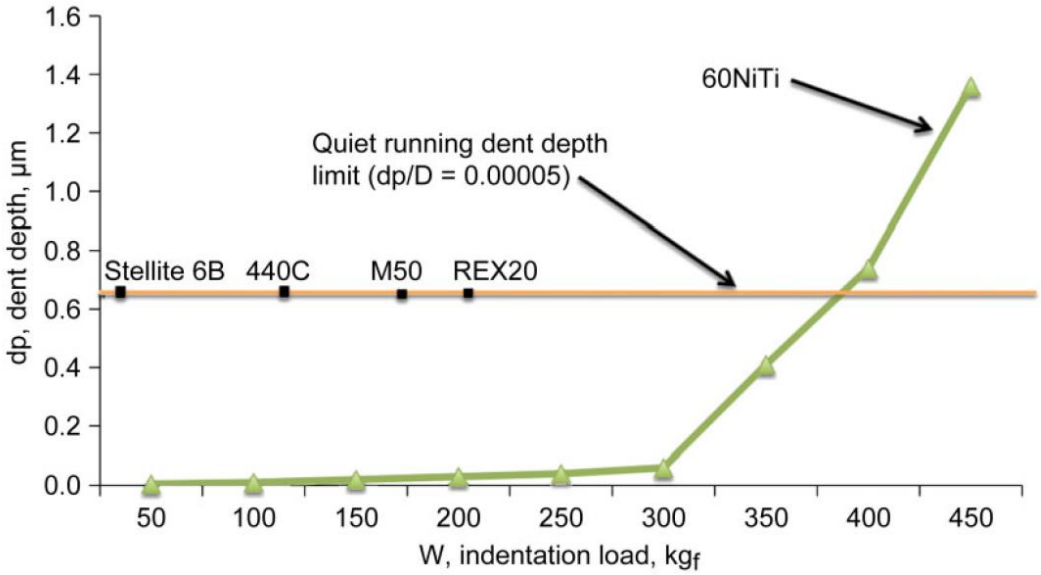

Figure 1-13**:** Indent depths for 60NiTi plate as a function of load when contacted by a 12.7 mm diameter Si_3N_4 indenter ball [29].

As discussed before, pre-stressing is a technique that can be employed on hardened 60NiTi to assure its maximum degree of elastic behavior. Pre-stressing of 60NiTi at 2.70 GPa before conducting static indentation tests, resulted in a 50% improvement in static load threshold. Pre-stressing must be performed after the final hardening stage. If pre-stressing is done before this stage then all its effects will be annihilated due to the high temperature required for hardening treatment [19, 45].

1.6 Tribological properties

Based on classical theories such as Archard's theory, hardness is assumed to be the main critical factor affecting wear characteristics of a material. Based on Archard's theory, the wear resistance of materials is ranked based on their hardness. In other words, the greater the hardness of a material, the more wear resistant it is expected to be [49]. 60NiTi with proper heat treatment exhibits high hardness of approximately 60 RC [41]. This hardness is in the same range as those of typical bearing steels. Considering this fact, hardened 60NiTi is expected to exhibit high wear resistance.

Oberle suggests that hardness is not the only parameter affecting wear [4]. He explains that the elastic deformation of a material under a specific load is another factor that needs to be considered when evaluating the wear resistance of a material. Elastic deformation under a given load results in increased contact area and this leads to reduced peak Hertz stress, hence, reducing wear damage. As a result, Oberle ranks the wear resistance of materials based on their H/E ratio. Hardened 60NiTi, due to its high hardness and low elastic modulus, has an H/E ratio twice that of hardened steels. This high H/E ratio is calculated without considering the effect of superelasticity in reducing the elastic modulus [4]. Meanwhile, according to Li [42] and Lin et al. [14, 50], the variant accommodation and superelasticity will absorb the strain energy at crack tips leading to their stabilization and blunting; this phenomenon prevents (or slows) the propagation of cracks. Considering all these factors, hardened 60NiTi is expected to exhibit high wear resistance comparable, if not superior, to hardened steels.

The wear properties and mechanisms of hardened 60NiTi under unlubricated conditions have not been extensively explored to date. Results of some limited tests suggest that 60NiTi, even under unlubricated conditions, is a good tribological alloy. DellaCorte et al. [1, 5] reported that 60NiTi sliding under unlubricated conditions on 440C plate did not show any sign of galling (figure 1-14), though the reported coefficient of friction (CoF) was high and about 0.3 to 0.4. A higher CoF of 1.1 was obtained under unidirectional ball-on-disk sliding friction experiments done by Miyoshi et al [51]. Zeng and Dong [52] evaluated the wear characteristics of 60NiTi by conducting pin-on-disk tests. In these tests, 60NiTi pin was slid over GCr15 steel. The observed CoF after passing the initial stage was around 0.6 and adhesion was defined as the main mechanism of wear based on surface analysis of the wear tracks with SEM.

The effects of heat treatment and test temperature on the tribological properties of 60NiTi were tested by Nasehi et al. [53]. They conducted pin-on-disk tribology tests using tungsten carbide pins and 60NiTi disks. Tests were conducted at two different temperatures of 25°C and 200°C. Other than the typical hardened 60NiTi samples, a series of hardened and aged (400°C) samples were also tested. The aged samples (aged at 400°C for 1 h) showed Vickers hardness of 650 HV and the hardened ones exhibited a hardness of 560 HV. Regardless of the test temperature, higher hardness of these aged 60NiTi samples did not result in superior wear resistance compared to the non-aged hardened ones. This was attributed to higher toughness and work hardening ability in hardened 60NiTi compared to aged 60NiTi. In addition, both types of sample, despite showing higher wear rates at a high temperature of 400°C than at room

temperature, displayed more stable coefficients of friction at 400°C. Formation of an oxide layer on the surface of 60NiTi at higher temperatures is considered to be an explanation for this observation. These oxide layers may act as solid lubricants. In any case, the coefficients of friction were high at approximately 0.5.

In another research, Neupane and Farhat [10] conducted tribology tests using tungsten carbide ball sliding over 60NiTi plate in a reciprocating ball-on-plate tribology machine. Hardened 60NiTi and aged 60NiTi (400°C for 30 to 60 min) were used in order to examine the effect of heat treatment on the tribological properties. The results obtained in these tests were in agreement with the results that Nasehi et al. [53] reported. The improved hardness of aged 60NiTi did not lead to superior wear properties as compared to non-aged hardened 60NiTi. Adhesion and abrasion were defined as the main wear mechanisms in these alloys. In addition, an average coefficient of friction of 0.6 was observed in unlubricated conditions for both types of this alloy.

In another research, DellaCorte et al. [54] conducted a series of pin-on-disk sliding wear tests and observed unexpected low frictions of just 0.18 for self-mated hardened 60NiTi. Despite observing low friction, the surfaces of the self-mated 60NiTi were rough. The contradiction between this observed low coefficient of friction and other reported relatively high coefficients of frictions could be explained by the sliding speed of the tests. A high coefficient of friction of 1.1 was observed under a test with low sliding speeds of 0.119 m/s while a low coefficient of friction of 0.18 was obtained for the test at a speed of 2.7 m/s [51, 54].

In order to clarify the effect of speed on the obtained coefficients of friction, DellaCorte et al. [54] performed some short duration pin-on-disk tests on self-mated hardened 60NiTi parts sliding over each other. The speed of the sliding varied from 0.27 m/s to 5.4 m/s; it was observed that by increasing the speed, the coefficient of friction dropped from 0.45 to 0.2 in a continuous manner. These were in agreement with the results of the reciprocating sliding wear tests done by Neupane and Farhat [10] where the coefficient of friction dropped from 0.59 to 0.46 due to a rise in sliding frequency from 5 to 20 Hz. 60NiTi is a material with low thermal conductivity of around 10 W/(m.K). It is possible that under high sliding speeds, the heating of self-mated 60NiTi sliding bodies causes the formation of surface oxides. These surface oxides can act as a lubricant and result in the drop in the coefficient of friction [54]. Heating of the sliding counterfaces can also cause the softening of the parts causing the decrease of the surface shear strength. This correspondingly causes a drop in the coefficient of friction [10].

More systematic studies are needed in future for a confident understanding of the causes of this phenomenon.

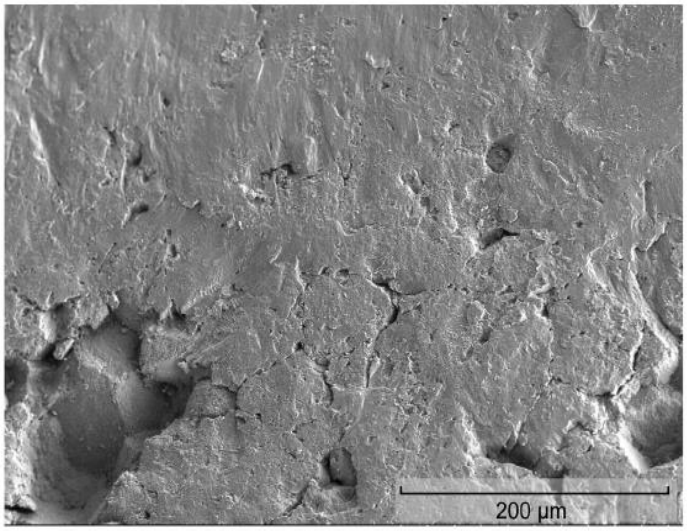

Figure 1-14**:** Surface of a 60NiTi ball sliding under unlubricated condition on 440C plate [5].

Addition of solid or liquid lubricants is a common method used for decreasing the coefficient of friction and consequently wear rate. Deposition of conventional graphite and PTFE (Teflon) dry film lubricants (DFL) was found to successfully decrease coefficients of friction and wear in hardened 60NiTi alloy. These were confirmed by pin-on-disk tests that were performed by DellaCorte et al. [54]. Unlubricated self-mated 60NiTi parts sliding on each other in these tests showed a coefficient of friction of 0.18. Depositing graphite and PTFE dry film lubricants (DFL) dropped the coefficient of friction to 0.15 and 0.17 respectively and resulted in long wear lives in both cases.

Despite these promising mechanical properties, there has been a concern regarding the tribochemical properties of hardened 60NiTi. Metallic alloys with high Ti contents respond poorly to organic fluid lubricants. Ti-6Al-4V is a good example of an alloy with high concentrations of Ti that responds poorly to organic fluids and exhibits galling behavior in lubricated dynamic contacts leading to rough surfaces. This concern of reacting poorly to organic fluid lubricants was evaluated for 60NiTi alloy by performing systematic tribology tests [1, 5, 35, 55, 56].

A tribological study was conducted by using a vacuum spiral orbit tribometer (SOT) to understand the feasibility of lubricating 60NiTi with organic fluids [4]. In this experiment, a hardened 60NiTi-bearing ball slid against 440C plates under boundary conditions lubricated

by Pennzane 2001A oil. By comparing the tribological characteristics of 60NiTi with 440C stainless steel balls tested under the same conditions, it was concluded that 60NiTi alloy exhibits promising lubrication and wear properties. Friction of 60NiTi was lower than 440C. Low (<0.2), constant and noise-free coefficient of friction for 30000 to 50000 disk revolutions in a system lubricated with a few μg of lubricant is an evidence of an acceptable lubrication lifetime. This behavior confirms the mild tribo-chemical properties of 60NiTi (figure 1-15). Additionally, 60NiTi did not show galling behavior when the test was continued beyond the lubricant life of Pennzane 2001A oil. The ability of 60NiTi to be lubricated with other common oils such as Krytox 143AC and Castrol 815Z was confirmed by further tests [1, 4, 5, 35, 55-57].

In another experiment, which was done by a pin-on-disk tribometer, hardened 60NiTi pin sliding on GCr15 steel disk lubricated with poly alpha olefin (PAO) displayed steady and low coefficient of friction of 0.11. This is another piece of evidence confirming the feasibility of lubricating 60NiTi with hydrocarbon and fluorocarbon oils [58].

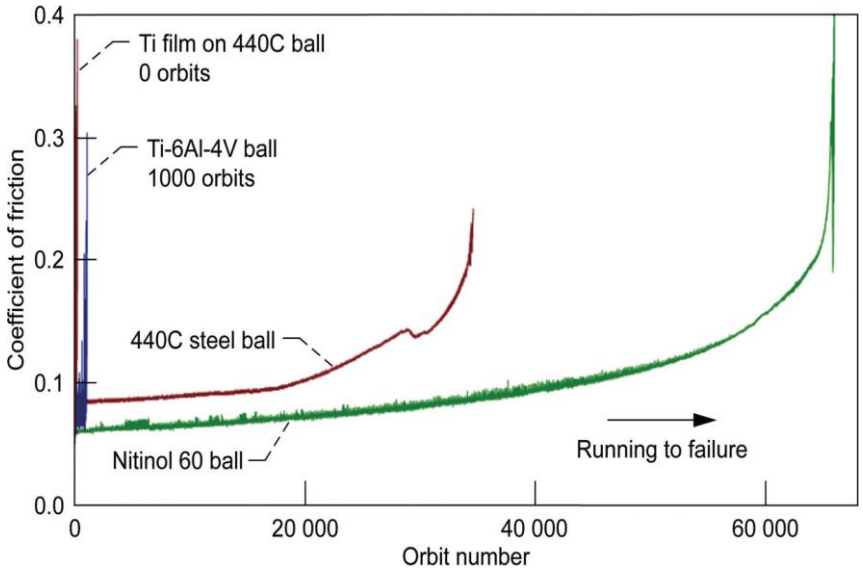

Figure 1-15**:** Friction traces for a 440C steel ball and a 60NiTi ball rolling against 440C plates (right) in boundary-lubricated condition [4].

The fundamental reason for the chemical aggressiveness of Ti metallic alloys toward hydrocarbon and fluorocarbon oils is not well understood yet [5]. In contrast to Ti metallic alloys, some ceramic materials with high concentrations of Ti such as TiC and TiO_2 show good tribo-chemical properties. The benign tribo-chemical properties of hardened 60NiTi as an intermetallic can be attributed to its atomic bonding. The high degree of atomic ordering in this

alloy makes this material behave like a ceramic. In this structure, Ti atoms are passivated by being bonded to Ni ones [1, 5, 35, 56, 57, 59].

For a more fundamental understanding of the observed benign tribo-chemical behavior of hardened 60NiTi, Stott et al. [59] performed a systematic study by using computational tools such as Density of States (DOS) and Density Functional Theory (DFT). They correlated this observation to the delocalized metallic bonding and negative charge accumulation in the Ni lattice.

Synthetic vegetable oils are another source for lubrication of hardened 60NiTi. Applications of these bio-derived vegetable oils are in demand due to their biodegradibility and renewability. Results of the pin-on-disk tests performed by Zeng et al. [52, 60] indicated that boundary lubrication of 60NiTi with different vegetable oils such as caster, turbine, seed and paraffin oils result in low coefficients of frictions. The load applied in these tests was 30N, sliding speed was 0.034 m/s and different counterfaces such as GCr15 steel, HSS tool steel, copper and 60NiTi itself were used as disks against 60NiTi pin. Amongst all these vegetable oils, castor oil was the most effective one and caused the super low coefficient of fiction of 0.008 when steel disks were used against hardened 60NiTi pin. Moreover, worn surfaces of the steel samples, which were boundary lubricated with castor oil were smooth and did not show any visible scar (figure 1-16). This super low coefficient of friction being less than 0.01 is considered to be superlubricity and can have a great number of practical engineering applications. In this state, sliding is approaching rolling and friction is almost not present.

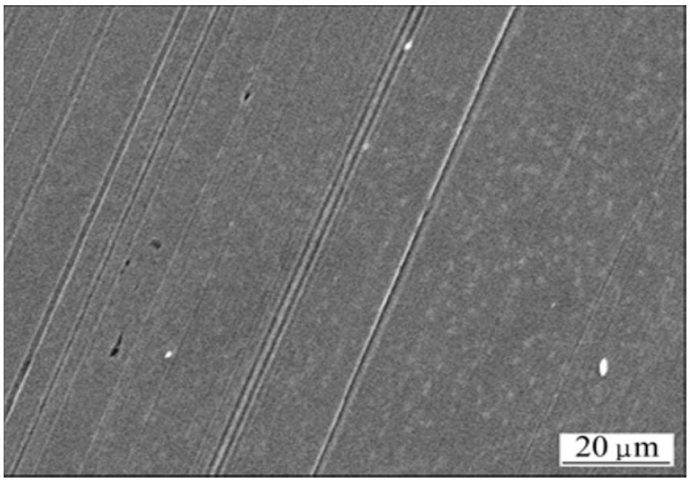

Figure 1-16**:** SEM image of worn surface of 60NiTi alloy pin after 12h wear test [52].

Zeng and Dong [61] conducted a series of pin-on-disk tests with castor oil and with a number of varying parameters for better understanding of this unexpected observation. Load and sliding speed were two of the main parameters that were varied under these tests, in which 60NiTi pin slid over GCr15 steel. Changing the load from 10 to 80 N under a constant speed of 0.034 m/s decreased the stable coefficient of friction from 0.006 to 0.003. Changing sliding speed from 0.034 m/s to 0.667 m/s under a normal load of 30N increased the coefficient of friction from 0.004 to 0.030.

The increase in coefficient of friction with increase in sliding speed was attributed to the poor viscosity index of castor oil. The castor oil heats under high sliding speeds, due to its low thermal conductivity, causing its oxidation and concomitant drop in viscosity. On the other hand, castor oil shows good load-carrying capacity, which is attributed to its high viscosity; high viscosity of castor oil is due to the existence of long and polar fatty acid chains in its structure [61].

A model was proposed by Zeng and Dong [60] to support and explain this excellent superlubricity behavior. Based on this model, the superlubricity is achieved between 60NiTi and only a steel counterface due to the formation of a unique boundary film providing strong repulsive electrostatic forces on the surfaces of the present parts [60].

The 60NiTi's coefficients of friction that are reported in different sources are listed in the following table.

Table 1-2: Coefficient of Friction (CoF) of 60NiTi reported in different sources [1, 10, 51-54, 56, 58, 60].

Pin/ball material	Plate/disk material	Lubrication type and mode	Humidity	Temperature	Load	Sliding speed-Frequency	Steady-state CoF	Initial CoF
60NiTi ball	60NiTi plate	No lubrication	Vacuum	NM*	NM	NM	0.35	
60NiTi ball	440C plate	Pennzane 2001A oil-Boundary	Vacuum	NM	NM	NM	<0.2	<0.1
60NiTi ball	60NiTi plate	Krytox oil-Boundary	Vacuum	NM	NM	NM	<0.2	0.15
60NiTi ball	60NiTi plate	Castrol oil-Boundary	Vacuum	NM	NM	NM	<0.2	0.09
60NiTi ball	60NiTi plate	Pennzane 2001A oil-Boundary	Vacuum	NM	NM	NM	<0.2	0.054

Sapphire ball	60NiTi disk	No lubrication	50% relative humidity	23 °C	NM	0.038 to 0.119 m/s	1.1	
60NiTi pin coated with SP21	60NiTi disk	No lubrication	NM	NM	4.9 N	2.7 m/s	0.15±0.03	
60NiTi pin	60NiTi disk	No lubrication	50% to 60% relative humidity	NM	4.9 N	2.7 m/s	0.18±0.03	
60NiTi pin	60NiTi disk	PTFE (Teflon) - Dry film lubrication	50% to 60% relative humidity	25°C	4.9 N	2.7 m/s	0.15±0.02	
60NiTi pin	60NiTi disk	Graphite-Dry film lubrication	50% to 60% relative humidity	25°C	4.9 N	2.7 m/s	0.17±0.02	
60NiTi pin	GCr15 steel disk	No lubrication	30% relative humidity	24°C	30 N	0.034 m/s	0.6	0.2
60NiTi pin	GCr15 steel disk	Castor oil-Boundary	30% relative humidity	24°C	30 N	0.034 m/s	0.008	0.12
60NiTi pin	GCr15 steel disk	Turbine oil-Boundary	30% relative humidity	24°C	30 N	0.034 m/s	0.2	0.09
60NiTi pin	GCr15 steel disk	Seed oil-Boundary	30% relative humidity	24°C	30 N	0.034 m/s	0.034	0.08
60NiTi pin	GCr15 steel disk	Paraffin oil-Boundary	30% relative humidity	24°C	30 N	0.034 m/s	0.037	0.13
60NiTi pin	60NiTi disk	Castor oil-Boundary	30% relative humidity	24°C	30 N	0.034 m/s	0.3	0.1
60NiTi pin	HSS steel disk	Castor oil-Boundary	30% relative humidity	24°C	30 N		<0.01	<0.01
60NiTi pin	Copper flat	Castor oil-Boundary	30% relative humidity	24°C	30 N		~0.1	~0.1
WC pin	60NiTi disk	No lubrication	NM	25°C	60 N	0.3 m/s	~0.5	
WC pin	60NiTi disk	No lubrication	NM	400 °C	60 N	0.3 m/s	~0.5	
WC ball	60NiTi plate	No lubrication	NM	NM		5 Hz	0.59	
60NiTi pin	GCr15 steel disk	Poly alpha olefin (PAO)	30% relative humidity	24°C	22.9 N	0.2 m/s	0.1	

		-Boundary						

*NM: not mentioned in the source

1.7 Shape memory and superelasticity effects

Many researchers have investigated the effect of Ni concentrations in NiTi phase on the transformation temperatures. These results have been summarized by Tang [62]. Content of Ni in the NiTi composition is a parameter that tremendously affects transformation temperatures in Ni-Ti alloys [1, 3]. As an example, an increase in Ni composition from 50 at.% to 51.5 at.% shifts the martensite start temperature from around 20°C to -100°C (figure 1-17) [37, 44].

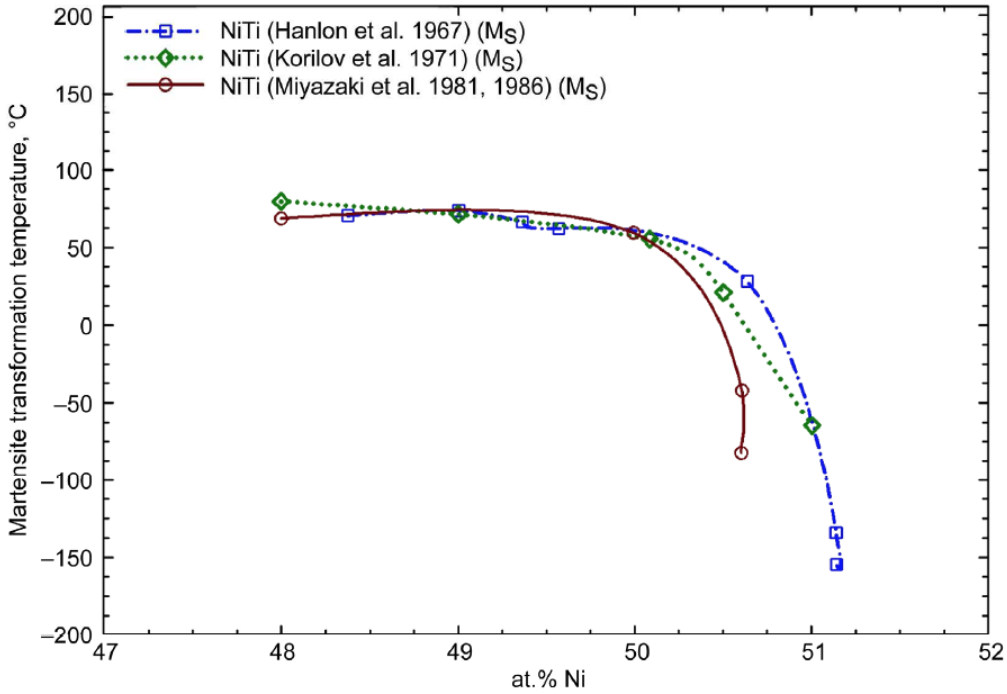

Figure 1-17: Effects of Ni's content in Ni-Ti composition on the martensitic transition temperature exhibiting that at high Ni-contents the martensite transformation temperature drops down to very low temperatures [5].

The results of differential scanning calorimetry (DSC) demonstrate that furnace cooled 60NiTi parts manufactured via HIP powder metallurgy process do not show phase transformation (austenite to martensite) until below -15°C. Standard solution treatment and quenching can shift this temperature to below -100°C making this alloy properly useable as a structural alloy with appropriate dimensional stability (figure 1-18). This is because hardening treatment results in generation of a more Ni-rich NiTi phase than conditions where parts are furnace cooled, as this process solves Ni-rich Ni_3Ti and Ni_3Ti_2 phases inside NiTi [1, 5, 55, 56]. 60NiTi heat treated in this condition is categorized in the family of superelastic materials, as the

austenitic NiTi is stable to below -100°C, and exhibits large recoverable strain of over 5% [9, 30]. In contrast to equiatomic NiTinol, the superelastic effect in hardened 60NiTi is not limited to only approximately 50 degrees above the austenite final temperature; it can be observed until at least 600°C [9].

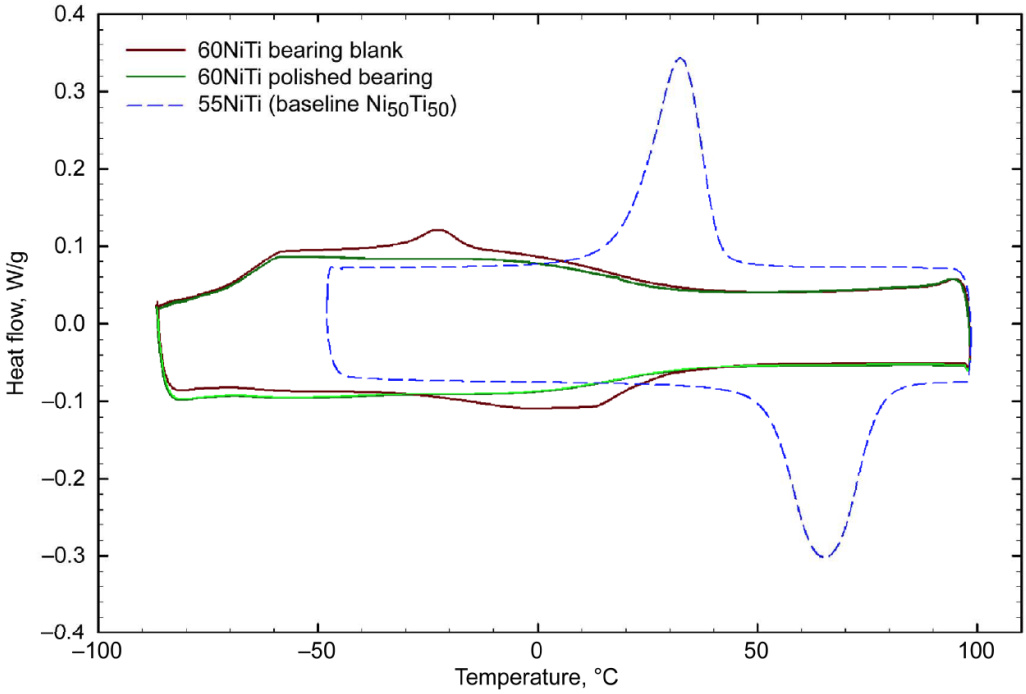

Figure 1-18: DSC behavior of the 60NiTi in the softened (red line) and hardened (green line) conditions in comparison to conventional equiatomic NiTinol [5].

Phase transformation temperatures and consequently the possibility of exploiting shape memory and superelasticity effects in 60NiTi can be tuned and engineered by applying proper heat treatment procedures [3, 5, 44, 63]. Precipitation of stable and metastable Ni-rich phases make the NiTi matrix less Ni-rich and consequently alters the transformation temperatures [44]. Results of research carried out by the Boeing Company indicate that 60NiTi has the potential to be exploited as a shape memory alloy. The transition temperature of 60NiTi is dependent on heat treatment and can be varied extensively [64]. In another research, Adharapurapu and Vecchio [44] investigated the effects of aging on the microstructural evolution. They indicated that basic mechanical properties of 60NiTi such as its toughness and fracture elongation were dependent on aging heat treatment. These changes in mechanical properties were ascribed to the potential of aging heat treatment in tuning superelasticity effects. Wojcik [6] presented an invention that provides efficient methods of predictably controlling the desired austenite transformation temperatures. These findings indicate that 60NiTi could be successfully

exploited as a shape memory or superelastic alloy based on the particular necessity or application.

1.8 Corrosion resistance and biocompatibility

Hardened 60NiTi is expected to show immunity to harsh corrosive agents. Unlike stainless steels, formation of a chrome rich passive layer is not the mechanism making Ni alloys immune to corrosion. Ni is intrinsically highly resistant to aqueous acidic corrosion agents. Ti is highly reactive and its exposure to air and/or moisture results in the formation of a very stable, re-healable and protective oxide film on its surface [25, 65]. Furthermore, 60NiTi does not contain any iron so it is protected against atmospheric rusting [29]. Results of high velocity impingement, cavitation-erosion, stress corrosion and crevice corrosion tests performed by the U.S Navy laboratory prove that 60NiTi has suitable seawater corrosion resistance [8].

60NiTi has the potential to be used in biomedical applications due to its good biocompatibility [9, 66, 67]. That said, the high amount of Ni in 60NiTi (60 wt.%) might cause concern at its use in biomedical applications, due to its toxicity [66, 68]. However, the bonding force in this intermetallic is so strong that it results in passivation of the atoms and prevents their release [9, 69]. In addition, the formation of a TiO_2 passive surface-layer creates a barrier preventing the release of Ni atoms into the body. Furthermore, the toxicity of Ni is less than the toxicity of cobalt, which is used in common CoCr implants [66]. Despite these factors, corrosion and wear could cause the release of Ni atoms into the body and more research regarding the biocompatibility of this alloy and any possible harmful effects is needed.

1.9 Oxidation behavior

The oxidation behavior of 60NiTi is strongly dependent on parameters such as oxygen pressure and environment temperature [3]. Oxidation of Ti is thermodynamically much more favourable than the oxidation of Ni. This results in breakage of Ni-Ti bonding in NiTi phase and preferential oxidation of Ti when 60NiTi is brought into contact with atmosphere containing oxygen. As a result, an excessive content of Ni atoms is left available which cause the formation of the Ni-rich Ni_3Ti_2 and Ni_3Ti regions in the NiTi matrix [59]. Results obtained by Smialek et al. [70] and Firstov et al. [71] indicate the sensitivity of Ni-Ti alloys to high temperature heat treatments in air atmosphere. High temperature heat treatments of over 300°C on these alloys resulted in the formation of Ti-oxides such as TiO_2 and $NiTiO_3$.

Results of experiments conducted by Miyoshi et al. [51] indicate that oxidation of 60NiTi can be beneficial for its tribological properties. Placing the 60NiTi disks in an air furnace and heating them at temperatures between 850°C and 950°C for approximately 2 hrs, followed by rapid quenching, resulted in the formation of a layer primarily consisting of Ti and oxygen on hardened 60NiTi. Results of the unidirectional ball-on-disk sliding experiments indicated that the formation of this TiO_2 film on 60NiTi disks decreased the steady-state coefficient of friction by a factor of 4 (from 1.1 to ~0.26) and increased more than 10 times the wear resistance compared to base hardened 60NiTi.

Formation of an oxide ceramic layer on the surface of hardened 60NiTi parts can be beneficial based on corrosion resistance and from the point of view of biocompatibility [30, 71, 72]. Julien [30] presented an invention that provides a method for the formation of a thin ceramic layer on hardened 60NiTi parts. Based on this invention, heating the 60NiTi parts in an air furnace to about 950°C and then quenching them result in the formation of a hard integral ceramic surface on NiTi matrix. This ceramic layer believed to be a complex mixture of Ti oxides and nitrides, increases the surface hardness from 62 RC of the base material to around 70 RC-80 RC and improves the corrosion resistance. He also proposed that decorative gold ceramic surfaces can be obtained by applying the same procedure at a lower temperature of about 600°C.

1.10 Applications of 60NiTi

Hardened 60NiTi contains promising mechanical properties: high strength, high hardness, moderate elastic modulus, good toughness in compression and superelasticity [2, 4, 25]. This alloy is electrically conductive, non-magnetic and has a thermal expansion coefficient that matches closely with conventional structural materials and has relatively low density [2, 5].

So far, Julien has used hardened 60NiTi in making horsehoes and ski equipment [73, 74]. Furthermore, at this time, this alloy is emerging as a bearing alloy used in ball bearing components for applications that experience shock loads and corrosive environments [45]. Dellacorte et al. [75] showed that bearings made from this alloy are suitable for aerospace applications. There are in fact very many areas in which the presence of hardened 60NiTi can be beneficial. As Julien explains [30], its combination of good mechanical and physical properties with chemical inertness makes this alloy a very desirable material to be employed in chemical and refining plants, ships, applications in and around salt water, food processing and aerospace fields and sectors. DellaCorte and Glennon [35] proposed 60NiTi to be used in

fluid control devices including valves, rotors, shafts and vanes. Good biocompatibility of hardened 60NiTi makes it possible for it to be employed in biomedical applications [9].

However, using 60NiTi is not just limited to its hardened state. The possibility to tune superelasticity and shape memory effects, through the employment of different heat treatment procedures, defines non-hardened 60NiTi as a substitute of equiatomic NiTinol. Actuators, vascular and non-vascular stents and materials for blast mitigation and energy-absorbing structures are amongst those applications where shape memory or superelasticity effects can be exploited [9, 37, 64].

The potential of hardened 60NiTi to be used as a material in biomedical applications and reasons for its recognition to be employed as a material in ball bearing components are explained and discussed in more detail in the following.

Steels (440C, M50, and 52100) and silicon carbide are commonly employed as materials for the manufacture of ball bearings and races [3, 5, 30, 55]. However, all these materials have some deficiencies and none of them contain all the ideal required properties [30, 55]. Steels are hard, have reasonably low cost and their processing is relatively easy. Despite this, steels, even 440C martensitic steel, are prone to corrosion and are highly magnetic. These can limit the employability of these materials in certain applications [1, 5]. Silicon nitride is hard, corrosion proof and is nonmagnetic. The relatively low density of silicon nitride leads to decreased centrifugal forces and is beneficial for the fatigue life of this material. On the other hand, this ceramic is electrically insulating and exhibits a low thermal expansion coefficient causing challenges in certain applications. Furthermore, processing of silicon nitride and specifically making balls from this ceramic is complex and very costly [1, 2, 5, 55]. Moreover, these materials (silicon nitride and steels) are prone to Brinell damage due to their limited recoverable strain of less than 1%. In the event of shock impacts, denting or Brinell damage can occur in these materials leading to poor fatigue behavior [4, 10, 29].

Table 1-3 presents 60NiTi's material properties as compared to common bearing materials. 60NiTi, in a hardened state, shows a high hardness, has a low elastic modulus (as mentioned already, half of steels and one-third of ceramic) and exhibits superelasticity. The combination of these properties results in extraordinary resiliency in this alloy, making this intermetallic very resistant to probable shock loads. Moreover, 60NiTi has relatively low density (15% lighter than steels), is non-magnetic, electrically conductive and has a thermal expansion

coefficient comparable to that of steels. Furthermore, hardened 60NiTi is intrinsically corrosion-resistant and chemically inert. Machining of 60NiTi to the final shapes of ball and race is also readily practical before the final heat treatment. The combination of all these properties is not found in any of the other traditional materials; this makes 60NiTi an attractive candidate for these applications [2, 5, 27, 36, 57].

Table 1-3: Thermophysical and mechanical properties of 60NiTi and other common bearing materials [2].

Property	**60NiTi**	**440C steel**	**Si_3N_4**	**M-50**
Density	6.7 g/cm^3	7.7 g/cm^3	3.2 g/cm^3	8.0 g/cm^3
Hardness	56-62 HRC	58-62 HRC	1300-1500 Hv	60-65 HRC
Thermal cond. W/m-^{0}K	~9-14	24	33	~36
Thermal expansion	~11.2x10^{-6}/^{0}C	10x10^{-6}/^{0}C	2.6x10^{-6}/^{0}C	~11x10^{-6}/^{0}C
Magnetic	Non	Magnetic	Non	Magnetic
Corrosion resistance	Excellent (Aqueous and acidic)	Marginal	Excellent	Poor
Tensile/(Flexural strength)	~1000(1500) MPa	1900 MPa	(600 to 1200) MPa	2500 MPa
Young's Modulus	~95 GPa	200 GPa	310 GPa	210 GPa
Poisson's ratio	~0.34	~0.30	~0.27	~0.30
Fracture toughness	~20 MPa/$\sqrt{m}$	22 MPa/$\sqrt{m}$	5 to 7 MPa/$\sqrt{m}$	20 to 23 MPa/$\sqrt{m}$
Maximum use temp	~400 °C	~400 °C	~1100 °C	~400 °C
Electrical resistivity	~1.04 x 10^{-6} Ω-m	~0.60 x 10^{-6} Ω-m	Insulator	~0.18 x 10^{-6} Ω-m

Minimally invasive surgical tools such as knives, clamps, scissors and cutters are commonly made up of stainless steel and Ti [3]. Hardened 60NiTi has higher strength than Ti and exhibits better corrosion resistance than stainless steel [9, 19, 76]. In addition, it has relatively low density and good biocompatibility [2, 9]. As a result, 60NiTi can be considered as a substitute for stainless steel and Ti in these applications [3, 35].

Artificial joint surfaces and implants are made of materials with high hardness, high toughness, good tribological properties, resistance to corrosion and good biocompatibility [76-79]. CoCr alloys, Ti6Al4V, 316L stainless steel and some ceramics are common materials used in making artificial joints [79, 80]. Despite combining good biocompatibility and mechanical strength, ceramics lack adequate toughness [76, 78]. CoCr alloys exhibit good mechanical and tribological properties but their stiffness (~240 GPa) is considerably higher than bone (11-23 GPa for cortical bone) [76, 77]. This high stiffness of CoCr implants compared to bone results

in the detrimental phenomenon of stress shielding, which causes bone resorption [76]. Ti6Al4V alloy exhibits excellent corrosion resistant, have relatively low elastic modulus and excellent biocompatibility but do not show good tribological properties, which can result in aseptic loosening. Aseptic loosening is a common issue caused by excessive wear between artificial articulating surfaces [76]. 60NiTi shows good tribological properties (as it does not show any sign of galling under sliding wear conditions) and has high toughness in compression mode. Its elastic modulus (~100GPa) is in the same range as Ti6Al4V and significantly lower than CoCr, and would therefore result in a reduction of the stress shielding phenomenon [27, 35, 76]. Moreover, 60NiTi has excellent corrosion resistance, good biocompatibility and allows fine surface finishes that is very important to decrease the failure susceptibility in implants [9, 35, 44]. Due to all these attributes, 60NiTi can be proposed as a suitable material for employment in load bearing joint replacement applications [35].

1.11 Outline and objectives of the thesis

As explained, hardened 60NiTi shows a hardness of around 60 HRC and a low elastic modulus of ~100GPa [2]. This alloy has a hardness of the same range and an H/E ratio that is twice that of typical hardened bearing steels such as 440C stainless steel [4]. Under macroscopic tensile tests, 60NiTi and 440C steel show similar high strengths. In addition, 60NiTi shows high toughness in compression, hindering nucleation and propagation of cracks [50]. Furthermore, materials with high H/E ratios are thought to deform in sinking mode and not piling up mode under indentation. This deformation mode results in less shear stress needed for detachment of the adhered surfaces than the situation where deformation happens in piling up mode. As a result, materials with a high H/E ratio are expected to show low coefficients of friction [81, 82]. Considering all the above mentioned factors and classical wear theories such as Archard's and the model proposed by Oberle, 60NiTi is expected to show sliding wear levels comparable, if not superior, to competing alloys such as 440C stainless steel [4, 49].

However, so far the sliding wear properties of hardened 60NiTi have not been compared to conventional sliding wear resistant alloys, e.g. 440C steel. It is not known whether the sliding wear behavior of 60NiTi follows the mentioned conventional wear theories or whether it is practically a suitable candidate to be used as a load bearing wear resistant alloy in sliding applications. This case is proposed here to be an important topic requiring further research and investigation. In this thesis, a series of comprehensive lubricated and unlubricated reciprocating sliding wear, scratch, indentation and microscopy experiments are conducted under moderate

and extreme stress conditions to compare and evaluate the possibility of employing 60NiTi as an alternative to 440C steel, a conventional wear resistant alloy, in sliding applications such as gears where contacting materials slide over each other. Further, localized sliding arises in rolling contact bearings, especially those used at low speeds and high loads where NiTi alloys are expected to be applied. In this respect, the sliding tests can be viewed as an accelerated and more aggressive simulation of a ball bearing.

As part of these investigations, Chapter 2 discusses the general sliding wear properties of 60NiTi as compared to 440C steel, investigates the mechanisms causing damage and wear in 60NiTi and 440C steel and conditions where 60NiTi shows a different sliding wear property than 440C steel. The reasons behind these observations and the differences in the sliding wear behavior of 60NiTi and 440C steel are investigated in Chapter 3. In addition, using a stress model and experimentation, the precise conditions under which 60NiTi shows a proper sliding behavior for sliding applications are defined. This research, in addition to introducing 60NiTi as a material having the potential for use in load bearing applications other than rolling, will help the engineering community to properly apply 60NiTi in situations where materials slide over each other.

The addition of small amounts of other elements such as Hf has decreased the solutionizing temperature, has resulted in microstructural homogeneity and has improved the fatigue behavior of 60NiTi [34]. As explained, these findings have caused an interest in considering a NiTi-Hf alloy (54 at.% Ni- 45 at.%Ti-1 at.% Hf) as a substitute or alternative for 60NiTi alloy. The effect of Hf-addition on other mechanical properties and specifically sliding wear characteristics are also part of the investigations carried out in the current research (Chapter 4). Again, careful scratch, indentation, microscopy and sliding wear tests with the same test devices and under the same types of lubrication are conducted for a better understanding of mechanical properties and damage mechanisms causing wear of this ternary compound as compared to the forerunner 60NiTi. Results obtained from this research help in better recognition and development of this NiTi-Hf alloy and evaluate the possibility of being a substitute for baseline 60NiTi in sliding conditions.

Chapters 5, 6 and 7 discuss the possibility of employing 60NiTi in another distinct load bearing area. As discussed before, hardened 60NiTi possessing outstanding mechanical properties and also good biocompatibility, is a suitable alloy for use in load bearing biomedical applications. For general bone replacement applications such as spinal or cranial inserts, implants with a

porous structure are desirable. Such a structure helps lower the unwelcome stress-shielding phenomenon as it results in a decrease of the elastic modulus of an implant [27, 35, 76]. Furthermore, an interconnected porous structure results in better bone ingrowth which is beneficial in terms of bone healing [83, 84]. These chapters discuss the possibility of developing porous hardened 60NiTi parts, suitable for general bone replacement applications, by the cost-effective conventional press-and-sinter method using blended Ni and Ti powders. Due to the importance and role of the sintering procedure on the properties of the final parts, Chapter 5 will specifically investigate the effect of critical processing parameters such as pressing pressure, sintering temperature, heating rate and sintering holding on the dimensional stability, density, porosity characteristics, microstructural properties and phase structure of the as-sintered parts.

Chapter 6 investigates the possibility of homogenizing porous 60NiTi by a cost-effective hardening treatment, as hardening treatment is an essential part to obtain homogenous biocompatible 60NiTi parts suitable for biomedical applications. As an outcome, a cost-effective hardening method is proposed in this chapter to successfully solutionize and homogenize porous 60NiTi parts. Effects of the hardening treatment on the microstructure and mechanical properties of as-sintered 60NiTi parts are investigated in Chapter 7. This chapter also discusses the relation between the microstructure and the mechanical properties of hardened 60NiTi parts containing different amounts of open porosity. In addition, the possibility of applying these porous structures for general bone replacements, in terms of microstructural, mechanical and chemical properties, are discussed in this chapter.

At last, chapter 8 provides the main conclusions of the thesis and suggests potential areas deserving further research and investigation.

Note that, other than the general review provided in this chapter, to better clarify the topic, each separate chapter (Chapters1-7) also contains a specific literature review and introduction suitable for the purpose of the topic under discussion.

Chapter 2 Reciprocating sliding wear behavior of 60NiTi as compared to 440C steel under lubricated and unlubricated conditions[2]

[2] **Khanlari K**, Ramezani M, Kelly P, Cao P, Neitzert T. Reciprocating sliding wear behavior of 60NiTi as compared to 440C steel under lubricated and unlubricated conditions. *Tribology Transactions*, https://doi.org/10.1080/10402004.2018.1460434.

As discussed in the introductory chapter, NiTi alloy has a unique set of desirable properties. These include showing high hardness (~60 HRC), compressive strength (~2500 MPa), exhibiting a superelasticity effect, and having high corrosion resistance [2, 4, 19, 25, 26]. In order to obtain these properties 60NiTi must be used in the hardened condition which is achieved through solutionization followed by rapid cooling (as discussed in section 1.3).

Classical wear theories such as Archard's theory consider hardness to be the main factor playing a role in the wear characteristics of a material [49]. As discussed in section 1.6, Oberle suggests using the hardness to elastic modulus ratio (H/E) as a factor influencing the wear resistance of alloys [4]. Based on these theories and models, 60NiTi is expected to exhibit a high wear resistance, as its hardness is in the same range and its H/E ratio is twice that of hardened steels [4], implying that it can be employed as a wear resistant alloy in applications where parts are sliding over each other.

To date, the sliding wear properties of 60NiTi have not been comprehensively investigated. According to limited sliding wear tests, 60NiTi exhibits high coefficients of friction (CoF) and a rough surface under unlubricated conditions [1, 5, 51, 52, 54]. Neupane and Farhat [10] performed sliding wear tests using a WC ball mating 60NiTi plate. They determined adhesion and abrasion as the main wear mechanisms in this alloy. However, in another research, Zeng and Dong [52] evaluated the wear behavior of 60NiTi pins sliding over GCr15 steel and defined adhesion to be the main wear mechanism of this alloy.

As discussed in section 1.6, Ti metallic alloys generally show poor response to hydrocarbon and fluorocarbon oils due to their chemical aggressiveness toward these chemicals [1, 5, 35, 55, 56] . This has resulted in a concern regarding the possibility of lubricating 60NiTi with

these types of oils. However, results of different lubricated tribology tests conducted on 60NiTi show the opposite. Low (<0.2) and steady coefficients of friction with acceptable lifetimes were obtained under boundary lubricated conditions with hydrocarbon and fluorocarbon oils such as poly alpha olefin (PAO) and multiply-alkylated cyclopentane (MAC) oil [1, 4, 5, 35, 55-58].

Despite this, sliding wear behavior of hardened 60NiTi has not yet been systematically studied and compared with other hard materials. It is not yet clear if the wear resistance of 60NiTi follows the conventional wear theories, such as that of Archard and the model proposed by Oberle. To the best of our knowledge, no investigation has been conducted so far to compare the wear resistance of 60NiTi with other materials that have relatively the same hardness.

In this chapter, the sliding wear behavior of hardened 60NiTi is compared to 440C steel through reciprocating sliding tests (ball-on-plate) under lubricated and unlubricated conditions. 440C steel, which is a conventional ball bearing and wear resistant alloy, has approximately the same hardness as 60NiTi and as a result is appropriate to be compared with 60NiTi to answer the questions mentioned above. Results of this study, other than answering the earlier questions mentioned before, help in better understanding of the wear behavior, the mechanisms causing damage and wear in 60NiTi and 440C steel, and the conditions where 60NiTi shows a different sliding wear property than 440C steel. Moreover, these results can be used to evaluate the suitability of 60NiTi for use as a wear resistant alloy in sliding contact conditions.

2.1 Materials and experimental methods

2.1.1 60NiTi and 440C steel specimen preparation and testing

Hardened 60NiTi samples were received from the National Aeronautics and Space Administration (NASA), Glenn Research Center in Cleveland, Ohio. These samples were processed through Hot Isostatic Pressing (HIP) method. The details regarding the fabrication of the 60NiTi parts are given in [32]. Residual thermal stresses that are created by the quenching step might lead to fracture during subsequent cutting of the samples. To avoid this, these samples were cut into plates (of a suitable size to fit in the tribology machine) prior to conduction of the final hardening treatment [1]. To obtain a high hardness of ~60HRC, samples were hardened through a solutionizing treatment carried out at ~1050°C under an open atmosphere condition followed by water quenching. Similar to the 60NiTi samples, 440C steel bars received in a soft annealed condition were first cut into plates of a size suitable for the

tribology machine. The samples were next hardened and tempered using the following procedure: 1) Samples were annealed at 680°C for one hour and afterwards were air-cooled to ambient temperature. 2) Samples were solutionized at 1030°C for 30 minutes after being preheated at two different temperatures of 640°C and 860°C for 30 minutes. All these procedures were conducted under nitrogen protective atmosphere. 3) Solutionized samples were quenched with nitrogen gas to 350°C and then fan air-cooled to ambient temperature. 4) Samples were tempered for two hours at 180°C twice.

Grinding and polishing processes were carried out to an average surface roughness (R_a) of about 0.03 μm for all samples prior to conduction of any test. This procedure was carried out using SiC abrasive papers of P80, P180, P360, P800, P1200 and P2400. However, to reveal the different phases existing in the microstructure, samples used for the microstructural studies were additionally etched. 60NiTi samples were swab-etched with a room temperature aqueous solution of 1 vol. % HF and 10 Vol. % HNO_3 for 90 seconds [85]. In addition, a room temperature solution, consisting of 15cm^3 HCl, 10 cm^3 glycerol and 5cm^3 HNO_3 was used to swab-etch the 440C steel samples. Microstructure and phase composition of these hardened samples were studied using a Hitachi-su70 scanning electron microscopy (SEM) machine (working based on the emissions received from the secondary electrons) equipped with an energy dispersive spectroscopy (EDS) and an X-ray diffraction (XRD) machine using Cu Kα radiation. Note that in this study, the EDS elemental analysis were conducted based on the emissions received from the secondary electrons and to confidently ascertain the elemental ratio of precipitates, these studies were done at different spots.

2.1.2 Macro hardness and sliding wear testing

A Rockwell C hardness tester was used to measure the surface hardness of the samples. The wear tests were performed on a linear reciprocating tribometer using 60NiTi and 440C steel plates against WC balls (purchased from ABOTTBALL company) with a diameter 6 mm. The friction forces and CoF values were simultaneously recorded by a data acquisition system during the wear tests. The wear tests were conducted at varying loads of 2, 5, 10, 30 and 40 N under unlubricated and lubricated conditions at room temperature. These tests were performed under a constant frequency of 2 Hz for 1 hour and 42 minutes and a constant wear track length of 20 mm. These parameters were selected to cover the sliding distance of 500 m. Lubricated tests were performed using two different lubricants: castor oil and a fully formulated PAO gear

oil. A small quantity of oil (2-3 droplets) was dropped onto the plate before starting each test to ensure that the lubricated tests are conducted under boundary lubrication regime.

Carrying out the experiments under lubricated and unlubricated conditions under a wide range of loads allows the evaluation of the response of 60NiTi to a range of low-to-high sliding-induced tensile stresses. Since such tensile stresses are thought to be a main contributor to damage for brittle materials under sliding motions, the use of a hard counterface (6 mm diameter WC ball) may help elucidate the wear processes and damage behavior, as it results in the generation of high stresses [86]. In addition, the high stresses mimic the localized high-stress micro-sliding that occurs in rolling contact bearings.

A stylus profiler was employed to obtain the cross-sectional profiles of the wear tracks. Next, the wear areas were computed from these profiles using an imaging analysis software. Finally, the averaged wear areas were multiplied by the wear track length (20 mm) to conclude the wear volume of the wear tracks. In addition, the SEM machine and EDS elemental analysis method were employed to study the surface and subsurface microstructures of samples, generated debris and counterface balls after the tribology tests.

All the tests mentioned above were repeated three times and the average obtained results are reported.

2.2 Results and discussion

2.2.1 Microstructural and phase compositional studies

Figure 2-1 shows the surface microstructural features of 60NiTi and 440C steel samples (Apart from undergoing the grinding and polishing procedure, samples were additionally etched to reveal the microstructure.)

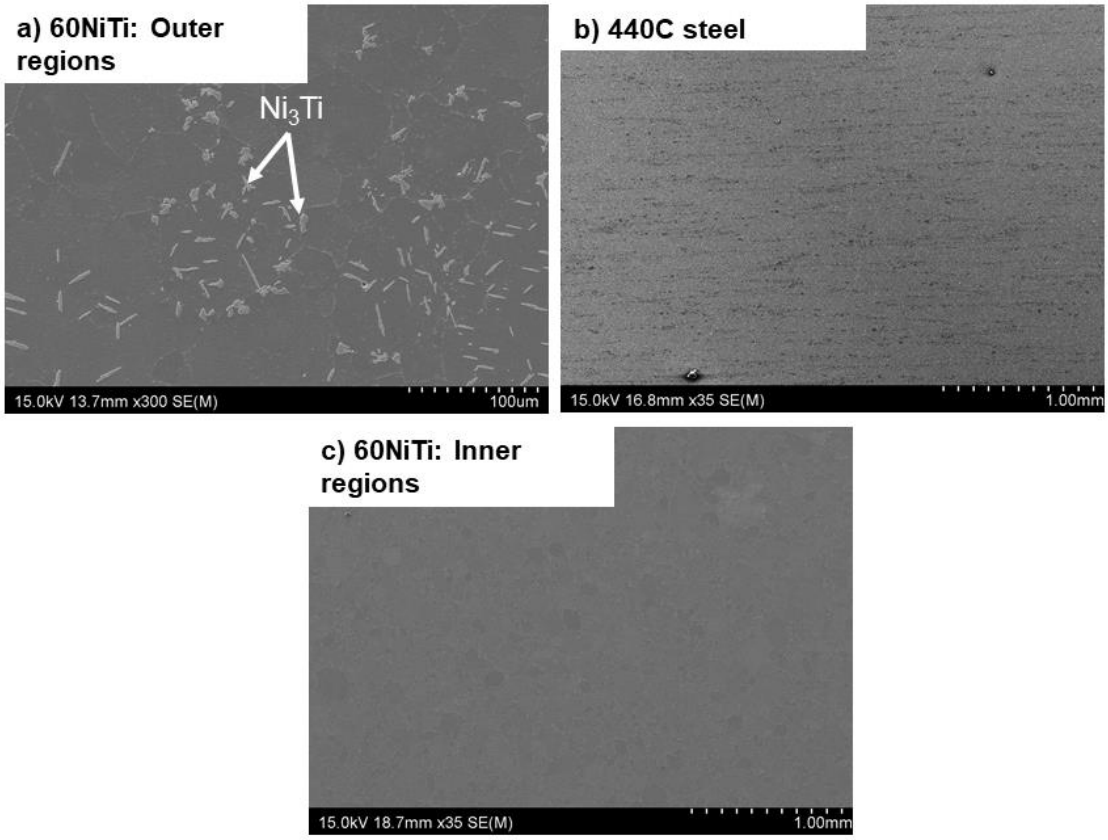

Figure 2-1: SEM images showing the microstructure of a) 60NiTi, outer surface regions, b) 440C steel samples, outer surface regions and c) 60NiTi, inner surface regions. Note that these samples have been etched to reveal the microstructure.

As explained by Hornbuckle et al. [18], hardened 60NiTi is expected to have a uniform NiTi structure with fine Ni_4Ti_3 phases smaller than the resolution of the SEM. However, some bright precipitates are seen in the matrix of 60NiTi samples (figure 2-1.a). As shown by the EDS elemental analysis tests carried out over different areas, the bright phases contain about 76 wt.% Ni and about 24 wt.% Ti. This indicates the formation of Ni-rich Ni_3Ti (based on the

Ni:Ti ratio reported in [35]) in the matrix containing about 57 wt.% Ni and about 43 wt.% Ti (figure 2-2.a).

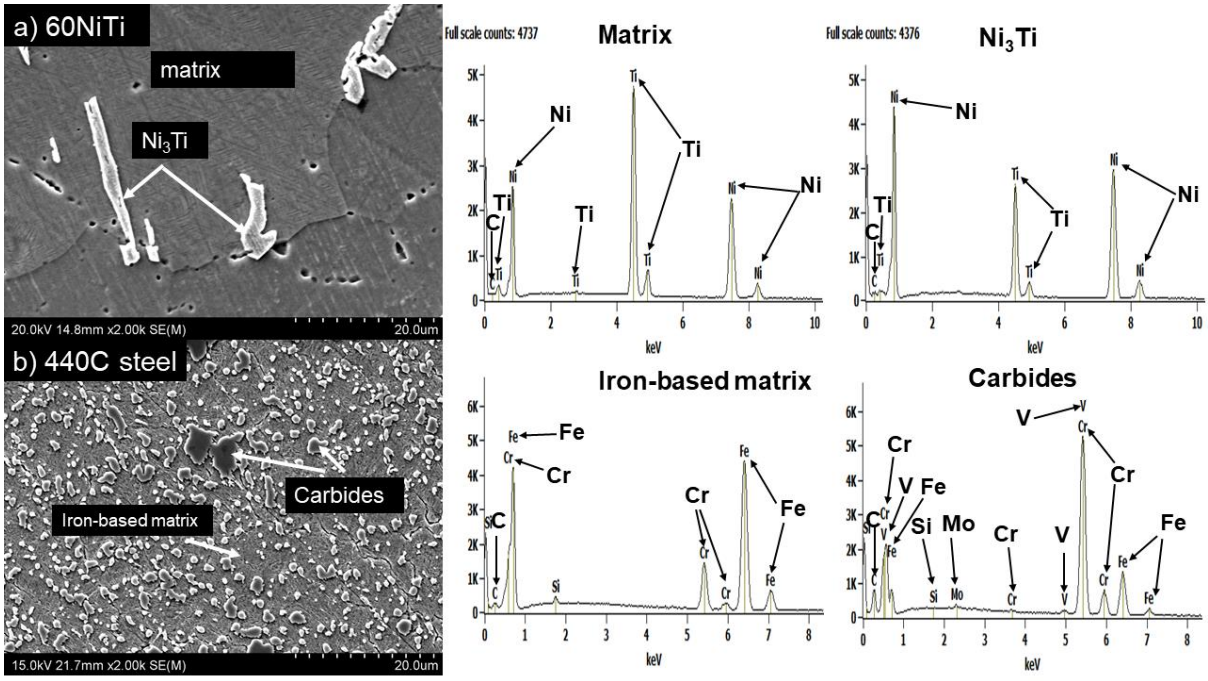

Figure 2-2: SEM image and EDS elemental analysis of a) 60NiTi and b) 440C steel. Note that EDS is not an accurate technique for characterization and quantification of light elements such as C and O due to their low atomic number.

Solutionizing heat treatment for 60NiTi alloy was conducted under open atmosphere condition. At the high temperatures solutionizing procedure, Ti existing on the surface layer reacted with oxygen gas in air causing the formation of an oxide layer over the 60NiTi matrix. This resulted in the formation of an atmosphere-affected region on the surface, due to the reaction of Ti with oxygen gas existing in air, causing depletion of Ti in the matrix. This consequently resulted in precipitation of Ni-rich (bright phase) phases in the Ti-depleted matrix (figure 2-1.a). These precipitates are visible in the etched microstructure after the removal of the oxide layer by the grinding and polishing procedure.

XRD analysis of 60NiTi samples obtained from outer surface regions confirmed the results of the microstructural studies (figure 2-3). The major peaks detected in the pattern of 60NiTi samples were correlated to austenitic NiTi and Ni_4Ti_3. In addition, a very small peak attributed to Ni_3Ti is observed. Since the peak correlated to this phase is very small, it can be concluded that this phase has low volume fraction in these samples. Note, however, that the formation of

these precipitates was avoided in the inner regions of 60NiTi as these areas were not exposed to air during the heat treatment procedure (figure 2-1.c).

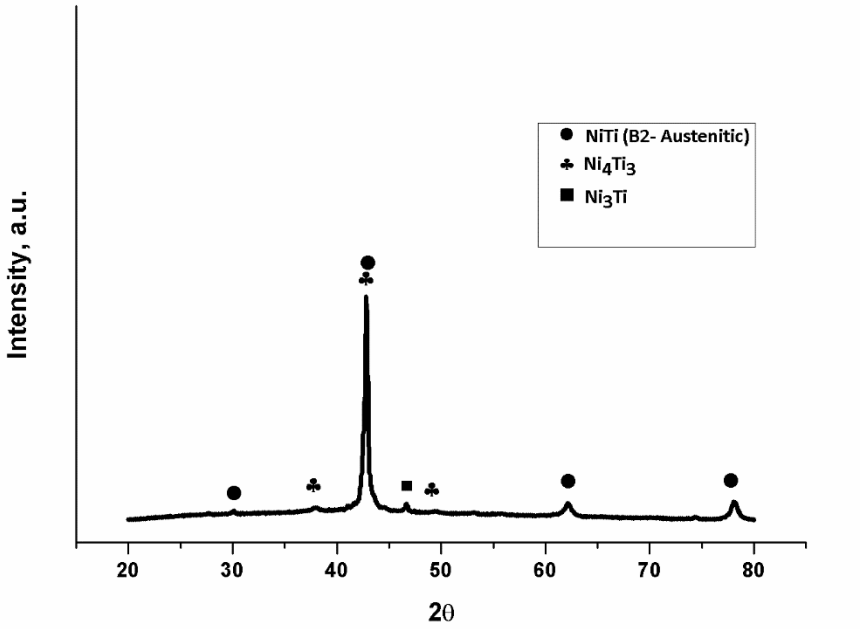

Figure 2-3: XRD pattern of 60NiTi.

Note that the Ni_4Ti_3 precipitates, being responsible for the hardening of 60NiTi parts, are not visible in this microstructural image (figure 2-1.a, c). This is because these precipitates are in nano-scale making them impossible to be observed by SEM under this magnification. However, under a SEM image obtained at a very high magnification of 25.0 k (figure 2-4), a large volume fraction of nano-scale bright platelets could be observed that are bound in narrow matrix channels. Unfortunately, the EDS elemental analysis has insufficient lateral resolution to identify the compositional difference existing between the bright platelets and the matrix spacing them. Hornbuckle et al. [18], using multiple beam bright field and scanning TEM-high angle annular dark field (STEM-HAADF) imaging methods, attributed these nanoscale precipitates to hard Ni_4Ti_3 phase that is formed with narrow channels of austenitic NiTi. They identified the austenitic NiTi channel width to be from ~5 to 10 nm and the volume fraction of Ni_4Ti_3 precipitates to be ~69%.

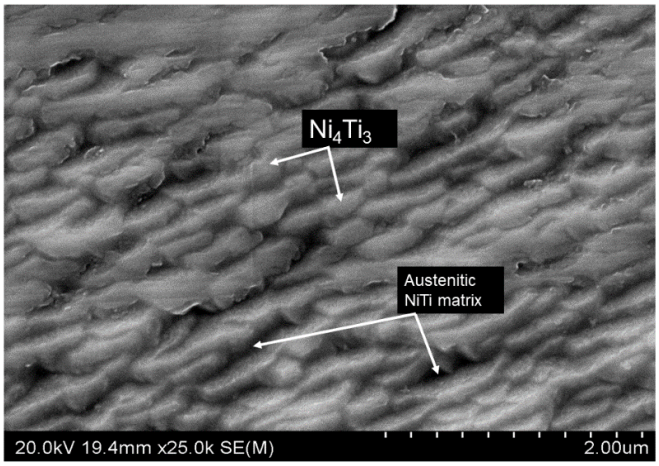

Figure 2-4: High magnification SEM image showing a high portion of Ni_4Ti_3 precipitates in narrow channels of austenitic NiTi matrix.

As shown in figure 2-1.b and 2-2.b, 440C steel consists of large particles in the matrix. Note that EDS is not an accurate technique for characterization and quantification of light elements such as C and O due to their low atomic number. However, based on the results of microstructural studies carried out on the etched 440C steel samples [87, 88], these particles are attributed to brittle carbides formed by precipitation in an iron-based matrix.

2.2.2 Macro hardness and sliding test studies

Results of the standard Rockwell C hardness tests, similar to the microstructural and phase compositional studies, confirm that the final hardening treatment has been successful in rendering the studied alloys into their hardened state. This is because both 60NiTi and 440C steel showed expected high hardness. Based on the results obtained from the hardness tests, 60NiTi exhibited greater hardness values (~59.6 HRC) than 440C steel (~58 HRC). These hardness values were the average of three tests and the standard deviations of the results were less than 0.4. Combining this with the lower stiffness of 60NiTi as compared to 440C steel [27] imply that, according to Archard's theory and Oberle's model, 60NiTi is expected to show comparable (Archard model) or superior (Oberle model) wear resistance to 440C steel. In contradiction, as seen in table 2-1 and figure 2-5, under dry sliding condition, 60NiTi showed poor wear performance compared to 440C. Despite comparable hardness and compressive strength, the average specific wear rate of 60NiTi was ~15 (under 40 N) to ~133 times (under 5 N) higher than 440C steel.

Table 2-1: Wear properties of 60NiTi and 440C steel under unlubricated conditions.

Material	Load (N)	Average CoF	Average specific wear rate (mm^3 / m.N)
60NiTi	2	1.64	1.33E-04
440C steel	2	1.37	3.14E-06
60NiTi	5	1.18	2.41E-04
440C steel	5	0.99	1.80E-06
60NiTi	10	1.03	2.12E-04
440C steel	10	0.85	4.87E-06
60NiTi	30	0.83	1.17E-04
440C steel	30	0.71	5.45E-06
60NiTi	40	0.80	9.34E-05
440C steel	40	0.67	6.13E-06

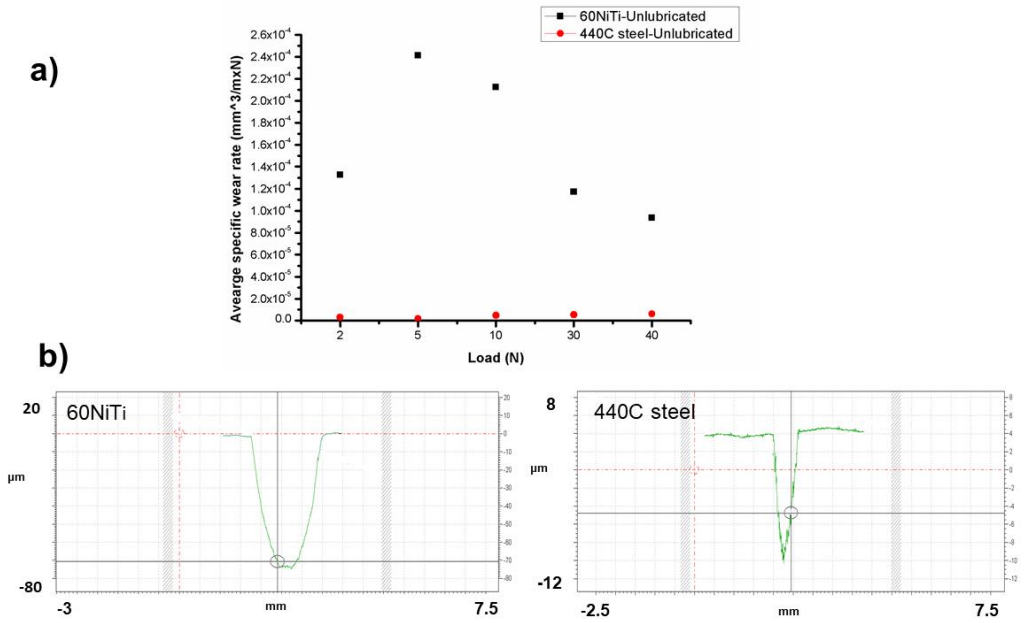

Figure 2-5: Graph showing a) Specific wear rates of 60NiTi and 440C steel under unlubricated conditions and b) Cross-sectional profiles of the wear tracks worn under 40N load. Note that the maximum value for the standard deviation in all the loads was 0.1×10^{-4} (mm^3/m.N) for 60NiTi and 0.1×10^{-5} (mm^3/m.N) for 440C steel.

Some morphologies of the unlubricated worn surfaces are demonstrated in figures 2-6.a-d. As can be seen, abrasive wear was the main mechanism of wear for 440C steel. In 440C steel, the abrasive wear was governed by plastic deformation resulting in ploughing grooves under both low and high loads (figure 2-6.b, d and f). Different from the steel, grooves on the worn surfaces of 60NiTi did not show much ploughing and plastic deformation (figure 2-6.a, c, and e). As seen in figure 2-7, the wear surface in 60NiTi consisted of a series of parallel grooves, scratch marks and fine wear debris. These are also characteristic of abrasive wear [89] but on a different (higher wear rate) scale than for the 440C specimens. The wear for 60NiTi appears to be abrasive wear that is possibly enhanced by adhesion between the WC ball and the 60NiTi as will be discussed in more detail later.

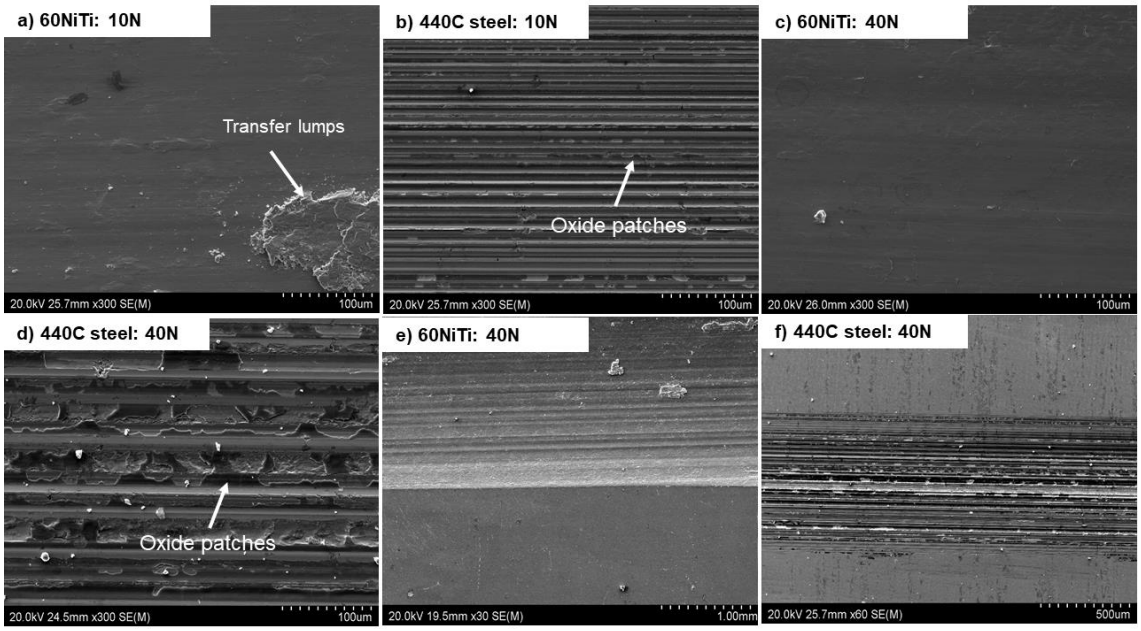

Figure 2-6: SEM images of 60NiTi and 440C wear tracks tested under unlubricated conditions. a) 60NiTi: 10N, b) 440C steel: 10N, c) 60NiTi: 40N, d) 440C steel: 40N, e) 60NiTi: 40N load, showing the unworn (and unetched) baseline area beside the wear track, f) 440C steel: 40N load, showing the unworn (and unetched) baseline area beside the wear track.

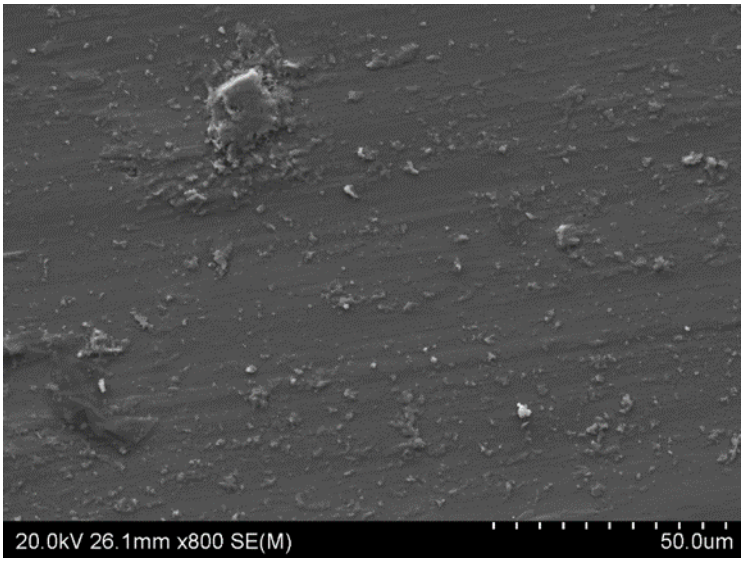

Figure 2-7: SEM image of 60NiTi, showing fine wear debris on the wear track, tested under an unlubricated condition and 5 N load.

Moreover, it was found that at a high load of 40N micro-cracks are developed and extended perpendicular to the sliding direction (figure 2-8). These micro-cracks would be due to stresses that become tensile behind the moving ball and eventually lead to the fracture of material.

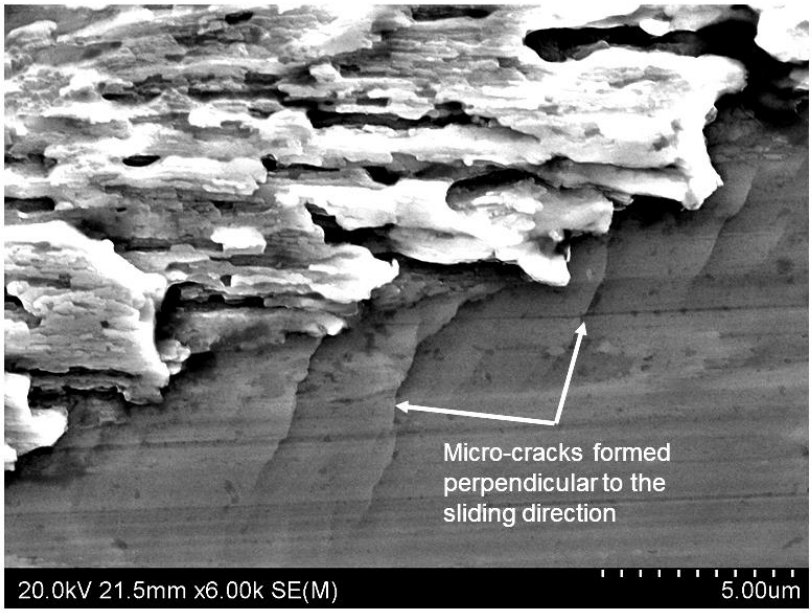

Figure 2-8: SEM image of 60NiTi wear tracks tested under an unlubricated condition and 40 N load.

In addition, some transferred lumps are seen in the SEM images of the 60NiTi samples worn under lower loads (figure 2-6.a, figure 2-9).

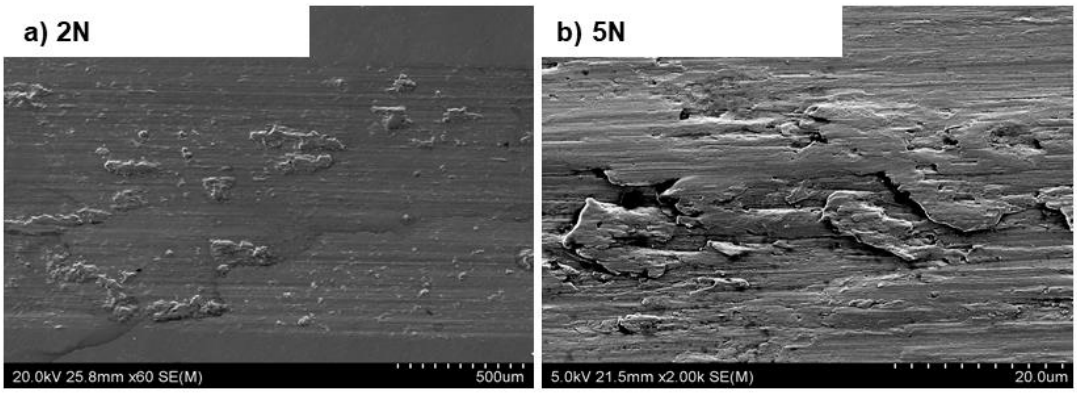

Figure 2-9: SEM images of 60NiTi wear tracks tested under an unlubricated condition a) 2N load and b) 5N load.

EDS elemental analysis tests showed that these lumps lack appreciable amounts of W (<1 at.%) and mainly consist of Ni, Ti and O in their composition (figure 2-10). This suggests that these lumps were not formed on the 60NiTi wear surfaces due to the wear of the counterface WC.

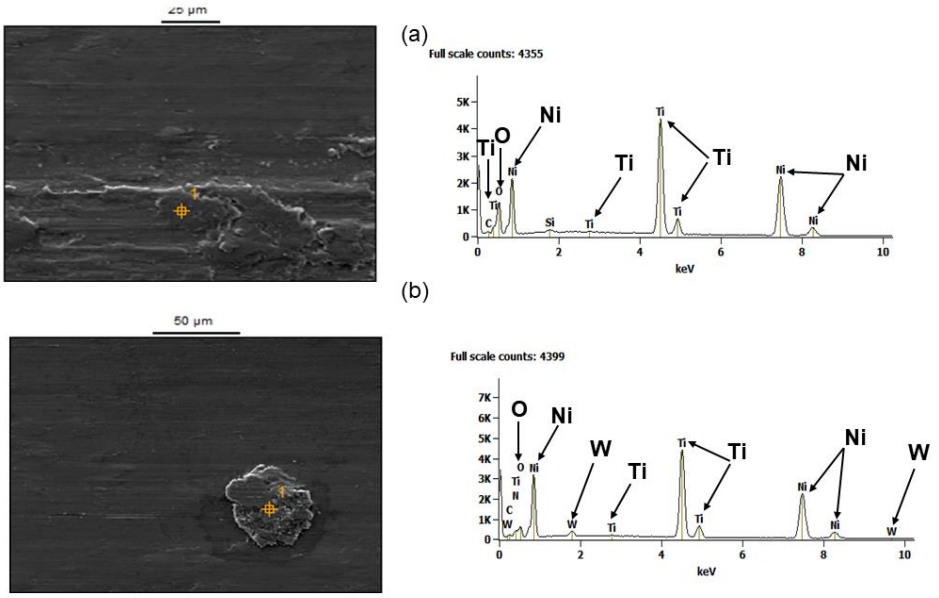

Figure 2-10: EDS elemental analysis done on two different transferred lumps of (a) and (b).

These lumps could be formed due to different reasons and it is not straightforward to confidently justify the main reason for their formation. It is possible that these are compacted wear debris, plastically adhered material or plowed accumulations. Further, these lumps were

seen much less frequently in samples tested under higher loads (figure 2-6.c). It is possible that high loads wear away the lumps faster than they form.

It can be difficult to determine the dominant and active wear modes from examination of the wear surfaces alone. The surface is often covered by compacted wear debris, plastically adhered material and/or plowed accumulations. To further investigate the wear mechanisms, the subsurface areas of the wear tracks were studied (figure 2-11).

Subsurface damage was seen in the cross section of the wear tracks of the 60NiTi samples. This clearly shows the brittle fracture type damage which resulted from repeated shear stresses due to sliding. This eventually led to fatigue crack formation, growth and then spalling and finally liberation of wear debris. Note that these subsurface damages were absent in the cross section of the wear tracks of the 440C steel samples.

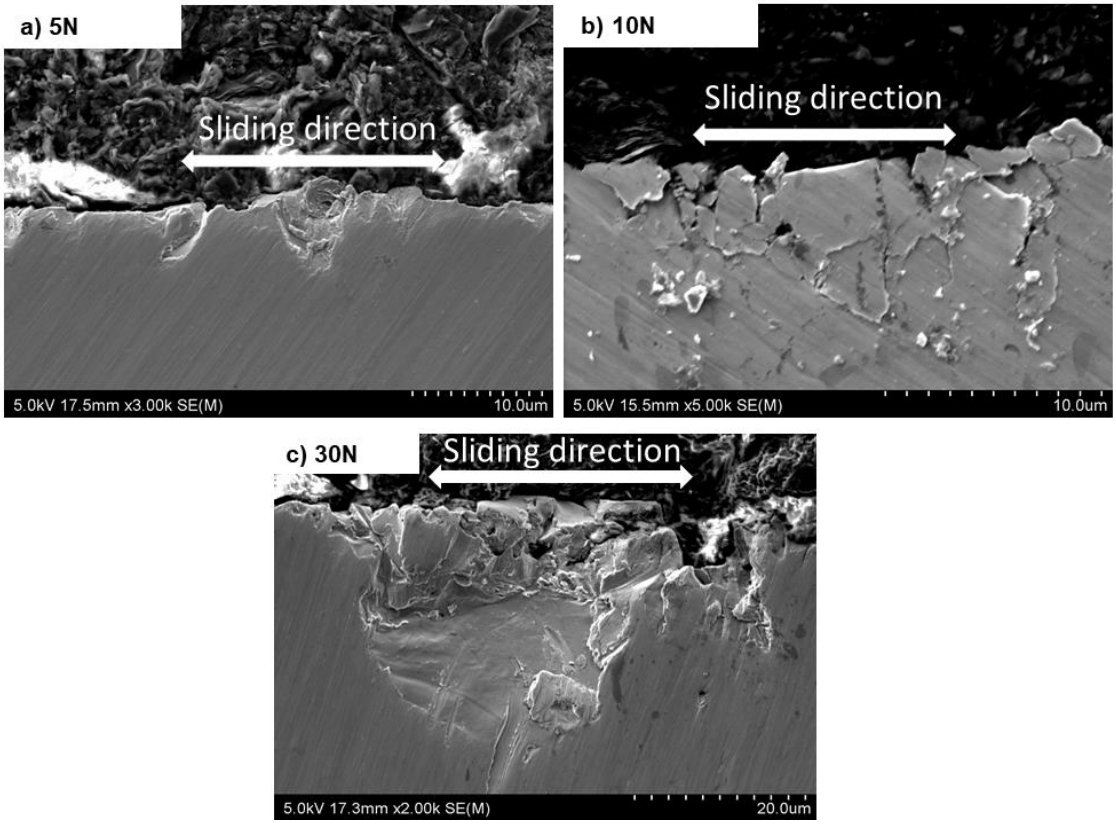

Figure 2-11: Subsurface SEM images of 60NiTi wear tracks tested under an unlubricated condition with a) 5 N load, b) 10N load, and c) 30N load.

To further investigate the wear modes damaging 60NiTi under unlubricated condition, wear debris released and accumulated at the end of the wear track were studied. Further, the surface of counterface WC ball was characterized through SEM and EDS elemental analysis studies.

In the wear debris, fine equiaxed debris with irregular morphologies and sheet-like flakes were observed (figure 2-12.a). The EDS elemental analysis (figure 2-12.b) of these particles indicated that, similar to the transfer lumps seen on the surface of wear tracks, they mainly consist of Ni, Ti and a small amount of O in their compositions. The fine debris are a result of abrasive wear, whereas flakes are speculated to form due to surface cracks and subsurface fatigue that eventually lead to flakes breaking off.

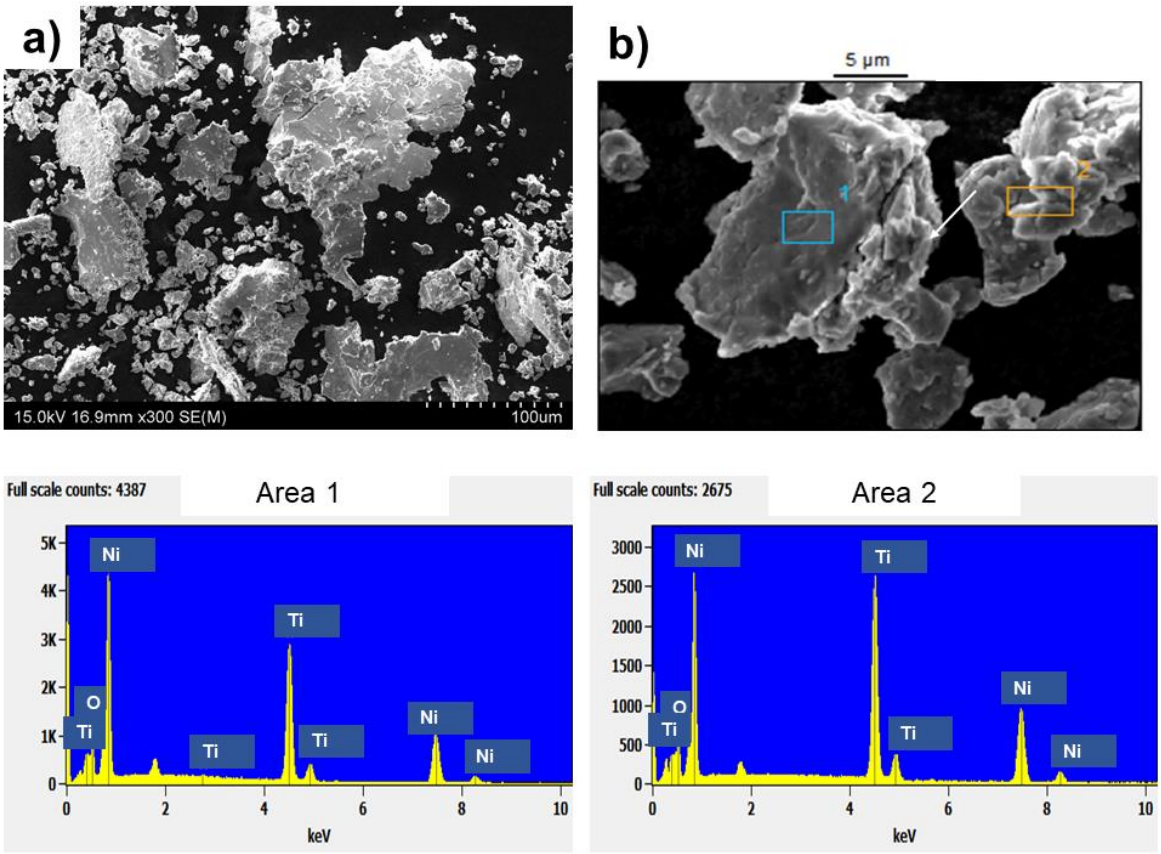

Figure 2-12: Graphs showing the wear debris released in the end of wear track of 60NiTi samples worn under an unlubricated condition and 10N load. a) The SEM image of the wear debris, and b) The EDS elemental analysis conducted on these particles.

Further, SEM micrographs (figure 2-13.a) and EDS elemental analysis (figure 2-13.b) showed the existence of fragments, mainly consisting of Ni and Ti, on the surface of counterface WC ball. 60NiTi is much softer than WC (~85 HRC); therefore, fragments of NiTi might have been formed due to adhesive wear and adhered to the surface of the WC ball. Moreover, this observation implies that other than the reasons explained before, classical adhesive wear of 60NiTi may also have played a role in the formation of lumps seen on the surface of the wear tracks or flakes in wear debris. In fact, the strong adhesion between the WC ball and 60NiTi plate might have caused the generation of fragments which further have adhered on the wear

surface and WC ball surface or released as wear debris. However, orthogonal marks found perpendicular to the sliding direction, sometimes characteristic of adhesive wear [13], were not observed on the 60NiTi surface. This suggests that these fragments are possibly adhered regions of smaller abraded or delaminated NiTi wear particles.

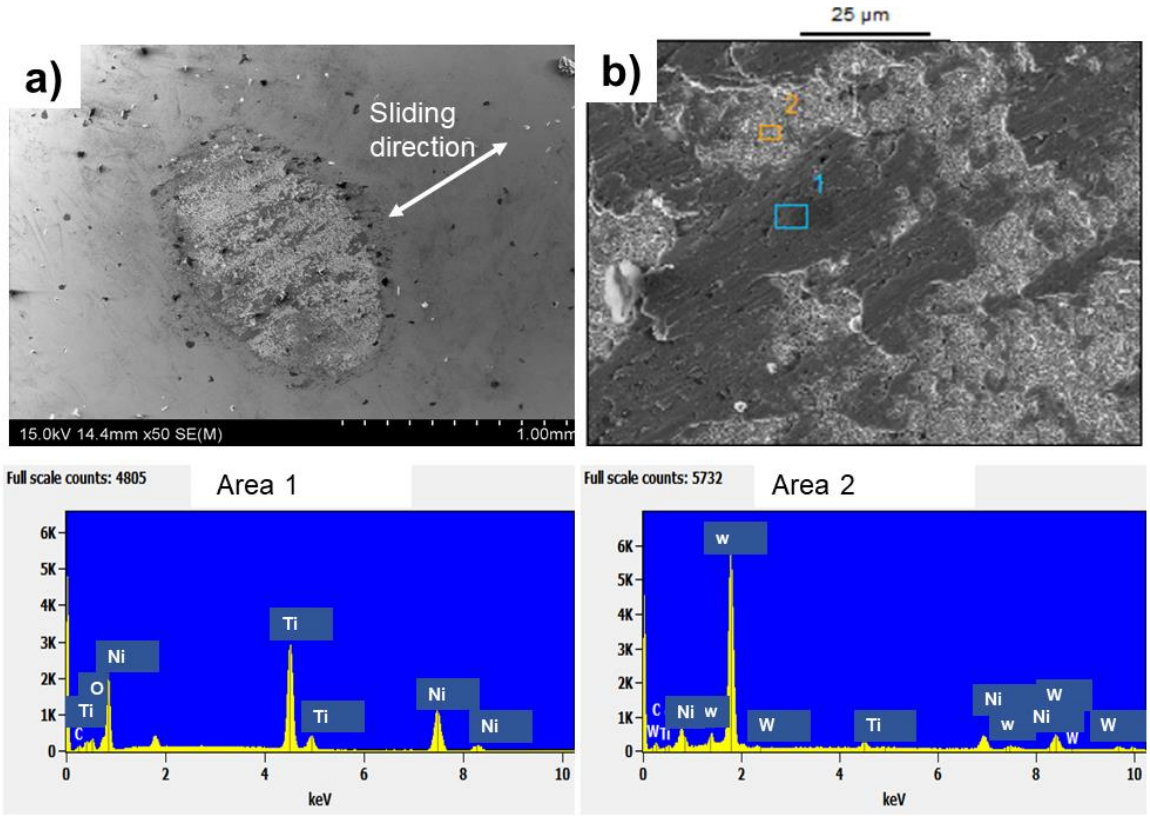

Figure 2-13: Graphs showing the surface microstructure of WC ball mating 60NiTi worn under an unlubricated condition and 10N load. A) The SEM image of the WC counterface ball, and b) The EDS elemental analysis conducted on the fragments (area 1) and ball surface (area 2).

Based on the EDS results obtained from the wear debris particles released in the end of the wear track (figure 2-12.b) or on the surface (figure 2-10) or adhered to the WC ball (figure 2-13.b), the ratio between the intensity of Ni and Ti peaks is changing in different spots and areas. In fact, some spots and areas are richer in Ni and others are richer in Ti. When sliding occurs in air using an essentially flat-on-flat geometry (which is the case as soon as some ball wear occurs), localized "flash heating" may have occurred leading to oxidation of the wear debris. Oxide formation could then have resulted in the selective depletion of Ti and Ni from the 60NiTi causing a shift in Ni-Ti ratio.

As seen in table 2-1, the average CoF values of 60NiTi under each specific load were higher than that of 440C steel. Furthermore, 60NiTi exhibited CoF curves with larger data scatter heights under unlubricated condition as compared to 440C steel (figure 2-14). As seen in the SEM images (figure 2-6), a dark layer was formed on the wear tracks of 440C steel alloy. EDS elemental analysis results indicated that these patches (darker regions) are oxygen rich, containing ~28 atomic % oxygen and 62 atomic % iron, as compared to the other regions that contain only ~4 atomic % oxygen. This could indicate the formation of iron based oxides on the wear surfaces of the 440C steel samples. These dark thick patches were not seen on the wear surfaces of the 60NiTi alloy. This suggests that 60NiTi does not have the ability to form or preserve stable oxide layers under the tested conditions. Absence of these thick oxide tribo-layers in 60NiTi resulted in direct contact of the WC ball with metallic surfaces leading to high average CoF values with irregular traces. On the other hand, as oxide layers formed on the 440C steel wear tracks, the CoF value dropped and continued in a smooth mode (figure 2-14). These layers prevent the direct contact of the WC ball with metallic surfaces, reducing the adhesion between the contacting surfaces [90]. As a result, the absence of this layer on the 60NiTi wear track resulted in the increased possibility of adhesion between the WC ball and the 60NiTi samples, which other than enhancing the abrasive and fatigue wear in this alloy, may have caused the occurrence of classical adhesive wear. Often, both abrasion and adhesion occur alongside brittle fracture and subsequent grinding down of small particles.

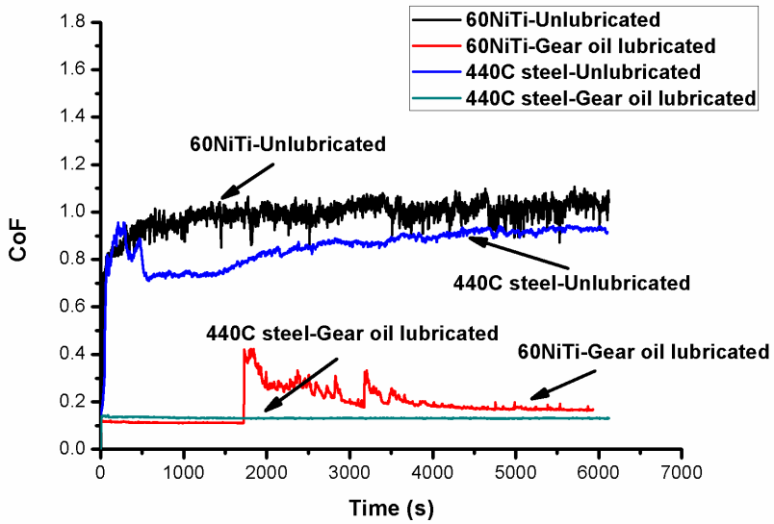

Figure 2-14: Curves showing the variations of CoF vs. time for 440C steel and 60NiTi under different unlubricated and gear oil lubricated conditions and 10 N load.

Another series of tests were carried out, which consisted of conducting lubricated tests with castor oil and a fully formulated PAO gear oil.

Properties of the lubricant and the chemical and physical characteristics of the contacting materials directly influence the surface lubrication [61]. Irrespective of the applied load or the lubricant used, 440 C steel did not show measurable wear and the CoF values were always low (<0.2), constant and stable (figure 2-14). These clearly indicate that the direct contact of ball and 440C steel plate was avoided under these experimental conditions.

Lubrication of 60NiTi with these oils reduced the CoF values of this alloy under each specific load. As seen in table 2-2, under some conditions, the CoF showed a two-stage mode and under some others, samples did not exhibit the first stage where CoF values are low, smooth and noise-free (figure 2-14). The low friction observed in stage one is an indicator for formation of a perfect lubricating film preventing the direct contact of mating materials. In these conditions, 60NiTi did not wear (as observed by the naked eye during the tests) and wear started to occur during the second stage where the CoF value increased due to the probable partial breakage of the lubricant film. The First stage was lengthier under the gear oil lubrication than the castor oil lubrication under each specific load. For example, 60NiTi passed approximately 66 and 38 minutes of the total test time (102 minutes) with low and stable CoF values when lubricated with the gear oil, but just approximately 7 and 14 minutes when lubricated with castor oil under, respectively, 2 and 10 N applied loads (table 2-2).

Table 2-2: Wear properties of 60NiTi worn under lubricated and unlubricated conditions.

Condition	**Load (N)**	**Average CoF and its duration* (stage 1)**	**Average CoF (stage 2)**	**Average total CoF**	**Average specific wear rate (mm^3 / m.N)**
Unlubricated	2	-	-	1.64	1.33E-04
Gear oil lubricated	2	0.21 (66.3 minutes)	0.45	0.3	1.60E-05
Castor oil lubricated	2	0.21 (7.3 minutes)	0.74	0.57	5.11E-05
Unlubricated	5	-	-	1.18	2.41E-04
Gear oil lubricated	5	0.11 (34.2 minutes)	0.28	0.22	3.54E-05
Castor oil lubricated	5	0.16 (1.3 minutes)	0.39	0.38	6.54E-05

Unlubricated	10	-	-	1.03	2.12E-04
Gear oil lubricated	10	0.11 (37.9 minutes)	0.23	0.17	3.00E-05
Castor oil lubricated	10	0.10 (14.3 minutes)	0.32	0.29	5.58E-05
Unlubricated	30	-	-	0.83	1.17E-04
Gear oil lubricated	30	0.10 (9.5 minutes)	0.40	0.36	1.85E-04
Castor oil lubricated	30	-	-	0.24	5.95E-05
Unlubricated	40	-	-	0.80	9.34E-05
Gear oil lubricated	40	-	-	0.44	2.30E-04
Castor oil lubricated	40	-	-	0.22	7.08E-05

The shift in CoF from low to higher values in 60NiTi can be attributed to different causes such as oil degradation and oxidation. Ti is a chemically aggressive material toward hydrocarbon and fluorocarbon oils [5]. The presence of this element in 60NiTi alloy could have played a role in the degradation of the gear oil. At the same time, since just a small quantity of oil was used in these tests, both castor oil and gear oil could have been consumed and degraded after some time. Oxidation is another factor that needs to be considered in the occurrence of a two-stage CoF mode in the lubricated 60NiTi tests. As Zeng and Dong [61] explained, a temperature rise during the wear tests can result in the oxidation of the lubrication oils. This can explain the more noticeable low CoF stage (stage 1) in the gear oil lubricated conditions as compared to castor oil lubricated conditions: Castor oil is a type of oil with high viscosity but low viscosity index. Lower viscosity index of castor oil (ASTM D2270:~89) as compared to the gear oil used in these tests (ASTM D2270:~187) results in a decrease in its viscosity when the temperature rises and this oil gets oxidized. This makes castor oil films more vulnerable to breakage than the gear oil films [61]. All the above factors could have impacted the lubrication behavior of 60NiTi and led to the occurrence of a two stage CoF mode. However, it cannot be confidently stated at this stage which of the above factors plays the dominant role in this phenomenon.

Two different procedures were evaluated in this research to ensure that the shift in CoF from low to higher values in 60NiTi is due to oil consumption caused by one of the reasons discussed above. In the first procedure, immediately after the emergence of the second stage where the

CoF value is high and erratic, the test was stopped and old oil was replaced by new oil. In this procedure, tissue and ethanol was used to fully clean the surface of the sample as well as the counterface ball holder and ball from the old oil. However, this procedure was not successful in lowering of the CoF value to the low values observed in the first stage (figure 2-15.a).

Another strategy was evaluated for 60NiTi samples lubricated with gear oil and worn under 10 N load. As seen in table 2-2, the average duration of stage 1 under this condition was about 38 minutes. In this procedure, the same careful method used in the previous experiment was used at every 15 minutes interval to replace the oil and clean the sample surface, counterface ball holder and ball. This procedure was repeated 12 times and the test continued successfully at the low CoF value observed under stage 1 for 3 hours without the emergence of a second stage (figure 2-15.b).

These results suggest that perhaps the undamaged NiTi surface readily accepts oil boundary lubrication films, but once the surface is worn and covered with the debris layer (which contains oxided Ni and Ti particles), the oil is no longer providing effective lubrication.

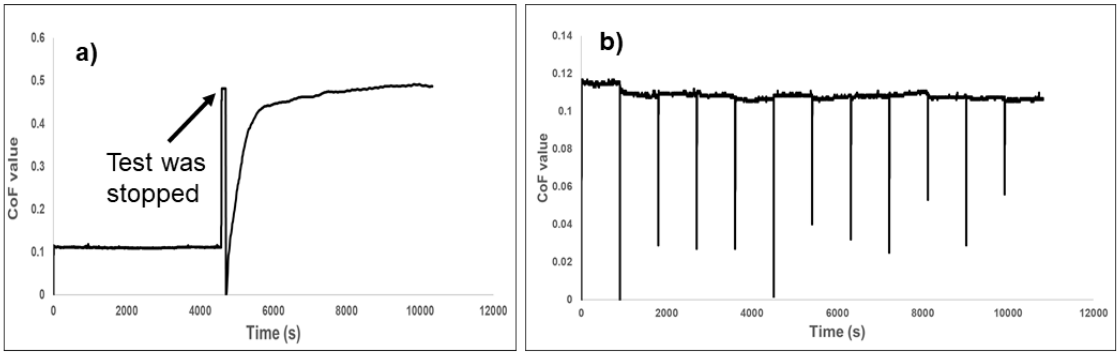

Figure 2-15: Two different strategies used to ensure that oil consumption is the reason for the emergence of second stage, where the CoF values increase, in 60NiTi alloy. a) Oil was replaced right after the emergence of the second stage, b) Oil was replaced in every 15 minutes interval.

Results of the average specific wear rates of 60NiTi under lubricated conditions as compared to unlubricated conditions are displayed in figure 2-16 and table 2-2.

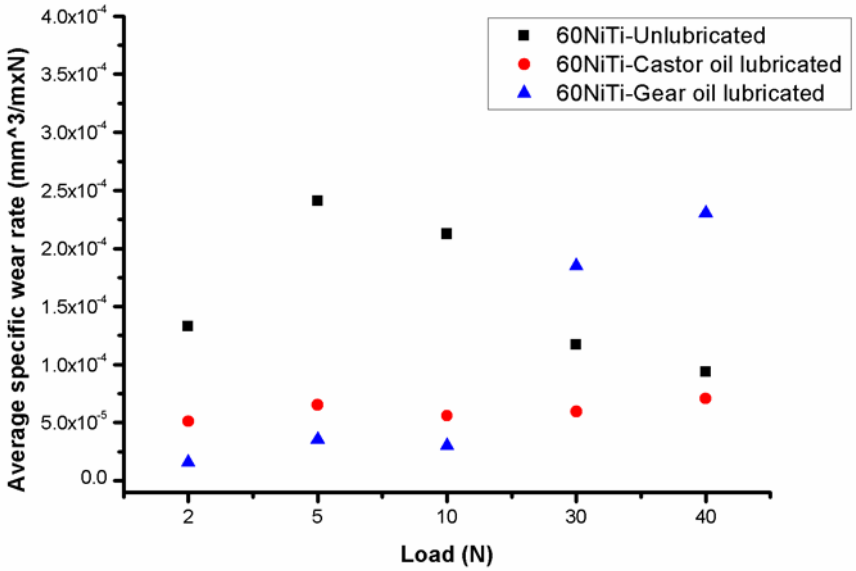

Figure 2-16: Specific wear rates of 60NiTi under different lubricated and unlubricated conditions. Note that the maximum value for the standard deviation in all the loads was 0.1×10^{-4} (mm^3/m.N).

Lubrication with castor oil resulted in a significant decrease of specific wear rates as compared to the situation where the tests were conducted under an unlubricated condition. As seen in the SEM images (figure 2-17), the castor oil lubricated samples under both relatively low load of 10 N and high load of 40 N showed different wear mechanisms than their unlubricated ones. The mechanism of abrasive wear shifted from severe abrasion causing aggressive removal of material to abrasion dominated by plastic deformation resulting in formation of ploughing grooves in lubricated samples. This can be considered to be the main reason for the mild wear of 60NiTi observed under these lubricated conditions.

Further, these results suggest the high load-carrying capability of castor oil. Even under high applied loads of 30 and 40 N, castor oil, despite being unable to form a perfect lubricant film, could still lead to the shift of wear mechanism in 60NiTi alloy and result in lower average CoF values as compared to the tests with lower applied loads (figure 2-18). This high load-carrying capacity of castor oil can be attributed to specific characteristics of this oil such as containing long and polar fatty acid chains [52, 58, 60, 61].

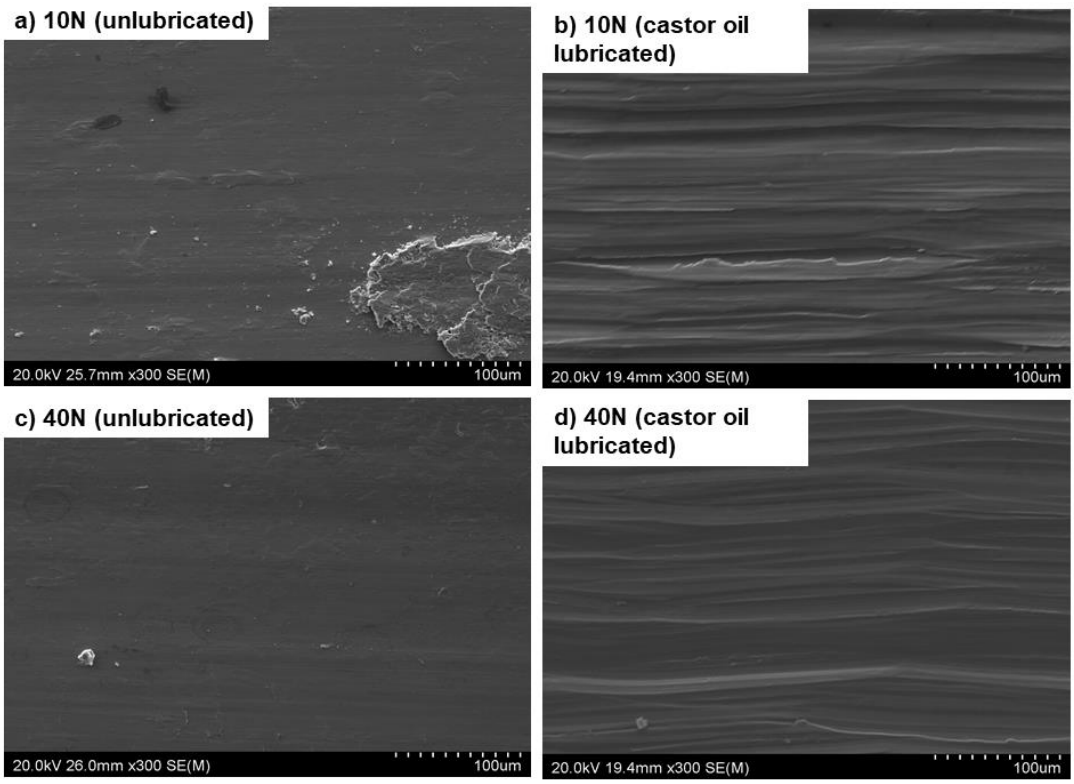

Figure 2-17: SEM images of 60NiTi wear tracks tested under unlubricated and castor oil lubricated conditions. a) Unlubricated: 10 N, b) Castor oil lubricated: 10 N, c) Unlubricated: 40 N, d) Castor oil lubricated: 40 N.

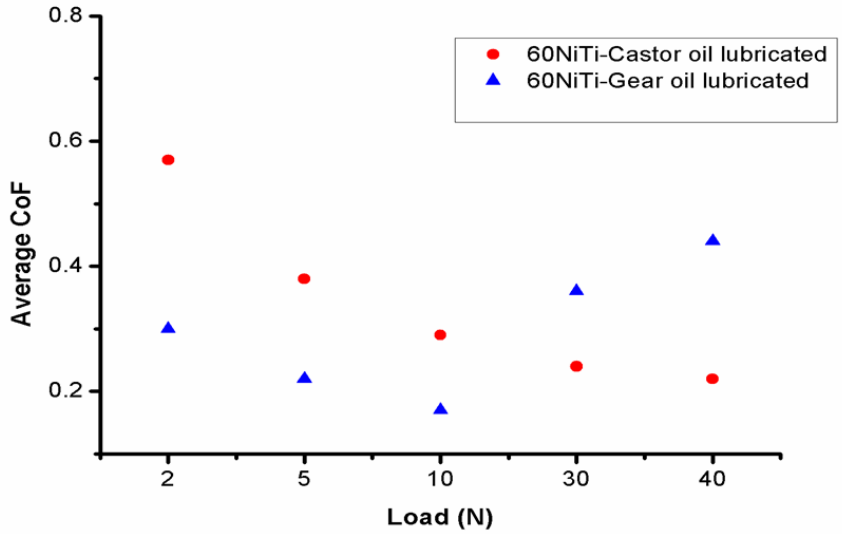

Figure 2-18: Average CoF values of 60NiTi lubricated by castor oil and the gear oil.

Under higher loads of 30 N and 40 N, the gear oil lubricated 60NiTi passed shorter durations of time in stage 1 and also exhibited relatively higher average CoF values as compared to lower loads of 2, 5 and 10 N (table 2-2, figure 2-18). In addition, under these conditions, 60NiTi

exhibited higher specific wear rates than even unlubricated conditions (figure 2-16). These results are in accordance with the SEM images of the lubricated wear tracks (figure 2-19.b, d). As seen, under 10 N applied load, the gear oil could shift the abrasive wear mechanism from severe abrasion causing aggressive removal of material to abrasive wear dominated by plastic deformation resulting in formation of ploughing grooves (figure 2-19.a, b). In contrast, 60NiTi again exhibited severe abrasive wear leading to a smooth wear surface under 40 N applied load indicating ineffectiveness of the gear oil to lubricate 60NiTi under these conditions (figure 2-19.c, d). Applied load and its consequent stress is another parameter which affects the performance of lubricated contacts. It could be that the gear oil film is mainly broken under conditions where a high load is applied. Alternatively, agglomeration of wear particles could have also played a role in the ineffectiveness of the gear oil under these conditions. The existence of debris in oil and its agglomeration could have resulted in accelerated damage leading to higher specific wear rates of 60NiTi observed under these conditions as compared to unlubricated conditions [91].

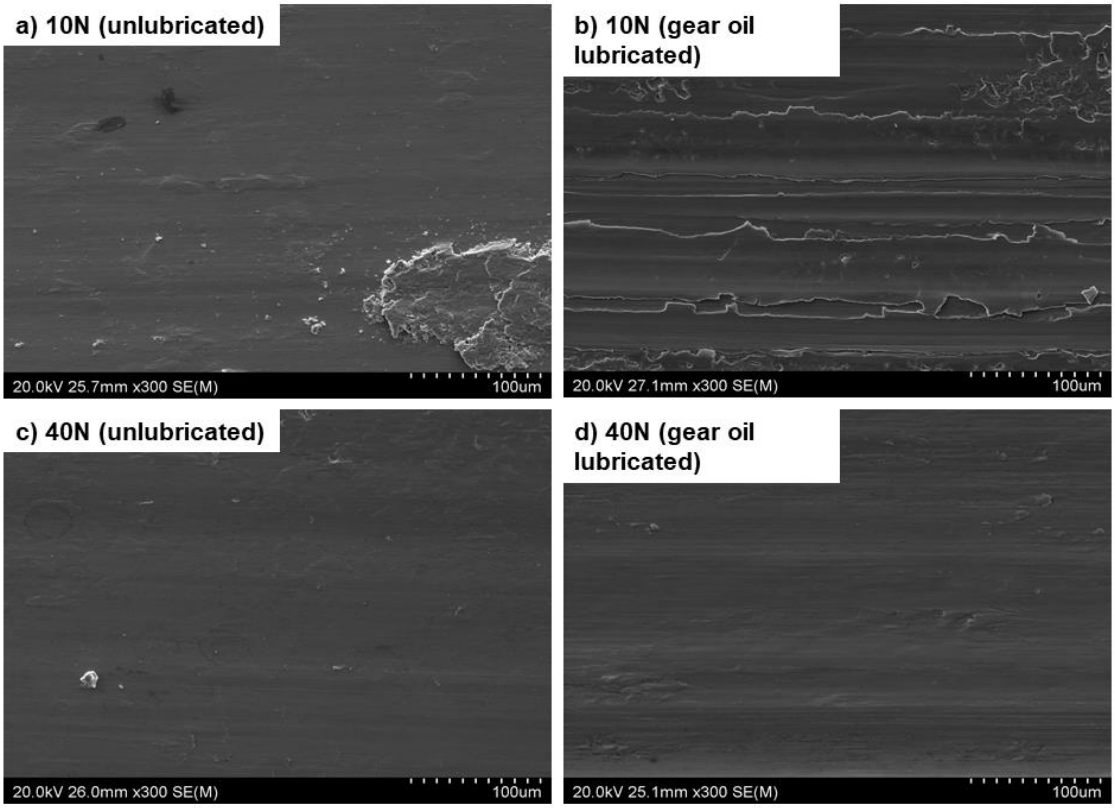

Figure 2-19: SEM images of 60NiTi wear tracks tested under unlubricated and the gear oil lubricated conditions. a) Unlubricated: 10 N, b) Gear oil lubricated: 10 N, c) Unlubricated: 40 N, d) Gear oil lubricated: 40 N.

2.3 Conclusions

In this chapter, lubricated and unlubricated reciprocating sliding wear behavior of 60NiTi was compared to that of 440C steel as a conventional bearing and wear resistant alloy. Results of sliding wear tests carried out under different loads show that 60NiTi, despite having a higher hardness, exhibits a significantly inferior wear behavior, in terms of specific wear rates and CoF values, under dry conditions in comparison to 440C steel. These unexpected results indicate that 60NiTi does not follow conventional wear theories where the wear of materials has an inverse relationship to their hardness.

Abrasion and fatigue, possibly enhanced by adhesive effects, were deduced to be the main wear mechanisms for this alloy under these conditions. Classical adhesive wear could also have played a role in the wear of this alloy as fragments, mainly consisted of Ni and Ti, were observed on the surface of counterface WC ball.

Regardless of the applied load or the lubricant used, 440 C steel did not show measurable wear under lubricated conditions and the CoF values were always low (<0.2) and stable throughout the tests. Instead, in 60NiTi, this low, stable and smooth CoF mode was observed only under some lubricated conditions and for shorter periods. After this stage, the CoF values increased causing wear in 60NiTi samples. This first stage was lengthier under the gear oil lubricated conditions than for the castor oil lubricated ones. It was ensured through experiments that the shift in CoF from low to higher values in 60NiTi under these lubricated conditions is due to oil consumption. In any case, lubrication with castor oil significantly decreased the specific wear rates and average CoF values of this alloy. This decrease in specific wear rates was attributed to the shift in abrasive wear mechanism from aggressive abrasion causing severe damage and material removal to abrasive wear dominated by plastic deformation due to the decrease of contact stresses. This trend was also seen in 60NiTi alloys lubricated with a synthetics gear oil under conditions where the applied loads were relatively low. These results indicate the importance of good lubrication (so the stage 1 friction mode is preserved) and stress design for applications where 60NiTi is employed as a sliding wear resistant alloy.

The reasons for this unexpected observed wear behavior of 60NiTi as compared to 440C steel is discussed in the next chapter. Moreover, the precise conditions under which wear is prevented in 60NiTi are defined using a stress model and experimentation. These obtained results define and clarify the conditions where 60NiTi can be applied in sliding applications as a wear resistant alloy.

Chapter 3 An investigation into the causes of inferior unlubricated sliding wear performance of 60NiTi as compared to 440C steel[3]

[3] **Khanlari K**, Ramezani M, Kelly P, Cao P, Neitzert T. An investigation on reasons causing inferiority in unlubricated sliding wear performance of 60NiTi as compared to 440C steel. *Tribology Transactions*, 2018.

As discussed already in section 1.11 and the introduction to the previous chapter, 60NiTi has a similar Rockwell C hardness and a lower elastic modulus, about half that of 440C steel. Moreover, both 60NiTi and 440C steel show similar high tensile strengths [2, 20, 33, 44]. Consequently based on conventional wear theories such as Archard's theory or Oberle's model that take account of macroscopic mechanical properties (macro hardness and elastic modulus), 60NiTi is expected to show similar or even superior sliding wear properties than 440C steel [4, 49]. However, results of the study provided in Chapter 2, comparing the sliding wear properties of 60NiTi and 440C steel plates mating with WC balls, show that 60NiTi displays a very much inferior wear resistance than 440C steel under unlubricated conditions. In particular, 60NiTi exhibited ~42, ~133 and ~121 times higher specific wear rates than 440C steel under 2, 5 and 10N loads, respectively (table 3-1). While mild abrasion was the ruling wear mechanism for 440C steel, severe abrasion and fatigue wear (enhanced by adhesive effects) were deduced to be the main wear mechanisms damaging 60NiTi under these unlubricated conditions [92].

On the other hand, under good lubricated conditions, 60NiTi was able to form a perfect lubricating film causing a significant drop in the CoF values. Under such conditions, 60NiTi showed a similar behavior to 440C steel and did not wear. However, the occurrence of this wear-free condition was limited to reduced loads and good lubricated conditions.

Table 3-1: Wear properties of 60NiTi and 440C steel as obtained from reciprocating dry sliding wear tests under unlubricated conditions.

Material	Load (N)	Average CoF	Average specific wear rate ($mm^3/m.N$)
60NiTi	2	1.64	1.33E-04
440C steel	2	1.37	3.14E-06
60NiTi	5	1.18	2.41E-04
440C steel	5	0.99	1.80E-06
60NiTi	10	1.03	2.12E-04
440C steel	10	0.85	4.87E-06

These results, other than showing the importance of stress design for sliding applications where 60NiTi is employed, are in contrast to the expected behavior deduced from the conventional wear theories mentioned above, as 60NiTi shows significantly higher specific wear rates than 440C steel under unlubricated conditions.

As a result, there is a necessity to investigate the reasons leading to this observed wear behavior of 60NiTi and also to precisely define the condition where 60NiTi does not wear. In this chapter, to elucidate the reasons behind this unexpected wear behavior of 60NiTi as compared to 440C steel, general macro and micro mechanical properties of 60NiTi and 440C steel are investigated through indentation and hardness tests using respectively conical and pyramidal indenter geometries. In addition, single pass scratch tests are carried out using conical and spherical indenters to further investigate the microscopic mechanical properties and damaging mechanisms in these alloys. Moreover, to understand the sliding conditions where these materials exhibit similar and dissimilar behavior, reciprocating ball-on-plate sliding wear experiments are conducted under both moderate and extreme conditions. Results obtained from these sliding tests are used to define specific stress ranges where 60NiTi shows divergence in its response. These findings, other than helping in a better understanding of the wear mechanisms of 60NiTi and generally NiTi alloys, may help the engineering community to properly apply 60NiTi in different load bearing applications.

3.1 Materials and experimental methods

3.1.1 60NiTi and 440C steel specimens preparation and testing

Samples were cut, hardened, prepared and characterized under the same circumstances discussed in the previous chapter: information regarding samples preparation procedures

(cutting, hardening, grinding, polishing and testing) are provided in “Materials and experimental methods” section, section 2.1, of the previous chapter.

3.1.2 Macro and micro hardness testing

To evaluate the macro hardness properties of these alloys, a multifunctional tribometer was employed to conduct indentation tests using a conical indenter (200-μm diamond tip) used in standard Rockwell C macro hardness tests. These tests were performed at varying loads of 25, 50, 100 and 150N at the loading and unloading rate of 40N/min. Since the tribometer used in this study was not capable of applying loads above 200N, a Rockwell hardness tester was employed to apply other higher loads of 60, 100 and 150 kgf using the same conical indenter. These correspond to, respectively, approximately 588, 980 and 1471N loads. In the next stage, the indent depth resulting from each of these tests was measured by an optical profilometer. Additionally, to define the micro hardness of these alloys, Vickers hardness of the samples were measured at varying loads of 0.5, 1, 2.5, 5 and 10 kgf by a micro-indentation hardness machine, with pyramidal indenters.

3.1.3 Scratch testing

Single pass scratch tests were performed employing the same multifunctional tribometer (capable of recording CoF and applying loads up to 200N) using different indenter geometries: conical (200-μm diamond tip, Rockwell C indenter) and spherical (Ø 2.5 mm WC). The sliding velocity of the indenter in these tests was low and constant (0.1 mm/s). Low speeds were used so the frictional bulk heating, that would normally cause surface oxides to grow (as in a high-speed ball-on-plate test), does not come into play. This allows the observation of microstructural features and mechanisms responsible for damaging the alloys during sliding wear tests.

In the next step, the scratch grooves formed under these tests were inspected using a Hitachi-su70 scanning electron microscopy (SEM) machine (working based on the emissions received from the secondary electrons) equipped with an energy dispersive spectroscopy (EDS) to investigate the mechanisms that at a microscopic level cause damage in these materials. These single pass scratch tests were performed at different constant loads and a constant low velocity of 0.1 mm/s. Tests conducted using the spherical indenter were done just at a 30N load. However, scratch tests using the conical indenter were carried out at different constant loads of 2, 5, 7, 10, 15, 20, 30 and 40 N. This is because single-pass scratch tests carried out with a

conical indenter simulate single pass sliding of small, hard asperities on alloy surfaces. In consequence, results obtained from these tests are suitable for interpreting sliding wear properties of the materials where microscopic asperities interact and stresses are extremely high [68, 93].

Furthermore, general characteristics of the scratches, formed specifically with the conical indenter, such as scratch depth (S_D), scratch width (S_W) and the ratio between the cross-sectional area of the lateral pile-up (A_P) and the cross-sectional area of the groove (A_G) were measured and calculated using cross-sectional profile images of scratches obtained by an optical profilometer.

3.1.4 Sliding wear testing

Similar to the previous chapter, the wear tests were performed at room temperature on a linear reciprocating tribometer (capable of recording CoF and applying loads up to 40N). Experimental specifications used for sliding wear tests such as sliding frequency, testing time, wear track length, counterface material and its size were identical to the ones used in the previous chapter. However, to approach the aims of this chapter and define specific stress ranges where 60NiTi shows divergence in its response, a larger number of testing loads (with smaller gaps in between) were used in the sliding test carried out in this chapter. These experiments were conducted under lubricated conditions (under a boundary lubrication regime using a fully formulated PAO gear oil) at varying loads of 2, 5, 10, 12, 13, 14, 15, 17, 20, 23, 24, 25, 30, 32, 34 and 40N. The method used to measure and calculate the specific wear rates ($mm^3/N.m$) of samples for each specific test was the same as the one explained in the previous chapter under “Materials and experimental methods” section. Again, the surface microstructures of the worn samples were studied using the SEM.

All the tests mentioned above were repeated three times and the average obtained results are reported.

3.2 Results and discussion

3.2.1 Microstructural, phase compositional, indentation and hardness studies

The information regarding the microstructural and phase analysis of the samples were provided in the previous chapter in section 2.2. To avoid the repetition, these analyses are not discussed again here.

Table 3-2 shows results of the indentation tests carried out using a Rockwell C conical indenter under different loads. As can be seen, 60NiTi exhibits relatively less permanent indent depths at all the applied loads than those of 440C steel (table 3-2, figure 3-1).

Table 3-2: Permanent indent depth of 60NiTi as compared to 440C steel and the ratio existing between the indent depths of 440C steel to 60NiTi (D_R) under different loads. Note that these tests were carried out using a conical indenter (200-µm diamond tip).

Load(N)	Material	Depth (µm)	D_R
25	440C steel	3.0	2.14
	60NiTi	1.4	
50	440C steel	6.0	1.87
	60NiTi	3.2	
100	440C steel	10.5	1.45
	60NiTi	7.2	
150	440C steel	14.3	1.21
	60NiTi	11.8	
588	440C steel	49.4	1.03
	60NiTi	47.6	
980	440C steel	72.13	1.03
	60NiTi	69.9	
1471	440C steel	95.9	1.00
	60NiTi	95.3	

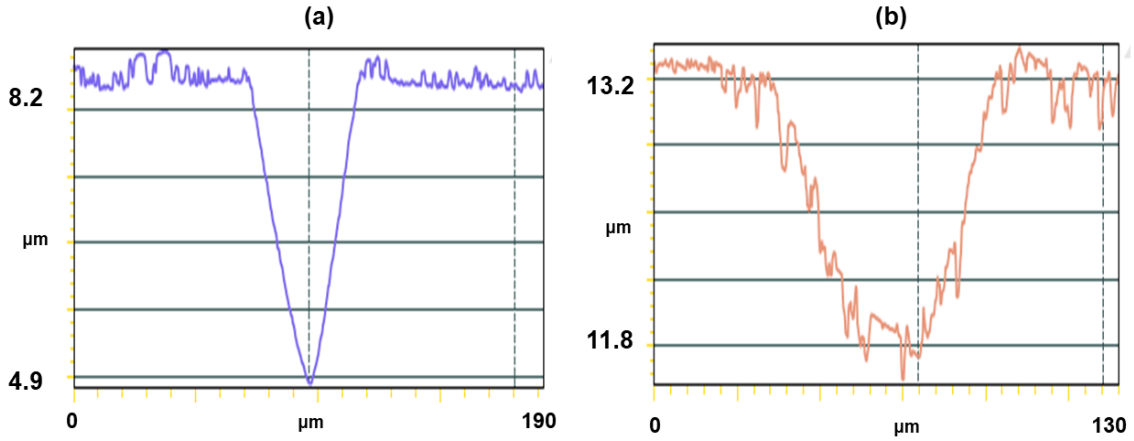

Figure 3-1: Cross-sectional profile of the indents formed in (a) 440C steel, and (b) 60NiTi under 20N load using a conical indenter (200-µm diamond tip).

However, the ratio existing between the indent depths of 440C steel to 60NiTi (D_R), under each specific load, appears to be decreasing as the load is increasing. As an example, this ratio is 2.57 in the tests done under 2.5N load, but is approximately 1 in the tests done under a high load of 1471N load (table 3-2). To further investigate the reasons behind this observation, indentation loads (L) were plotted against the indentation depths (I) in a log-log plot and the

slope of the linear fit of the results was calculated using Origin software (figure 3-2). As seen, this slope appears to be smaller for 60NiTi (~0.96) than 440C steel (~1.22).

These mean that as the load is increasing, the hardness trend is shifting from higher values of 60NiTi causing smaller indents than 440C steel to similar hardness values leading to approximately identical indent depths. This can be due to a combination of different reasons: (1) It can be that 60NiTi has a lower strain hardening rate (with a slope of ~0.96) than 440C steel (with a slope of ~1.22) causing a larger growth in the amount of permanent deformation in 60NiTi under the situations where the indentation load is increased from 25N to 1471N. As explained by Alcala et al. [82] there is a direct correlation between the strain hardening rate and this slope for spherical contact conditions. In fact, higher strain hardening rates result in larger slopes of log L-log I plots and vice versa. (2) 60NiTi, in its hardened condition, exhibits superelasticity effects [4, 9, 19]. The superelasticity effect is defined as the reversible transformation of austenitic NiTi to martensitic NiTi caused by external stress. This transformation occurs above a critical stress and is followed by detwinning of martensite (no dislocation is generated) resulting in high strains. After unloading, the martensite phase is no longer stable and reverts to the austenite phase. This reversion leads to recovery of strain [6, 9, 17]. However, dislocations which are generated due to the occurrence of plastic deformation in the indented zone might prevent the reversion of martensite to the austenite phase causing extra nonrecoverable deformations [15]. It may be that at higher loads, due to the generation of larger number of dislocations caused by plastic deformations, a larger portion of detwinned martensite stuck behind the dislocations resulting in more nonrecoverable deformations in 60NiTi.

The level of resulting permanent indent depths generated in static indentation tests carried out using Rockwell indenters are mainly ruled by yield behavior and strain hardening rate factors [94]. As mentioned, 60NiTi exhibits a much lower elastic modulus (about half) and larger elastic deformation than 440C steel [2, 4, 19, 29, 36, 45]. It may be that, under identical low localized loads, 60NiTi shows a larger expansion of the contact area causing a more significant decrease in peak contact Hertz stress as compared to 440C steel leading to reduced yielding and damage in 60NiTi [4, 19, 25, 29]. However, as the indentation load increases, the effect of strain hardening or generated dislocations caused by plastic deformation overcomes the effects of other factors discussed earlier (lower elastic modulus and larger elastic deformations causing

a reduced Hertz peak stress and consequent damage in 60NiTi) causing similar indent depths under the indentation load of 1471N.

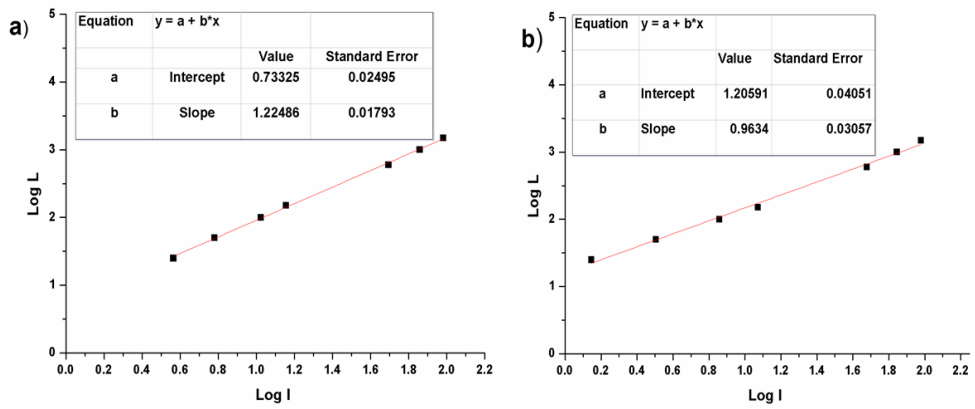

Figure 3-2: : Indentations loads (L) plotted against the indentation depths (I) in Log L-Log I format and the calculated slope of the linear line fitting the results in a) 440C steel, and b) 60NiTi.

On the other hand, based on the results obtained from Vickers hardness tests, 440C steel appears to have a higher Vickers hardness (under all the applied loads) as compared to 60NiTi (figure 3-3). Vickers hardness tests employing sharp pyramidal indenters can be used to interpret and evaluate the fracture response of the materials. This is because large strains (between 25% and 36%) are generated within the indented zone causing significant fracture when sharp pyramidal indenters are employed [95, 96]. Considering this, it can be concluded that, 440C steel shows a higher ability to resist tearing and fracture as compared to 60NiTi.

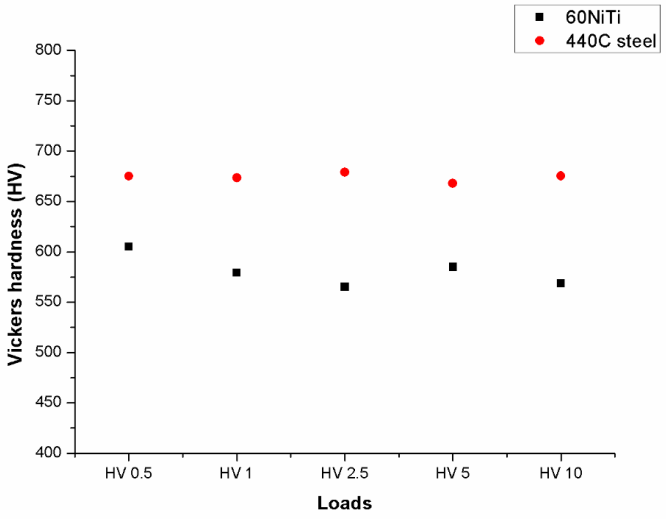

Figure 3-3: Vickers hardness of the 60NiTi and 440C steel samples under different loads.

3.2.2 Scratch test studies

Next follows a discussion of the results of scratch tests performed using spherical and Rockwell C conical indenters.

Table 3-3 presents information on general characteristics for scratches (S_D, S_W, A_P/A_G) formed under different loads of 2, 5, 10 and 20N using a Rockwell C conical indenter. As explained in the materials and experimental methods section (section 3.1.3), these were measured and calculated using cross-sectional profile images of formed scratches obtained by an optical profilometer (figure 3-4). Moreover, table 3-3 also displays the CoF values recorded during scratch tests.

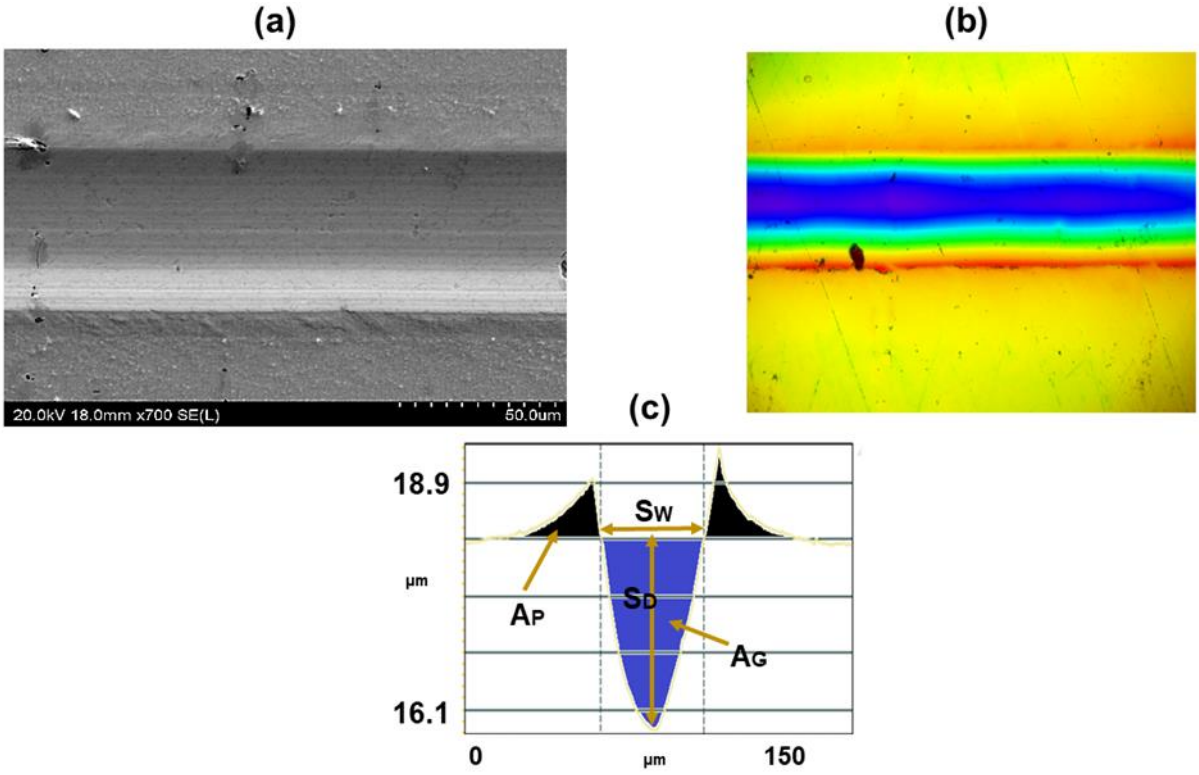

Figure 3-4: (a) SEM micrograph of a scratch scar formed under a constant load of 20N on a 440 C sample, (b) image of the formed scratch scar obtained by an optical profilometer, and (c) a cross-sectional profile of the formed scratch scar with schematics of the scratch depth (S_D), scratch width (S_W), cross-sectional area of the lateral pile-up (A_P) and cross-sectional area of the groove (A_G).

Table 3-3: Scratch geometries and COF values for scratch tests under constant loads of 2, 5, 10 and 20N. Note, the A_P/A_G was only measured for loads of 10 and 20N as they formed measurable amounts of piled-up area.

Material	**Load (N)**	**S_D (µm)**	**S_W (excluding the piled-up zone) (µm)**	**A_P/A_G**	**CoF value**
60NiTi	2	0.02	9.8	-	0.05
440C steel	2	0.30	17.2	-	0.05
60NiTi	5	0.30	14.9	-	0.05
440C steel	5	0.59	26.2	-	0.09
60NiTi	10	0.76	34.6	0.03	0.06
440C steel	10	1.14	34.6	0.14	0.09
60NiTi	20	1.41	44.2	0.1	0.08
440C steel	20	2.30	44.4	0.4	0.10

As can be seen in table 3-3, 440C steel shows relatively larger S_D and S_W values under all the loads than for 60NiTi. Specifically, under 2N load, the measured S_D value of the formed scratch scar is negligible in 60NiTi but much larger in 440C steel (0.30). These results are in accordance with the results of the static indentation tests (carried out with a Rockwell C indenter) and confirm the positive role of larger elastic deformation and lower elastic modulus of 60NiTi in reducing the permanent depth to which the indenter penetrates as compared to 440C steel.

On the other hand, 440C steel shows a much higher A_P/A_G ratio than 60NiTi under both loads of 10 and 20N (table 3-3, figure 3-5). As Bolelli et al. explained [68], in scratch tests performed using a sharp indenter such as a Rockwell C indenter, contact stresses are estimated to be higher than the yield strength of most metallic materials. As a result, the A_p/A_G ratio is dependent on the strain to failure of a material under dynamic contact stresses. In essence, the larger this value, the higher the plastic deformability of a material under dynamic contact stresses [68, 97]. This shows that 440C steel exhibits a much higher microscopic ductility than 60NiTi under sliding motions where microscopic asperities contact one another [68, 97].

This observed behavior is unexpected as under macroscopic tensile tests, both these alloys show similar high strengths and exhibit brittleness with very little plastic elongation before tensile failure [2, 20, 33, 44]. 440C steel is macroscopically brittle as it consists of large brittle carbide particles (formed by precipitation) stuck together in a martensitic iron-based matrix [87, 88]. Similarly, 60NiTi contains a large portion (~69 %) of nano-scale brittle Ni_4Ti_3 particles (precipitates) that are bound by an intermetallic NiTi phase [18].

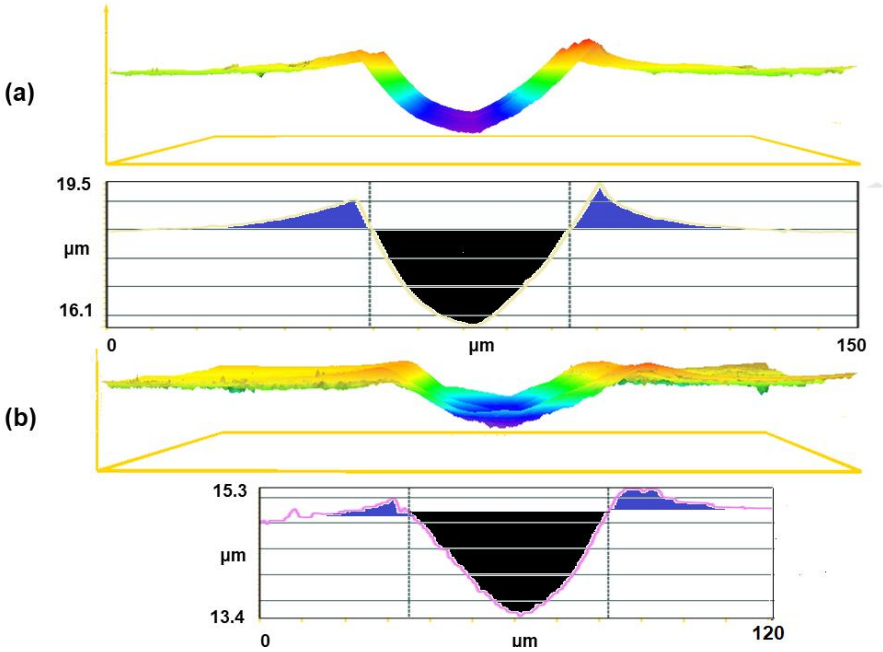

Figure 3-5: Graph showing images obtained by an optical profilometer and cross-sectional profiles of the scratch scars formed under 20N load using a conical indenter (200-µm diamond tip): (a) 440C steel, and (b) 60NiTi.

To understand the reasons for the observed behavior and investigate the damage mechanisms in the studied alloys, the scratch grooves were inspected using SEM and EDS elemental analysis (figures 3-6 to 3-9).

As can be seen in figure 3-6, depending on the amount of load, 60NiTi is damaged by different mechanisms of shear banding and cracking. Note that, as explained by Sliney and Spalvins [86], under static conditions where a sphere is contacting a flat surface, the generated stresses are compressive within the contact circle but are tensile just outside of the circle. However, under sliding motions, the tensile stress component is increased by a considerable amount due to the effect of tangential forces caused by friction [86]. In fact, the stresses are compressive ahead and alongside the indenter, but tensile behind the indenter under sliding motions [98].

Cracks are not observed under the tested loads of below 20N and just shear bands are seen in the SEM images of samples. These shear bands are signs of the occurrence of severe plastic deformations in the tested samples and are thought to be formed due to an excessive amount of shear stress caused by both compressive and tensile stress components. However, the amount of plastic deformation in the samples, despite being severe and causing the appearance of shear bands, seems to be small. This is because the level of A_P/A_G ratio, specifically tested under 10N load, is not considerable under these conditions (table 3-3). On the other hand, cracks,

which are approximately orthogonal to the sliding direction, are observed between the shear bands under the higher tested loads (20N and above). In fact, these images show the shear bands that eventually give rise to cracks at higher loads (20N and above). The generation of cracks in brittle materials is mainly attributed to the sliding induced tensile stress component generated behind the indenter. These tensile stresses upon exceeding the tensile strength result in fracture and the formation of cracks [86].

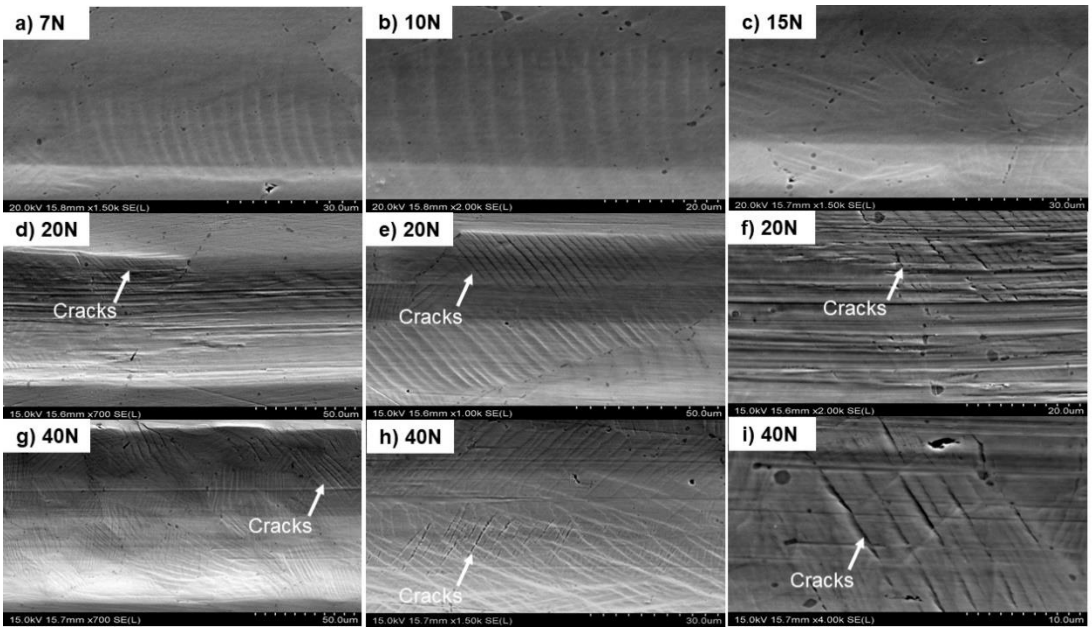

Figure 3-6: SEM images of scratch scars formed on 60NiTi samples using a Rockwell C indenter under different constant loads. a) 7N load, b) 10N load, c) 15N load, d, e and f) 20N load, g, h and i) 40N load.

As seen in figure 3-7, the cracks are seen in 440C steel even under 7N load. This suggests that the wear process for both 440C steel and 60NiTi hard materials is eventually driven by fracture.

However, a careful observation shows that these cracks are mostly limited to carbides and their propagation is arrested when the iron-based matrix is reached (figure 3-8). That is why the cracks are very small under the tested loads. It is only under a very high load of 40N that cracks in 440C steel seem to start propagation (likely by joining adjacent carbides).

440C steel is basically a composite material. Brittle and hard carbide particles are bound together by a soft and ductile iron-based matrix. The scratch tip easily penetrates and damages the soft and ductile matrix causing the formation of deep grooves and pile ups (A_P/A_G ratio) at different loads of scratching (table 3-3). Furthermore, this plastic ductile matrix arrests the

propagation of cracks formed in the brittle carbides as it allows for localized stress relief in sliding contacts. In contrast, the propagation of formed cracks in 60NiTi is not stopped. This is because the intermetallic bonding in 60NiTi, the NiTi matrix bounding a large portion of Ni_3Ti_4 particles, has very limited ductility thus causing a small A_P/A_G ratio and consequently is not able to prevent cracks propagating as well as the iron "glue" in 440C steel [18, 21].

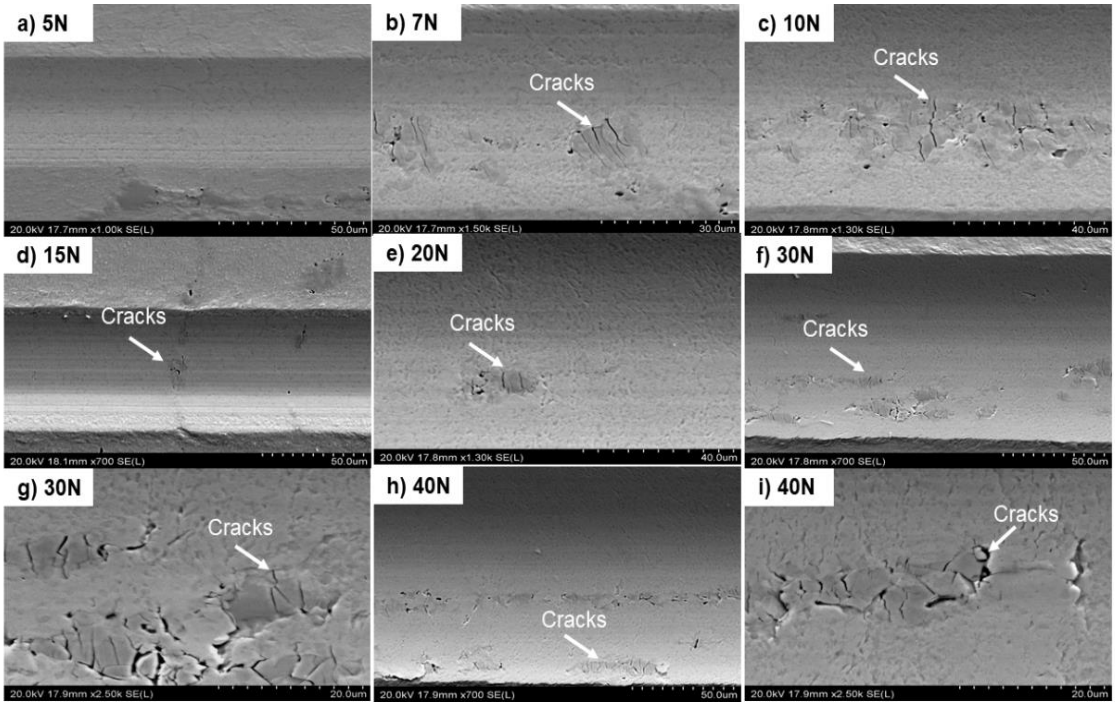

Figure 3-7: SEM images of scratch scars formed on 440C steel samples using a Rockwell C indenter under different constant loads. a) 5N load, b) 7N load, c) 10N load, d) 15N load, e) 20N load, f and g) 30N load, h and i) 40N load.

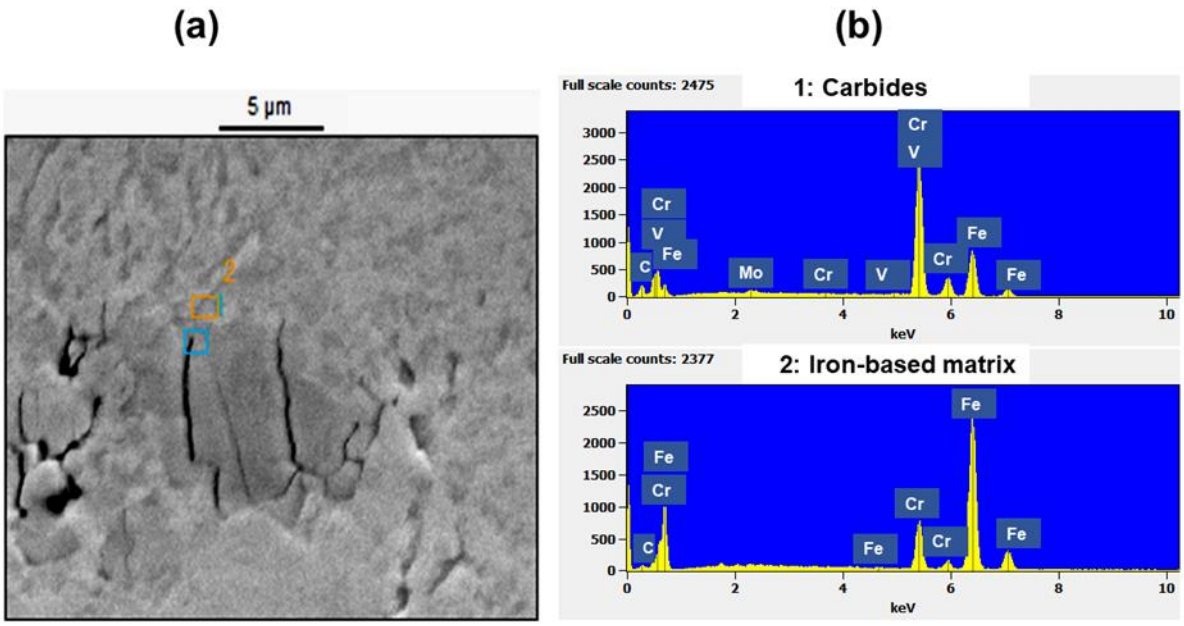

Figure 3-8: SEM image and EDS analysis showing iron-based matrix halting the propagation of cracks formed in carbides.

The results obtained from the scratch tests done with WC ball are consistent with the ones carried out using the Rockwell C indenter. The amount of observed plastic deformation in the 440C steel samples is large, causing localized tearing (which requires a large amount of plastic deformation) in the very center of the track under the 30N load. In contrast, 60NiTi has very little ductility and only exhibits ductility and plasticity at stress levels very close to the fracture strength; thus shear bands and cracks can be seen, but not tearing (figure 3-9).

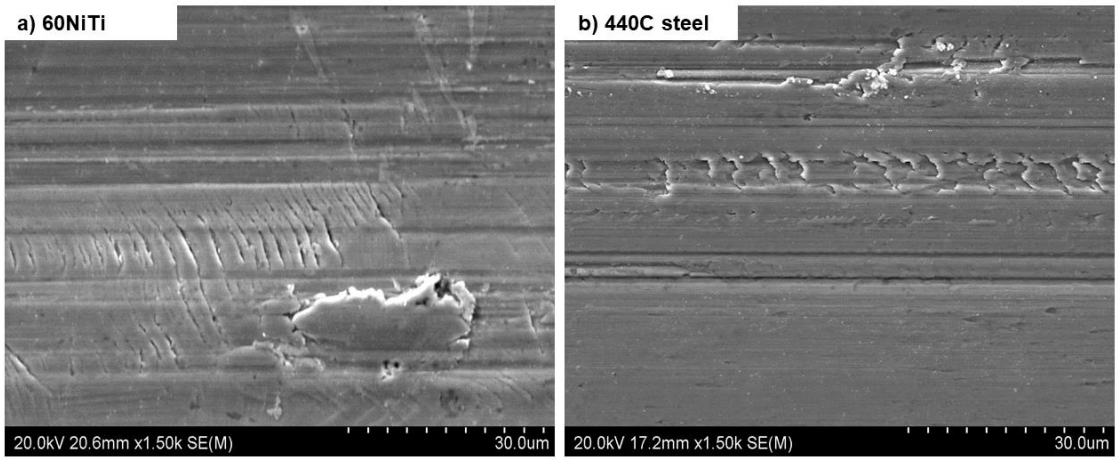

Figure 3-9: SEM images of scratch scars formed under 30N load on 60NiTi and 440C steel samples using a (Ø 2.5 mm) WC ball. a) 60NiTi, b) 440C steel.

These results appear to be the essence of the explanation as to why sliding wear of 60NiTi differs from that of 440C steel. At the macroscopic length scale, these two alloys show similar mechanical properties such as macro hardness, tensile strength and ductility. Thus, if one only considers the macroscopic properties of these alloys, it could be concluded that they will behave similarly in a high stress tribo-test such as a reciprocating sliding test. However, at the microscopic length scale, as observed in Vickers micro hardness tests or single pass scratch tests, these material classes are entirely different with different microscopic behavior that influence the wear processes and cause different responses. 440C steel has large hard carbides to promote hardness and wear resistance and a soft ductile matrix material to halt microcracks from growing large enough to cause fracture or liberate wear particles (much like tungsten carbide-Co cutting tools), whereas 60NiTi (getting its hardness through an Orowan strengthening mechanism) does not have a ductile matrix to arrest propagation of tensile cracks formed on surface or subsurface areas due to abrasive or fatigue wear.

3.2.3 Sliding tests and Stress modelling

This section starts with a discussion explaining the role that different stress components play in damaging 60NiTi and 440C steel samples under unlubricated sliding wear tests (table 3-1). In these sliding tests 60NiTi and 440C steel plates mated 6 mm diameter WC balls. As observed in Chapter 2, 60NiTi exhibits higher wear than 440C steel.

According to the Hertzian theory, the mean compressive stress (H_0) is calculated by the following equation [86, 99]:

$$H_0 = 0.385\left(\frac{W\,E^2}{R^2}\right)^{1/3} \tag{3.1}$$

where W is the applied load, R is the effective radius related to the radius of the contacting components calculated by:

$$\frac{1}{R} = \left(\frac{1}{R_1}\right) + \left(\frac{1}{R_2}\right) \tag{3.2}$$

In this study, the 440C and 60NiTi samples were flat, so that $R_2 = \infty$ and $R = R_1$. E is the reduced elastic modulus given by:

$$\frac{1}{E} = \left(\frac{1 - {\nu_1}^2}{E_1}\right) + \left(\frac{1 - {\nu_2}^2}{E_2}\right) \tag{3.3}$$

where ν_1 and ν_2 are the Poisson's ratios of the contacting materials and E_1 and E_2 are the corresponding elastic moduli.

As deduced from equation 1, the load at each specific compressive stress can be calculated using:

$$W = \frac{{H_0}^3 R^2}{E^2 (0.385)^3} \tag{3.4}$$

Using this equation and employing the critical compressive yield stress for H_0, one can calculate the threshold compressive load at which plastic deformation is expected to begin. Based on the results of the uniaxial compression tests carried out, 440C steel and 60NiTi show yielding at stresses of ~2000 MPa and ~2500MPa respectively [19].

Considering these and using the material properties data presented in table 3-4, the threshold compressive load expected to cause yield in 440C steel and 60NiTi are ~46N and ~210N respectively. Consequently, all the loads applied in the dry sliding wear tests (table 3-1) are lower than the values expected to cause any compressive yielding in both 60NiTi and 440C steel samples.

Table 3-4: Data for stress analysis [27, 45, 99].

Material Characteristics	**E (GPa)**	**ν**	**R (mm)**	**A**	**Compressive yield stress (MPa)**	**Tensile yield stress (MPa)**
WC	600	0.26	3	-	-	-
60NiTi	100	0.34	∞	15.97	~2500	~912
440C steel	200	0.3	∞	12.66	~2000	~1320

On the other hand, as Sliney and Spalvins [86] explained, the critical stress to cause tensile damage in brittle materials can be obtained using:

$$Tensile\ damage\ stress\ = \frac{1}{2}\,(1 - 2v)\ \times\ Vickers\ hardness\ (MPa) \tag{3.5}$$

In this study, 580 HV is considered to be the hardness of 60NiTi and 674 HV for 440C, corresponding to, respectively, ~5700 and ~6600 MPa. Note that these values are obtained based on the average of hardness values measured under different loads (figure 3-3).

Considering equation 3.5 and using the Poisson's ratios of 60NiTi and 440C steel and their Vickers hardness values, 60NiTi and 440C steel are expected to tolerate respectively ~912 and ~1320 MPa tensile stress before incurring permanent damage. Note that, as observed under macroscopic tensile tests and microscopic scratch tests, and as mentioned previously, 60NiTi has very little ductility and only exhibits ductility and plasticity at stress levels very close to the fracture strength. As a result, ~912 MPa is expected to be very close to the specific stress where cracking and tensile fracture is expected to occur in 60NiTi.

The tensile stress component in sliding motions is greatly dependent on the normal load and the CoF value and can be computed as follow [86]:

$$\sigma_{\mu} = (1 + A\mu)\left(\frac{1}{2} - \nu\right)H_0 \tag{3.6}$$

where μ is the CoF and A is given by:

$$A = \frac{3\pi\,(4 + \nu)}{8\,(1 - 2\nu)} \tag{3.7}$$

Considering the Poisson's ratios presented in table 3-4, A is 15.97 for 60NiTi and 12.66 for 440C steel.

Using equations 3.1 and 3.6 and considering the average friction coefficients reported in table 3-1 and the material properties shown in table 3-4, the tensile stresses generated during the sliding wear of 60NiTi and 440C steel plates (mating WC balls under different loads of 2, 5 and 10N) can be calculated. Based on these calculations, the generated tensile stresses under all the applied loads are much higher than the threshold tensile stresses causing damage in both 60NiTi and 440C steel. (Note that although Hertzian analysis is developed for the elastic region and is not applicable to plastic and ductile regions, this analysis can be used confidently to determine whether the generated stresses are above the damage threshold stress or not.)

From the above, it can be concluded that it is the tensile stress component that is responsible for damaging the studied alloys causing wear under the experimented unlubricated reciprocating sliding tests reported in Chapter 2 and presented in table 3-1. Considering this, it is implied that, in accordance with the results obtained from the scratch tests, these are tensile

cracking and the material response to cracks that are the essence of why sliding wear of 60NiTi differs from 440C steel. In 440C, there may be as much damage as seen in 60NiTi, but permanent material loss (wear) in 440C steel may be low because the damage only moves material around whereas in 60NiTi the damage always leads to particle generation and material loss. Clearly, if the sliding induced tensile stresses are reduced enough, then generation of cracks leading to particle liberation and excessive wear is avoided in 60NiTi and it is expected that 60NiTi will show a similar sliding behavior as 440C steel.

Discussed next will be the results of the lubricated sliding wear tests carried out on 60NiTi and 440C steel samples under different (low and high) loads. These tests are implemented using 6 mm diameter WC balls, the same diameter as the ones used in the unlubricated tests reported in table 3-1. Under such conditions, as predicted by the Hertzian stress analysis, the compressive stresses are kept below compressive yielding in both 60NiTi and 440C steel samples. Consequently, carrying out these tests under a range of different loads/stresses provides the opportunity to investigate the effect of friction induced tensile stress on the sliding behavior of these alloys and to explore the conditions where they show divergence in response. This was done by comparing the generated tensile stresses during the sliding wear of 60NiTi and 440C steel plates, using equations 3.1 and 3.6, and considering the material properties presented in table 3-4, and their specific wear rates obtained under different conditions.

As seen in table 3-5 and figure 3-10, friction in 60NiTi does not show a monotonic behavior. Up to 32N, the friction in 60NiTi is low, constant and noise free. Above 32N the CoF is high and erratic. In fact, 32N is the highest load at which 60NiTi appears to be able to form a prefect lubricating film causing low, constant and noise free CoF values. In addition, even under these loading conditions, friction does not show a stable mode and, after passing some time, a second stage (called stage 2) with high and erratic friction emerges (figure 3-10). The reason for the shift in CoF from low to higher values is attributed to oil consumption and is explained in detail in [92].

It is only below a load of 32N (and only in the first stage of friction) that wear does not occur in 60NiTi, as observed by the naked eye during the experiments. Under all other conditions, as presented in table 3-5, 60NiTi wears out. This is because the maximum tensile stress generated under stage 1 conditions is ~589 MPa, well below the aforementioned threshold level of 912 MPa. Note that this stress is generated under 32N load and the CoF value of 0.11. In fact, with a CoF value of 0.11, 60NiTi is expected to tolerate loads up to 119N before experiencing any

tensile stress induced damage under sliding conditions. However, as mentioned, 60NiTi does not show the stage 1 friction at loads above 32N, causing the generated tensile stresses to be well above the critical damaging stress. It can be concluded that ~589 MPa is the highest stress at which a perfect lubricating film is able to be formed on 60NiTi preventing the tensile stresses to exceed the threshold damaging stress. This can be attributed to the properties of the lubricant and the chemical and physical characteristics of the contacting materials.

Note that, considering the average CoF values in stage 2, the maximum generated sliding induced tensile stress amongst the applied loads of up to 17N is 808 MPa. This stress is generated under 17N load and the average CoF value of 0.23. Considering this, it is expected that wear will be prevented under this loading range (up to 17N) in 60NiTi as the amount of generated tensile stresses are below ~912 MPa. In contrast, as seen in table 3-5, wear is occurring under these non-perfect lubrication conditions. As mentioned before and as seen in figure 3-10, 60NiTi exhibits CoF curves with large data scatter heights under these conditions. This makes the calculations of tensile stresses using the average CoF values and equation 6 not accurate. As an example, based on the calculations, the CoF value required to generate tensile stresses equivalent to ~912 under 17N applied load is 0.27. As seen in figure 3-10, the CoF value is actually for long times well above 0.27 causing damage in 60NiTi. These CoF values, being higher than 0.27, are not considered in calculations carried out based on the average CoF value of 0.23.

On the other hand, irrespective of the applied load, 440C steel did not wear and the CoF values were always low (~0.13), constant and noise-free under the total test timing of 142 minutes (figure 3-10). This is because the maximum amount of tensile stress under these conditions is 907 MPa (generated at a load of 40N) which is smaller than the threshold tensile damaging stress of 1320 MPa. In fact, 440C steel is expected to tolerate the threshold load of 180N before experiencing any tensile damage, if the CoF value is considered as 0.13. These results emphasize and confirm that, under conditions where generated tensile stresses in 60NiTi are reduced enough below critical damaging stresses, 60NiTi shows a similar behavior to 440C steel under sliding conditions.

Table 3-5: Wear properties of 60NiTi under gear oil lubricated conditions.

Load (N)	Average CoF and its duration (stage 1)	Average time passed under stage 1 (minutes)	Average CoF (stage 2)	Average specific wear rate (stage 2) ($mm^3/m.N$)
2	0.21	~66	0.45	4.54×10^{-5}
5	0.11	~34	0.28	5.26×10^{-5}
10	0.11	~37	0.23	4.67×10^{-5}
12	0.13	~12	0.24	3.47×10^{-5}
13	0.12	~27	0.27	5.34×10^{-5}
14	0.12	~69	0.24	4.50×10^{-5}
15	0.11	~12	0.27	8.17×10^{-5}
17	0.11	~31	0.23	7.26×10^{-5}
20	0.11	~11	0.31	9.80×10^{-5}
23	0.12	~19	0.33	1.07×10^{-4}
24	0.11	~8	0.40	1.78×10^{-4}
25	0.12	~6	0.44	1.67×10^{-4}
30	0.10	~9	0.40	2.02×10^{-4}
32	0.11	~4	0.45	1.70×10^{-4}
Load		**Average CoF**		**Average specific wear rate ($mm^3/m.N$)**
34		0.46		1.90×10^{-4}
40		0.44		2.30×10^{-4}

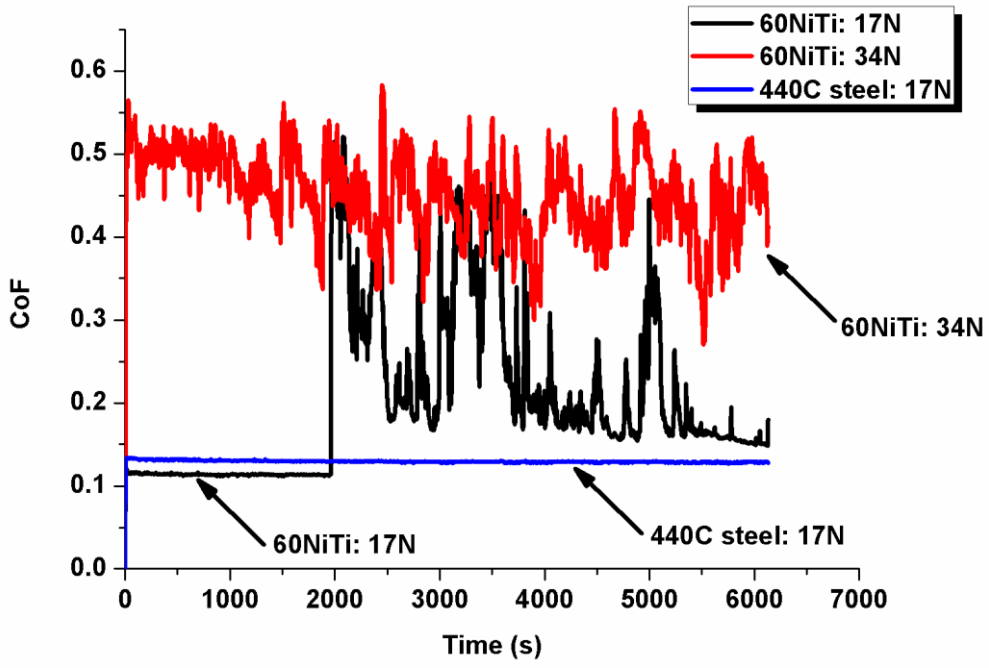

Figure 3-10: Graph showing different types of friction curves formed in gear oil lubricated 440C steel and 60NiTi.

Results of the average specific wear rates of 60NiTi under gear oil lubricated conditions are displayed in figure 3-11. Note that the distance used in these calculations to compute the

specific wear rates was based on the average distance that wear occurred in a sample. For the tested loads of 34N and 40N, this distance is equal to the total distance. However, for the loads below 34N, where the samples show a two-stage friction mode and wear does not occur under the first stage, the distance passed under stage 1 was excluded in calculations. This was done to increase the accuracy of comparisons carried out between the wear rates under different loads.

Since the tensile stress amplitude is greatly dependent on the normal load and the CoF value [86, 98], frictional forces (average friction coefficient times load) are computed in this study to compare the specific wear rates of samples under different loads and CoF values (figure 3-11.b). These calculated forces, despite not being perfectly accurate, as they rely on average CoF values and neglect the scatter heights, provide a clear insight into the role that friction forces play in damaging 60NiTi. A comparison between the plot showing specific wear rates versus load, and the plot showing friction forces versus load, exhibits a direct relationship between the average friction forces and the specific wear rates in 60NiTi samples (figure 3-11). As a general trend, the specific wear rates increase as friction forces, which cause the larger tensile stresses, rise. These results indicate the importance of good lubrication to reduce the CoF values and subsequently tensile stresses for applications where 60NiTi is employed as a wear resistant alloy. In addition, as seen, above 17N load the wear rate appears to increase abruptly. This is because, as mentioned, under such conditions the average tensile stresses are above the tensile damage threshold.

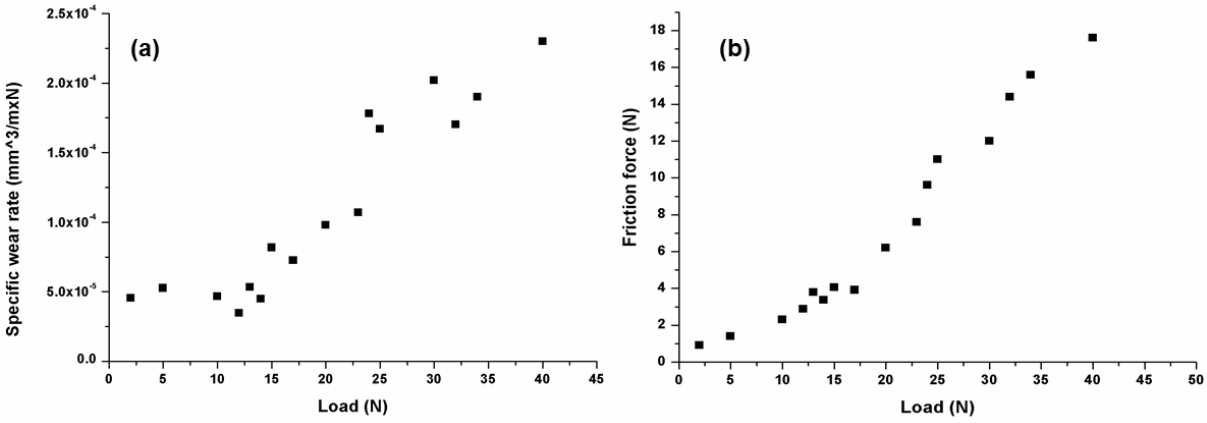

Figure 3-11: Graph showing (a) specific wear rates of 60NiTi samples worn under gear oil lubricated conditions and different loads, and (b) friction forces generated under different loads and CoF values.

In addition, the wear mechanism appears to be shifting from plastic deformation to fracture causing higher wear rates as the friction force is increasing. As seen in the microstructural images (figure 3-12), the surfaces are ploughed and grooves are observed under milder sliding conditions (an evidence showing the dominancy of plastic deformation), but as the condition is getting extremer, the surfaces look smoother due to aggressive removal of material. This is because, under the conditions where the generated friction forces are relatively low, the majority of generated tensile stresses are lower than the fracture strength and are probably in the narrow range where 60NiTi shows plastic deformation. In contrast, as the friction force is increasing, the generated tensile stresses are shifting to higher values causing the formation of shear bands and cracks resulting in imminent fracture in samples (figure 3-13).

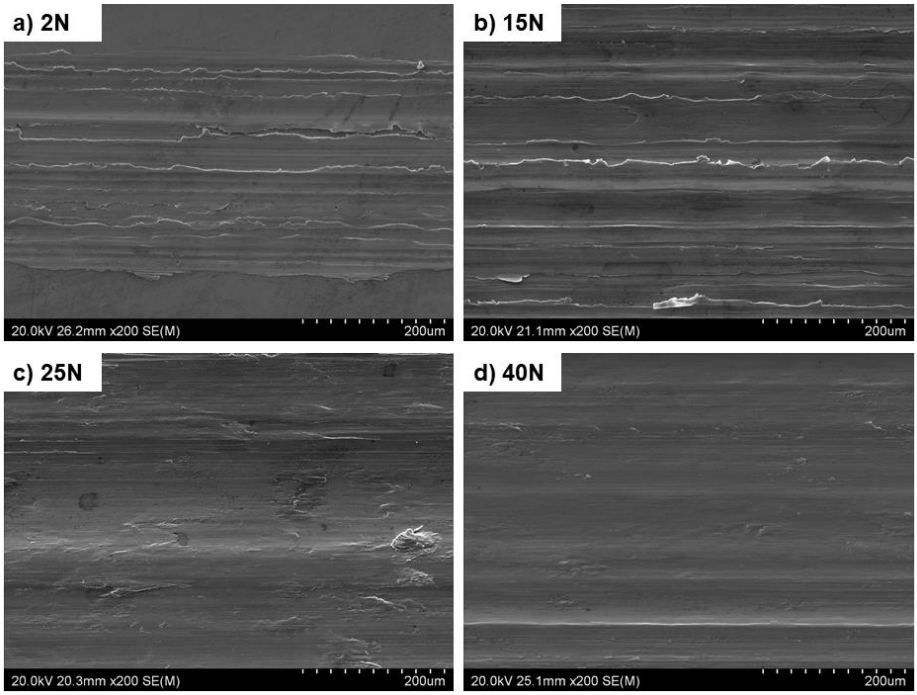

Figure 3-12: SEM images of 60NiTi wear tracks tested under gear oil lubricated condition. a) 2N, b) 15N, c) 25N, d) 40N.

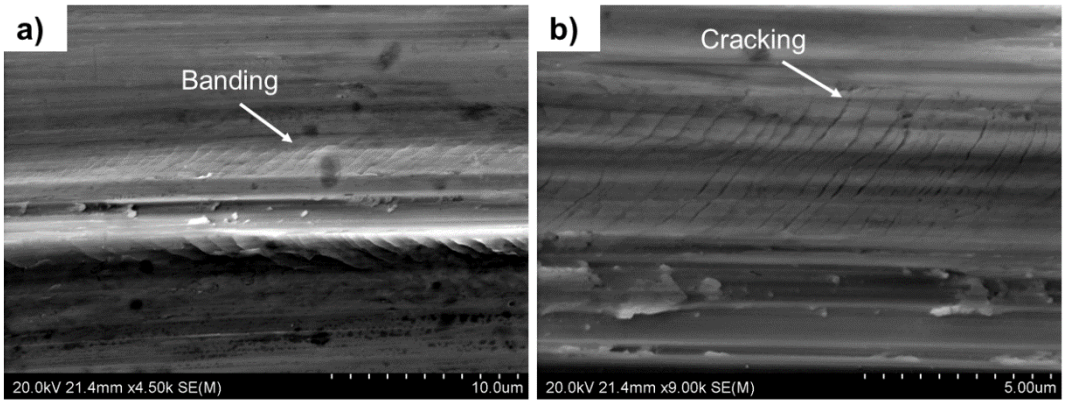

Figure 3-13: SEM micrographs of 60NiTi surfaces showing the formation of a) shear bands, and b) cracks in gear oil lubricated samples worn under 30N load.

3.3 Conclusions

The purpose of the study reported in this chapter was to ascertain why 60NiTi displays a very much inferior sliding wear resistance than 440C steel under unlubricated conditions. This was done through microstructural studies, micro and macro hardness tests and scratch tests. Furthermore, sliding conditions where 60NiTi does not wear and showed a similar behavior as 440C steel were defined using a stress model and lubricated sliding wear tests.

Detailed results show that, despite comparable hardness, 440C steel has a slightly higher damage threshold stress than 60NiTi. In addition, owing to its higher microscale ductility, sliding damage in 440C steel does not necessarily result in material loss as the propagation of generated tensile microcracks are halted. In contrast, the intrinsic brittleness of 60NiTi leads to the formation and growth of microcracks between the shear bands causing subsequent wear particle generation. These lead to the particle liberation and material loss through more aggressive abrasion processes in 60NiTi than 440C steel. This is why the Oberle and Archard models fail to predict 60NiTi wear performance. They only take account of macroscopic properties (macro hardness and elastic modulus), but sliding wear occurs at the microscopic level where asperities interact and stresses are extremely high.

These findings help to explain why 60NiTi performs well when lubricated. 60NiTi is expected to tolerate ~912 MPa tensile stress before yielding. Under good lubricated conditions where a perfect lubricating film is formed, friction induced tensile stresses fall below the damage threshold of 60NiTi and wear is prevented, as it is in 440C steel. When the thresholds are exceeded, damage in the more brittle 60NiTi results in high wear rates compared to 440C. As a result, to ensure good tribological performance of 60NiTi, surface generated tensile stresses must be kept below the damage threshold through good lubrication and load reduction. Above this stress level, 60NiTi appears to be unable to form a perfect lubricating film as the CoF values are high and erratic, causing the generated tensile stresses to exceed the critical damaging stress.

In the next chapter the mechanical properties, and specifically sliding wear performance, of 58Ni39Ti-3Hf (54 at.% Ni- 45 at.%Ti-1 at.% Hf) alloy is evaluated and compared with the baseline 60NiTi. The chapter will investigate how the addition of Hf affects the mechanical properties and damage mechanisms causing wear of baseline 60NiTi and whether this ternary compound can be considered as a substitute of 60NiTi in sliding applications or not.

Chapter 4 Comparison of the reciprocating sliding wear of 58NiTi-3Hf alloy and baseline 60NiTi[4]

[4]**Khanlari K**, Ramezani M, Kelly P, Cao P, Neitzert T. Comparison of the reciprocating sliding wear of 58Ni39Ti-3Hf alloy and baseline 60NiTi. *Wear*, 2018; **408-409**: 120-130.

As discussed in Chapter 1, section 1.1 and section 1.3, 60NiTi, in order to attain the desirable mechanical and chemical properties such as high hardness (~60 HRC), high compressive strength (~2500 MPa), as well as excellent corrosion resistance, needs to be employed in a hardened condition. To harden 60NiTi, it must be heated to high temperatures of approximately ~1050°C so that all precipitates are dissolved and a single phase B2 austenitic NiTi is formed. Subsequent quenching under a very fast cooling rate prevents the formation of soft Ni_3Ti and Ni_3Ti_2 phases. However, even under a very fast cooling rate, precipitation of a high fraction of hard nanoscale Ni_4Ti_3 is nearly inevitable as this metastable phase is formed extremely rapidly in just tens to hundreds of milliseconds [18, 21, 25]. These consequently result in a high hardness through the activation of an Orowan strengthening mechanism [18]. However, rapid quenching from such high temperatures of ~1050°C results in the generation of significant residual stresses leading to quench cracking in treated parts [20, 21, 25, 34]. Recent studies show that the addition of Hf, even in low concentrations, decreases the temperature (more than 100°C) needed to solutionize 60NiTi to obtain a single phase B2 austenitic NiTi [48]. This consequently will decrease the amount of generated residual stresses in hardened parts [34, 43]. In addition, it was found that Hf-addition slows the formation of Ni_3Ti and Ni_3Ti_2 Ni-rich phases and reduces the kinetics of Ni_4Ti_3 coarsening. This also helps to reduce residual stresses since a lower cooling rate is needed to prevent the formation and coarsening of the mentioned phases in the quenching process [22, 39].

Further, Hf additions appear to have a positive effect on the microstructural homogeneity of 60NiTi. This is because Hf acts as an oxygen "getter" reducing the amount of contaminant phases in 60NiTi parts resulting in more homogenized structures [34]. Based on the results obtained by DellaCorte et al. [34], the addition of ~3 wt.% Hf to the baseline 60NiTi composition results in an improved rolling contact fatigue (RCF) stress capability of cast parts. This observation was correlated to the positive effect of Hf on the microstructural homogeneity.

These findings have caused an interest in considering a more complex ternary NiTi-Hf alloy (~58 wt.% Ni-~39 wt.% Ti-~3 wt.% Hf) as a substitute or alternative for 60NiTi alloy. This ternary compound is now under development at NASA as a substitute for baseline 60NiTi [34, 48]. The exact composition by weight percent is 57.6 % Ni-39.2 % Ti-3.2 % Hf (54 at.% Ni-45 at.%Ti-1 at.% Hf) and is designated as 58Ni39Ti-3Hf [34].

Despite the positive interest in this alloy, direct comparisons of the sliding behavior of 58Ni-39Ti-3Hf and the forerunner 60NiTi alloy have not been made. Considering this, there exists a critical requirement to evaluate and compare the sliding performance of 58Ni39Ti-3Hf with baseline 60NiTi for applications such as gears where contacting materials slide over each other.

In this chapter, reciprocating (ball-on-plate) sliding wear tests will be discussed: tests were conducted under lubricated and unlubricated conditions and a range of low to high loads to evaluate how the sliding properties of 58Ni39Ti-3Hf differ from those of 60NiTi under both moderate and large sliding-induced tensile stresses. In addition, to fully understand the reasons causing divergence in the wear response of both materials, mechanical and micro-tribological properties of these two alloys were investigated and compared through indentation, hardness and scratch tests. Results obtained will help in understanding how the addition of Hf affects the wear responses and the mechanisms that at a microscopic level cause damage in 60NiTi.

4.1 Materials and experimental methods

4.1.1 60NiTi and 58Ni39Ti-3Hf specimen preparation and testing

As for 60NiTi, hardened NiTi-Hf (~58 wt.% Ni-~39 wt.% Ti-~3 wt.% Hf) samples were received from NASA, Glenn Research Center in Cleveland, Ohio. 58Ni39Ti-3Hf samples were cut, hardened and prepared under the same circumstances of 60NiTi. The information regarding the concerned procedures (cutting, hardening, grinding, polishing) are provided in the section 2.1 of Chapter 2.

In addition, similar to the previous studies, samples used for the microstructural studies were additionally etched with a room temperature aqueous solution of 1 vol. % HF and 10 Vol. % HNO_3 for 90 seconds [32]. A Hitachi-su70 scanning electron microscopy (SEM) machine (working based on the emissions received from the secondary electrons) equipped with an energy dispersive spectroscopy (EDS) and an X-ray diffraction (XRD) machine using Cu Kα radiation were employed to compare the microstructure and phase composition of hardened 58Ni39Ti-3Hf samples to 60NiTi ones.

4.1.2 Macro and micro hardness testing

The procedures used to conduct and study macro and micro indentation and hardness tests were identical to the ones explained in Chapter 3. Indentation tests were conducted at varying loads of 25, 50, 100 and 150N under the loading and unloading rate of 40N/min using a Rockwell C indenter (200 μm diamond tip conical indenter) by a tribometer capable of applying normal loads up to 200N. Additionally (as similar to the previous chapter), a Rockwell C hardness tester was employed to apply other higher loads of 60, 100 and 150 kgf, corresponding to, approximately 588, 980 and 1471N loads, respectively. An optical profilometer was used to measure the indent depths that resulted from these tests. Further, a micro-indentation hardness machine was used to measure the Vickers hardness of the samples at varying loads of 0.5, 1, 2.5, 5 and 10 kgf.

4.1.3 Sliding wear testing

The machine used to conduct the reciprocating sliding tests and experimental specifications employed for these tests such as sliding frequency, testing time, wear track length, used lubricants, counterface material, its size and geometry were the same as the ones used in chapter 2. Again, the procedure used to measure and calculate the specific wear rates (mm^3/N.m) of samples for each specific test was the same as the one explained in Chapter 2, section 2.1. To further reveal the differences in the wear response, other than studying the wear tracks, the subsurface regions of wear tracking was additionally studied using the SEM machine.

4.1.4 Scratch testing

Similar to the previous studies (section 3.1), single pass scratch tests were carried out in order to investigate the micro-mechanical properties of these alloys and to reveal the mechanisms responsible for damage in these materials. The tests were performed using the same Rockwell C indenter and tribometer (capable of recording CoF and applying loads up to 200N) employed in the indentation tests at different constant loads of 2, 5, 7, 10, 15 and 20 N.

In an identical manner to the study reported in the previous chapter, the scratch grooves were inspected by SEM and an optical profilometer. Inspection by optical profilometry enabled the computation of pile-up/groove area ratio (A_p/A_g) through the measurement of the cross-sectional area of the lateral pile-up (A_p) and the cross-sectional area of the groove (A_g). The pile-up to groove area ratio (A_p/A_g) is directly related to the plastic deformability of the materials [68]. In addition, further inspections were conducted on the grooves by SEM analysis.

These studies revealed the mechanisms that cause damage at the microscale and the approximate critical loads for the onset of specific damages in these alloys.

All the mechanical tests mentioned above were repeated three times and the average obtained results are reported.

4.2 Results and discussion

4.2.1 Microstructural, phase compositional, indentation and hardness studies

Figure 4-1 shows the surface microstructural features of 60NiTi and 58Ni39Ti-3Hf samples. The Ni-rich Ni_3Ti phase, observed in the SEM images of the outer surface regions of 60NiTi samples (figure 4-1.a), were not seen under surface SEM images got from 58Ni39Ti-3Hf samples (figure 4-1.b). Hf acts as a "getter" and the Hf addition is known to help remove oxygen from the alloy and tie it up in HfO_2 phases. Therefore, the addition of this element reduces the reaction amongst Ti and oxygen, as the solutionizing treatments were carried out under open atmosphere conditions, preventing subsequent Ni_3Ti phase formations [34]. Hf-addition in NiTi compositions also reduces the kinetics of Ni_3Ti and Ni_3Ti_2 phase formations and coarsening [39]. This might be another reason for the absence of these phases in 58Ni39Ti-3Hf samples quenched under the same cooling rate as 60NiTi samples. Thus, it appears that the addition of Hf to the alloy results in a more uniform and homogenous microstructure.

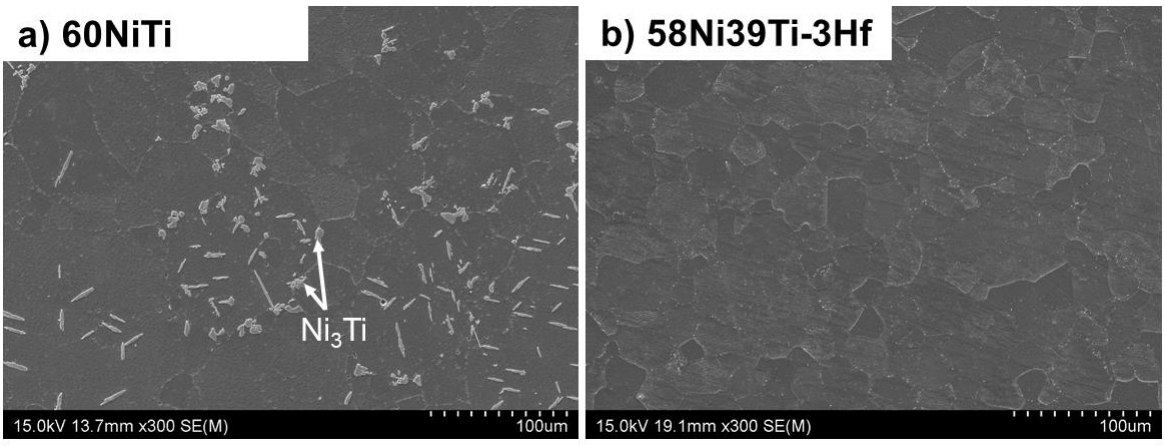

Figure 4-1: SEM images showing the typical surface microstructure of a) 60NiTi, and b) 58Ni39Ti-3Hf.

X-ray diffraction of these hardened materials (figure 4-2) confirmed that the hardening treatment has been successful in rendering the materials in their desired hardened state. This is

because the only major peaks observed in the XRD patterns are correlated to austenitic NiTi and hard Ni_4Ti_3 phases. Moreover, the absence of a major peak correlating to a Ni_3Ti phase in the XRD pattern of the 60NiTi samples (figure 4-2) indicates that this phase has low volume fraction in these samples.

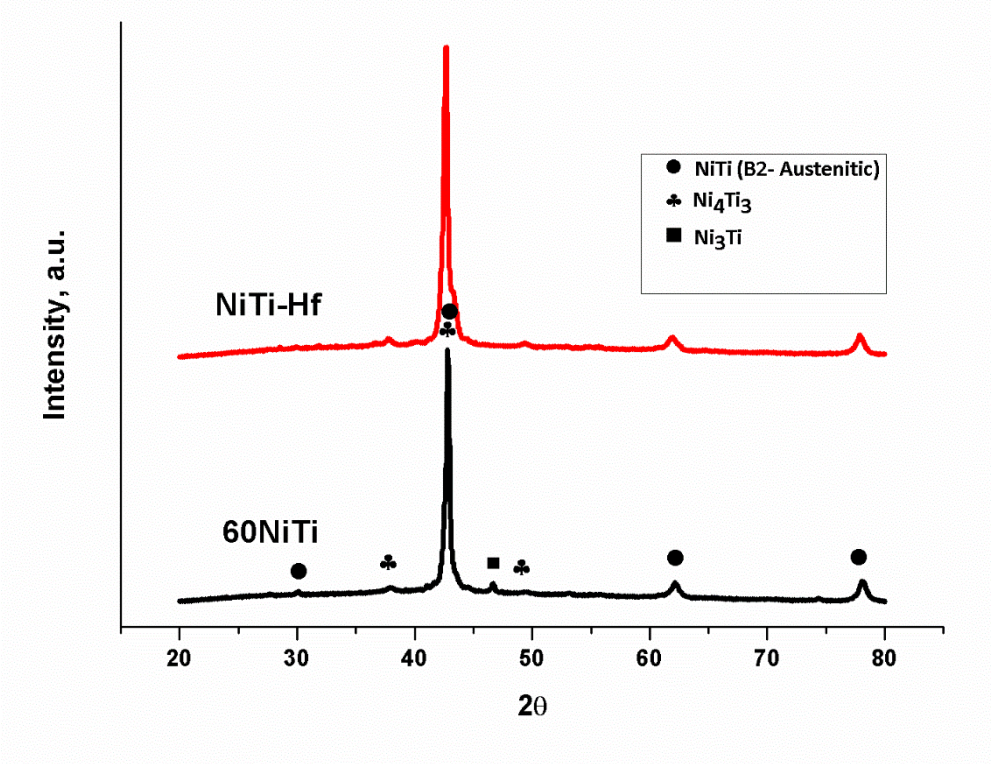

Figure 4-2: XRD pattern of 60NiTi and 58Ni39Ti-3Hf samples.

Results of the indentation tests carried out using a Rockwell C indenter under different loads are displayed in figure 4-3. As can be seen, 58Ni39Ti-3Hf and 60NiTi exhibit approximately the same amount of indent depths under different low and high loads. Furthermore, based on the results obtained from the standard Rockwell C hardness tests, both these intermetallics exhibit equal hardness values of about ~60 HRC. This means that the addition of Hf to the 60NiTi composition, if not improving the observed high hardness of this alloy tested using a Rockwell C indenter, does not cause the loss of it.

The level of resulting permanent indent depths generated in static indentation tests carried out using Rockwell indenters are mainly ruled by yield behavior and strain hardening rate factors [94]. Note that there is a direct correlation between the strain hardening rate and the slopes of load and indentation depth plots for spherical contact conditions [82]. In fact, the indentation tests using Rockwell indenters were carried out under different loads to reveal these differences

in mechanical behavior characteristics of these alloys. However, 58Ni39Ti-3Hf and 60NiTi exhibited approximately the same amount of indent depth under different low and high loads. Considering that, 60NiTi and 58Ni39Ti-3Hf appear to exhibit a similar yield behavior and strain hardening rate.

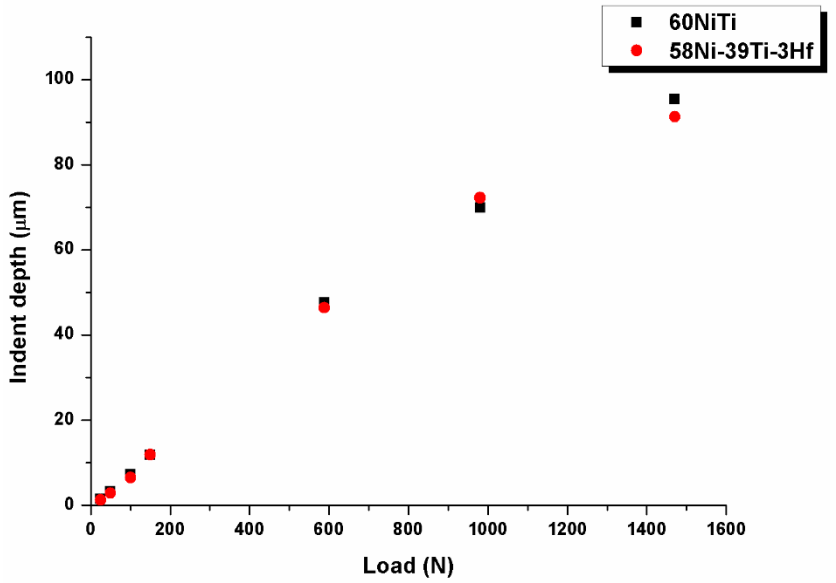

Figure 4-3: Indent depth for indentation tests done by a Rockwell C indenter under different loads of 25, 50, 100, 150, 588, 980 and 1471N on 60NiTi and 58Ni39Ti-3Hf samples. Note that the maximum value of the standard deviation for indent depth in all the loads in both alloys was 0.5 μm.

Figure 4-4 shows the results of the Vickers hardness tests. As seen, 60NiTi appears to have higher Vickers hardness under all tested loads (0.5, 1, 2.5, 5 and 10 kgf) as compared to 58Ni39Ti-3Hf.

The Vickers hardness tests employing sharp pyramidal indenters are used to evaluate the fracture response of the studied materials [95, 96]. Vickers indenters can generate large strains (between 0.25 and 0.36) within the indented zone leading to considerable fracture [95, 96]. As a result, these hardness tests, other than evaluating the resistance of NiTi alloys to permanent deformation under different loads, allow for assessing the resistance to fracture and tearing in the samples. Considering this, it can be concluded that 60NiTi shows a higher ability to resist tearing compared to a 58Ni39Ti-3Hf alloying system when indented by sharp pyramidal indenters that cause high stresses.

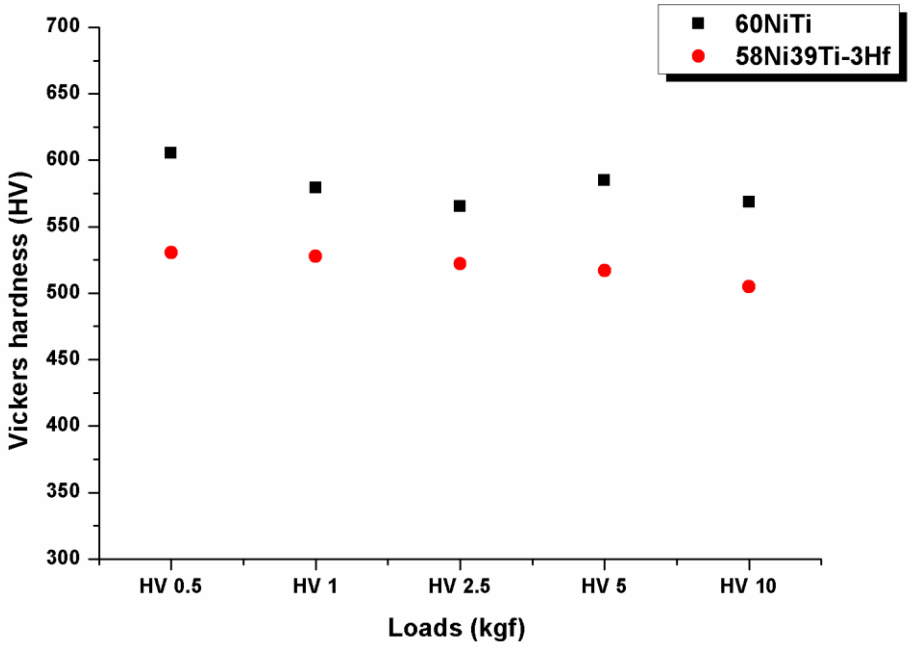

Figure 4-4: Vickers hardness of the 60NiTi and 58Ni39Ti-3Hf samples under different loads. Note that the maximum value of the standard deviation for Vickers hardness in all the loads in both alloys was 26 HV.

4.2.2 Sliding and scratch tests studies

Next discussed are the results of the unlubricated sliding wear tests carried out on 60NiTi and 58Ni39Ti-3Hf alloys. 60NiTi and 58Ni39Ti-3Hf seem to show approximately similar sliding wear behavior under unlubricated conditions (figure 4-5). However, 58Ni39Ti-3Hf appears to show a slightly higher wear resistance as compared to 60NiTi, as the specific wear rate of this alloy is a bit less under 2, 10 and 30N than baseline 60NiTi.

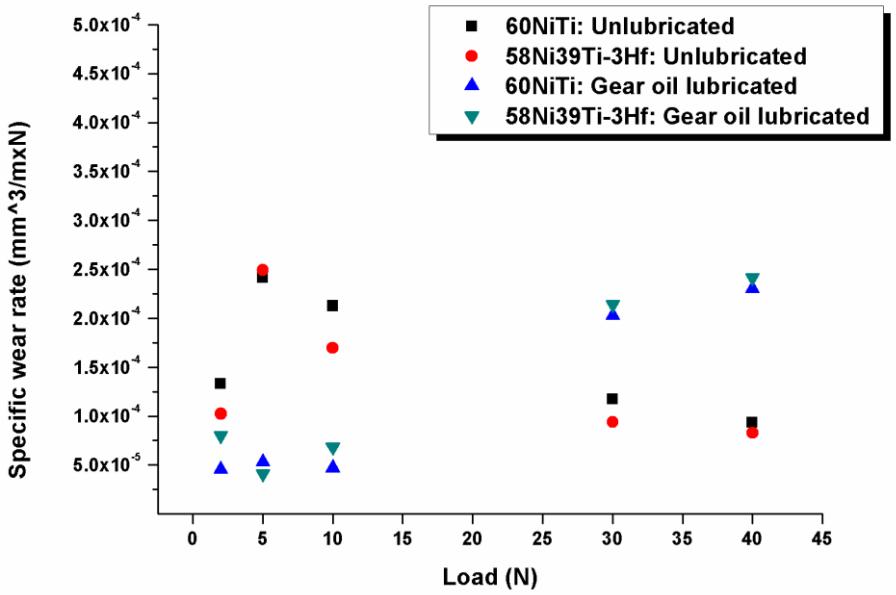

Figure 4-5: Specific wear rates of 60NiTi and 58Ni39Ti-3Hf samples worn under unlubricated and gear oil lubricated conditions. Note that the maximum value of the standard deviation for specific wear rate in all the loads in both alloys was 0.1×10^{-4} (mm^3/m.N).

According to the Archard equation, the specific wear rate for each of 60NiTi and 58Ni39Ti-3Hf samples, is expected to be a constant value under different loads [49]. However, as seen in figure 4-5, this value is changing under different loads. This is an evidence showing that the wear behavior of NiTi alloys is not following the conventional theories as reported in other researches [53, 92].

In addition, both these alloys exhibit high CoF under unlubricated conditions against WC balls (table 4-1).

Table 4-1: CoF values of 60NiTi and 58Ni39Ti-3Hf worn under unlubricated conditions.

Material	Load (N)	Average CoF
60NiTi	2	1.64
58Ni39Ti-3Hf	2	1.64
60NiTi	5	1.18
58Ni39Ti-3Hf	5	1.20
60NiTi	10	1.03
58Ni39Ti-3Hf	10	1.03
60NiTi	30	0.83
58Ni39Ti-3Hf	30	0.80
60NiTi	40	0.80
58Ni39Ti-3Hf	40	0.75

As seen in table 4-1, CoF decreases as the applied normal load increases. In friction tests, when the load increases, the friction force increases. The rate of the increase is the CoF and this rate is not necessarily a constant value. The CoF is essentially a measure of the shear strength of the interface and is controlled by the true area of contact (interacting peaks, for instance) which is never exactly known. With all these variables, it is not uncommon for the friction coefficient to drop with load until a higher load is reached that leads to other friction effects, like asperity peak welding. Stanford [48] speculated that since a reversible austenite to martensite stress-induced phase transformation occurs in these superelastic materials under high contact stresses [4, 17, 19], the bonded asperities of these NiTi alloys (to the mating WC ball) might transform from their hardened austenitic state to a soft martensitic state. As a result, in a larger area where many asperities are bonded together, the contacting surfaces would then have less resistance toward opposing motion under higher loads as it is easier for the softer asperities to deform [48].

Some SEM micrographs of the wear tracks worn under unlubricated conditions are shown in figure 4-6. Since the wear tracks of these NiTi alloys formed under low and high loads look very similar to each other, it can be concluded that the wear of these alloys follows the same mechanisms. As explained in detail in [92], 60NiTi wears through abrasive and fatigue wear that are possibly enhanced by adhesion. Other than faint striations and grooves parallel to the sliding direction in their wear tracks, lumps and deposits are also frequently seen on the wear surface of these alloys. In fact, the repetitive sliding of WC balls results in the deformation of these alloys (due to cutting or ploughing action) leading to the formation of grooves on the surfaces of these alloys. This is an indicator showing that abrasion is one of the mechanisms that results in the wear of these NiTi alloys [48]. The formation of lumps on the surface of the wear tracks are attributed to different reasons such as compaction of the wear debris, plowed accumulations or adherence of plastically deformed materials.

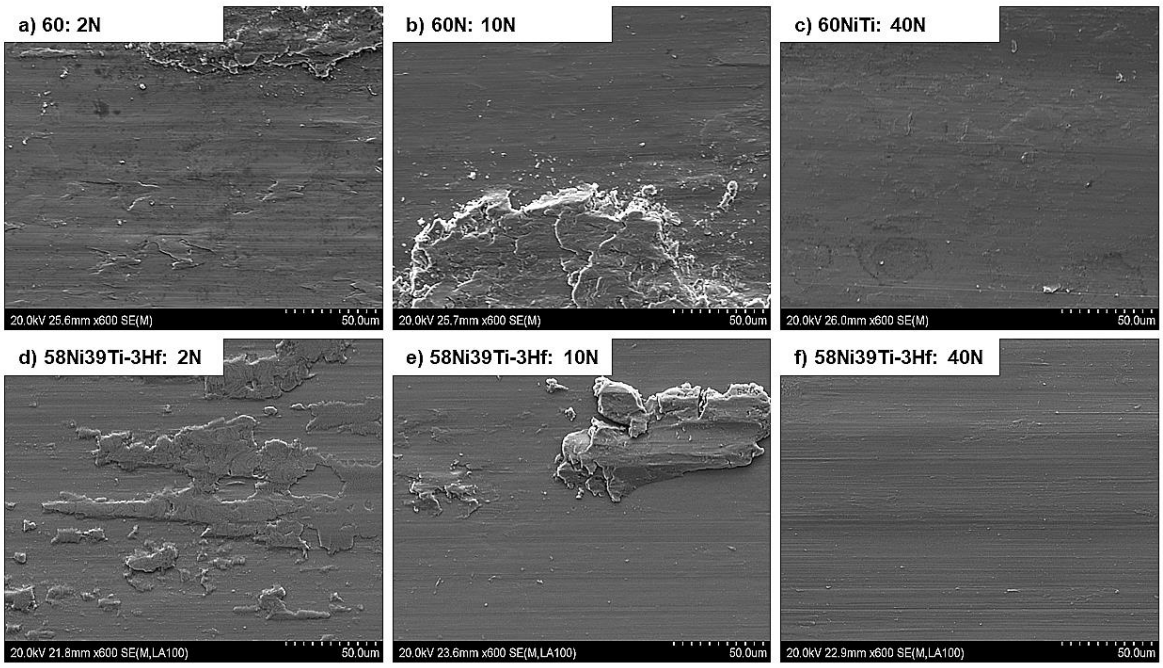

Figure 4-6: SEM images of wear tracks formed in 60NiTi and 58Ni39Ti-3Hf samples tested under an unlubricated condition and different loads. a) 60NiTi: 2N load, b) 60NiTi: 10N load, c) 60NiTi: 40N load, d) 58Ni39Ti-3Hf: 2N load, e) 58Ni39Ti-3Hf: 10N load and f) 58Ni39Ti-3Hf: 40N load. Note the unworn (and unetched) baseline areas beside the wear tracks which can be seen in the 60NiTi and NiTi-Hf samples worn under 2N load.

Figure 4-7 exhibits the cross-sectional SEM images of the 60NiTi and 58Ni39Ti-3Hf wear tracks. Cracks can be observed in these subsurface images. Different reasons can be considered for the generation of these cracks. It might be that the strong adhesion between the WC ball and the NiTi surfaces, resulting in large shear stresses above the damaging threshold, have caused the generation of these cracks or even immediate fracture. Alternatively, these cracks can be formed due to the repeated milder shear stresses formed under sliding movements. These formed cracks are propagated under further cyclic stresses leading to the fracture of the material [48]. These results confirm that fracture caused by adhesion or fatigue wear are amongst primary wear mechanisms causing damage and wear in these NiTi alloys. Furthermore, the dry sliding cross-sections of 60NiTi seem to show more cracks and crack propagations than 58Ni39Ti-3Hf ones. This can be interpreted as evidence of improved fatigue wear resistance of 58Ni39Ti-3Hf than 60NiTi and is in accordance with the published results which show that 58Ni39Ti-3Hf alloy exhibits superior fatigue properties than 60NiTi [34].

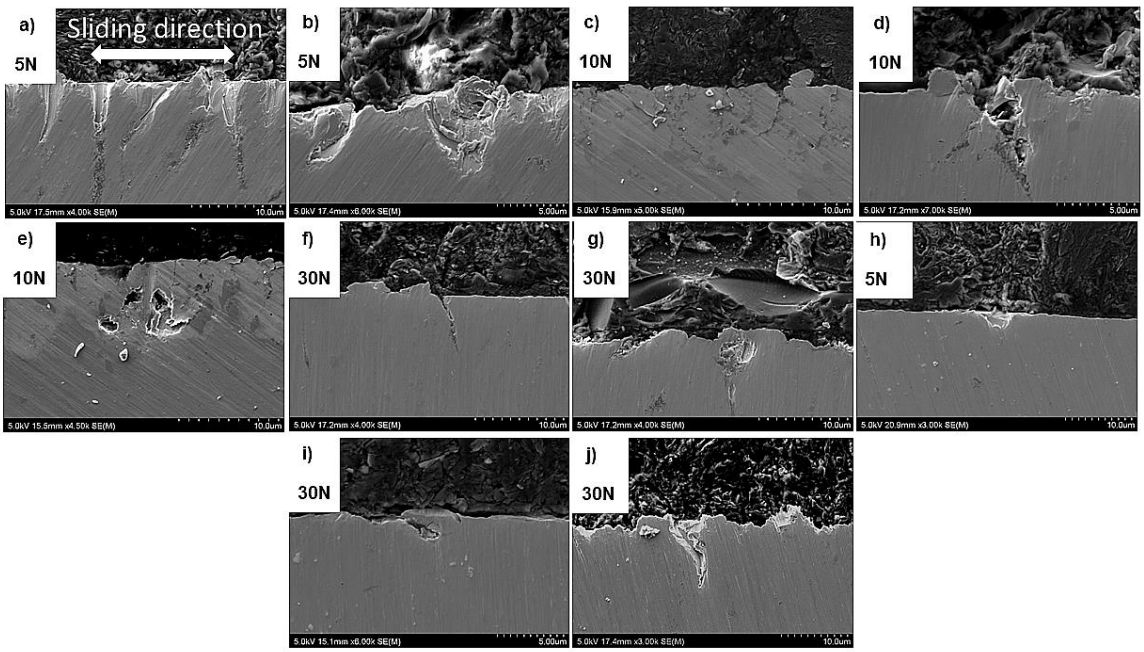

Figure 4-7: Subsurface SEM images of wear tracks formed in 60NiTi and 58Ni39Ti-3Hf samples tested under unlubricated condition and different loads. a and b) 60NiTi: 5N load, c, d and e) 60NiTi: 10N load, f and g) 60NiTi: 30N load, h) 58Ni39Ti-3Hf: 5N load, i and j) 58Ni39Ti-3Hf: 30N load. The sliding direction as indicated in (a) has the same orientation in all images.

Next follows is a discussion of the results of tests carried out under lubricated conditions. Lubrication of the studied NiTi alloys with gear oil reduces the CoF values under each specific load (figure 4-8 and table 4-2). As seen in table 4-2 and figure 4-8, and as already discussed in Chapter 2, section 2.2.2, the friction shows a two-stage mode under 2, 5 and 10N loads. In stage 1, where the friction is low, smooth and noise-free, both 60NiTi and 58Ni39Ti-3Hf do not wear (as observed by the naked eye during the tests) and wear starts to occur during the second stage where the CoF value increases due to the partial breakage of the lubricant film caused by oil consumption [92]. These results prove that these NiTi alloys do not wear under selected loads and good lubrication conditions where the CoF values are under stage 1. This is perhaps because under these conditions the sliding induced tensile stress is lower than the threshold amount causing damage in these alloys. These findings imply the importance of good lubrication and stress design for applications where 60NiTi and 58Ni39Ti-3Hf are employed as wear-resistant alloys.

Table 4-2: CoF values of 60NiTi and 58Ni39Ti-3Hf samples worn under gear oil lubricated conditions. Please note that the total duration of each test was 102 minutes.

Material	Load (N)	Average CoF and its duration (stage 1)	Average CoF (stage 2)
60NiTi	2	0.21 (~66 minutes)	0.45
58Ni39Ti-3Hf	2	0.23 (~50 minutes)	0.54
60NiTi	5	0.11 (~34 minutes)	0.28
58Ni39Ti-3Hf	5	0.12 (~34 minutes)	0.27
60NiTi	10	0.11 (~37 minutes)	0.23
58Ni39Ti-3Hf	10	0.11 (~36 minutes)	0.24
60NiTi	30	0.10 (~9 minutes)	0.40
Material	**Load (N)**	**Average CoF**	
58Ni39Ti-3Hf	30	0.40	
60NiTi	40	0.44	
58Ni39Ti-3Hf	40	0.42	

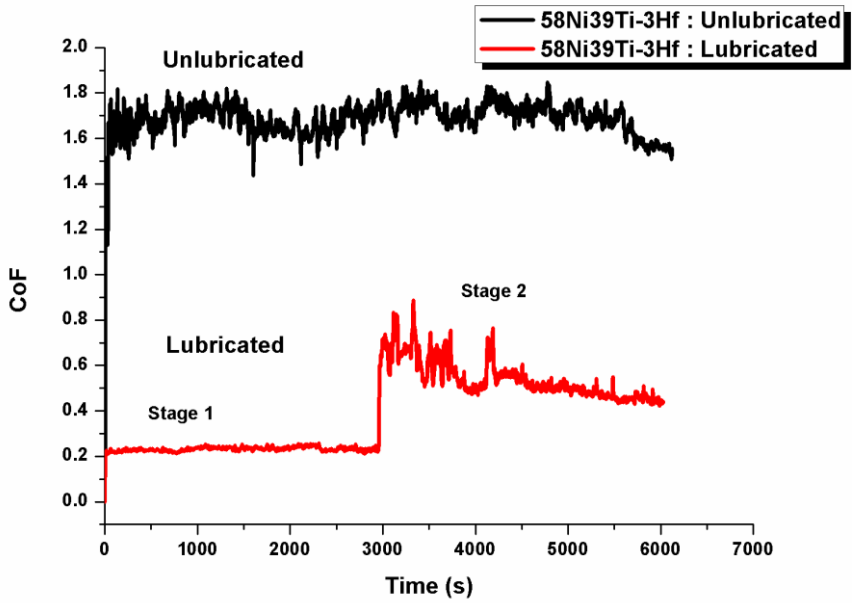

Figure 4-8: CoF curves of 58Ni39Ti-3Hf worn under unlubricated and gear oil lubricated conditions (2N load).

Results of the average specific wear rates of 60NiTi and 58Ni39Ti-3Hf under gear oil lubricated condition as compared to unlubricated condition are displayed in figure 4-5. These values were calculated based on the average distances that these alloys pass under the second stage of friction, where the wear occurs. In other words, the sliding distance used to determine the specific wear rates shown in the table are only a portion of the total 102 minutes test time, the portion of time under which stage 2 (high friction and wear) occurs.

These results will help designers to have a better understanding of the friction and wear characteristics of 60NiTi and 58Ni39Ti-3Hf under emergency conditions where the lubricating oil is consumed and not replaced.

As seen, under 2, 5 and 10N loads, the average specific wear rates of these alloys are reduced as compared to unlubricated ones. However, under 30 and 40N loads, the specific wear rates increased significantly up to high values comparable to unlubricated conditions (5 and 10N).

In addition, both alloys show approximately equal specific wear rates under each specific load. However, 58Ni39Ti-3Hf exhibits a slightly higher specific wear rate under 2N load. This might be due to the higher average CoF value that this alloys shows (0.54) under the second stage of friction as compared to 60NiTi (0.45), causing higher sliding induced tensile stresses.

As seen in the SEM images of the gear oil lubricated wear tracks (figure 4-9), the wear surfaces look smoother under a high load of 40N than lower loads of 2 and 10N where the surfaces look ploughed. These suggest that the low specific wear rates of 60NiTi and 58Ni39Ti-3Hf observed under the relatively low loads of 2, 5 and 10N are because under these conditions the abrasive wear is governed by plastic deformation (mild abrasion) resulting in formation of ploughing grooves. On the other hand, under the high loads of 30 and 40N, as with the unlubricated condition, the abrasive wear is severe causing fracture and aggressive removal of material.

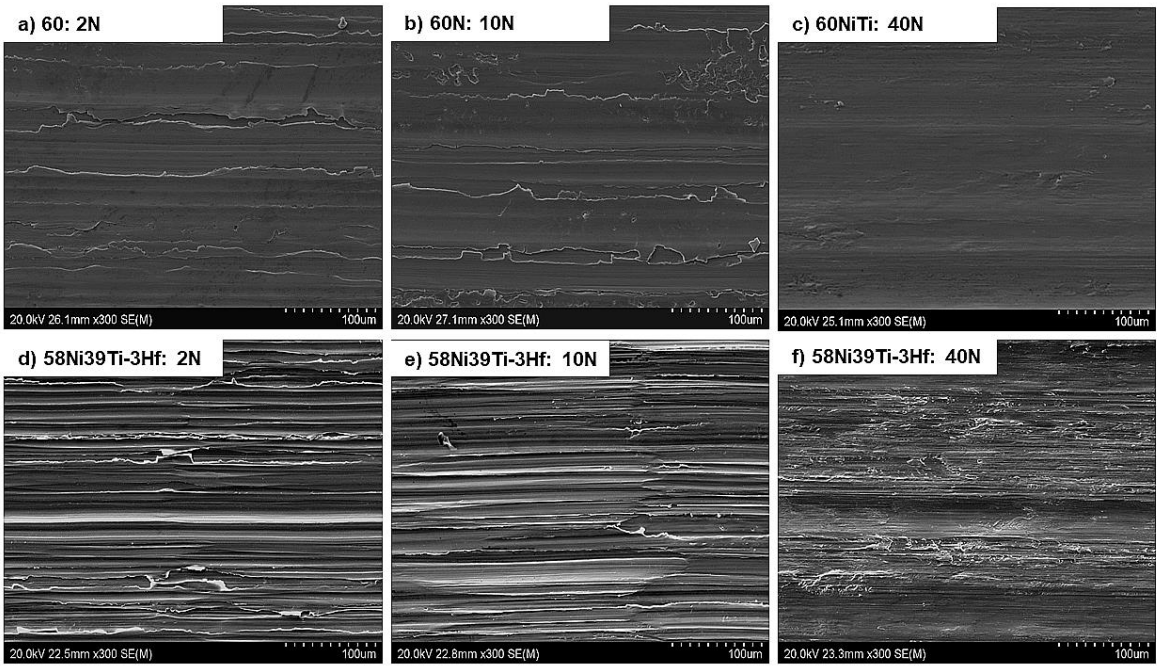

Figure 4-9: SEM images of wear tracks formed in 60NiTi and 58Ni39Ti-3Hf samples tested under a gear oil lubricated condition and different loads. a) 60NiTi: 2N load, b) 60NiTi: 10N

load, c) 60NiTi: 40N load, d) 58Ni39Ti-3Hf: 2N load, e) 58Ni39Ti-3Hf: 10N load, and f) 58Ni39Ti-3Hf: 40N load.

Another series of lubricated sliding wear tests were carried out using castor oil. Castor oil is a vegetable oil and as such is considered to be a green (environmentally friendly) lubricant, as it is biodegradable and renewable [60]. Results of different researches show that low coefficients of friction can be obtained when 60NiTi is lubricated under boundary regime with castor oil [52, 60, 67].

However, results of castor oil sliding wear tests carried out in this research showed that friction under stage 1 (where the CoF value is low and wear does not occur) is experienced only for a few minutes under each specific load (table 4-3). These results suggest that castor oil is not a good substitute for the synthetic gear oil in applications where near-perfect lubrication and the absence of wear in 60NiTi and 58Ni39Ti-3Hf are crucial.

In terms of the time that these materials pass under the stage 1 of friction, as seen in table 4-2 and table 4-3, 58Ni39Ti-3Hf exhibits slightly shorter times than 60NiTi. The reason for this observation is not fully understood at this time; it might be related to slight differences in surface chemistry due to the addition of Hf to the 60NiTi composition. This is because the chemical properties of the contacting materials directly influence the surface lubrication [61]. However, this does not seem to be a concern for the application of 58Ni39Ti-3Hf as a substitute of 60NiTi as this difference in time is very small (average ~7 minutes).

Table 4-3: CoF values of 60NiTi and 58Ni39Ti-3Hf samples worn under castor oil lubricated condition. Please note that the total duration of each test was 102 minutes.

Material	**Load (N)**	**Average CoF and its duration (stage 1)**	**Average CoF (stage 2)**
60NiTi	2	0.21 (~7 minutes)	0.74
58Ni39Ti-3Hf	2	0.22 (~2 minutes)	0.59
60NiTi	5	0.16 (~1 minute)	0.39
58Ni39Ti-3Hf	5	0.11 (~1 minute)	0.37
60NiTi	10	0.10 (14.3 minutes)	0.32
Material	**Load (N)**	**Average CoF**	
58Ni39Ti-3Hf	10	0.31	
60NiTi	30	0.24	
58Ni39Ti-3Hf	30	0.23	
60NiTi	40	0.22	
58Ni39Ti-3Hf	40	0.22	

Figure 4-10 exhibits the results of the average specific wear rates of 60NiTi and 58Ni39Ti-3Hf alloys lubricated by castor oil. As with the sliding wear tests carried out with the gear oil, these values were calculated based on the average distances that these alloys passed under the second stage of friction. In fact, the sliding distance used to calculate the wear rate is only counted after the jump in friction from stage 1 to stage 2 was observed. This method is used because no wear was observed during stage 1.

As observed under the applied loads of 2, 5 and 10N, the specific wear rates of these alloys are in the same range as the ones carried out with the gear oil (figure 4-10). However, under the higher loads of 30 and 40N, the specific wear rates of these NiTi alloys are drastically lower than the gear oil lubricated ones. This is because, under these applied loads, the average CoF values of these alloys are lower (0.22) than gear oil lubricated ones (~0.44) resulting in lower sliding induced tensile stresses.

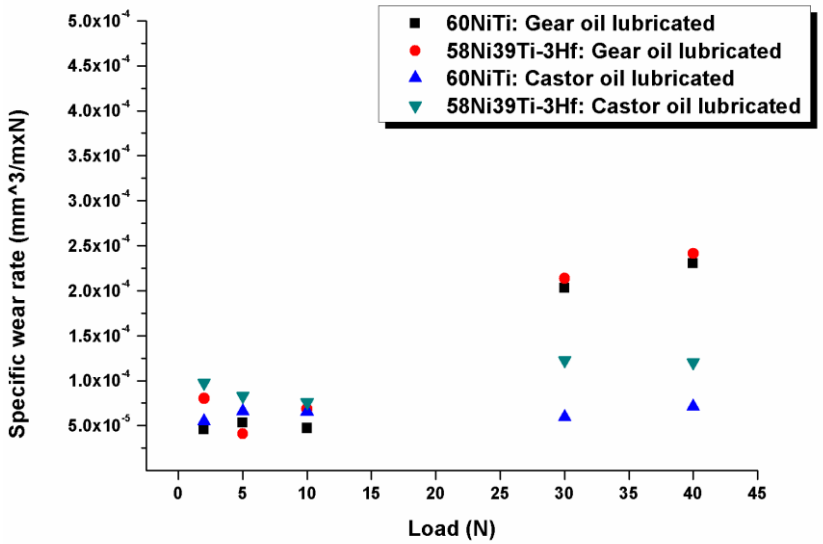

Figure 4-10: Specific wear rates of 60NiTi and 58Ni39Ti-3Hf worn under castor oil and gear oil lubricated conditions. Note that the maximum value for the standard deviation in all the loads in both alloys was 0.1×10^{-4} (mm^3/m.N).

In fact, based on the SEM microstructural images obtained from the surface of castor oil lubricated wear tracks, in all the applied loads (including a high load of 40N) the abrasive wear mechanism is ruled by plastic deformation causing the formation of grooves (figure 4-11). In essence, the occurrence of fracture dominated abrasion, causing high specific wear rates, was prevented under castor oil lubrication.

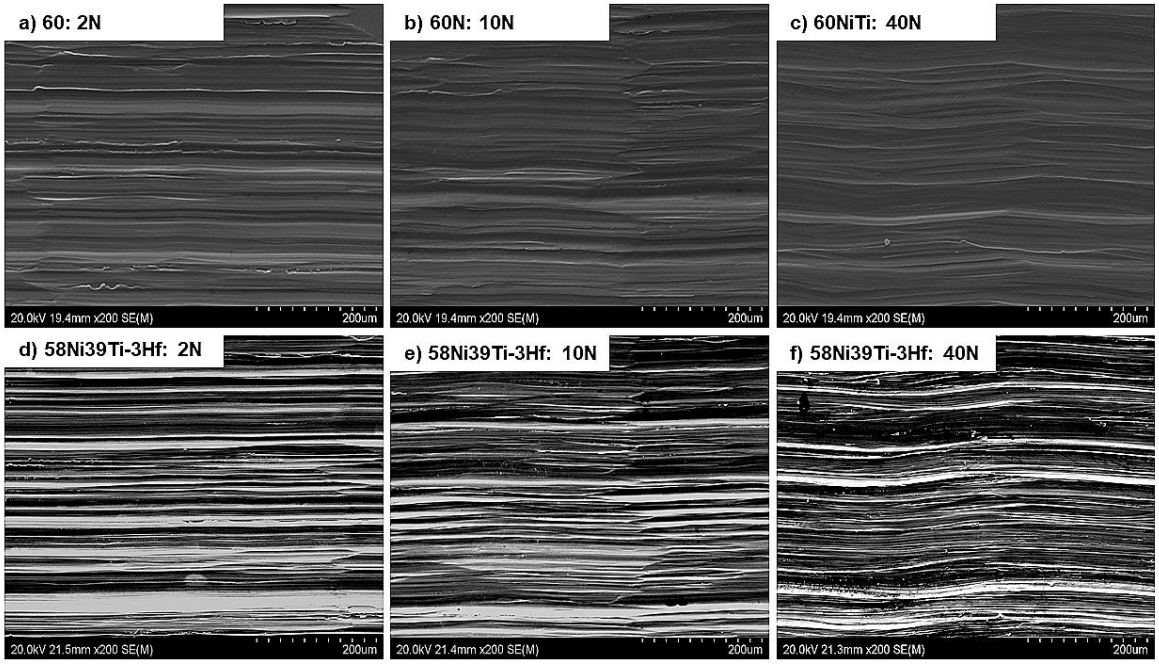

Figure 4-11: SEM images of wear tracks formed in 60NiTi and 58Ni39Ti-3Hf samples tested under castor oil lubricated condition and different loads. a) 60NiTi: 2N load, b) 60NiTi: 10N load, c) 60NiTi: 40N load, d) 58Ni39Ti-3Hf: 2N load, e) 58Ni39Ti-3Hf: 10N load, and f) 58Ni39Ti-3Hf: 40N load.

In addition, as seen in figure 4-10, 58Ni39Ti-3Hf shows an inferior wear resistance than baseline 60NiTi under most of the loads (especially under higher loads of 30 and 40N) with castor oil lubrication. This is despite the fact that 58Ni39Ti-3Hf exhibits lower, or approximately the same, CoF values (causing relatively lower sliding induced tensile stresses) under each specific load as compared to 60NiTi (table 4-3). This shows a difference in the mechanical properties of these alloys.

Single-pass scratch tests using a sharp conical indenter simulate single pass sliding of small, hard asperities on alloy surfaces. Therefore, results obtained from these tests are suitable for interpreting the microscopic-level abrasive wear mechanisms that damage the studied materials [68, 93]. As mentioned, scratch tests were conducted under a constant speed and different loads of 2, 5, 7, 10, 15 and 20 N.

Table 4-4 presents information on general characteristics for these scratches formed under different loads of 2, 5, 10 and 20N, such as scratch depth (S_D), scratch width (S_W) and the ratio between the cross-sectional area of the lateral pile-up (A_P) and the cross-sectional area of the groove (A_G). These were measured and calculated using cross-sectional profile images of

scratches obtained by an optical profilometer (figure 4-12). In addition, table 4-4 also presents the CoF values recorded during scratch tests.

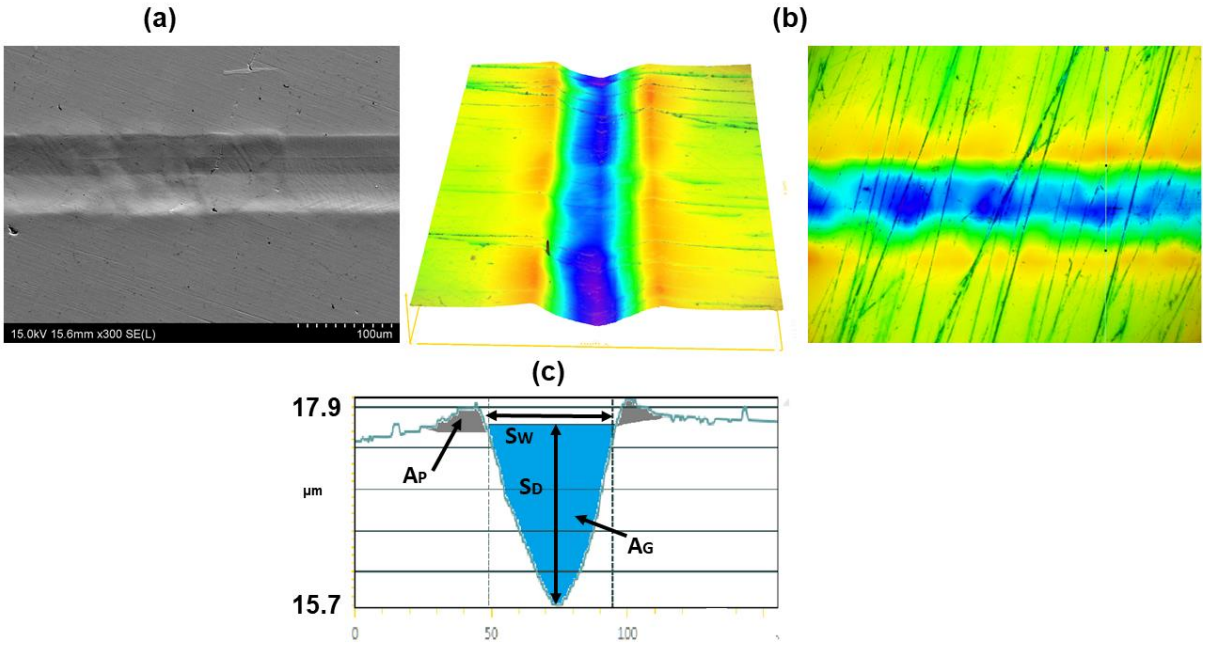

Figure 4-12: (a) SEM micrograph of a scratch scar formed under the constant load of 20N on a 58Ni39Ti-3Hf sample, (b) images of the formed scratch scar from different perspectives obtained by an optical profilometer, and (c) a cross-sectional profile of the formed scratch scar with schematics of the scratch depth (S_D), scratch width (S_W), cross-sectional area of the lateral pile-up (A_P) and cross-sectional area of the groove (A_G).

Table 4-4: Scratch geometries and COF values for scratch tests under constant loads of 2,5, 10 and 20N. Note, the A_P/A_G was only measured for loads of 10 and 20N as they formed measurable amounts of piled-up area.

Material	**Load (N)**	**S_D (µm)**	**S_W (excluding the piled-up zone) (µm)**	**A_P/A_G**	**CoF value**
60NiTi	2	0.02	9.8	-	0.05
58Ni39Ti-3Hf	2	Negligible	Negligible	-	0.04
60NiTi	5	0.3	14.9	-	0.05
58Ni39Ti-3Hf	5	0.21	9.8	-	0.05
60NiTi	10	0.76	34.6	0.03	0.06
58Ni39Ti-3Hf	10	0.63	34	0.01	0.05
60NiTi	20	1.41	44.2	0.10	0.08
58Ni39Ti-3Hf	20	1.46	46.7	0.10	0.07

As can be seen in table 4-4, 58Ni39Ti-3Hf shows relatively smaller S_D and S_W values under the lower loads of 2, 5 and 10N than 60NiTi. In particular, the measured S_D and S_W values of the scratch scar formed under 2N were negligible in 58Ni39Ti-3Hf samples, but these values

were respectively 0.02 and 9.8 μm in 60NiTi. These results can be interpreted as the higher resistance of 58Ni39Ti-3Hf than 60NiTi to allow the penetration of conical indenters under the mentioned loads.

In addition, these two alloys show approximately similar A_P/A_G ratios. However, this ratio is slightly larger in 60NiTi than 58Ni39Ti-3Hf alloy under an applied load of 10N. Contact stresses are estimated to exceed the yield strength of most metallic materials when scratch tests are carried out using a Rockwell C indenter [97]. As a result, as Bolelli et al. [68] explained, this ratio depends on the strain to failure of a material and is correlated to the plastic deformability of a material under dynamic contact stresses. In short, the larger this value, the lower the tendency of the near-surface material to brittle fracture under abrasive conditions [68].

To further investigate the mechanisms responsible for causing damage in these materials, the scratch grooves were inspected by SEM (figure 4-13). These micrographs, with plastic deformation and cracking, emphasize and confirm the dual nature of the abrasive damage mechanisms for these NiTi alloys. These images show the shear bands (figure 4-13 a-d and figure 4-13.f) that eventually give rise to cracks at higher loads (figure 4-13.e and 4-13.g). Separation (cracking or tensile failure) between slip bands can be clearly seen in these images (figure 4-13.e and 4-13.i). As a result, two types of abrasive damage are occurring in these alloys. Shear bands formed ahead and alongside the indenter due to excessive compressive stresses, and behind the indenter due to tensile stresses, is one type of abrasive damage. The other type involves tensile cracks opening up behind the indenter that are orthogonal to the slide direction. In addition, the shear bands are oriented differently from grain to grain (figure 4-13.d). This shows that there must be a preferred slip orientation for the NiTi phase.
Furthermore, as seen in figure 4-13, the load needed to initiate cracking is lower in 58Ni39Ti-3Hf alloy (10N) as compared to 60NiTi (20N). In fact, while there is a considerable amount of plasticity followed by fracture in 60NiTi (figure 4-13.a-d), not much banding is seen in 58Ni39Ti-3Hf before cracks occur (figure 4-13.f-g). The results corroborate with the slightly smaller A_P/A_G of 58Ni39Ti-3Hf under 10N load than 60NiTi (table 4-4) and the inferior Vickers hardness of this alloy. These suggest the higher tendency of 58Ni39Ti-3Hf alloy to cracking and brittle fracture than 60NiTi under abrasive conditions.

These results confirm that it is the stress levels and material response (plastic deformability, tensile fracture strength) that is in fact controlling abrasive damage and wear in these alloys.

Clearly if the sliding induced tensile stresses are lower than the tensile strength (lower loads and CoF values), then cracks are not formed and tensile fracture does not occur.

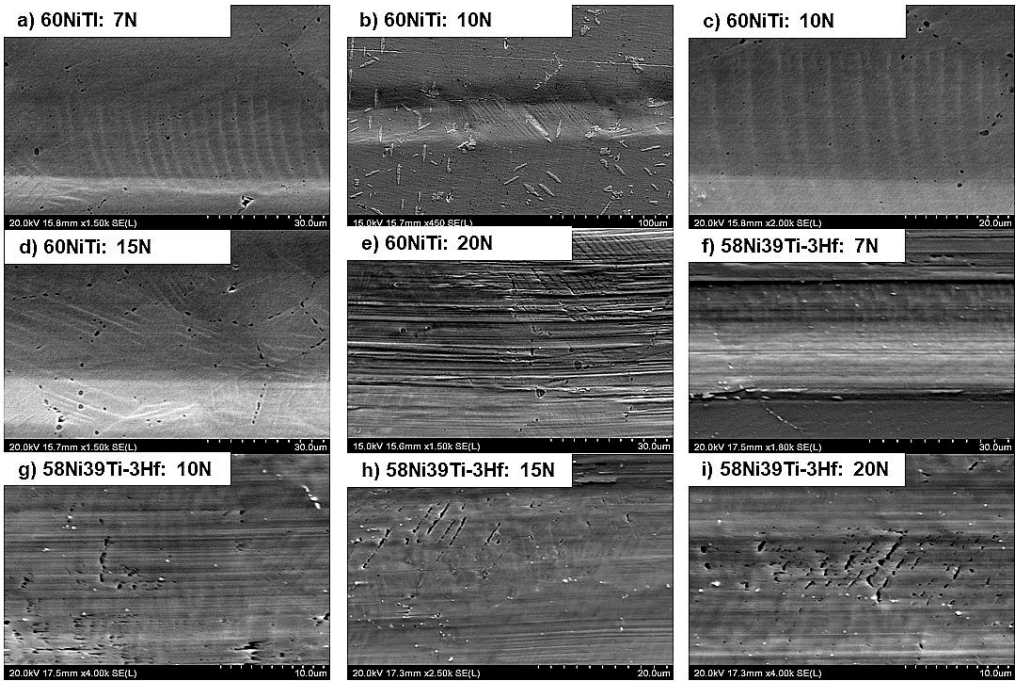

Figure 4-13: SEM images of scratch scars formed on 60NiTi and NiTi-Hf samples using a Rockwell C indenter under different constant loads. A) 60NiTi: 7N load, b and c) 60NiTi: 10N load, d) 60NiTi: 15N load, e) 60NiTi: 20N load, f) 58Ni39Ti-3Hf: 7N load, g) 58Ni39Ti-3Hf: 10N load, h) 58Ni39Ti-3Hf: 15N load and i) 58Ni39Ti-3Hf: 20N load.

These microscale damaging features are not observed clearly in surface micrographs of wear tracks formed under unlubricated sliding wear tests. Perhaps they have been covered by wear debris making them difficult to detect, especially as they are at the microscopic length scale. However, these features indicating the mechanisms causing damage in these NiTi alloys are observable in the wear tracks of lubricated samples (figure 4-14).

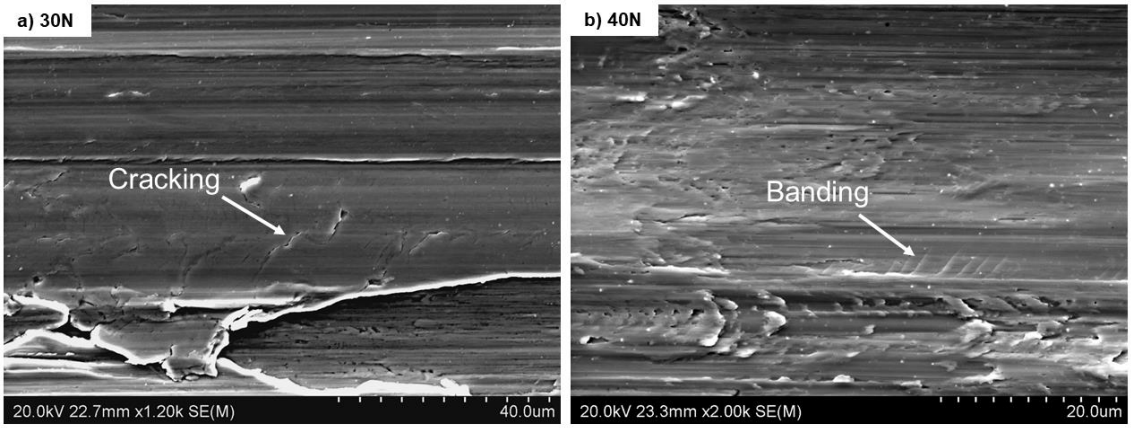

Figure 4-14: SEM micrographs showing the formation of shear bands and cracks in a) 58Ni39Ti-3Hf samples lubricated with the gear oil and worn under 30N load, and b) 58Ni39Ti-3Hf samples lubricated with the gear oil and worn under 40N load.

Under sliding motions, this is the tensile stress component which is mainly responsible for causing fracture in brittle materials such as 60NiTi and 58Ni39Ti-3Hf intermetallics [86]. These findings (obtained from single pass scratch tests) appear to justify the results of the sliding wear tests. As discussed, under non-perfect lubricated conditions, the abrasive wear mechanism is mainly ruled by plastic deformation causing mild wear. This is perhaps because, under these conditions, the generated sliding induced tensile stresses are mostly high, but not more than the tensile strength. On the other hand, under unlubricated conditions where the CoF values are high or some specific non-perfect gear oil lubricating conditions where both loads and CoF values are high, the generated tensile stresses are severe, exceeding the tensile strength and, as a result, the abrasive wear is dominated by fracture and heavy removal of material. Moreover, 58Ni39Ti-3Hf shows to a small degree inferior resistance in castor oil lubricated sliding wear tests under high loads of 30 and 40N than 60NiTi. This confirms the tendency of 58Ni39Ti-3Hf to show more cracking and brittle fracture under abrasive conditions compared to 60NiTi and is in agreement with the results obtained in scratch tests and Vickers indentation tests.

On the contrary, as mentioned before, this trend changes under unlubricated conditions and 58Ni39Ti-3Hf exhibits a slight decrease in specific wear rate than 60NiTi.

Other than abrasion, fatigue wear caused by cyclic loading also plays a role in damaging these alloys (figure 4-7). Under unlubricated conditions (as the sliding induced tensile stresses are high), it is thought that the effect of fatigue wear causing subsurface damage overcomes the

effects caused by sliding of small, hard asperities on these alloys resulting in abrasion. As mentioned, more cracks and crack propagations were observed in dry sliding cross-sections of 60NiTi as compared to 58Ni39Ti-3Hf interpreted as evidence of improved fatigue wear resistance of 58Ni39Ti-3Hf than 60NiTi (figure 4-7). As a result, 58Ni39Ti-3Hf, due to its improved fatigue properties, shows slightly improved wear resistance than 60NiTi or at least it does not exhibit an inferior behavior.

The enhanced fatigue properties of 58Ni39Ti-3Hf as compared to 60NiTi can be attributed to the positive effect of Hf on the microstructural homogeneity. As explained, Hf acts as an oxygen "getter" reducing the amount of contaminant phases in 60NiTi parts resulting in more homogenized structures [34]. Such contaminants are weak spots that may allow subsurface initiated cracks to more easily propagate in 60NiTi than in 58Ni39Ti-3Hf. Further, as the microstructural images show (figure 4-1), addition of 3 wt.% Hf to 60NiTi composition has fully prevented the precipitation of Ni_3Ti phases. As Benafan et al. [38] explained, Ni_3Ti is a soft phase and damages the fatigue properties of 60NiTi. One other speculative thought could be that, again based on the work of Benafan et al. [38], 60NiTi undergoes a transient phase transformation under tension from NiTi to Ni_3Ti and the weaker Ni_3Ti allows a crack to grow under cyclic motions and causes a flake. In contrast, Benefan's work suggests that 58Ni39Ti-3Hf is immune to the formation of Ni_3Ti and thus crack growth is slower. Proving this theory is beyond the scope of the current research, but it is one worth further investigation in the future.

The common theme derived from these experimental results is that the enhanced microsturctural homegeneity of the Hf containing material leads to a delay in observed damage until high levels of surface stress is encountered.

However, it should be noted that the addition of Hf, despite improving the unlubricated sliding wear of 60NiTi, could not result in an alloy with sliding wear properties comparable to 440C steel. 440C steel has a similar HRC hardness compared to 60NiTi and 58Ni39Ti-3Hf alloy and, as discussed earlier, is conventionally considered to be a load bearing alloy. Comparing the unlubricated sliding wear rates of 60NiTi and 58Ni39Ti-3Hf to the results of a research studying the reciprocating sliding wear properties of 440C steel plates mating 6mm diameter WC balls, both 60NiTi and 58Ni39Ti-3Hf alloys display much higher specific wear rates and CoF values than 440C steel under identical loading conditions [92]. In particular, these alloys exhibit one to two orders of magnitude higher specific wear rates than 440C steel under 2, 5

and 10N loads. These results show that both 60NiTi and 58Ni39Ti-3Hf are not desirable in some extreme situations where loss or consumption of oil results in dry sliding of the contacting materials and the generation of a high level of sliding induced tensile stress, e.g. a helicopter gear box experiencing a catastrophic loss of oil.

4.3 Conclusions

The purpose of the study reported in this chapter was to compare sliding wear properties of 58Ni39Ti-3Hf and 60NiTi. This was done through reciprocating sliding wear tests of 58Ni39Ti-3Hf and baseline 60NiTi against 6 mm diameter WC balls and under different lubricated and unlubricated conditions. Furthermore, results obtained from the indentation, hardness and single pass scratch tests were employed to better analyse the damaging mechanisms causing wear in these alloys.

Results of these experiments showed that, in general, 58Ni39Ti-3Hf shows similar sliding wear properties to 60NiTi. These results emphasize the possibility of substituting 60NiTi with the 58Ni39Ti-3Hf alloy in applications. In essence, under good lubrication conditions and selected loads, these Ni-rich intermetallics do not wear, making them suitable for sliding applications. However, under dry sliding conditions where the amount of sliding induced tensile stresses are significant, both 60NiTi and 58Ni39Ti-3Hf show excessive wear. These results show the importance of good lubrication and stress design for sliding applications where these alloys are exploited as wear resistant alloys.

Detailed results obtained in this investigation show that:

1- In terms of hardness, tests carried out using a Rockwell C indenter exhibit that both of these alloys show approximately equal hardness under different loads.

2- Regarding the unlubricated sliding wear tests, both alloys are damaged by the same wear mechanisms of severe abrasion causing heavy removal of material and fatigue wear that are possibly enhanced by adhesion. However, 58Ni39Ti-3Hf seems to exhibit more resistance to subsurface crack initiation and propagation than 60NiTi under cyclic sliding movements. This is an indicator showing superior fatigue properties of 58Ni39Ti-3Hf than 60NiTi and is interpreted as the reason for the slightly increased wear resistance of this ternary alloy in unlubricated conditions as compared to 60NiTi.

3- With respect to lubrication properties, both alloys show roughly similar properties as they exhibit approximately the same CoF values and friction trends under both castor oil and gear oil lubricated conditions. Furthermore, they follow the same wear mechanisms under these lubricated conditions.

4- Friction curves showed a two-stage mode under conditions where a gear oil is used as a lubricant and applied loads are relatively low. In stage 1, where the friction is low, smooth and noise-free, these alloys do not wear. This is because under these conditions the level of sliding induced tensile stress is lower than the threshold stress required to cause damage in these alloys. Under the second friction stage, where the CoF value increases and alloys start to wear out, the abrasive wear in these alloys is mild as the wear tracks show plastic deformation and are ploughed. However, under higher loads (30 and 40N), similar to unlubricated conditions, the abrasive wear is severe, causing fracture and aggressive removal of material.

5- Lubrication with castor oil shifts the abrasive wear mechanism in these alloys from severe abrasion to mild abrasion under all the applied loads. However, the length of the first friction stage (where the CoF values are low preventing the occurrence of wear) was so short showing that this oil is not a good substitute for the gear oil. In addition, 60NiTi, despite having inferior fatigue wear resistance than 58Ni39Ti-3Hf and showing higher CoF values, shows to a small degree superior wear resistance than 58Ni39Ti-3Hf under higher loads of 30 and 40N in castor oil lubricated condition. This shows the higher tendency of 58Ni39Ti-3Hf to develop cracking, brittle fracture and tearing compared to 60NiTi under the single pass scratch tests and Vickers hardness tests. These results show that, in contrast to unlubricated conditions, fatigue wear does not play the main role, and wear of these alloys is ruled mainly by abrasive wear under these lubricated conditions. Furthermore, scratch testing proved the dual nature of the abrasive damage mechanisms for these NiTi alloys. That is, there is plastic deformation under stresses below the fracture strength and cracking under conditions where sliding induced tensile stresses exceed the tensile strength.

Discussions and studies regarding the possibility of employing 60NiTi in the other area of interest, i.e. as a porous structure suitable for general bone replacement applications, begins in the next chapter.

Chapter 5 Synthesis of as-sintered 60NiTi parts with a high open porosity level[5]

[5]**Khanlari K**, Ramezani M, Kelly P, Cao P, Neitzert T. Synthesis of as-sintered 60NiTi parts with a high open porosity level. *Materials Research,* 2018.

As mentioned earlier, 60NiTi, when employed in a hardened state, contains a unique set of desirable properties, including high hardness, low elastic modulus, corrosion resistance and superelasticity. This makes it an attractive candidate for biomedical applications.

Some of 60NiTi's properties are compared with those of other common biomedical materials in table 5-1. As can be seen, 60NiTi, despite having a higher density than Ti6Al4V, is in many respects such as strength, elastic modulus and resistance to corrosion, more desirable than other biomedical materials.

In addition, hardened 60NiTi is approximately twice as hard as near equiatomic NiTi alloys (~55 wt.% Ni) which, due to their shape memory properties, are commonly used as stents and other medical components [8, 40]. Moreover, hardened 60NiTi, in contrast to near equiatomic NiTi alloys which show large dimensional changes under an applied stress, holds a dimensional stability and tolerance [3, 4]. These properties and qualities make 60NiTi a more favourable alloy than conventional Ni-Ti alloys for load bearing biomedical applications.

Table 5-1: Properties of 60NiTi as compared to other common biomedical materials [2, 4, 9, 19, 25-27, 35, 38, 66, 76, 100].

Material / **Property**	**60NiTi (Solutionized)**	**Stainless steel 316 (Annealed)**	**Cast CoCrMo**	**Ti6Al4V**
Density (g/cm^3)	6.7	8	8.3	4.43
Elastic modulus (GPa)	100	200	240	112
Tensile strength (MPa)	1500	517	655	985
Corrosion resistance	Excellent	High	Very high	Excellent
Biocompatibility	Good	Good	Good	Excellent

For general bone replacement applications such as spinal or cranial inserts, implants with a porous structure are desirable. Such a structure helps lower the unwelcome stress shielding phenomenon as it results in a decrease of elastic modulus of an implant [27, 35, 76]. Furthermore, an interconnected porous structure results in a better bone ingrowth which is beneficial in terms of bone healing [83, 84]. Note that the requirements of implants for general bone replacement applications is explained in Chapter 7.

60NiTi, despite having the above-mentioned attractive properties, has not yet been fully exploited for biomedical applications. This is because the presence of substantial amounts of inclusions and contaminants, such as oxides in 60NiTi components produced by casting processes, makes the high temperature workability and also the machining of 60NiTi unfavourable [8, 19, 20, 27]. However, using powder metallurgy methods, the fabrication of complex 60NiTi parts for different applications is possible [3].

In this chapter the conventional press-and-sinter powder metallurgy process will be discussed, as an economical processing method [101] for the manufacture porous 60NiTi samples from elemental Ni and Ti powders. In this process, the powder is first pressed into a green compact at ambient temperature. Depending on the particle size, morphology and impurity level, the pressing pressure normally varies from 100 to 1100 MPa. Subsequently, the green compact is sintered either in a protective atmosphere or under vacuum at high temperatures [102]. Blended Ni and Ti powders provide the possibility of a liquid forming in the samples during sintering [103]. As seen in the binary phase diagram (Figure 1-3) [16, 104], the first eutectic liquid occurs at 942°C at a composition of 24.5% Ni amongst β-Ti and Ti_2Ni intermetallic phases (Eq. 5-1).

$$\beta - Ti + Ti_2Ni \rightarrow Liquid \qquad (5.1)$$

The amount of porosity developed in 60NiTi parts can be tuned by controlling the amount of this generated liquid. Applying slow heating rates for temperatures below 942°C decreases the formation of liquid as compared to the situation where a high heating rate is applied. This is because applying a slow heating rate gives more time for Ti to react with Ni and other phases, so that Ti will be more effectively removed before reaching the eutectic point at 942°C [103]. Based on the results published previously on the less Ni-rich NiTi alloys, an increase in the amount of liquid increases the porosity and vice versa [103, 105].

The effects of critical processing parameters such as pressing pressure, sintering temperature, heating rate and sintering holding time on the dimensional stability, density, porosity

characteristics, microstructural properties and phase structure of the as-sintered samples will be examined. Since processing of as-sintered parts is the first step to obtain biocompatible 60NiTi parts, results obtained will help in the successful production of porous biocompatible 60NiTi parts.

5.1 Processing and characterization methods

5.1.1 Materials and sintering procedure

In this study, elemental Ni and Ti powders were used to process and manufacture the samples.

To process, Ni and Ti powders were mixed to make a batch with a nominal composition of approximately 60 wt.% Ni and 40 wt.% Ti. A ball miller (without inserting the balls) was used to mix the powders to the homogeneous nominal composition.

In the next stage, the mixtures were compressed into a cylindrical shape (20 mm in diameter and 5 mm thick) by a single-action steel die. To investigate the effect of pressing pressure on microstructure and dimensional stability of the samples, two different pressures of 200 MPa and 400 MPa were used for manufacturing the samples. Green samples with densities of 4.31 g/cm^3 and 4.65 g/cm^3 were obtained under, respectively, 200 and 400 MPa compaction pressures.

The pressed samples were then sintered in a vacuum furnace working at 3×10^{-3} Pa pressure, under two different final temperatures of 850°C and 1050°C and two different heating rates (table 5-2). Eutectic liquid generation was avoided in samples sintered at 850°C while sintering at 1050°C resulted in the generation of the eutectic liquid at 942°C.

Table 5-2: Summary of the processing parameters.

Processing condition	Pressing pressure	Sintering final temperature	Heating rate	Sintering holding time
1	200 MPa	850°C	10°C/min	30 min
2	400 MPa	850°C	10°C/min	30 min
3	200 MPa	1050°C	Ambient to 700°C:10°C/min. 700°C to 900°C: 2°C/min. 900°C to 1050°C: 10°C/min.	30 min

4	400 MPa	1050°C	Ambient to 700°C:10°C/min. 700°C to 900°C: 2°C/min. 900°C to 1050°C: 10°C/min.	30 min
5	200 MPa	1050°C	10°C/min	30 min
6	200 MPa	1050°C	Ambient to 700°C:10°C/min. 700°C to 900°C: 2°C/min. 900°C to 1050°C: 10°C/min.	4 h

5.1.2 Characterization methods

The Hitachi-su70 SEM equipped with an EDS system and an XRD machine, using a copper K_α radiation, were employed to obtain images (based on the emissions received from the secondary electrons), provide information on elemental distribution at different spots and conduct phase analysis from the cross section of the samples. Samples were ground and polished before conducting phase analysis. The sample preparation procedure consisted of using P80, P180, P360, P800 and P1200 SiC papers at 300 rpm for grinding the samples. Vibratory polishing with 6 μm, 3 μm and 1 μm diamond paste solutions was applied to conclude the grinding procedure. Finally, to help better distinguish phases in the microstructural and elemental distribution studies, the ground and polished samples were swab-etched with a room temperature aqueous solution of 1 Vol.% HF and 10 Vol.% HNO_3 for 85 seconds.

Anisotropy of dimensional change occurs in the radial and axial directions during the sintering of soft metal powders [106]. Control over the dimensions of parts during sintering is vital for their successful processing. Changes in the length of the sintered samples in the radial (perpendicular to the direction of the applied force) and axial (parallel to the direction of the applied force) directions were measured and compared with the green samples.

Density and open porosity (conditions 3-6) of samples were respectively measured by the Archimedes and liquid weighing methods as specified in the ASTMB962-08 standard [107]. General porosity can be divided into two types: open porosity and closed porosity. Open pores

are the pores that are interconnected with each other and have a route to the surface of the material [84].

In addition, the relative density *R* and the general porosity ε were calculated using the following formulas respectively [84]:

$$R = \left(\frac{\rho}{\rho_0}\right) \times 100 \qquad (5.2)$$

$$\varepsilon = \left(1 - \frac{\rho}{\rho_0}\right) \times 100 \qquad (5.3)$$

where ρ stands for sintered/green density and ρ_0 stands for theoretical density.

The average pore size in the sintered parts was determined by the line-intercept method (ASTM E112-13) as $1.12L_0/N_{pore}$ using SEM images, where L_0 is the line length, and N_{pore} is the number of pores on that line [108]. Three lines in two different images were used to determine the pore size using the mentioned method.

The geometry of a pore can be divided into two different areas of pore-mouth and pore-throat (figure 5-1) [109]. Large pore-mouth sizes can facilitate bone growth into the porous implants. In addition, a pore-throat should not be too narrow; otherwise, the interconnectivity between the pores is lost. A Porosity Size Distribution Analyser (PSDA), functioning based on the methods explained by Yu and Yan et al. [109, 110], was employed to measure the diameter of the smallest pore-throat and largest pore-mouth of the samples.

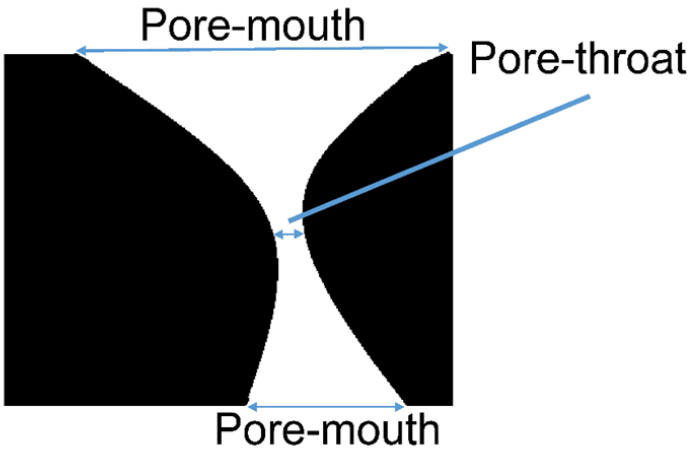

Figure 5-1: Schematic of a pore tunnel. Pore geometry can be divided into two regions of pore-mouth and pore-throat.

To increase the accuracy of the results, microstructural experiments such as dimensional, density and open porosity measurements were conducted on three samples and the average values are reported here.

5.2 Results and discussion

5.2.1 Powder characterization and phase analysis

A laser diffraction particle sizing method was used to measure the mean particle size of both Ni and Ti particles. Further, a Leco machine was employed to determine the amount of common impurities such as oxygen (O), carbon (C) and nitrogen (N) in the powders; these impurities lead to the generation of oxides and nitrides due to their reaction with Ti, which lead to a degradation of the mechanical properties and embrittlement of the finals parts [104, 111]. Table 5-3 demonstrates the relevant information on the starting powders. The mean particle sizes for Ti and Ni powders were 27.2µm and 12.57µm, respectively.

Table 5-3: Particle size and impurity content of the starting powders.

Powder	Particle size* (µm)			O (wt.%)	C (wt.%)	N (wt.%)
	D_{10}	D_{50}	D_{90}			
Ti	11.74	27.2	49.04	0.111	0.004	0.047
Ni	4.33	12.57	42.50	0.100	0.066	0.021

* D10, D50 and D90 correspond to the particle size at the respectively 10, 50 and 90 percent points on the cumulative distribution.

Images obtained from SEM were used to determine the morphologies of the powders. Figure 5-2 shows that Ti powders have spherical morphology while Ni powders are spiky with needle-like texture.

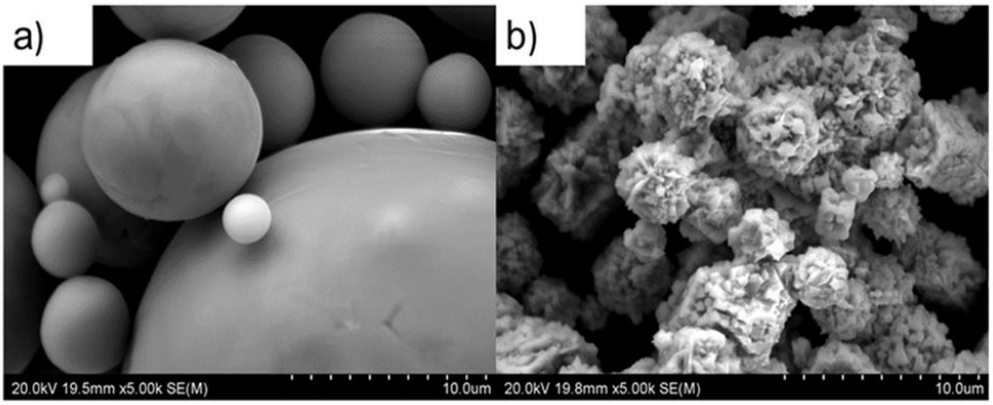

Figure 5-2: Morphologies of the starting powders. a) Ti, b) Ni.

In the first trial, samples were sintered at 850°C for 30 minutes by employing a 10°C/min heating rate, i.e. samples were processed under conditions 1 and 2 (table 5-2).

Based on the XRD phase analysis results, sintering the samples at 850 °C (conditions 1 and 2), although successful in forming phases such as NiTi, Ni_3Ti, Ni_3Ti_2 and Ti_2Ni, did not result in the complete removal of Ni and Ti elements (Figure 5-3).

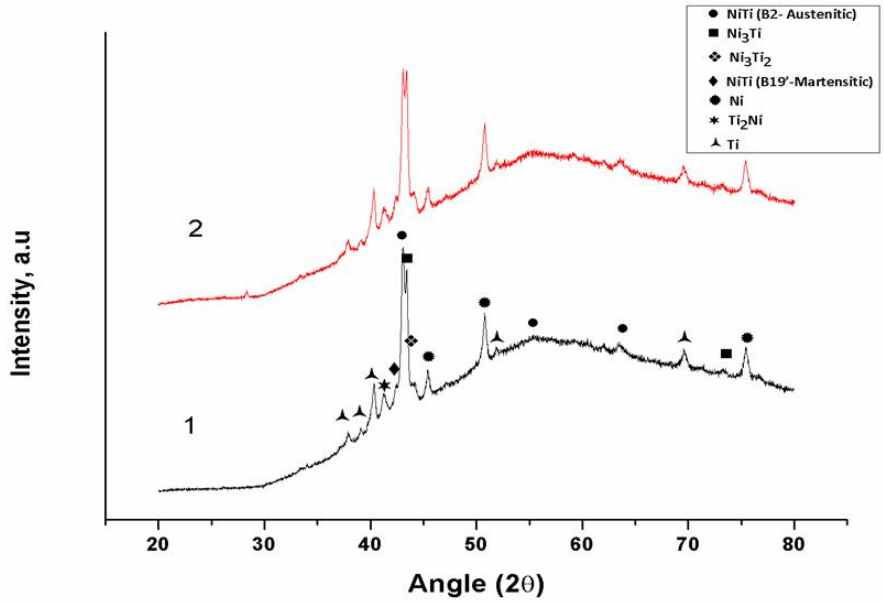

Figure 5-3: XRD patterns of samples processed under conditions 1&2.

Further SEM/EDS studies and elemental dot mapping were used to confirm the existence of these phases. Since elemental Ni and Ti were detected in samples sintered at 850°C, these samples were not etched for microstructural analysis and, as for the XRD tests, they were simply grinded and polished. This is because etching could remove these elements from the top layer of the samples. Results obtained from elemental dot mapping clearly showed the existence of Ni-rich and Ti-rich areas. In fact, dark regions in the Ti map are bright regions in the Ni map showing the existence of Ni-rich phases and vice versa (figure 5-4.a, b).

Elemental ratios obtained from EDS analysis showed that Ti-rich areas contain ~8 wt.% Ni, suggesting the formation of βTi. These regions were darkest under the SEM images. On the other hand, the brightest areas were Ni-rich, containing ~2-8 wt.% Ti. These areas seem to be the original cores of the Ti and Ni elemental particles, respectively. Based on the results obtained from EDS analysis and interpreting the elemental ratios [35], the region between these two extreme areas are filled with other phases in a gradient way. Areas attributed to elemental Ti were surrounded by Ti-rich Ti_2Ni and elemental Ni areas were next to Ni-rich Ni_3Ti with a grey NiTi phase in the middle of these areas (figure 5-4.c). This gradient phase structure was formed due to solid-state diffusion of elements occurring during the sintering process.

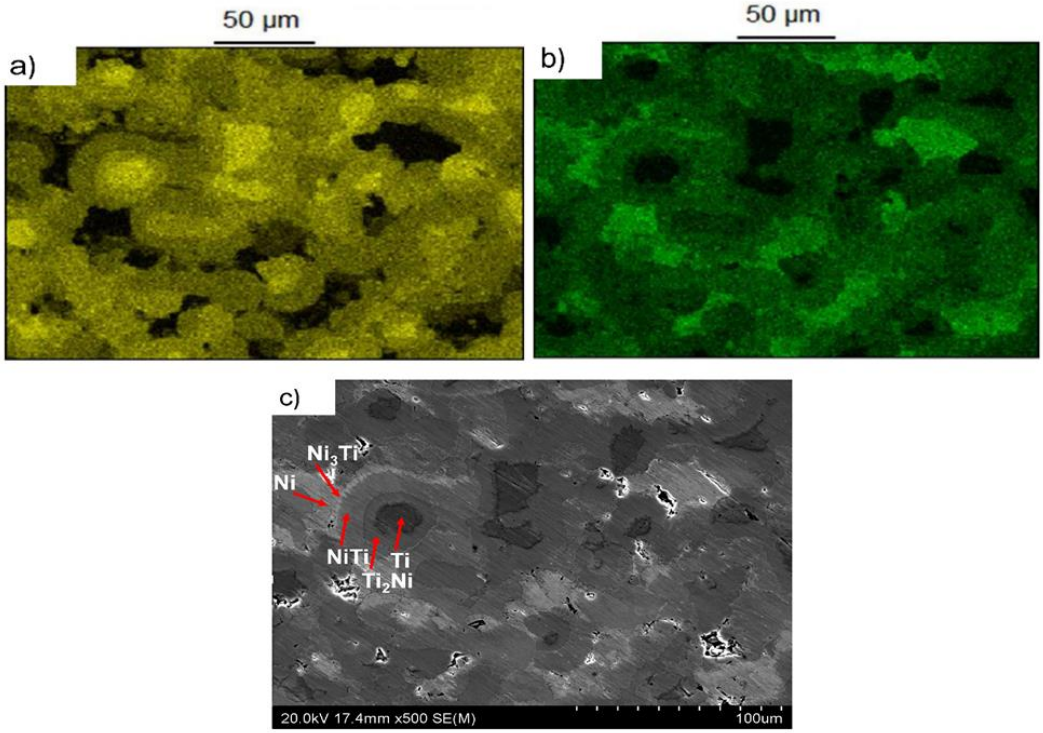

Figure 5-4: Results of elemental dot mapping (Ti (a) and Ni (b)) and EDS elemental ratio studies (c) on samples processed under condition 2.

These results indicated that 30 minutes sintering at 850°C is too short to result in complete reaction between these elemental powders. It is expected that sintering at this temperature for longer times will result in complete removal of these elements; however, this strategy was not evaluated in this research. As mentioned before, the aim of this research is to obtain porous parts. However, the microstructure of these samples (provided in section 5.2.3) did not show appreciable interconnected porosities and increasing the sintering holding time is expected to result in the shrinkage of pores leading to decreased sintered porosity [84].

To achieve fully reacted 60NiTi with a porous structure, the mixed pressed powders were sintered at 1050°C, i.e. above the required temperature of 942°C for generation of eutectic liquid. However, the effect of formation of eutectic liquid on dimensional stability of the samples needed a close attention. The generation of liquid can result in the expansion of the samples altering their initial designed geometry [106]. To avoid such a phenomenon, the heating rate was decreased to 2°C/min above 700°C until 900°C. This increased sintering time below 942°C and reduced the amount of elemental Ti that causes liquid generation (conditions 3 and 4, table 5-2). Cylindrical samples with stable dimensional sizes were achieved under these conditions. Despite this, the samples processed under both conditions 3 and 4 could not

obtain volumetric open porosity of around 30 Vol.%. The maximum open porosity achieved under these conditions was ~23 Vol.% (condition 3) (table 5-4).

Table 5-4: Summary of dimensional and microstructural studies.

Condition	Diameter (mm)	Height (mm)	Volume (mm^3)	Density (g/cm^3)	Open porosity (Volume %)	Total porosity (Volume %)
200 MPa pressed-Not sintered	20.00	7.40	2.32	4.31	Not defined	~32
400 MPa pressed-Not sintered	20.00	6.84	2.14	4.65	Not defined	~27
1	20.00	7.24	2.27	4.42	Negligible (Based on microstructural images)	~31
2	20.30	6.34	2.05	4.81	Negligible (Based on microstructural images)	~25
3	20.60	7.14	2.37	4.14	~23	~36
4	21.12	6.56	2.29	4.38	~19	~32
5	20.60	7.60	2.53	3.90	~28	~38
6	20.42	7.06	2.31	4.29	~18	~33

To obtain parts with a greater amount of open porosity, despite concerns regarding the dimensional stability of the parts, samples were heated to 1050°C under a fast heating rate of 10°C/min (condition 5). Results showed that the obtained samples exhibited ~9% volumetric change compared to the 200 MPa pressed powder mixture in the green state. This amount is ~7% more compared to the samples sintered under condition 3 (table 5-4). Despite this, these sintered samples could retain their cylindrical shape and no irregularity due to expansion or shrinkage was observed. This sintering procedure resulted in parts with increased open porosity (~28 Vol.%) compared to condition 3 (table 5-4).

Sintering holding time is a factor that can affect the homogeneity of the sintered parts [112]. Processing condition 6 was designed to evaluate the effect of this parameter on the homogeneity of sintered 60NiTi samples. The effect of holding time along with other sintering

parameters on the homogeneity of samples, their microstructure and generated phases are discussed in the following.

XRD patterns of samples sintered at 1050°C did not show any evidence of Ni or Ti elements (figure 5-5). The absence of elemental Ni and Ti in these samples was confirmed by elemental dot mapping (figure 5-6.a, b). This map, which was obtained from samples prepared under condition 5 does not show any dramatic uneven distribution of elements as is the case for samples sintered at 850°C (figure 5-4.a, b). The dark areas seen in this map is common for both Ti and Ni so these regions are related to pores where no element exists (figure 5-6.c). These all can be attributed to a higher sintering temperature and possible formation of eutectic liquid at 942°C, which due to increased reaction rate results in enhanced homogeneity and crystallinity in samples [112].

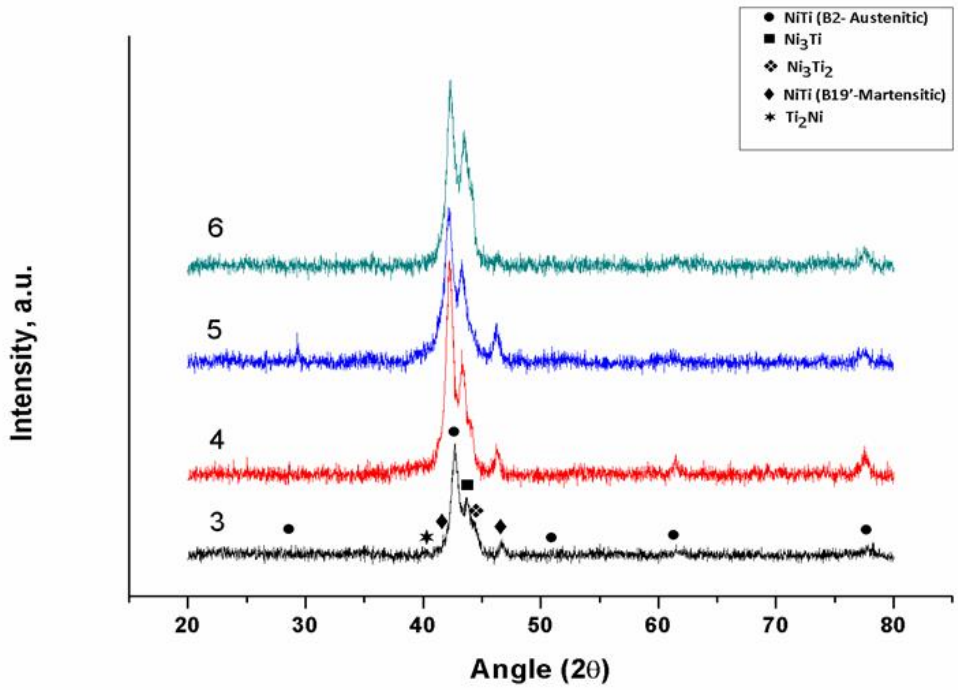

Figure 5-5: XRD patterns of samples sintered at 1050°C (conditions 3, 4, 5 and 6).

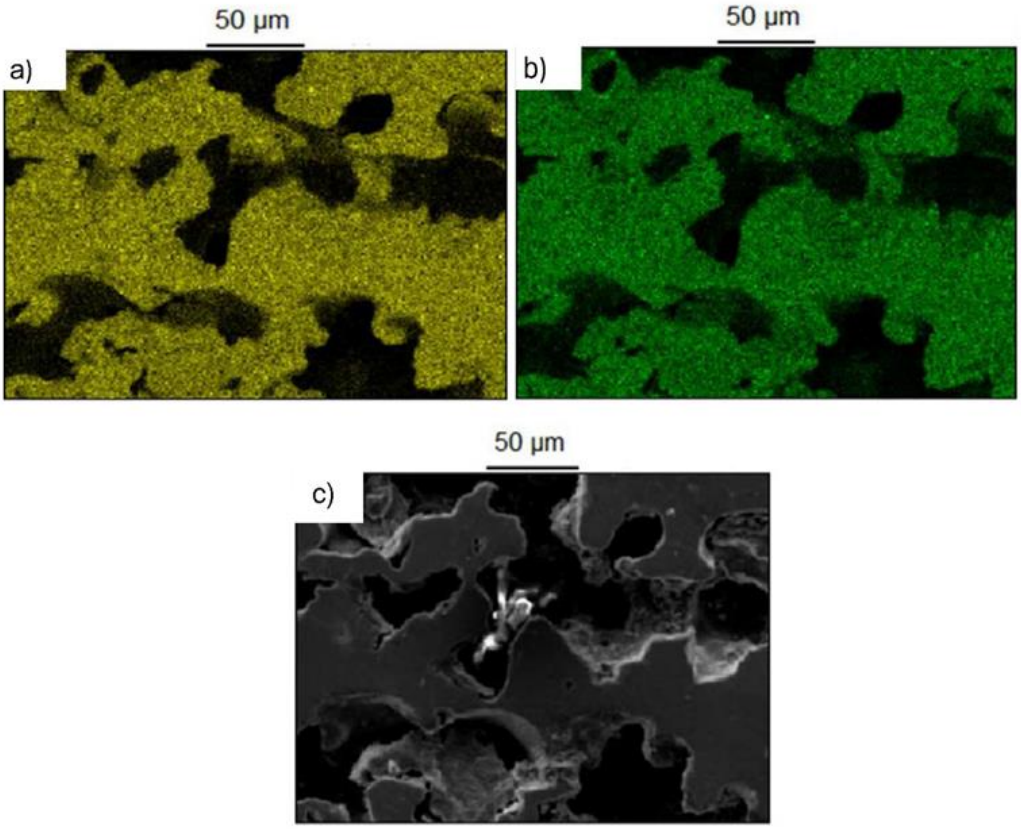

Figure 5-6: Results of elemental dot mapping (Ti (a) and Ni (b)) on samples processed under condition 5 (c).

For samples sintered at 1050°C, no matter which pressure, heating rate or sintering holding time were used, all samples contained the same phase composition (figure 5-5). Obtained peaks could be attributed to NiTi (B2-Austenitic), NiTi (B19'-Martensitic), Ni_3Ti, Ni_3Ti_2 and Ti_2Ni. However, the NiTi (B2-Austenitic) peak located at 2θ=~28 could be seen for some conditions, and could not be seen for others sintered at the same temperature of 1050°C (figure 5-5). This can be attributed to the orientation effect [113].

EDS elemental analysis was applied to identify NiTi, Ni_3Ti, Ni_3Ti_2 and Ti_2Ni phases based on a possible range of elemental ratios in each composition as specified in the literature [35]. As an example, results of SEM morphological and EDS elemental analysis are shown for samples sintered under condition 4 (figure 5-7).

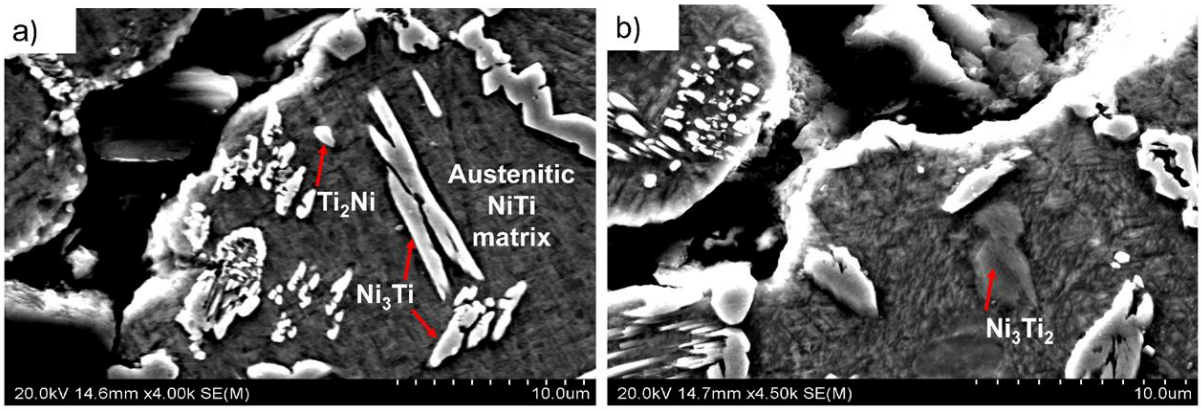

Figure 5-7: SEM images of sintered samples processed under condition 4. Different phases have been identified based on EDS elemental analysis. (a) Austenitic NiTi, Ni_3Ti and Ti_2Ni (b) Ni_3Ti_2.

In addition, a fine structure with needle-like contrast was also observed in high magnification SEM images (figure 5-8). This is also an evidence indicating the existence of martensitic NiTi in these samples, as reported by Berthville et al. [111]. Alternatively, these particles may also be attributed to Ni_4Ti_3. As it is almost impossible to differentiate between austenitic and martensitic NiTi using the type of SEM sample preparation employed in this research. Since these particles are not sufficiently coarse, the EDS analysis could not detect the difference in phase composition between these particles and the matrix. However, Undisz et al. [114] suggested that the surface structures observed on NiTi alloys need to be interpreted with caution. This is because these structures are not always attributed to the bulk structure and might be artifacts formed due to the effect of etching with hydrofluoric acid.

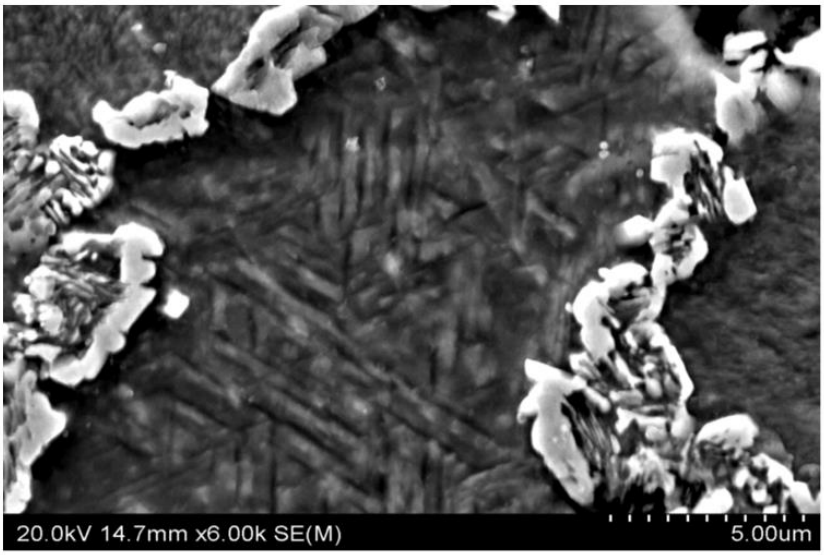

Figure 5-8: High magnification SEM image of sintered samples processed under condition 4 showing the fine structure with needle-like contrast.

Ni_4Ti_3 is another metastable phase that might have been formed due to different reasons such as slow cooling rates upon cooling the sintered parts from 1050°C. However, the existence of this phase cannot be confirmed or denied in furnace cooled as-sintered samples using only XRD and SEM studies. The main XRD peaks of this phase overlap with NiTi (B2) and Ni_3Ti phases and also SEM images cannot easily detect this nanoscale phase [111]. For these reasons, it is assumed here that this phase has not formed during sintering and furnace cooling of the samples. The reasons for the formation of phases such as $NiTi_2$, Ni_3Ti_2, Ni_3Ti and NiTi in two different phase structures of austenitic and martensitic are explained next.

Stable Ni_3Ti, Ti_2Ni and metastable Ni_3Ti_2 phases might have been generated due to different causes. Cooling the sintered parts with a slow rate from 1050°C can be considered to be the main cause of the generation of Ni_3Ti and Ni_3Ti_2 phases [18]. On the other hand, all the above mentioned phases can be produced due to the incomplete reaction among the elemental particles during the sintering process [83]. Increasing sintering temperatures or holding times can result in decomposition of Ni_3Ti_2 to stable Ni_3Ti, but stable Ni_3Ti, once formed, is very difficult to be removed as it is thermodynamically more stable than the NiTi phase, even if sintering of the parts is done under high temperatures such as 1050°C [18, 111, 115, 116]. This is the same for Ti_2Ni as it is another stable compound in the binary Ni-Ti system phase and its formation is even more thermodynamically favoured than Ni_3Ti [83, 115, 116]. Eutectoid decomposition of the NiTi phase at 620°C during furnace cooling can be considered as another

source for the generation of Ni_3Ti and Ti_2Ni phases [83]. Additionally, Ti_2Ni can also be formed during cooling of the sintered parts due to two other sources. In both of these sources, the liquid generated originally at 942°C due to eutectic reaction between βTi and Ti_2Ni (βTi + $Ti_2Ni \rightarrow$ L) causes the generation of the Ti_2Ni phase once the parts are being cooled. Peritectic reaction at 984°C between this liquid and NiTi phase (L+NiTi→Ti_2Ni) and eutectic solidification (L→βTi + Ti_2Ni) at 942°C are these sources [83]. However, given the absence of elemental Ti in sintered samples at 1050°C, Ti_2Ni generation under eutectic solidification at 942°C is not considered possible. Furthermore, it is estimated that all the liquid produced due to the eutectic reaction at 942°C is reacted and consumed by other phases. As a result, the possibility of the occurrence of peritectic reaction at 984°C is also considered to be negligible.

Based on phase analysis and SEM/EDS studies, in samples sintered at 1050°C, both austenitic and martensitic phase structures are present. NiTi can generally exist in two different phase structures: austenitic and martensitic. Austenite is the phase with an ordered B2 caesium chloride structure and martensitic NiTi has a B19 type structure with a monoclinic or triclinic distortion. Austenite can transform to martensite either thermally or by applying stress. Austenitic NiTi begins to transform thermally to martensitic NiTi when it is cooled below the martensite start temperature (M_s). This diffusionless shear transformation finishes when the temperature is below the martensite finish temperature (M_f) [40, 104, 106]. These phase transformation temperatures are strongly dependent on the amount of Ni in the NiTi composition [1, 3]. As Cluff and Corbin [101] explained, the existence of approximately 50.5 at.% Ni in NiTi composition results in M_s values of approximately room temperature. However, this temperature drops to below -175°C for compositions above 51 at.% Ni.

This shows that the amount of Ni in NiTi composition is not uniform and compositional differences exist in the NiTi phase. This may have roots in short sintering holding times resulting in non-uniform distribution of Ni in NiTi composition. In fact, XRD peaks attributed to martensitic NiTi are less intense for samples sintered under 4 hours holding time (condition 6) compared to other conditions (figure 5-5). This is evidence for suggesting the role of sintering holding time in compositional homogenization of the sintered parts. Alternatively, the formation of Ni-rich phases such as Ni_3Ti results in depletion of Ni from the surrounding NiTi phase making it less concentrated compared to other regions [40]. Both the reasons given above result in a gradient of Ni concentration in the NiTi phase giving opportunity for the formation of NiTi with martensitic and austenitic structures.

5.2.2 Dimensional stability analysis

Based on the results obtained in this study, sintered samples, despite showing satisfactory dimensional stability exhibit anisotropy of dimensional change (table 5-4). Changes in the length of the sintered samples in the radial (perpendicular to the direction of applied force) and axial (parallel to the direction of the applied force) directions were measured and compared to green samples. In all the conditions, except condition 1, where no change was observed, sintered samples exhibited radial expansion while in all the sintered conditions, except condition 5, sintered samples demonstrated axial shrinkage (figure 5-9.a, b).

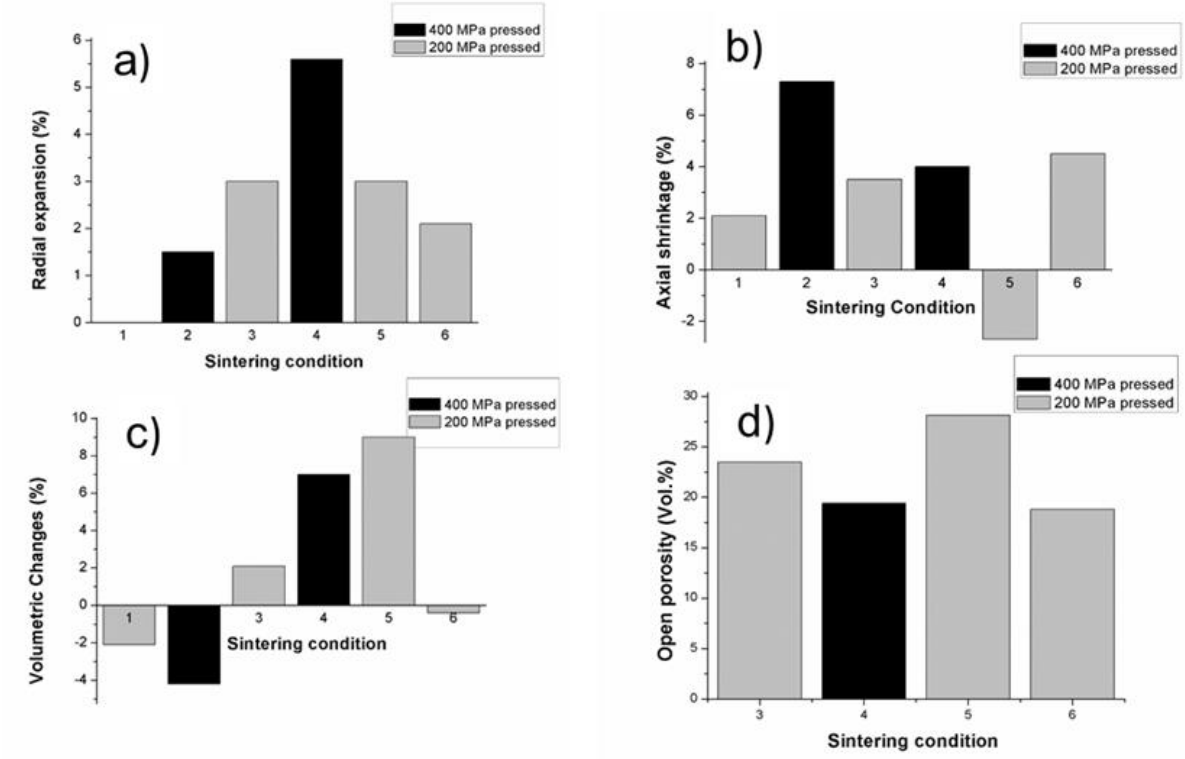

Figure 5-9: Graphs showing a) radial expansion of the sintered samples compared to green sample, b) axial shrinkage of the sintered samples compared to green samples, c) volumetric changes of sintered samples compared to green samples, and d) amounts of open porosity in sintered samples.

The anisotropy of dimensional change seen in the sintered samples is explained with the mechanism suggested by Igharo and Wood [106].

Based on this mechanism, for the samples sintered below 942°C, which is the temperature at which eutectic liquid forms, the diffusion is occurring in solid state. Considering the schematic of the segregated powder structure, faster diffusion of Ni compared to Ti (in solid state) will

result in a general positive flux of atoms toward the Ti particles. This will lead to an expansion in the radial direction (figure 5-10.a).

On the other hand, powder particles experience self-diffusion during solid state sintering. This is mainly because the same powder type particles are touching each other due to the difference in particle size, as illustrated in the schematic diagram figure 5-10.b. This self-diffusion between the same powder types (i.e. Ni-Ni and Ti-Ti) results in neck-growth and consequently axial shrinkage [106].

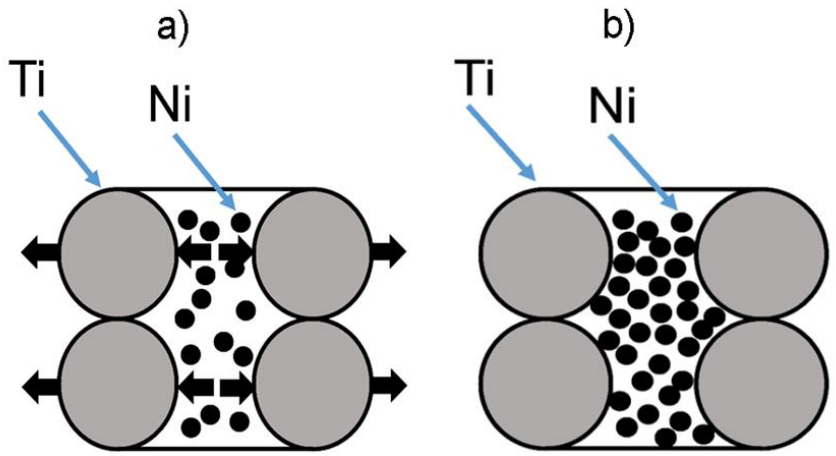

Figure 5-10: Schematic showing the interaction between the particles sintered below 942°C. a) General positive flux of Ni atoms toward the Ti particles in the radial direction, and b) Powder particles touching each other resulting in self-diffusion and axial shrinkage.

Conversely, when the sintering temperature is above 942°C, the generation of eutectic liquid and its subsequent penetration along the capillaries results in the expansion of parts in both radial and axial directions [106].

Considering this mechanism, the results obtained in this study can be interpreted as follows: As expected, the samples sintered at 850°C (conditions 1 and 2), because they are sintered under solid-state diffusion, exhibit axial shrinkage. In addition, the magnitude of the axial shrinkage increases with increasing compaction pressure. This is because, under higher pressure, particles touch each other more strongly with the effect that the amount of self-diffusion, and consequently, necking increases compared to samples pressed under lower pressures.

Conforming the mechanism explained by Igharo [106], the samples processed under condition 2 exhibited radial expansion. However, the samples processed under condition 1 did not show any measurable radial change. In addition, the magnitude of radial expansion for the samples processed under condition 2 was less than their axial shrinkage. This means that axial shrinkage and the necking effect are more prominent than radial expansion in 60NiTi parts sintered under solid-state diffusion.

Sintering the 400MPa pressed samples to 1050°C with slower heating rates (condition 4) resulted in a decrease of axial shrinkage, compared to samples processed under condition 2. This is attributed to the effect of the liquid generated above 942°C, which results in expansion of the parts. However, the axial shrinkage increased in samples processed under condition 3 compared to condition 1. This means that in samples processed under the lower pressure of 200MPa, the effect of solid-state diffusion causing necking and subsequently axial shrinkage overcompensates for the effect of liquid generation. On the other hand, samples processed under condition 5, which are sintered samples with faster heating rates, exhibited axial expansion. This could be due to the generation of more eutectic liquids in parts processed under faster heating rates compared to parts processed under slower heating rates, leading to axial expansion of parts processed under condition 5.

On the other hand, the effect of liquid generation on the radial expansion of the parts can clearly be observed when sintered at 1050°C. Parts processed under conditions 3 (in contrast to the shrinkage observed in radial direction) exhibited increased radial expansion compared to parts processed below 850°C. Moreover, the amount of radial expansion in samples processed under condition 3 (processed under a slow heating rate) is the same as with condition 5 (processed under a fast heating rate). In addition, for samples processed under condition 4, the rate of increase in radial expansion is more than the rate of axial expansion. These suggest the eutectic liquid generated at a temperature above 942°C has more tendency to move radially than axially in sintered parts.

Volumetric change of the samples is the result of a combination of their radial and axial changes. As seen in figure 5-9.c, samples sintered at 850°C were contracted compared to green samples. However, sintering the samples at 1050°C for 30min resulted in an expansion of the samples compared to green samples (conditions 3, 4 and 5). The volume increase was greater under condition 5 where a larger amount of liquid is estimated to be generated while sintering above 942°C.

Furthermore, increasing sintering holding time resulted in a contraction of samples in both radial and axial directions, condition 6 compared to condition 3. This can be attributed to the effect that sintering holding time plays in contraction of the original pores resulting in shrinkage of the sintered parts [84].

Volumetric change directly affects the density and amount of porosity in the samples. The contraction in samples compared to the green state leads to samples with increased density and decreased porosity. The opposite result is achieved when samples are expanded (table 5-4). The highest amount of density was achieved for samples processed under condition 2. This amount of density corresponds to a theoretical density of 74%.

5.2.3 Microstructural analysis

Different sources can result in the generation of pores in the sintered samples. Depending on some parameters such as powder size, powder morphology and applied compaction pressure, some pores are originally formed in compacted green samples. As Chen et al. [115] explain, phase transformations are considered as another source for the generation of porosity. Some phase transformations could cause volumetric changes resulting in shrinkage and subsequently porosity generation. Furthermore, solid-state diffusion of elements during sintering is another source for the generation of a specific type of porosity. This phenomenon known as the Kirkendall effect is due to the faster diffusion rate of Ni compared to Ti. This difference in diffusion rate leads to the generation of voids in original elemental Ni areas [112, 115, 117].

Kirkendall pores can clearly be observed in samples processed under conditions 1 and 2, where the sintering is done under solid-state diffusion (figure 5-11). While in samples sintered at 1050°C, the generated liquid can fill these voids.

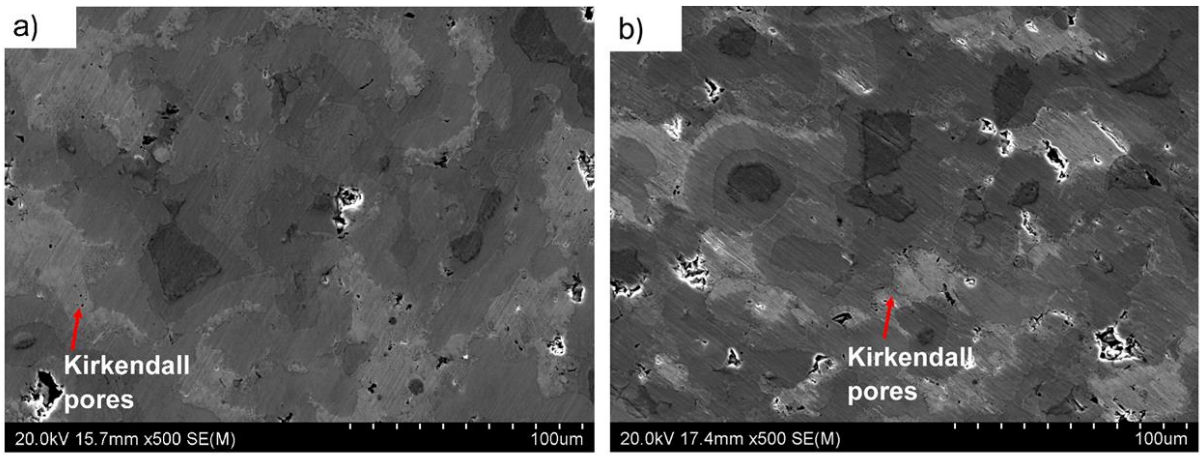

Figure 5-11: SEM images obtained from samples processed under a) condition 1, and b) condition 2.

Despite this, the total amount of porosity in samples processed under conditions 1 and 2 are decreased compared to their initial non-sintered state. As explained in the previous section, contraction in samples compared to their original green state leads to samples with increased density and decreased porosity (table 5-4).

On the other hand, the geometries of pores in samples sintered at 1050°C are quite different compared to samples sintered below 942°C (figure 5-12). Microstructures of these samples are quite porous with significant amounts of interconnected porosities. This is because liquid is generated in samples processed under these circumstances and its movement results in the generation of pores afterwards.

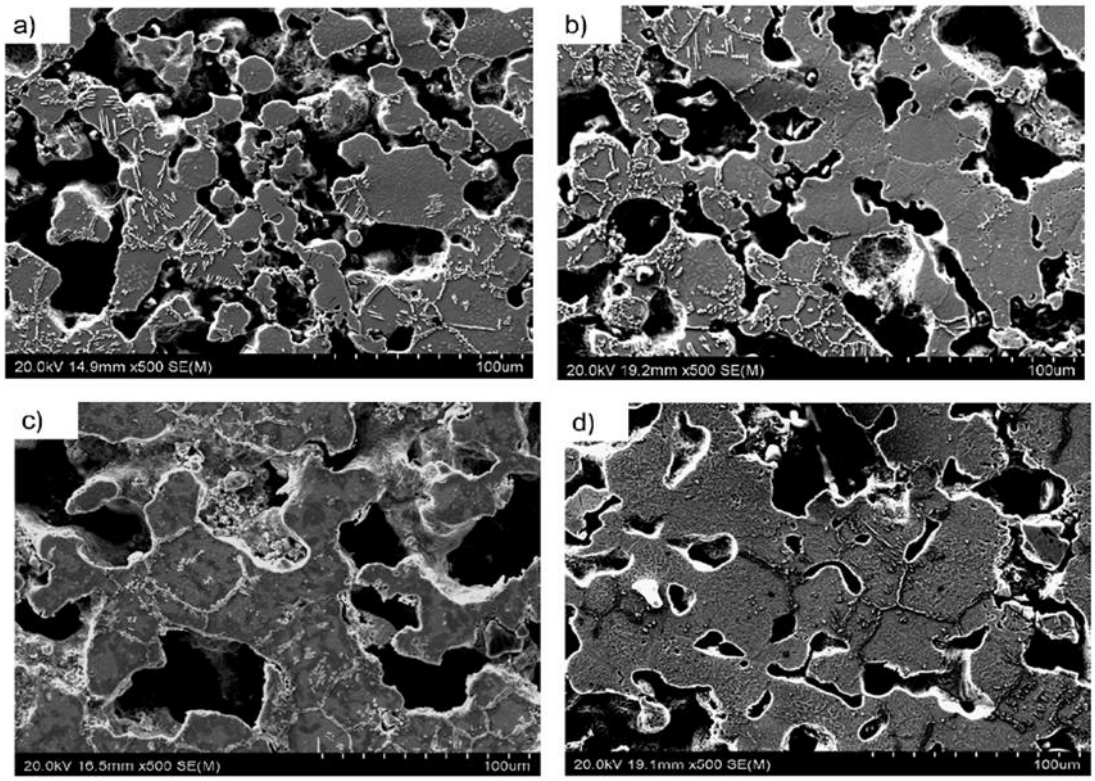

Figure 5-12: Microstructure of samples processed under a) condition 3, b) condition 4, c) condition 5, and d) condition 6.

For samples processed under conditions 3, 4 and 5, the samples processed under lower compaction pressure exhibited higher open porosity compared to the samples processed under the higher compaction pressure of 400MPa (figure 5-9.d). In addition, the amount of open porosity in samples processed under condition 5 (28.14 Vol.%) was higher than samples processed under condition 3 (23.14 Vol.%). This is because a greater amount of eutectic liquid is formed under this condition due to faster heating rates applied during sintering. In fact, the maximum amount of open porosity (~28 Vol.%) was obtained in samples processed under this condition (condition 5). Moreover, an increase in the sintering holding time results in a drop of the open porosity amount as it leads to increased density and decreased porosity. These results indicate that sintering above 942°C, fast sintering heating rates and decreased sintering holding times is beneficial in terms of producing parts with an increased amount of open porosity.

Based on the requirements needed for implants suitable for general bone replacement applications, it is desirable that pore sizes are in the range 100-600 μm [118]. Obtained results showed that the maximum pore-mouth size formed under the investigated processing conditions was 169.48 μm, which is within this range (table 5-5). Although the smallest pore-

throat sizes in all processing conditions were below 100 μm, results determined by the line-intercept method indicate that the average pore sizes of these samples were all above 100 μm, suggesting that the majority of pores are in the desirable size range. These results again confirm the important role of sintering process parameters for designing the porosity characteristics of parts.

Table 5-5: Summary of porosity characteristics in samples sintered at 1050°C.

Condition	Average pore size (μm)	smallest pore-throat size (μm)	Largest pore-mouth size (μm)
3	138.00	10.60	147.61
4	107.00	8.70	120.42
5	123.00	31.88	169.48
6	87.81	9.91	106.41

5.3 Conclusions

In this chapter, the conventional press-and-sinter method was employed to produce as-sintered porous 60NiTi. The effects of different process parameters such as compaction pressure, sinter heating rate, sinter final temperature and sinter holding time on the dimensional stability, density, porosity characteristics, microstructural properties and phase structure of the as-sintered samples were studied. It was found that liquid formed due to sintering of the parts above 942°C plays a positive role in homogenization of the parts and results in generation of open porosities. Applying a fast heating rate of 10°C/min resulted in increased amounts of open porosity as it possibly caused generation of more liquid compared to the situation where a slower heating rate was applied. However, the effect of liquid generation on the expansion of the parts needs to be considered to ensure that parts with good dimensional stability are manufactured. In addition, it was concluded that the eutectic liquid generated at a temperature above 942°C has more propensity to move radially than axially in sintered parts.

Compaction pressure is another factor which plays a role in the amount of generated open porosities. Lower compaction pressures result in increased porosity in green samples leading to higher open porosity in final parts. On the other hand, sintering holding time is a factor that, despite its positive role in homogenization of the samples, decreases the amount of open porosity, as it results in volume shrinkage and enhanced density of the sintered parts. For samples sintered at 1050°C, no matter which pressure, heating rate or sintering holding time used, the phase constituents were the same and all Ni and Ti elemental materials were removed.

Hardening treatment would be the next step in producing hard and biocompatible 60NiTi parts. Existence of Ni_3Ti and Ni_3Ti_2 phases in the matrix makes as-sintered samples unsuitable for biomedical applications as they act as preferential corrosion sites and make 60NiTi prone to corrosion. It is expected that these non-desirable phases existing in as-sintered parts will be mostly removed after applying a final hardening treatment. Further, the amount of open porosity is estimated to increase during the rapid cooling of quenching process.

In the next chapter, the possibility of obtaining homogenous solutionized porous 60NiTi parts through different cost-effective hardening treatment strategies will be evaluated. This will lead to the more widespread introduction of cost-effective methods for successful solutionizing of porous 60NiTi parts devoid of Ni_3Ti and Ni_3Ti_2 phases.

Chapter 6 An investigation on microstructural and mechanical properties of porous 60NiTi part solutionized by different cost-effective hardening methods[6]

[6] **Khanlari K**, Ramezani M, Kelly P, Hayat MD, Cao P, Neitzert T. An Investigation on Microstructural and Mechanical Properties of Porous 60NiTi Parts Solutionized by Different Cost-Effective Methods. *Metallography, Microstructure and Analysis*, 2018; **7**: 334-346.

60NiTi parts as produced by sintering, as discussed in the previous chapter, are not immediately suitable for biomedical applications. Slow furnace cooling rates result in precipitation of soft equilibrium Ni_3Ti and/or metastable Ni_3Ti_2 phases. Precipitation of these phases in the NiTi matrix makes 60NiTi prone to corrosion leading to the release of harmful Ni containing particles into the body. In addition, the existence of these phases leads to degradation of 60NiTi's fatigue properties [38].

Typical hardening treatment, which consists of heating this alloy to ~1050°C and then quenching the part with a fast cooling rate, is the appropriate procedure to obtain 60NiTi parts free of detrimental Ni_3Ti and Ni_3Ti_2 phases [21, 25]. Therefore, it is necessary to conduct hardening treatments to obtain hard, homogenized and corrosion-resistant 60NiTi parts suitable for biomedical applications.

To the best of our knowledge, in researches carried out previously, manufactured 60NiTi parts have been solutionized in vacuum furnaces or furnaces backfilled by inert argon gas (to prevent the reaction of Ti existing in 60NiTi with oxygen gas of air at high temperatures) and in the next step, the parts have been drop-quenched in water or oil to prevent the precipitation of soft equilibrium Ni_3Ti and and/or metastable Ni_3Ti_2 phases [19, 25, 29, 32]. Thomas [41] investigated the effect of different quenching environments such as water, oil, liquid N_2, etc. on the microstructural and mechanical properties of 60NiTi. It was concluded that all these various quenchants result in 60NiTi with a single authentic NiTi phase.

However, vacuum furnaces with the possibility of drop-quenching the specimen after solutionizing treatment are not always available due to practical difficulties. In addition,

backfilling the furnaces with inert argon gas, if not unavailable, is very expensive. This might dampen the interest of industries in conducting hardening treatments for porous 60NiTi parts.

In this chapter, different cost-effective and accessible hardening treatment strategies are evaluated, in order to obtain 60NiTi parts with proper phase structure suitable for biomedical applications. The effect of different hardening variants such as solutionizing atmosphere and quenching medium on the mechanical and microstructural properties of 60NiTi parts were examined and evaluated. Results obtained from this research should lead to a more widespread introduction of cost-effective accessible methods for successful homogenizing of 60NiTi.

6.1 Processing and experimental methods

6.1.1 Materials and sintering procedure

In this study, the same elemental Ni and Ti powders as in the previous study (Chapter 5) were employed to process and manufacture the samples. Ni and Ti powders were mixed to make a batch with nominal composition of approximatelly 60 wt.% Ni and 40 wt.% Ti. The powders were gently mixed in a ball miller (without inserting the balls) for 45 minutes to achieve a batch with a homogeneous nominal composition.

In the next step, the blended powders were poured into single-action steel dies with desirable geometries, for microstructural and mechanical tests, and were compacted under 400MPa pressure. Cylindrical disks with two different dimensions of Φ20mm×5mm and Φ12mm×20mm were pressed. These green samples (pressed powders before being sintered) were then inserted in a vacuum furnace working at 3×10^{-3} Pa pressure to be sintered.

Considering all the factors outlined above, the following heating profile was designed and adopted to sinter the samples: In the first stage, samples were heated to 700°C by applying a 10°C/min heating rate. In the second stage, the heating rate was slowed down to 2°C/min from 700°C to 900°C. A 10°C/min heating rate was applied again after passing 900°C to reach the final temperature of 1050°C, where 60NiTi exists in a single austenitic NiTi phase. Finally, samples were furnace cooled after being kept at this final temperature for 30 minutes.

6.1.2 Hardening treatments

As mentioned above, a typical hardening treatment of 60NiTi involves heating this alloy to ~1050°C (in a furnace with vacuum or inert gas atmosphere) and then quenching the parts in water or oil resulting in fast cooling rates [21, 25]. This method is expensive, resulting in

increased cost to manufacture 60NiTi parts. Different hardening strategies used in this chapter to solutionize/homogenize 60NiTi parts were chosen based on their availability and cost. In all these strategies explained below, sintered samples were solutionized at ~1050°C for 2 hours to obtain 60NiTi parts with B2 austenitic single phase and in the next step were quenched with the aim of freezing the structure obtained at ~1050°C.

In an initial trial, the samples were simply inserted naked in an electrically heated open-atmosphere furnace (muffle furnace) and were then quenched with ambient temperature water (table 6-1, processing condition a). In another trial, samples were wrapped with stainless steel foils, to avoid reaction of Ti with oxygen and/or nitrogen gas in air, with a small hole so that water could penetrate and quench the samples (table 6-1, processing condition b). Using a hole in the foils was essential to allow the direct contact of water with samples causing fast cooling rates. This is because these foils could not be wrapped around the samples without causing an air-filled gap zone between them and the samples. These air-filled gaps are thought to act as an insulator preventing the fast rate cooling of the quenched samples through an indirect contact of water. Another trial consisted of inserting the samples in a sealed quartz tube (table 6-1, processing condition c). In this method, quartz tube was evacuated to a low pressure of ~0.133 Pa with a rotary pump and then the tube was sealed so that air could not penetrate into the tube.

After solutionizing at ~1050°C for 2 hours, the tubes were removed from the muffle furnace, the same furnace used for solutionizing naked and stainless steel wrapped samples, and were broken open with pliers so samples could be immediately dropped into ambient temperature water. Another hardening method investigated in this research consisted of treating the samples in an Abar vacuum furnace pumped down to ~1.3×10^{-1} Pa (table 6-1, processing condition d). Nitrogen gas with high pressure back fill of ~10^5 Pa was used in this furnace as a quench medium resulting in a cooling rate of ~86°C/min (from 1050°C to 180°C).

The following table contains all the information mentioned above regarding the processing conditions used to sinter and harden the samples. The reason for choosing each of the hardening methods is explained in more detail in section 6.2.

Table 6-1: Processing conditions used to sinter and harden samples.

Processing condition	Pressing pressure applied to fabricate green samples	Sintering furnace	Sintering heating rate	Sintering final temperature	Sintering holding time	Solutionizing furnace	Solutionizng temperature	Solutionizing holding time	Sample condition	Quenching medium
a	400 MPa	vacuum furnace working at 3×10^{-3} Pa pressure	Ambient to 700°C: 10°C/min. 700°C to 900°C: 2°C/min. 900°C to 1050°C: 10°C/min.	1050°C	30 minutes	electrically heated open-atmosphere furnace	1050°C	2 hours	Naked	Room-temperature water
b	400 MPa	vacuum furnace working at 3×10^{-3} Pa pressure	Ambient to 700°C: 10°C/min. 700°C to 900°C: 2°C/min. 900°C to 1050°C: 10°C/min.	1050°C	30 minutes	electrically heated open-atmosphere furnace	1050°C	2 hours	Stainless steel wrapped (containing a small hole)	Room-temperature water
c	400 MPa	vacuum furnace working at 3×10^{-3} Pa pressure	Ambient to 700°C: 10°C/min. 700°C to 900°C: 2°C/min. 900°C to 1050°C: 10°C/min.	1050°C	30 minutes	electrically heated open-atmosphere furnace	1050°C	2 hours	Quartz tube (vacuumed to a low pressure of ~0.133 Pa) sealed	Room-temperature water
d	400 MPa	vacuum furnace working at 3×10^{-3} Pa pressure	Ambient to 700°C: 10°C/min. 700°C to 900°C: 2°C/min. 900°C to 1050°C: 10°C/min.	1050°C	30 minutes	Abar vacuum furnace pumped down to ~0.133 Pa	1050°C	2 hours	Naked	Nitrogen gas with high pressure back fill of $\sim10^5$ Pa

6.1.3 Characterization methods

The Hitachi-su70 scanning electron microscopy (SEM) machine equipped with an energy dispersive X-ray spectrometer (EDS) system was used to obtain images (based on the emissions received from the secondary electrons) from the cross section of sintered and hardened samples and to conduct EDS elemental analysis at different spots. Sample preparation procedure consisted of using 80,180, 500, 1200 and 2400 grit SiC papers at 300 rpm for grinding the samples. Vibratory polishing with 6μm, 3μm and 1μm diamond paste solution was applied to conclude the grinding procedure. Finally, the grinded and polished samples were swab-etched with a room temperature aqueous solution of 1 vol. % HF and 10 Vol. % HNO_3. Sintered and furnace cooled samples were etched for 85 seconds with this solution and hardened samples were etched for 90 seconds.

In addition, phase constituents of the cross section of the samples were identified by using an X-ray diffraction (XRD- Bruker D2 Phaser) machine. In this machine, X-ray diffraction studies were conducted using a copper K_α radiation and information was recorded in the angle 2θ from 20 to 80 degrees.

Dense samples, used in mechanical tests, were measured by the Archimedes method as specified in the ASTMB962-08 standard [107].

6.1.4 Compression and hardness tests

The sintered compression testing cylinders (12 mm in diameter and 20 mm-height) were machined into 5 mm diameter and 7.5 mm height cylinders; suitable height/diameter ratio for compression tests based on ASTME9-09 standard [119]. 60NiTi compression samples were machined to this size prior to the final hardening heat treatment procedure. This is because machining of 60NiTi in its hardened state is very difficult and is limited to many restrictions such as applying light feeds and slow speeds of cutting tools [8, 19, 21, 25]. Cylindrical compression samples were polished with 1200 and 2400 grit sandpapers to smooth the ends. Furtheremore, to avoid buckling of the samples, they were greased before being used in compression test.

The compressive properties of the hardened samples were measured by a MTS 810 universal machine. These tests were conducted in two different modes, monotonic and cyclic, at room temperature. Monotonic compression tests were carried out at a displacement rate of 0.01 mm/s until the fracture points of the materials were reached. The cyclic tests, on the other hand, were conducted with a load rate of 140 N/s. These tests included loading to pre-designed stress leves of intervals of 200 MPa, with 5 load-unload cycles conducted at each load level, before reloading to the next stress level and repeating the cyclic process. This procedure was continued until fracture in compression was reached. Three samples were used in each cyclic and monotonic test and an average mechanical property was reported for each specific test. In addition, an alignment cage was employed to ensure the parallelism of the samples during testing.

Finally, a Rockwell hardness tester was used to measure the Rockwell E (HRE) hardness from the polished cross section of samples. Results of these hardness tests (average of 3 tests) were analyzed based on the outcome of the microstructural and phase analysis studies.

6.2 Results and discussion

6.2.1 Microstructural and phase compositional studies

XRD phase identification results of sintered and furnace-cooled samples are shown in figure 6-1. As seen from the XRD pattern, other than B2 austenitic NiTi phase, soft Ni-rich Ni_3Ti and Ni_3Ti_2 phases are also present. Existence of Ni_4Ti_3 phase cannot be confirmed or rejected in

furnace-cooled samples as its main XRD peaks overlap with that of the NiTi (B2) and Ni_3Ti phases. Furthermore, SEM images cannot easily detect this phase as it is at the nanoscale. However, this phase might have been precipitated from the supersaturated NiTi solid solution upon cooling from 1050 °C [111]. Ni_4Ti_3 and Ni_3Ti_2 are metastable phases: these phases will decompose to equilibrium Ni_3Ti at increased temperatures or times [18, 111].

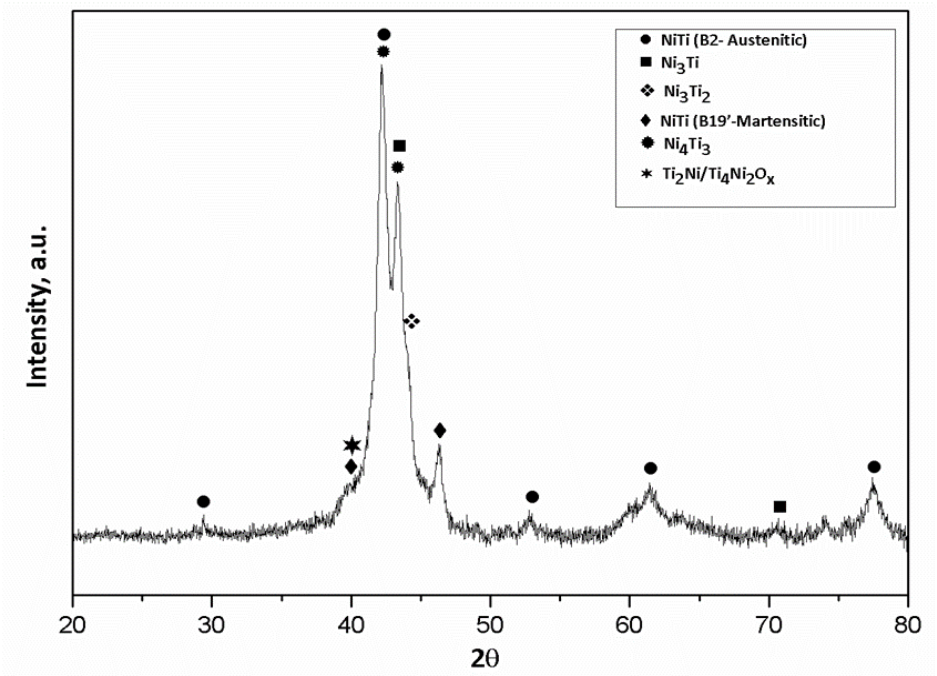

Figure 6-1: XRD pattern of sintered and furnace-cooled samples.

In addition, small peaks which can be correlated to Ti_2Ni, $Ti_4Ni_2O_x$ or martensitic B19' can also be observed in the XRD pattern. Ti_2Ni is a stable phase which can form during sintering due to the reaction amongst Ni and Ti elements. It is thermodynamically more stable than B2 austenitic NiTi, so it is difficult to remove that when it is formed [84, 111]. Because of this, it is speculated that, at 1050°C, austenitic B2 NiTi is not the only existing phase and that some Ti_2Ni phase may also be present [83]. Oxygen contamination existing in powders can react with Ni and Ti and result in $Ti_4Ni_2O_x$ phase formation [111, 117]. Alternatively, $Ti_4Ni_2O_x$ oxide can form as a result of reaction amongst NiTi and oxygen gas, since oxygen is almost insoluble in NiTi phase [120]. This oxide phase has the same structure as equilibrium Ti_2Ni, but larger lattice parameters [111]. This larger lattice parameter is due to the existence of some amount of dissolved oxygen in the structure [111]. These two phases will not be distinguished throughout this paper as they have very close XRD peaks and, further, EDS analysis cannot precisely quantify oxygen content [117].

As can be seen from the XRD graphs of the furnace cooled samples (figure 6-1), there is no evidence of Ni or Ti elements, even when sintering holding-time at the final temperature of ~1050°C was for only 30 minutes. Note that Ni is a carcinogenic element and its complete removal can be considered to be a success from the biomedical point of view [84].

XRD analysis alone is not sufficient to confidently identify the phases. As mentioned, some phases exhibit diffraction peaks very close to each other and this makes it difficult to distinguish them. For example, both Ti_2Ni and TiNi (B19') have their main peaks between $2\theta=41$ and $2\theta=42$ and austenitic B2 TiNi exhibits its main peak at $2\theta=42.2$ [113, 121, 122]. In addition, XRD pattern peaks are broad which means that the structures have relatively low crystallinity and high micro-strain [120]. These peaks might have overlapped and masked each other [117]. Moreover, depending on the processing route used and final heat-treatment applied, the position of peaks may exhibit slight shifts due to strain or change in chemical composition [120]. As a result, to confidently identify the phases, it is vital to use other phase identification methods such as EDS elemental analysis and morphological studies, alongside the XRD analysis. Based on the literature, NiTi phase contains Ni and Ti in atomic ratio of about 0.45:0.55 to about 0.55:0.45. Ni_3Ti contains Ni and Ti in an atomic ratio of about 0.70:0.30 to about 0.80:0.20. Ni_3Ti_2 comprises Ni and Ti in an atomic ratio of about 0.62:0.38 to about 0.70:0.28. This ratio (Ni:Ti) for Ti_2Ni varies from 0.25:075 to about 0.40:0.60 [35].

EDS elemental analysis conducted in this research confirms the existence of austenitic NiTi (Ni:Ti atomic ratio of ~51:49), Ni_3Ti (Ni:Ti atomic ratio of ~0.70:0.30), Ni_3Ti_2 (Ni:Ti atomic ratio of ~0.65:0.35) and $Ti_2Ni/Ti_4Ni_2O_x$ (Ni:Ti atomic ratio of ~ 32:58) phases in sintered and furnace cooled samples (figure 6-2.a, b).

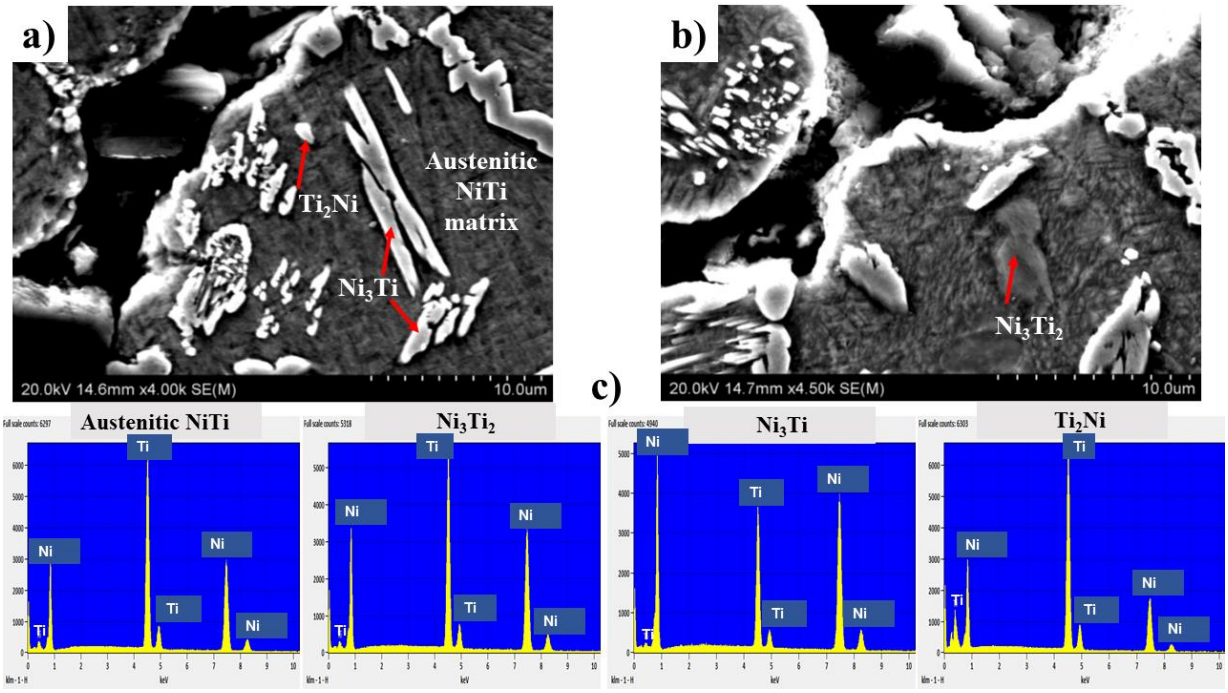

Figure 6-2: Scanning electron microscopy images (a and b) and EDS elemental analysis (c) of furnace-cooled and sintered samples. Different phases have been identified based on the results of EDS elemental analysis conducted at different spots. (a) Austenitic NiTi, Ni_3Ti, and Ti_2Ni, (b) Ni_3Ti_2

As discussed previously in section 1.1, NiTi when cooled from the austenite parent phase below the martensite start temperature (M_s), exhibits a thermoelastic phase change to highly twinned martensite. This transformation is completed when cooling is continued to below the martensite finish temperature (M_f) [4, 6, 8-15]. The temperature at which this transformation occurs is very sensitive to the amount of Ni in the composition. NiTi phase with Ni over 51 at.% exhibits austenitic structure to -175°C. Decreasing Ni content in the composition results in a rapid increase in the martensite start temperature (M_s). Results of Cluff and Corbin [101] indicate that M_s of NiTi phase reaches room temperature at approximately 50.5 at.% Ni. EDS elemental analysis is not a suitable method to detect martensitic NiTi as the precision of machine is not that high to distinguish the very small amount of difference in Ni composition, existing amongst martensitic and austenitic NiTi. Observation of the fine structure with needle-like contrast in high magnification SEM images might imply the formation of martensitic NiTi. This structure is attributed to self-accommodate martensite (figure 6-3) [111]. Formation of martensitic NiTi in furnace cooled samples studied in this research can be attributed to the precipitation of Ni-rich phases such as Ni_3Ti and Ni_3Ti_2. These phases withdraw Ni in austenitic NiTi phase and result in the formation of a localized region with a smaller amount of Ni in composition around the precipitates. This results in the increase of martensitic start

temperature and formation of martensitic NiTi in ambient temperature. However, it is almost impossible to differentiate between austenitic and martensitic NiTi using the type of SEM sample preparation employed in this research. It is thought that these particles may be Ni_4Ti_3. Since these particles are not sufficiently coarse, the EDS analysis could not detect the difference in phase composition between these particles and the matrix. That said, caution needs to be applied when interpreting these surface structures observed on NiTi alloys. This is because these structures are not always attributed to the bulk structure and might be artefacts formed due to the effect of etching with hydrofluoric acid [114].

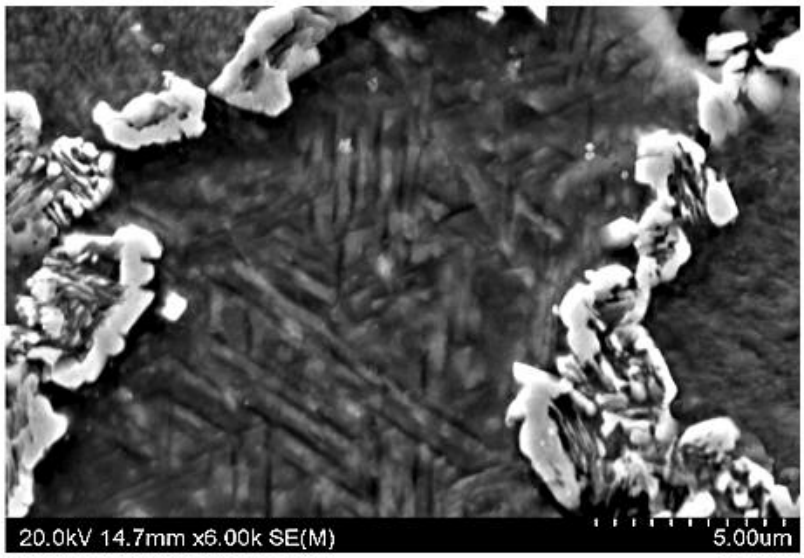

Figure 6-3: High magnification scanning electron microscopy image of sintered and furnace-cooled samples.

As a first attempt, sintered samples were hardened in an electrically heated open atmosphere furnace. Despite being aware of the fact that the NiTi phase does not solve oxygen [71], the extent of oxygen reaction with NiTi phase in 60NiTi alloy and its effect on mechanical properties was not clear to this author. In fact, 60NiTi is an intermetallic alloy with highly directional and strong bonding between nickel and titanium [5, 9]. It was expected that this strong bonding between nickel and titanium would prevent extensive reaction of Ti with oxygen and nitrogen gases in air. However, the results obtained proved that this is not the case. SEM images indicate the formation of a bright layer around the pores (figure 6-4.a). Reported results obtained from heat treatment of equiatomic NiTi in air show that this layer is a complex mixture of Ni and Ti oxides. Smialek et al. [70] heat-treated Ni-49Ti (at. %) isothermally in air over the temperature range of 500°C to 900°C. Results of their studies along the serial sections

of the formed layer indicated graded mixture formation of TiO_2, $NiTiO_3$ and NiO. Results obtained by Firstov et al. [71] proved the same. They heat treated NiTi alloy (50 at.% Ni) in air in the temperature range of 300-800°C. Their results confirmed the formation of rutile TiO_2 on the top surface (air/oxide interface) with a layer of $NiTiO_3$ below when NiTi is oxidized at 800°C.

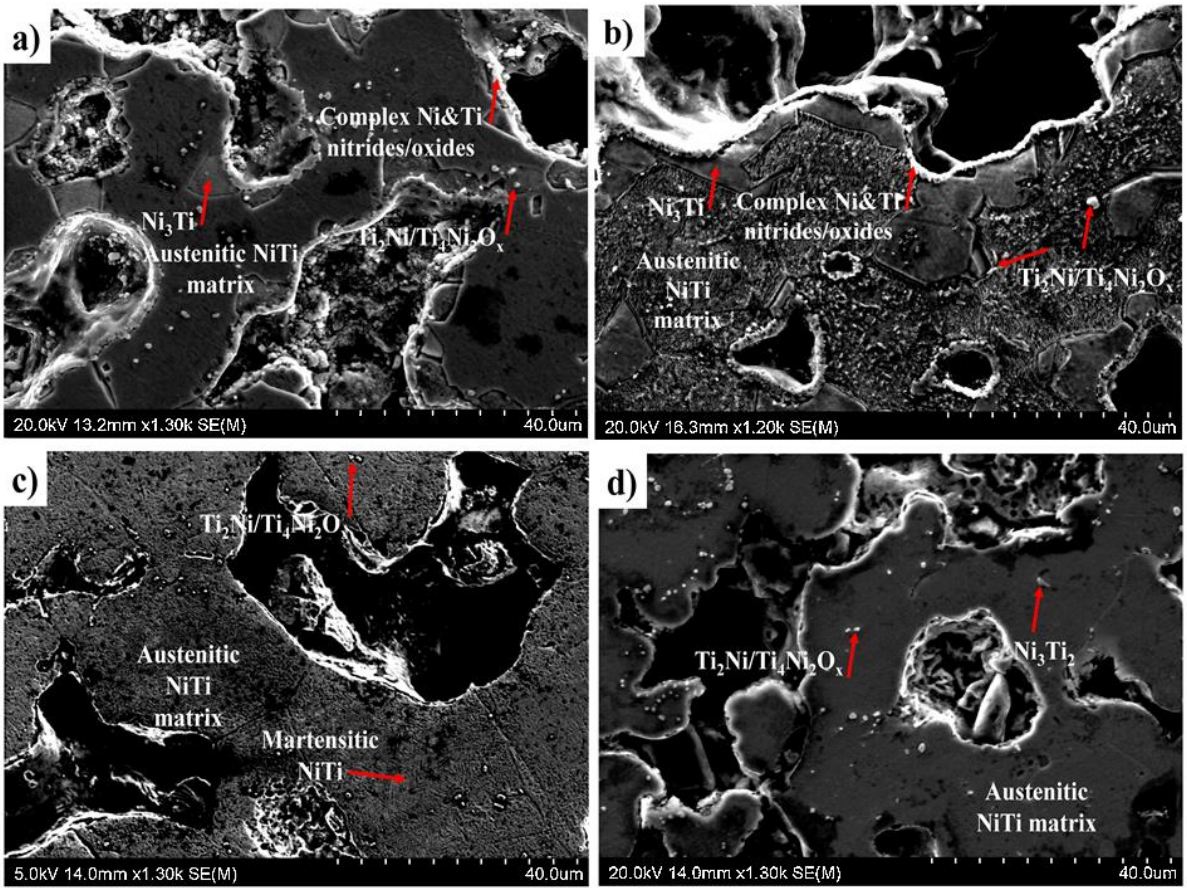

Figure 6-4: Scanning electron microscopy images of samples solutionized in different conditions. (a) Naked samples, (b) Stainless steel foil wrapped samples, (c) Samples solutionized in a vacuum furnace and quenched with nitrogen gas, and (d) Quartz tube sealed samples.

EDS analysis carried out in this research indicates the existence of a relatively small amount of Ni species at the air/bright complex compound interface (Ti:Ni (at%) of 43.48:1.95). The number of nitrogen and oxygen atoms are not reported here since they are not easily quantified accurately by EDS analysis [117]. Since Ni is insoluble in the oxides of Ti [71], detection of Ni by EDS is proof of the formation of Ni compounds. In addition, XRD analysis results show that other than the dominant TiO_2 phase, other phases such as Ni_3N, TiN, Ni_3Ti_3O and $Ti_4Ni_2O_x$ are also present. True identification of these compounds needs deeper investigation and analysis as they form in serial layers along the cross section [70]. XRD analysis is appropriate

for surface measurements only, due to its lack of penetration, so these detected phases are only valid for the surface tested and not for the layers below [38]. Due to the lack of certainty in the existence of these phases along the subsurface layers and overlapping of XRD peaks, phases related to this bright complex layer are taken to be complex Ni and Ti oxides/nitrides in the XRD pattern and SEM images (figures 6-4.a, 6-5.a), as described by Julien [30].

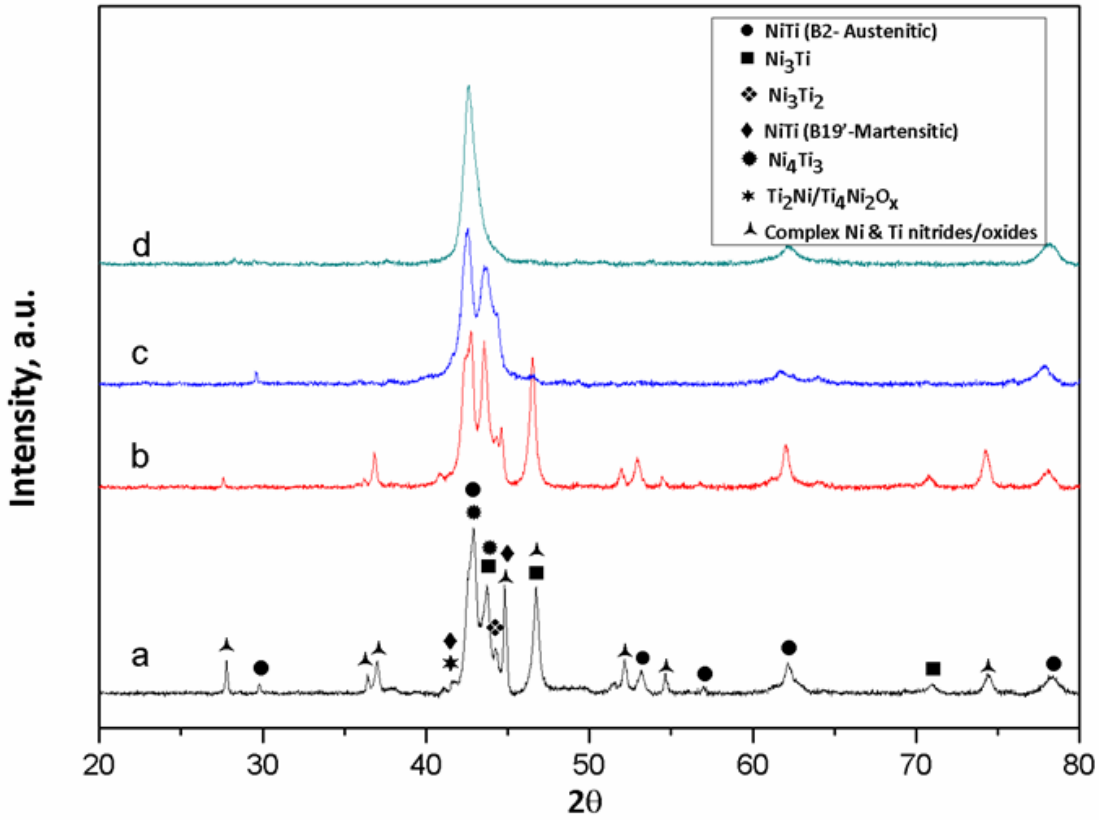

Figure 6-5: XRD patterns of samples solutionized in different conditions. (a) Naked samples, (b) Stainless steel foil wrapped samples, (c) Samples solutionized in a vacuum furnace and quenched with nitrogen gas, and (d) Quartz tube sealed samples. The position of peaks exhibits slight shifts relative to each other due to strain or change in chemical composition caused by applying different solutionizing strategies.

The formation of this layer, predominantly a Ti compound, results in substantial depletion of Ti from the Ni-rich matrix (Ni:Ti ratio of ~0.55:0.45) which causes the precipitation of Ni_3Ti phase (Ni:Ti at.% ratio of ~72:28) (figure 6-4.a) [70, 71]. This actually makes the hardening treatment ineffective as it was done to prevent the formation of soft Ni_3Ti and Ni_3Ti_2 phases. Despite this, formation of this Ti-rich layer is in favour of good biocompatibility of NiTi since it prevents the diffusion of Ni into the body [71]. In addition, this layer, as a ceramic, can increase the corrosion resistance of 60NiTi [30].

Furthermore, formation of oxides is not just limited to around the pores, but they are also formed in the matrix structure (figure 6-4.a). SEM images indicate the existence of spots with Ni:Ti atomic ratio comprising ~ 20.99: 46.55. As a result, these spots are either remained $Ti_2Ni/Ti_4Ni_2O_x$ phases formed during the sintering process or they can be newly formed $Ti_4Ni_2O_x$ particles. Extra $Ti_4Ni_2O_x$ oxide is reasoned to be formed due to reaction amongst austenitic B2 NiTi phase and oxygen gas as oxygen is almost insoluble in NiTi phase [120].

In the heat treatment of samples with stainless steel foil wrapping, the samples were fully wrapped with a piece of stainless steel foil as done by Ramezani et al. [123]. This method, commonly used by industry, is applied to avoid or at least reduce the influence of a sample's chemical and physical interaction with its surrounding atmosphere [123]. Here, the wrapping layer contained a very small hole so water could penetrate into the foil and cool the specimen upon being dropped in water. Unfortunately, this method was not successful and could not prevent the reaction amongst NiTi and surrounding atmosphere (air). XRD peaks were approximately the same as the one obtained for the unwrapped sample (figure 6-5.b); SEM images also showed the generation of a larger amount of $Ti_4Ni_2O_x/Ti_2Ni$ phase (brighter spots embedded in the dark austenitic B2 matrix) in the inner area (figure 6-4.b). The reason for the generation of larger amounts of this phase with this method compared to unwrapped/naked samples is not as yet clear, and needs further investigation.

Hardening treatment conducted with the Abar vacuum furnace was not successful in regard to prevention of Ni-rich phases. XRD peaks obtained from specimens hardened with this method (figure 6-5.c) indicate the existence of all the phases that were present in the sintered samples. However, some phases such as Ni_3Ti, Ni_3Ti_2 and martensitic B19' NiTi could not be distinguished clearly from SEM images obtained under magnification of X1300 (figure 6-4.c). However, higher magnification images combined with EDS elemental analysis was used to prove the existence of all the phases detected by XRD (figure 6-6). The cooling rate of this furnace (~86°C/min) was not high enough to prevent precipitation of Ni-rich phases, but could prevent their coarsening since the cooling rate was not as slow as in the furnace cooled conditions. The cooling rate applied in this method can be better understood by being compared to the cooling rate of water quenched samples. Note that based on the research carried out by Thomas [41], water quenching is estimated to result in cooling rates of ~200°C/s as it takes just 5 seconds for 60NiTi samples to cool down to room temperature from 1000°C.

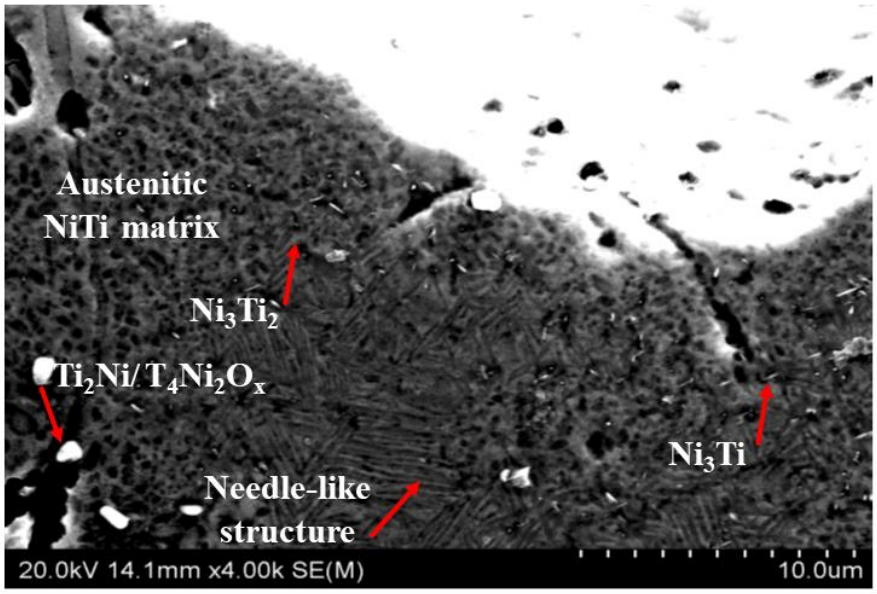

Figure 6-6: High magnification scanning electron microscopy image samples hardened in a vacuum furnace and quenched with nitrogen gas showing Ni_3Ti, Ni_3Ti_2 phases and the fine structure with needle-like contrast.

EDS elemental analysis could confirm the existence of austenitic NiTi (Ni:Ti atomic ratio of ~50.5:49.5) and $Ti_2Ni/Ti_4Ni_2O_x$ (Ni:Ti atomic ratio of ~ 35:52) phases in samples hardened by the Abar vacuum furnace. Ni_3Ti_2 phase was not coarse enough to be detected by EDS analysis. This phase appeared in SEM images as a bright grey phase embedded in darker NiTi matrix. The contrast is most probably just related to surface curvature, edges, roughness, etc. This is because, as explained, SEM images were obtained based on the emissions received from the secondary electrons having sensitivity to the topology of the precipitates. However, change in the amount of Ni in composition also results in brightness differences [103, 124]. The brightest phase with elongated needle shape morphology was ascribed as Ni_3Ti [40].

Similar to sintered and furnace cooled samples, fine structures with needle-like contrast were observed in the SEM images. This phase could not be observed under SEM images obtained from samples hardened with other methods. This is due to the formation of Ni-rich NiTi phases (over ~50.5 at. % Ni), which results in stabilization of austenite phase at room temperature or fast cooling rates preventing the coarsening of Ni_4Ti_3 phase [101]. Hardening of naked and stainless steel foil wrapped 60NiTi specimens with the muffle furnace shows that this alloy is very sensitive to air exposure and under high temperature treatments will easily react with oxygen and nitrogen gas in air. To avoid this, samples were sealed in a vacuumed quartz tube and were then solutionized at 1050°C with the same muffle furnace. The results obtained were

promising. The only intense peak in the XRD pattern was the one related to Ni-rich austenitic B2 NiTi (Ni:Ti ratio of ~0.55:0.45) and Ni_4Ti_3. In fact, as reported in the literature, both these phases exhibit their main peaks at 2θ=42.2 (figure 6- 5.d) [111, 113, 121, 122]. As explained before, formation of Ni_4Ti_3 is inevitable in solutionized and quenched 60NiTi samples as its formation takes just a few miliseconds [18]. Instead, since the cooling rate is slow for furnace cooled or nitrogen gas cooled samples, the existence of this phase cannot be confirmed with certainty for these treatments. This phase might have had enough time to decompose to Ni_3Ti_2 or stable Ni_3Ti phase through the precipitation sequence of: $Ni_4Ti_3 \rightarrow Ni_3Ti_2 \rightarrow Ni_3Ti$ [111].

Furthermore, the XRD pattern (figure 6-5.d) shows the presence of small amounts of complex Ni and Ti oxides/nitrides phases. Despite this, SEM images and EDS analysis studies could not confirm the formation of these phases (figure 6-4.d). These phases might have been formed in very small amounts due to the presence of very low-pressure air remaining in the tube after its vacuuming. Alternatively, these phases might have been formed due to exposure of the samples to open atmosphere occurring in the very short period of time between the breakage of the tube and the dropping of the sample into the water. In addition, SEM images and EDS studies could detect Ti-rich spots embedded in the austenitic B2 NiTi matrix. As explained, these spots are either remaining $Ti_2Ni/Ti_4Ni_2O_x$ phases formed during the sintering process, or they are newly formed $Ti_4Ni_2O_x$ particles. Moreover, based on the obtained results (figures 6-4.d, 6-5.d), a very small amount of Ni-rich Ni_3Ti_2 (Ni:Ti atomic ratio of ~0.65:0.35) is also formed. Formation of this phase could be attributed to the time delay mentioned earlier, between the breakage of the tube and the dropping of the samples into the water. Overall, this method can be considered to be a very practical and cost-effective solution for conducting hardening treatment to obtain homogenized/solutionized porous 60NiTi parts on occasions where argon-protected or vacuum furnaces, with the possibility of fast cooling rate quenching, are not available or desirable.

A detailed examination of the SEM images shows that, no matter which hardening treatment method is used, some spots with a darker colour than the matrix can be seen (figure 6-7). EDS analysis, however, did not reveal any compositional difference between these spots and the matrix. In addition, the samples were flat and not tilted during SEM imaging. As a result, it is thought that this difference in brightness is not correlated to the difference in the number and intensity of emitted secondary electrons. Since these samples are etched, the difference in etchant exposure time may have been responsible for this phenomenon.

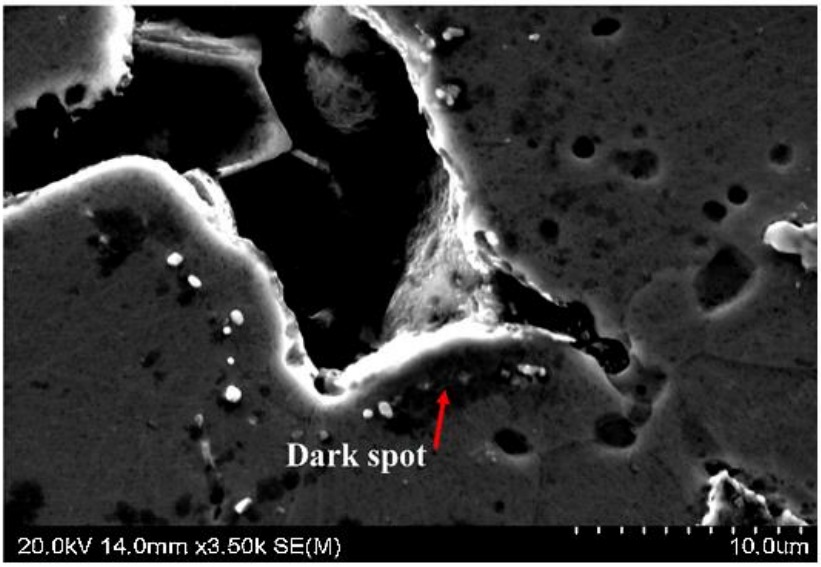

Figure 6-7: Scanning electron microscopy image showing the spots with darker color compared to the matrix, seen in hardened samples.

6.2.2 Compression and hardness tests

Samples solutionized in the Abar vacuum furnace and quenched with nitrogen gas cannot be employed in biomedical implants as they contain precipitated Ni_3Ti, Ni_3Ti_2 Ni-rich phases. These phases make 60NiTi prone to corrosion leading to release of harmful Ni-containing particles into the body [38]. On the other hand, naked and stainless steel wrapped samples solutionized in the muffle furnace and quenched with water, containing precipitated Ni_3Ti Ni-rich phases, formed a relatively Ni-free layer which is thought to prevent the release of Ni to the body [30, 71]. In addition, solutionizing the tube sealed samples in the muffle furnace and quenching in water could lead to a relatively homogenous biocompatible [9, 38] Ni-rich austenitic B2 NiTi phase. As a result, in this research, further mechanical and hardness tests were conducted on just the hardened tube sealed and naked samples, as the microstructure of the naked samples are similar to the stainless steel wrapped samples.

Naked samples show negligibly higher relative densities (65.04%) than tube sealed samples (64.74%). This observed difference in relative density values is attributed to the absorption of oxygen and nitrogen gas during the solutionizing treatment by the naked samples affecting their final weights. This is because these samples have been processed under identical sintering conditions and the only difference has been related to the conditions of the samples during solutionizing procedure (table 6-1). Since these values are very close to each other, the effect of density on the mechanical properties is not considered in this study.

Monotonic and cyclic compression tests were conducted to evaluate the mechanical properties of the produced specimens. Results of the monotonic compression fracture tests show that samples sealed in tube exhibit larger amounts of elongation and strength till fracture as compared to the specimens hardened in the naked condition (figure 6-8). Increased brittleness and inferior strength of naked hardened specimens is attributed to the generation of extensive amounts of oxides in this condition. High oxide content in NiTi alloys results in embrittlement of this alloy [111]. In addition, both types of specimen exhibit an increased and then decreased instantaneous stiffness after an initial linear deformation stage (figure 6-8). Porosities might decrease under compression test and this might lead to the increase in stiffness. Instead, the slight decrease seen in the stiffness of the samples before reaching the fracture point is an indication of the superelasticity effect.

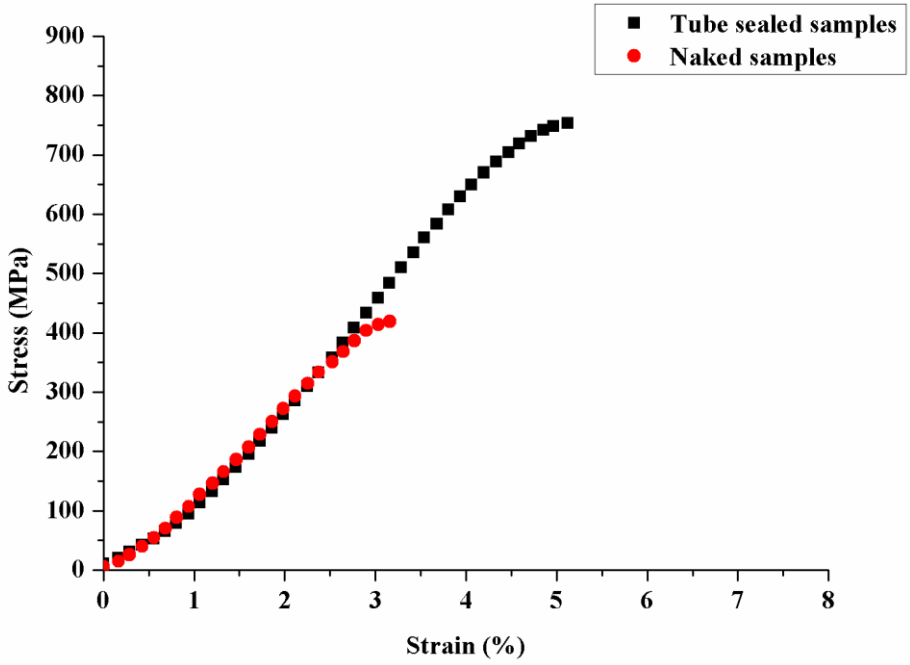

Figure 6-8: Monotonic compressive stress–strain diagrams of hardened tube sealed and naked samples.

Results obtained from cyclic compression tests agree with the monotonic tests. Naked samples were more brittle as compared to the specimens hardened in tube sealed conditions. Naked samples fractured in the second cycle after unloading from the 400 MPa stress (figure 6-9). Tube sealed samples, on the other hand, could successfully pass all the five load-unload cycles applied at stress levels of 200, 400 and 600 MPa until they failed at the loading cycle to 800 MPa, at around 737 MPa (figure 6-9).

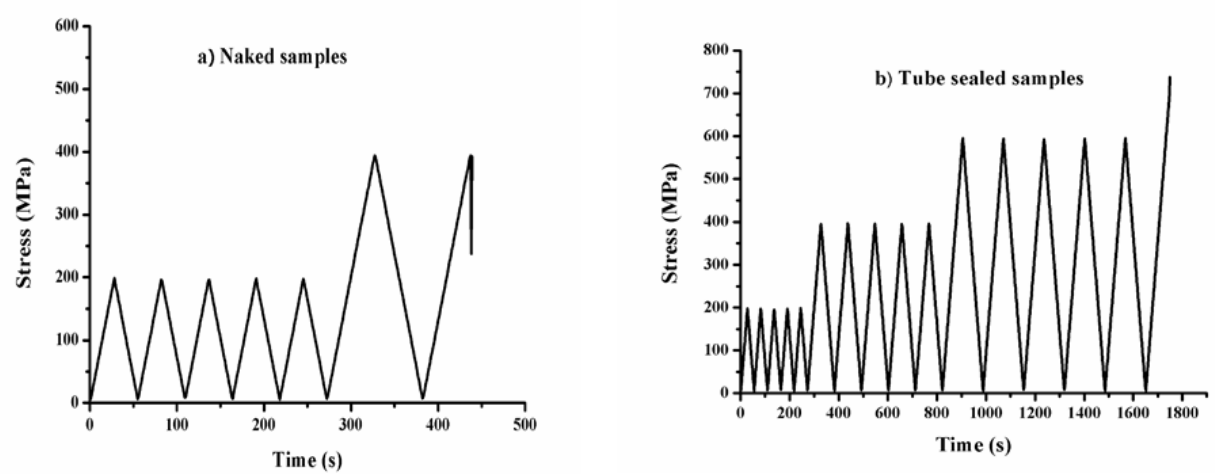

Figure 6-9: Cyclic compression tests of hardened samples conducted in stress intervals of 200 MPa. (a) Naked sample, (b) Tube sealed sample.

These results show that decreasing the oxide content in 60NiTi specimens enhances the obtained mechanical properties and results in its increased fracture elongation, strength and superior cyclic behavior.

Further, based on the results obtained from the HRE hardness tests, samples hardened in tube sealed conditions exhibited higher hardness values (102.2 HRE) than naked hardened samples (94.5 HRE). As mentioned previously, precipitation of soft Ni-rich phases were mostly prevented in specimens hardened in tube sealed conditions resulting in higher average hardness value in these samples as compared to naked hardened ones.

6.3 Conclusions

The conventional press-and-sinter (P&S) method has the potential to produce porous 60NiTi samples suitable for general bone replacement applications where bone diffusion is desirable. In this chapter, the possibility of obtaining solutionized porous 60NiTi with different cost-effective hardening methods was evaluated. Solutionizing the 60NiTi samples in an Abar vacuum furnace and quenching them with high-pressure back fill of ~10^5 Pa nitrogen gas could not prevent the formation of soft, non-biocompatible Ni_3Ti and Ni_3Ti_2 phases. It was found that conducting solutionizing treatment in an electrically heated open-atmosphere furnace results in the formation of a complex oxide and nitride layer on the surface and around the pores. Wrapping the samples in a stainless steel foil could not protect the samples from oxidizing/nitriding in this non-protected furnace. Formation of this layer, predominantly Ti compound, resulted in substantial depletion of Ti from the Ni-rich matrix and led to the

precipitation of Ni_3Ti phase. Despite this, these relatively Ni-free layers are thought to act as a barrier preventing the direct contact of the Ni_3Ti phase with the body. On the other hand, hardened samples which were tube sealed could successfully form a phase structure dominated by a biocompatible Ni-rich austenitic B2 NiTi phase.

Results obtained from cyclic and monotonic compression tests showed that the existence of oxides and nitrides in naked hardened samples are detrimental. These complex oxide and nitride layers, although increasing corrosion resistance, resulted in excessive embrittlement of 60NiTi parts. These samples exhibited inferior mechanical properties as compared to tube sealed samples. Moreover, tube sealed hardened samples had a greater average hardness value than naked samples. This was attributed to the absence of soft Ni-rich phases in these samples.

Vacuum furnaces or furnaces which work under an inert gas such as argon, which are typically used to solutionize 60NiTi, are clearly more costly than furnaces that are running under an open-atmosphere condition. This is because providing a vacuum atmosphere or using argon gas is very costly. As a result, hardening 60NiTi parts in electrically heated open-atmosphere furnaces through tube sealing would appear to be a more cost-effective method and more accessible than these mentioned furnaces to successfully solutionize and homogenize 60NiTi parts.

Chapter 7 Mechanical and microstructural characteristics of as-sintered and solutionized porous 60NiTi[7]

[7]**Khanlari K**, Ramezani M, Kelly P, Cao P, Neitzert T. Mechanical and microstructural characteristics of as-sintered and solutionized porous 60NiTi. *Intermetallics*, 2018; **100**: 32-43

In the previous two chapters, the effects of critical processing parameters, such as pressing pressure, sintering temperature, heating rate and sintering holding time, on the dimensional stability, density, porosity characteristics, microstructural properties and phase structure of as-sintered 60NiTi samples was investigated. A suitable accessible cost-effective method to homogenize as-sintered parts was developed and discussed. In this chapter, the possibility of developing homogenized porous 60NiTi parts possessing desirable structural and mechanical properties for general bone replacement applications is investigated (Note that microstructural and mechanical properties requirements for parts employed in general bone replacement applications are explained in the next sections of this chapter).

Critical processing parameters of the conventional press-and-sinter method such as heating rate and sintering holding time will be varied in order to obtain 60NiTi parts with different levels of open porosity (the pores that are interconnected and have a route to the surface of the part). These samples will then be hardened to acquire solutionized, hard, corrosion resistant and biocompatible 60NiTi parts, free of detrimental Ni_3Ti and Ni_3Ti_2 phases causing corrosion and a possible consequent release of harmful Ni into the body. This study, apart from containing a discussion of the effects of hardening treatment on the microstructure, phase composition and mechanical properties of as-sintered parts, will investigate the relationship between the microstructure and the mechanical properties of hardened 60NiTi parts with different amounts of open porosity. In addition, the suitability of using these porous structures for general bone replacement applications, in terms of microstructural, mechanical and chemical properties, is discussed in this chapter.

7.1 Processing and experimental methods

7.1.1 Materials, processing and characterization methods

The same spherical Ti powders (D_{50}: 27 μm) and spiky Ni powders with needle-shaped geometry (D_{50}:12.57 μm) from the previous chapters were used for this study, to fabricate porous 60NiTi parts by conventional press-and-sintering.

The powders were mixed for 45 minutes in a rotating mixer in the Ni:Ti weight ratio of 1.5:1. The compacts were prepared by pressing the mixed powders under a pressure of 400MPa into cylindrical disks (of 20 mm diameter and 5 mm height) for microstructural testing, and cylinders (of 12 mm diameter and 20 mm height) for compression testing. Sintering was carried out in a 3×10^{-3} Pa vacuum furnace at 1050°C for a short time of 30 minutes and a longer time of 4 hours. 1050°C was chosen as the final sintering temperature as this temperature is above 942°C, giving an opportunity for eutectic liquid generation in compacted blended powders, and since at this temperature 60NiTi is in its single austenitic NiTi phase [16]. In addition, as shown in the previous chapters, for samples sintered at 1050°C, regardless of the pressure, heating rate or sintering holding time used, all Ni and Ti elemental materials were removed. The heating rate is another factor which greatly affects the amount of liquid and consequently the porosity generated in samples [103]. Two different heating profiles were used to reach 1050°C, as follows: In heating profile 1, in the first stage, samples were heated at 10°C/min to 700°C, at 2°C/min from 700°C to 900°C and again at 10°C/min to the final temperature of 1050°C. In heating profile 2, the fast heating rate of 10°C/min was empoloyed to heat the samples from ambient room temperature directly to 1050°C. The different parameters and conditions used to process the sintered 60NiTi parts are summarized in table 7-1. Note that the samples were furnace cooled to room temperature after the conduction of the sintering process.

The resulting cylindrical samples (12 mm in diameter and 20 mm-thick) were then machined into 5 mm diameter and 7.5 mm height cylinders, a suitable size for compression tests based on ASTME9-09 standard [119]. A series of these machined cylindrical samples and microstructural testing disks (20 mm in diameter and 5 mm-thick) were sealed in a vacuum quartz tube and hardened in the electrically heated open-atmosphere furnace as follows: In the first stage, the samples were solutionized for 2 hours at 1050°C, where 60NiTi is in its single austenitic NiTi phase. In the next step, the glass tubes were rapidly broken with pliers outside of the furnace and were dropped into water to inhibit the precipitation of Ni_3Ti and Ni_3Ti_2 phases.

Microstructural testing disks (20 mm in diameter and 5 mm-thick) were used to measure the density and open porosity of the parts by the Archimedes and liquid weighing methods, respectively, as specified in ASTMB962-08 standard [107]. The SEM machine equipped with an EDS system and an X-ray diffraction (XRD) machine were employed to obtain images (based on the emissions received from the secondary electrons), provide information on elemental distribution and conduct phase analysis from the cross section of the samples at room temperature. Samples were grinded and polished before conducting phase analysis. To help better distinguish phases in microstructural and elemental distribution studies, samples were additionally etched with a room temperature aqueous solution of 1 vol. % HF and 10 Vol. % HNO_3 [85] (sintered samples: 85s; solutionized samples: 90s). The ASTM E112-13 standard line-intercept method as $1.12L_0/N_{pore}$, where L_0 is the line length, and N_{pore} is the number of pores on that line [108] was used to determine the average pore size of the samples.

A Leco macine was used to determine the amounts of oxygen in powders, as-sintered parts and solutionized specimens. A low temperature differential scanning calorimetry (DSC) machine (PerkinElmer DSC 8000) was also used to determine related latent heats and phase transformation temperatures of as-sintered and solutionized samples. In these tests, ~30mg samples were wire eroded from the microstructural testing disks and were cycled as per the following program: In the first stage, the samples were heated from ambient temperature till 80°C. In the second stage, they were cooled to -50°C and finally, in the last stage, they were heated from -50°C to 80°C. All these stages were conducted at a heating and cooling rate of 15°C/min while samples were protected under flowing nitrogen gas. The tangent method was used to define the transformation temperatures and the latent heats. A high temperature DSC machine (Pegasus DSC 404 F3) was employed to elucidate phase transformations during the sintering of Ni+Ti blended powders. Two batches of powder mixtures (~60 wt.% Ni and ~40 wt.% Ti) with ~10 mg weight were used to conduct the tests. These tests were done to investigate the effect of heating rate on the amount of eutectic liquid generated at 942°C during sintering of the blended compacts. Therefore, the heating rates used to sinter these blended powders in the DSC machine were identical to the ones (slower and faster) used to process the compacted powders during the sintering processing. These tests were carried out under flowing argon gas.

Table 7-1: Summary of the processing parameters used to sinter the samples.

Processing condition	Pressing pressure	Sintering final temperature	Heating rate	Sintering holding time
1	400 MPa	1050°C	Ambient to 700°C: 10°C/min. 700°C to 900°C: 2°C/min. 900°C to 1050°C: 10°C/min.	30 minutes
2	400 MPa	1050°C	10°C/min	30 minutes
3	400 MPa	1050°C	Ambient to 700°C:10°C/min. 700°C to 900°C: 2°C/min. 900°C to 1050°C: 10°C/min.	4 hours
4	400 MPa	1050°C	10°C/min	4 hours

7.1.2 Mechanical and hardness tests

The compressive properties of the samples before and after hardening treatment were measured in cyclic and monotonic modes using a MTS 810 universal machine. The displacement and applied force values were simultaneously recorded by a data acquisition system during the compression tests. The displacement was measured via a Linear Variable Differential Transformer (LVDT) that is within an actuator. The LVDT measures and controls the movement of the actuator, to which the loading plate is attached. These data were used to compute the strain and stress values based on the original length and diameter of each sample. Monotonic compression tests were conducted at a displacement rate of 0.01 mm/s until the fracture point of the specimens was reached. Cyclic tests were also conducted at a load rate of 140 N/s. The tests consisted of loading to pre-designed stress levels of 200, 400, 600, 800 and 1000 MPa. Five load-unload cycles were conducted at each stress level, before reloading to the

next stress level and repeating the cyclic process. This procedure was continued until fracture in compression was reached.

Moreover, a Rockwell hardness tester using a 1/8 inch (3.175mm) diameter steel spherical indenter applying 100Kg load was used to measure the Rockwell E (HRE) hardness from the polished cross section of the samples. All the experiments explained above were carried out for both as-sintered and solutionized samples processed under each specific condition mentioned in table 7-1. All mechanical tests (including cyclic and monotonic compressive tests) were carried out at room temperature. Further, to increase the accuracy of the results, mechanical tests and microstructural experiments such as density and open porosity measurements were conducted on three samples and the average values are reported here.

7.2 Results and discussion

7.2.1 Microstructure and phase composition analysis

Irrespective of the processing condition used, the phases detected by XRD in as-sintered samples were identical and no elemental Ni or Ti was observed (figure 7-1.a). This implies that 30 minutes of sintering at 1050°C was sufficient to result in full consumption of Ni and Ti elements, as also reported in previous studies, sections 5.2.1 and 6.2.1.

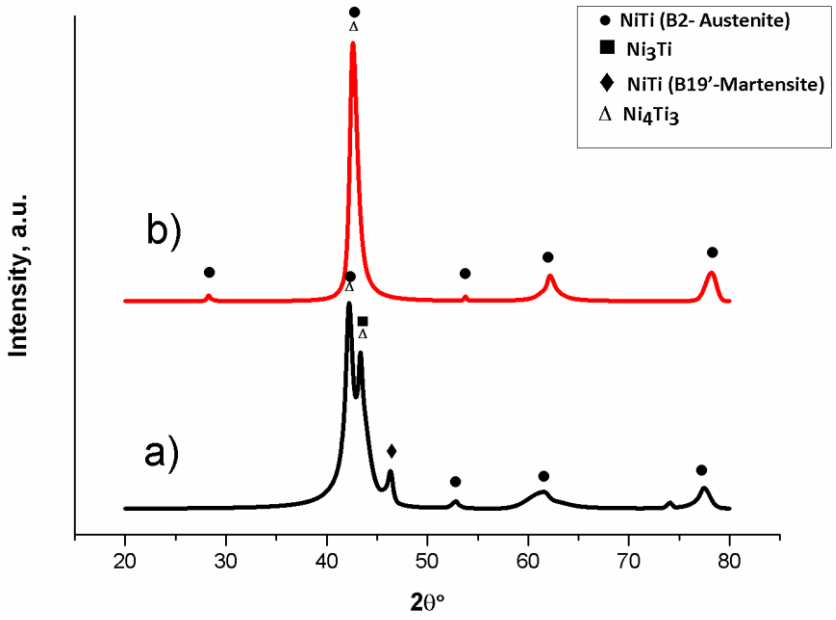

Figure 7-1: XRD pattern of a) as-sintered, and b) hardened samples (Similar to as as-sintered samples, all hardened samples showed identical patterns).

The main peaks observed in figure 7-1 are correlated to austenitic NiTi. As predicted, peaks related to Ni-rich phases such as Ni_3Ti and Ni_4Ti_3 were also observed in the XRD pattern of as-sintered samples. Ni_3Ti is formed due to the slow cooling rate applied during the cooling stage after sintering the samples. Existence of the Ni_4Ti_3 phase cannot be confidently confirmed or rejected in as-sintered samples. This is because the main XRD peaks of Ni_4Ti_3 overlap with those of the NiTi (B2) and Ni_3Ti phases [111, 113, 121, 122]. This metastable phase precipitates from the supersaturated NiTi solid solution upon cooling from high temperatures during the process [111]. It is speculated that, as discussed in section 6.2.1, at the elevated temperatures and longer times which occurred during the slow furnace cooling, this phase might have been mostly decomposed to stable Ni_3Ti through the precipitation sequence of: $Ni_4Ti_3 \rightarrow Ni_3Ti_2 \rightarrow Ni_3Ti$ [18, 111]. Furthermore, very small peaks attributed to martensitic $B19'$ can also be seen in the pattern of as-sintered samples.

Hardening treatment could successfully freeze the soft detrimental Ni-rich Ni_3Ti phases into solution and stop their precipitation (figure 7-1.b). As can be seen, austenitic NiTi and hard Ni_4Ti_3 phases are the only main phases formed in samples after conducting hardening treatment. The positions of the peaks correlating to these phases exhibit slight shifts as compared to as-sintered ones. This is because of strain or changes in chemical composition of samples caused by the applied final hardening treatment [120].

EDS elemental analysis and morphological studies were carried out to examine for the existence of these phases in the as-sintered and hardened samples. Furthermore, other phases in very small amounts might exist in as-sintered and hardened samples that the XRD might not detect.

The results of the EDS analysis on the observed phases are reported in table 7-2 and figure 7-2.c. The phases were identified in SEM images (figure 7-2.a, b) based on their Ni:Ti atomic ratio reported in [35]. As seen (table 2, figure 7-2), other than austenitic NiTi and Ni_3Ti phases detected by XRD phase analysis, other phases such as Ni_3Ti_2 and Ti_2Ni were also detected by the EDS elemental analysis in as-sintered samples. As seen in figure 7-2.a, the Ni_3Ti_2 phase has a globular morphology and is precipitated in the matrix of the NiTi phase, which has a darker grey color. The brighter phase, which is formed mostly around the grain boundaries but also in the matrix of NiTi phase, is Ni_3Ti. Based on the Ni-Ti binary phase diagram, figure 1.3, Ti_2Ni is a stable phase which is formed due to reaction between the elemental Ni and Ti materials. Since this phase is stable, its removal is very difficult once formed [84, 111]. In the

SEM images, this phase is seen as small particles with even brighter color than Ni-rich phases. As discussed before in section 6.2.1, the brighter contrast is most probably just related to surface curvature, edges, roughness, etc. This is because, as explained, SEM images were obtained based on the emissions received from the secondary electrons having sensitivity to the topology of the precipitates. Alternatively, this might be because Ti_2Ni has a solubility for O making it act as an insulator causing electron charge build-up [111, 117]. Results of impurity measurements done by Leco machine indicated that 0.1 and 0.11 wt.% oxygen exists in, respectively, the Ni and Ti powders. These might have been the source of oxygen which was solved in Ti_2Ni.

Note that it is expected that the NiTi matrix of the hardened samples contain a high portion of precipitated Ni_4Ti_3 particles. But the fine scale of these precipitates, as they are at the nanoscale after hardening treatment, prevented their observation by SEM at this magnification (figure 7-2.b) [18].

Table 7-2: Results of EDS elemental analysis conducted on the phases observed in the microstructural images.

Attributed phase	**Sample's condition**	**Ni:Ti atomic ratio**
Austenitic NiTi	As-sintered	~51:49
Ni_3Ti	As-sintered	~70:30
Ni_3Ti_2	As-sintered	~65:35
Ti_2Ni	As-sintered	~ 32:58
Austenitic NiTi	Hardened	~55:45
Ti_2Ni	Hardened	~21:47

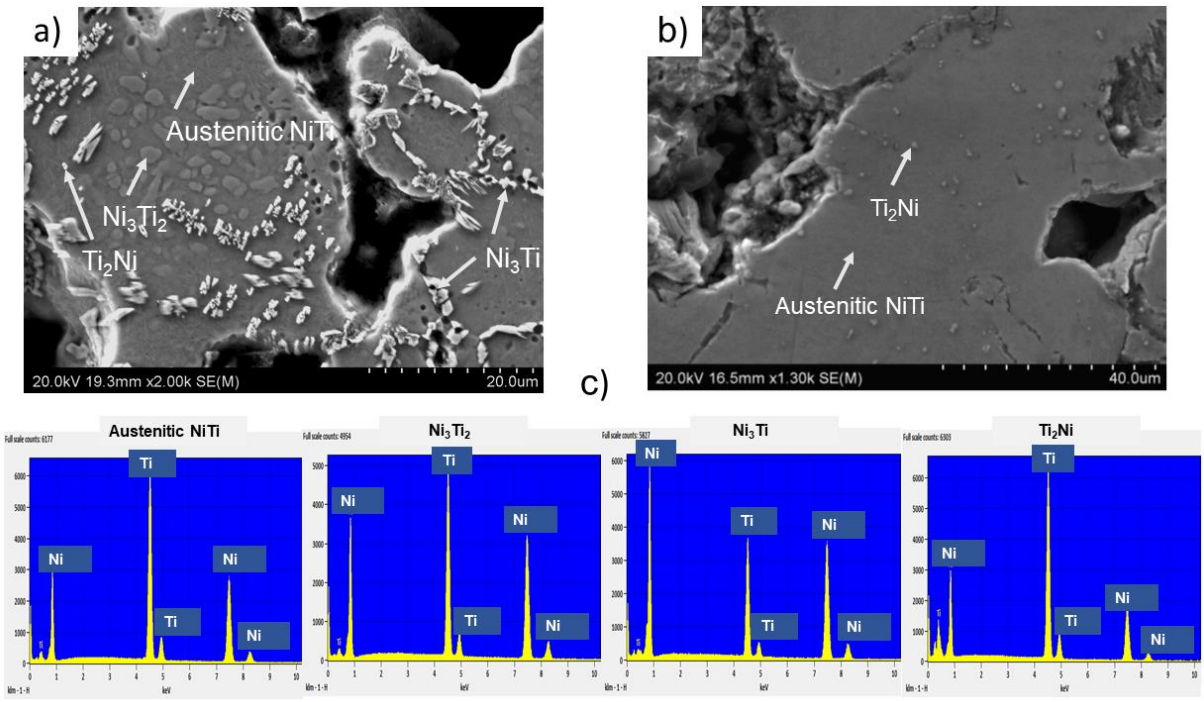

Figure 7-2: SEM images a) as sintered, and b) hardened samples prepared under processing condition 3 (see table 7-1).

As determined by Leco machine, the content of oxygen in hardened samples (~ 1.7 wt.%) was much more than as-sintered ones (~0.2). As seen in the elemental dot map of the as-sintered and hardened samples (figure 7-3), the amount of oxygen existing around the pores is much more in hardened samples compared to as-sintered ones. It is conjectured that some oxygen gas in the air remained in the sealed tubes vacuumed to a low pressure (~0.133 Pa), and penetrated into the pores, thereby increasing the oxygen content of the hardened samples. Additionally as discussed in section 6.2.1, the time delay between the breakage of the tube and the dropping of the samples into the water might have given time for the penetration of air.

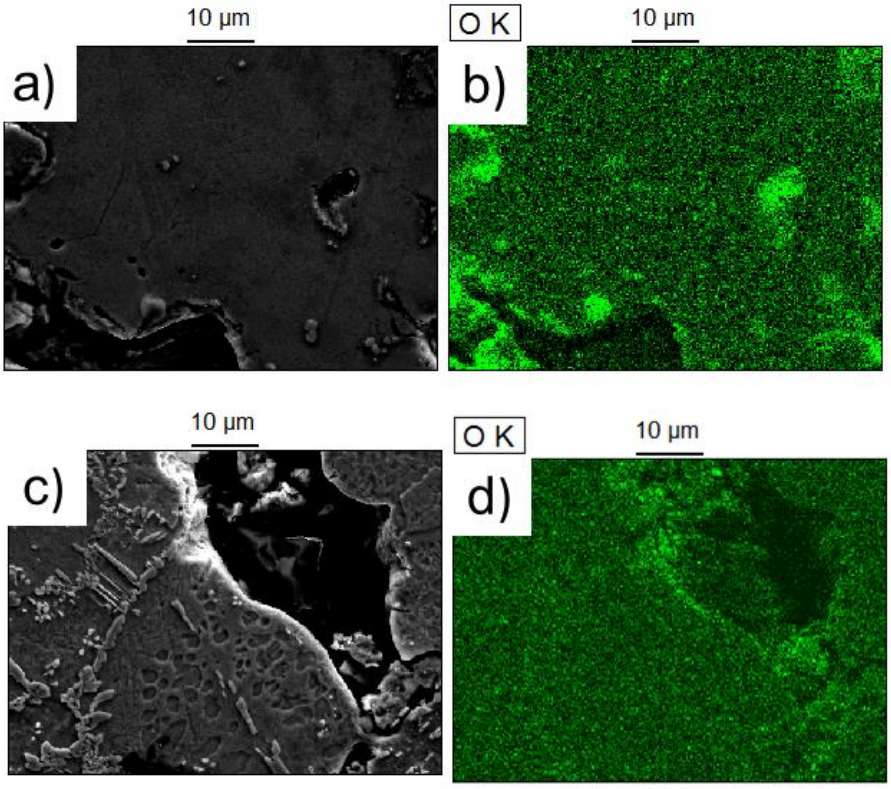

Figure 7-3: SEM images and elemental dot maps of respectively a,b) hardened, and c,d) as-sintered samples.

A fine structure containing needle-shaped particles was seen in the high magnification SEM images of as-sintered samples (figure 7-4). The possible reasons for the formation of this structure is explained in the previous chapters, sections 5.2.1 and 6.2.1: "Bertheville et al. [111] attributed this structure to martensitic NiTi. However, it is almost impossible to differentiate between austenitic and martensitic NiTi using the type of SEM sample preparation employed in this research. It is thought that these particles may be Ni_4Ti_3. Since these particles are not sufficiently coarse, the EDS analysis could not detect the difference in phase composition between these particles and the matrix. That said, caution needs to be applied when interpreting these surface structures observed on NiTi alloys. This is because these structures are not always attributed to the bulk structure and might be artefacts formed due to the effect of etching with hydrofluoric acid [114]".

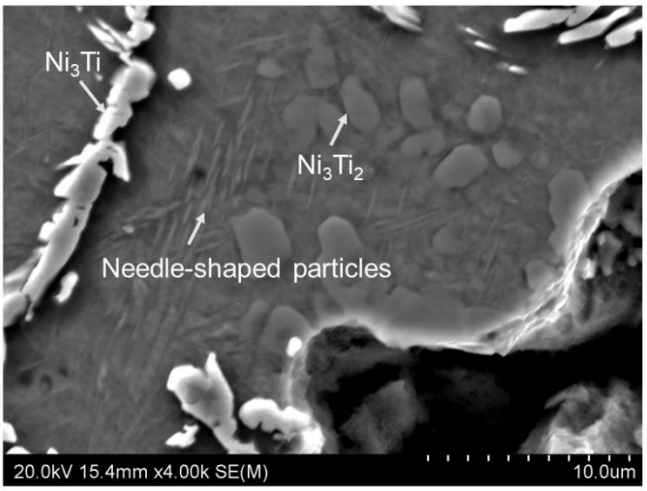

Figure 7-4: High magnification SEM image of as-sintered samples prepared under processing condition 3 (see table 7-1).

As discussed in section 1.1, NiTi generally exists in two different structures, austenite and martensite. Austenitic NiTi (B2 structure) starts to transform to twinned martensitic NiTi (B19' structure) as the temperature goes below the martensite start temperature (M_s). This reversible phase transformation is completed when the NiTi part is cooled below the martensite finish temperature (M_f).

Figure 7-5 exhibits the results obtained from low temperature DSC experiments done on as-sintered and hardened samples. All the peaks observed in these graphs are correlated to phase transformations occurring in the NiTi phase, as NiTi is the only phase which exhibits different phase structures depending on the temperature. During cooling, the transformations apparently consist of a single exothermic peak, attributed to B2 austenite → B19' martensite phase transformation. On the other hand, the reverse transformations occurring during the heating of the as-sintered samples apparently show dual endothermic peaks, attributed to B19' → B2 austenite. However, as observed, both exothermic and endothermic peaks are broad, much more broad than a melt-cast NiTi alloy [125]. It is likely that the more or less sharp transformation peaks observed in both heating and cooling stages do not represent all the transformation events occurring in the as-sintered samples. In fact, the transformation behavior in these samples is simply occurring in multiple continuous temperatures such that it cannot be rationalized just by considering individual sharp DSC peaks. This could explain the broad dual overlapping peaks formed during heating.

These can be due to the existence of micro-compositional gradients in the NiTi phase of the as-sintered samples produced in this research [126, 127]. There may be different reasons for the concentration differences of Ni in the NiTi composition. For example, in this study, the processing method to obtain intermetallics was based on sintering of elemental materials; this can result in a slight compositional heterogeneity in NiTi grains. Alternatively, the existence of precipitates such as Ni_3Ti and Ni_3Ti_2 in NiTi matrix leads to a difference in the amount of Ni around these precipitates as compared to other areas in the NiTi matrix [40, 121]. These micro-compositional differences existing in samples can lead to continuous events of phase transformations during heating and cooling, as the phase transformations are strongly dependent on Ni content in NiTi phase.

In addition to the curves related to as-sintered samples, a curve which belongs to a typical hardened sample can also be seen; all hardened samples showed identical patterns. Hardened samples did not show any peak corresponding to any phase transformation in the studied temperature range. This means that hardening treatment shifted the B2 austenite→ B19' martensite transformation to temperatures below -50°C. This is because hardening treatment resulted in the Ni enrichment of NiTi matrix which leads to the stabilization of B2 austenite to well below room temperature. The amount of Ni in the NiTi composition is a factor that strongly defines these specific phase transformation temperatures. The more Ni-rich the NiTi composition, the lower are the M_s and M_f values [4, 6, 8-16]. On the other hand, formation of Ni-rich precipitates in as-sintered samples results in a drop in the amount of Ni in local areas around these phases. This consequently increases the martensite start temperature (M_s) in these samples.

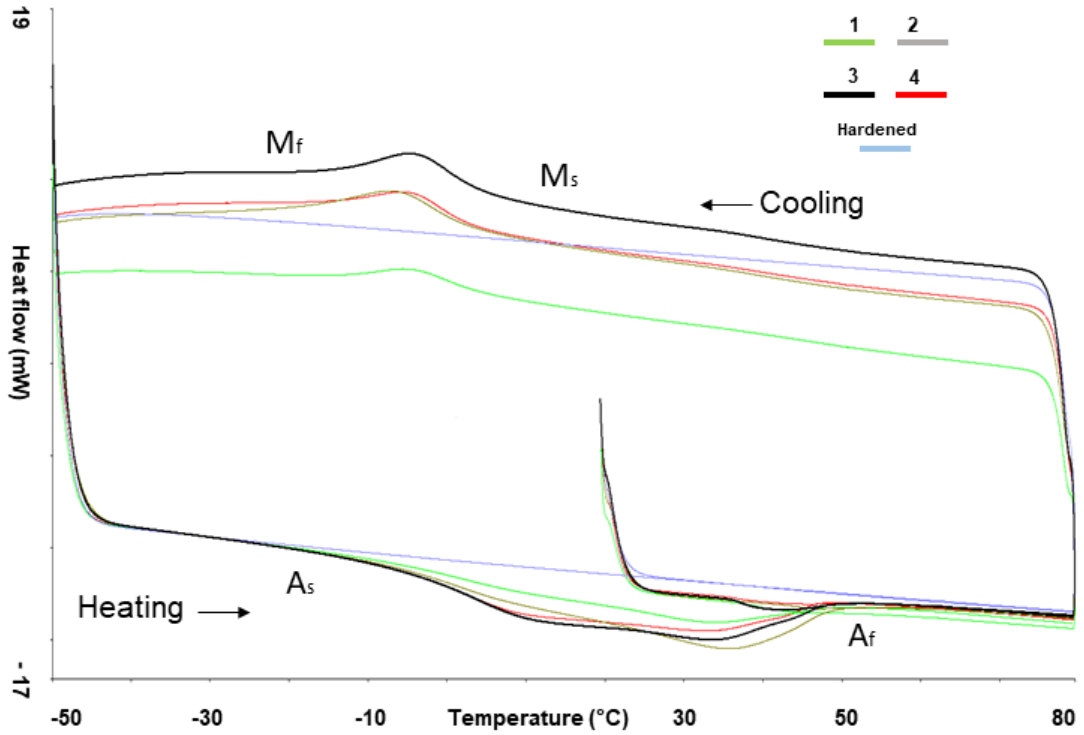

Figure 7-5: DSC curves of as-sintered samples prepared under different processing conditions (1, 2, 3 and 4, see table 7-1) and a typical hardened one.

Information regarding the phase transformation temperatures and the related latent heats for the as-sintered samples are summarized in table 7-3.

Table 7-3: Phase transformation temperatures and related latent heats for as-sintered samples with different processing conditions.

Processing condition	**A_s (°C)**	**A_f (°C)**	**ΔH_A (J/g)**	**M_s (°C)**	**M_f (°C)**	**ΔH_M (J/g)**
1	~-5	~52	~7	~12	~-17	~-3
2	~-4	~57	~11	~10	~-24	~-6
3	~-4	~56	~9	~13	~-20	~-5
4	~-6	~55	~9	~10	~-20	~-2

There was no correlation between the phase transformation temperatures and the processing conditions used to process the as-sintered samples. As seen, the differences in phase transformation temperatures of the processed samples were < ±8°C. This is perhaps because all samples were manufactured based on the same nominal composition. In addition, it was found that the M_s temperatures of these samples are higher than their A_s. In cast NiTi alloys,

the M_s temperature is below the A_s temperature. The existence of porosity raises the M_s temperature, while not affecting A_s, through increased martensite nucleation [121].

In addition, the transformation energies of these samples were much lower than those for the equiatomic cast NiTi alloys (ΔH_A=~27, ΔH_M=~-26**)** [117]. In fact, the existence of precipitates and oxides in NiTi matrix of these Ni-rich samples led to a lower amount of NiTi per mass as compared to equiatomic cast NiTi alloys. Another difference of these as-sintered samples as compared to cast NiTi alloys is the difference between the absolute latent heat of martensite phase transformation ($|\Delta H_M|$) and the latent heat of austenite phase transformation ($|\Delta H_A|$). As seen, $|\Delta H_M|$ is lower than $|\Delta H_A|$. In cast NiTi alloys, this difference is much lower. Li et al. [121] attributed this phenomenon to the existence of porosity and precipitates in NiTi alloys as they affect the energy required for the reversible austenite-martensite phase transformations. The equations which form the basis for the reason for this difference in latent heats is provided in [121].

The A_f temperature of all the samples prepared under different processing conditions are above the room temperature. This means that at room temperature where the XRD experiments were carried out, martensite did not fully transform to austenite and some martensitic NiTi still existed in the as-sintered samples. This is in accordance with the XRD results, which showed small peaks corresponding to martensitic NiTi.

Information regarding the relative density, porosity and open porosity levels in samples prepared under different processing and heat treatment conditions are summarized in table 7-4

Table 7-4: Summary of microstructural studies.

Processing condition	Sample condition	Relative density (%)	Total porosity (Vol.%)	Open porosity (Vol.%)	Open porosity:Total porosity ratio (%)
1	As-sintered	~67	~33	~19	~60
	Hardened	~65	~35	~24	~69
2	As-sintered	~64	~36	~26	~71
	Hardened	~60	~40	~29	~73
3	As-sintered	~68	~32	~16	~49
	Hardened	~65	~35	~22	~61
4	As-sintered	~65	~35	~23	~66
	Hardened	~61	~39	~25	~66

As seen in table 7-4, parts sintered under conditions where the faster heating rate was applied (processing conditions 2 and 4) exhibited lower relative density and consequently higher amounts of total porosity and open porosity volumes as compared to similar conditions where the slower heating rate was applied (processing conditions 1 and 3). In addition, increasing the sintering holding time at 1050°C led to enhanced density and decreased porosity and open porosity in samples. Samples sintered for a longer time of 4 hours at 1050°C exhibited higher density and decreased porosity and open porosity as compared to similar samples processed under the same sintering heating rate, sintered for just 30 minutes. However, heating rate clearly played a more dominant role than sintering hold time. There were larger differences between the relative density, porosity and open porosity of samples sintered at different heating rates than the differences seen in samples sintered for different holding times.

Based on the results obtained from high temperature DSC experiments done on blended powder batches (figure 7-6), both heating rates used in these experiments resulted in the generation of a eutectic liquid at ~942°C. Further, in both tests, the eutectic peak was immediately followed by an exothermic peak. These exothermic peaks are the result of the heat released due to the reaction between the generated eutectic liquid at 942°C and other present intermetallic phases such as Ni_3Ti, NiTi, etc. [83]. The exothermic peak observed in the high temperature DSC pattern of the powder batch sample sintered under the faster heating rate (figure 7-6.a) was larger than the one sintered with the slower heating rate (figure 7-6.b). This is an evidence for the generation of more liquid in the powder batch heated at the faster rate, because applying a faster heating rate gives less time for titanium to react with nickel and other phases, so that more Ti will be available at 942°C to react with Ti_2Ni and result in a eutectic liquid [18].

It can be concluded that more liquid was generated in parts processed under conditions 2 and 4 (faster heating rate) than those sintered under conditions 1 and 3 (slower heating rate). Generation of more liquid in these parts resulted in the generation of more porosity and also decreased density, as this liquid leads to the generation of porosity and expansion of the specimens [103, 105, 106], than the samples sintered at the slower heating rate.

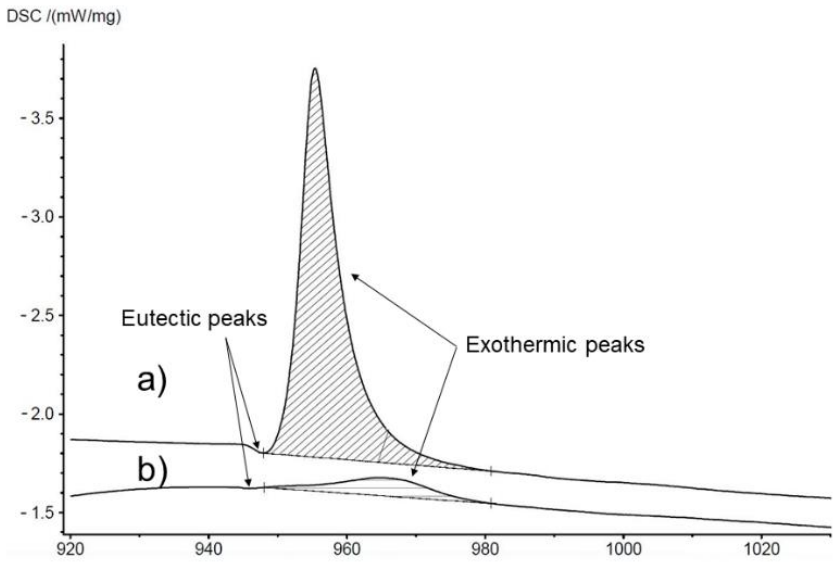

Figure 7-6: DSC trace of blended powders heated to 1050°C by a) the faster heating rate (10°C/min) used in processing conditions 2 and 4, b) the slower heating rate (ambient to 700°C: 10°C/min. 700°C to 900°C: 2°C/min. 900°C to 1050°C: 10°C/min.) used in processing conditions 1 and 3 (see table 7-1).

Further, hardening treatment resulted in a decrease in density and a subsequent increase in porosity in all as-sintered parts (table 7-4). These results were expected, as heating during the solutionizing treatment and their subsequent quenching results in an expansion and increase of volume. In addition, the results show that the rate of increase in open porosity, because of hardening treatment, was more than the rate of total porosity growth. As seen in table 7-4, the ratio of open porosity to total porosity was more in hardened samples than as-sintered samples (total porosity is the combination of open porosity and closed porosity). These results indicate that some of the closed porosities existing in as-sintered parts merged and became interconnected during the expansion of the parts occurred during the hardening treatment.

Alternatively, these can be attributed to the existence of some amount of Ti_2Ni in the as-sintered samples. This phase melts at 1050°C where the solutionizing treatments were conducted causing generation of liquid in samples. In addition, it is expected that austenitic NiTi adjacent to Ti_2Ni will also be liquid at this temperature. This is because Ti_2Ni forms at ~984°C by a peritectic reaction (figure 1.3. The generation of liquid can result in the expansion of the samples causing generation of porosity and decrease of volume.

Based on the requirements of implants for general bone replacement applications, it is desirable that pore sizes are in the range 100-600 μm and the amount of open porosity is at least 30

Vol.%, as the open porosity facilitates the growth of bone into the implant resulting in its fixation and bone healing [83, 84, 118]. Hardened samples processed under processing condition 2 (figure 7-7), which were sintered under the short sintering holding time and fast heating rate, obtained ~30 Vol.% open porosity and porosities with an average size of 254 μm. Since these samples are also corrosion resistant and biocompatible, due to the absence of Ni_3Ti and Ni_3Ti_2 phases, they can be considered chemically and microstructurally appropriate for use in general bone replacement applications.

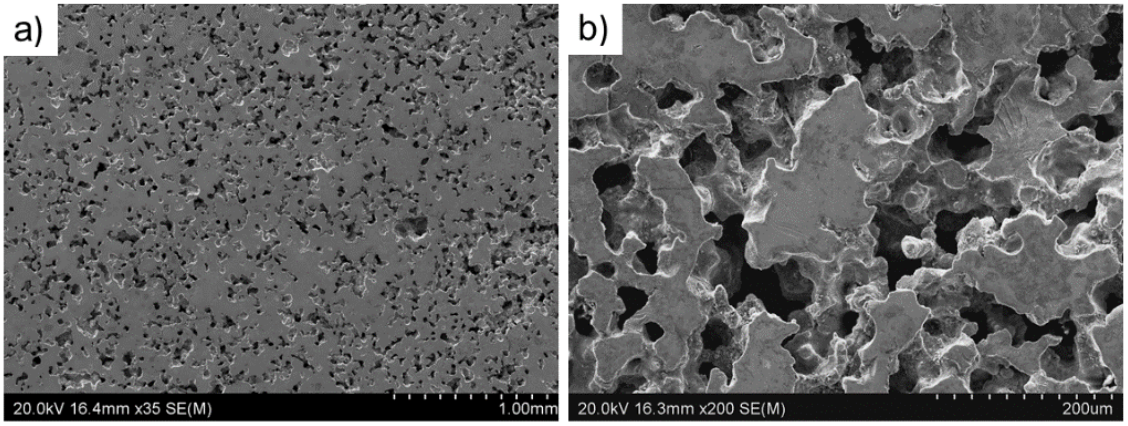

Figure 7-7: Hardened samples processed under processing condition 2 (see table 7-1).

7.2.2 Mechanical properties

Figure 7-8 shows the results of the HRE hardness tests obtained from both hardened and as-sintered samples processed under different conditions. Note that only "apparent" hardness values were obtained in these experiments. This is because these data differ from conventional hardness values, since different types of deformation mechanisms are or can be active during hardness testing of shape memory alloys. As discussed in section 1.1, the reversible austenite-to-martensite phase transformation is the reason for the observation of shape memory and superelasticity effects in NiTi alloys. During loading and the application of stress, the twinned martensitic phase detwins resulting in accompanying strain and deformation. Heating the detwinned martensitic structure above the A_s temperature, where the austenite phase is stable, results in recovery of deformation. This phenomenon is called the thermal shape memory effect. Under stress, austenitic NiTi transforms to twinned martensitic structure, which is followed by detwinning. Detwinning of this twinned martensitic structure results in high strains of over 5%. Martensitic phase reverts back to austenitic phase leading to recovery of strain after the removal of the applied stress. This effect is called superelasticity [40, 104].

Hardness values show a direct relation to sintering holding time, but an inverse relation to the sintering heating rate. Samples sintered for 4 hours at 1050°C exhibited higher hardness as compared to similar samples processed under the same sintering heating rate, sintered for just 30 minutes (samples processed under condition 3 as compared to 1 and 4 as compared to 2). On the other hand, samples prepared at the faster heating rate showed lower hardness than similar samples sintered for the same sintering holding time but at the slower heating rate (samples processed under condition 2 as compared to 1, and 4 as compared to 3). These results can be correlated to the density and porosity of the samples. Samples prepared under a slower heating rate or sintered for a longer time contained less porosity and as a result showed a higher hardness than those processed under, respectively, a faster heating rate or for a shorter sintering time (table 7-4). In essence, the lower the density or the higher the porosity, the lower the hardness in these as-sintered or hardened samples. In addition, again, the effect of heating rate was more pronounced than sintering holding time. There was a larger difference between the hardness of samples sintered under different heating rates (samples processed under condition 1 as compared to 2, and 3 as compared to 4) than the difference seen in samples sintered for different holding times (samples processed under condition 1 as compared to 3, and 2 as compared to 4).

Hardening, despite increasing the porosity and decreasing density (table 7-4), enhanced the hardness of the as-sintered samples. Hardening treatment prevents the precipitation of soft Ni_3Ti and Ni_3Ti_2 Ni-rich phases. These phases get solved into the NiTi matrix at 1050°C. Fast quenching freezes the structure of 60NiTi at 1050°C, however hard Ni_4Ti_3 phase will still form and help increase the hardness [18]. As discussed already, it is expected that the amount of hard Ni_4Ti_3 phase in hardened samples is more than the amount of this phase in as-sintered ones. Ni_4Ti_3 is a metastable phases which at the elevated temperatures and longer times occurring in slow furnace cooling can decompose to stable soft Ni_3Ti and Ni_3Ti_2 [18, 111].

Perhaps the existence of martensitic NiTi in as-sintered samples also plays a role in lowering the hardness of these samples, but not in hardened samples which do not contain this phase structure. As explained later, martensitic NiTi detwins under load. However, this deformation is not permanent and can be recovered by heating this phase above the M_s temperature. It is speculated that part of the deformation measured by the hardness machine in as-sintered samples is not permanent and can be recovered.

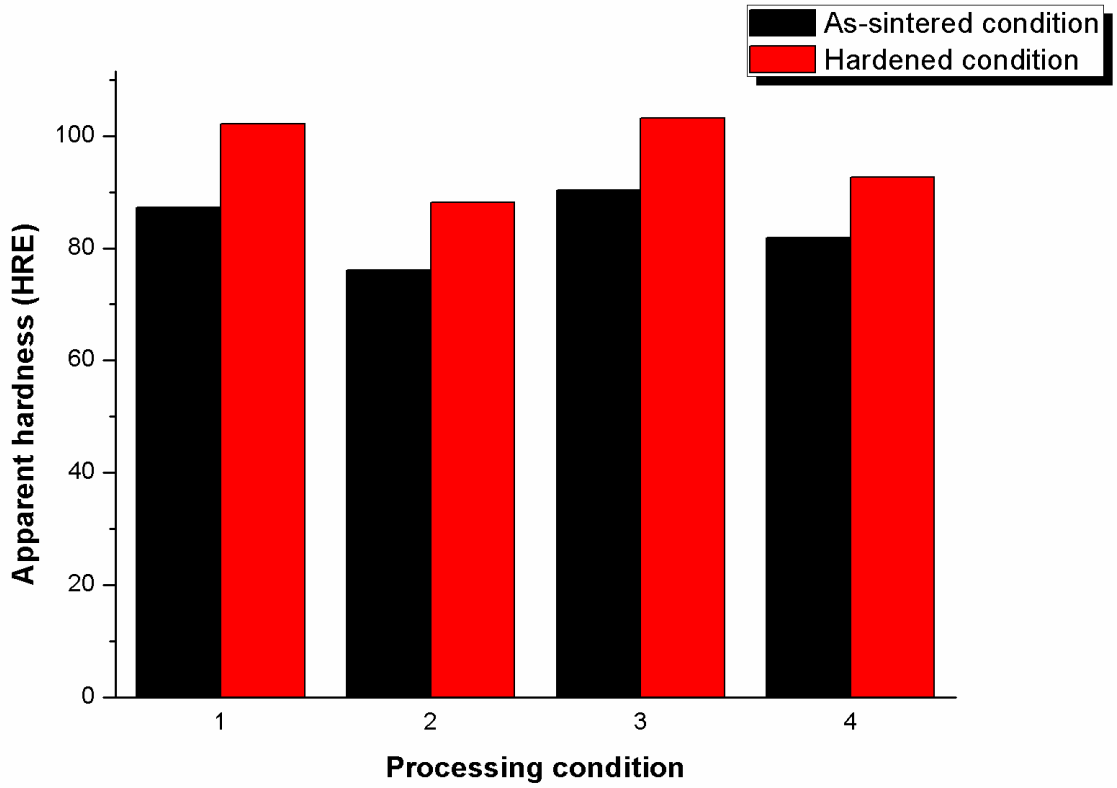

Figure 7-8: HRE apparent hardness values of as-sintered and hardened samples prepared under different conditions of 1, 2, 3 and 4 (see table 7-1).

Results of the monotonic compression mechanical tests done on the as-sintered and hardened samples are given in figure 7-9. Hardened samples exhibited approximately the same fracture strength as the as-sintered samples. This can be attributed to the effect of increased porosity (table 7-4) and oxygen content (figure 7-3) in hardened samples. These counteract the hardening effect of hardening treatment by causing increased brittleness. Heating rate and sintering holding time had the same influence on the strength of samples as they had on their hardness. Similar to what was observed in the hardness tests, the effect of heating rate was more pronounced than sintering holding time. This is because heating rate affected the amount of porosity in a more drastic way than sintering holding time. Porosity results in a decreased amount of load-bearing area and also acts as a source of stress raisers, causing a drop in strength [105, 128].

As seen in figure 7-9, the stress-strain curves show a nonlinear elastic deformation. Porous materials typically demonstrate a non-linear stress-strain curve. However, since both as-sintered and hardened samples contain austenitic NiTi, this non-linear (change in stiffness) behavior can also be attributed to stress induced austenite-to-martensite phase transformation

[83, 105, 128]. In addition, the decrease in stiffness was observed under a lower critical stress for the samples with a higher amount of porosity (samples processed under conditions 2 and 4) than samples with a lower amount of open porosity (samples processed under conditions 1 and 3). In fact, as Li et al. [129] explain, since porosity will reduce the quantity of austenitic NiTi existing per volume, the higher the porosity, the lower the critical stress required to cause the martensitic transformation.

The as-sintered samples demonstrated more elongation to fracture than hardened ones. In fact, the hardened samples showed a negligible amount of deformation after the point where the stiffness decreases. This could be due to a combination of different reasons: (1) Since the M_s temperature is much lower in hardened samples than as-sintered samples, the critical stress required to induce the austenite-to-martensite phase transformation is higher than the stress needed for the as-sintered samples [40, 99]. This effect can be observed in monotonic compressive tests done on samples processed in this research. As seen in figure 7-9, the decrease in stiffness, which is an indicator for the start of the superelasticity effect, is seen under higher stresses in hardened samples than as-sintered ones. This delay leads to less stress induced martensitic phase generation and consequently strain before the fracture of the samples. (2) Based on the results obtained from different phase analysis experiments, the NiTi phase in hardened samples is austenitic while as-sintered samples other than austenitic NiTi contain some amount of martensitic NiTi in their structures. Perhaps detwinning of the martensitic NiTi structure under stress has resulted in more elongation in these samples than hardened ones which lacked martensitic NiTi in their phase structures. (3) As with the amount of porosity, the content of oxygen in hardened samples (~ 1.7 wt.%) was much more than in as-sintered ones (~0.2). This could also have resulted in embrittlement of hardened samples preventing the perfect occurrence of superelasticity effect. As seen in figure 7-9, the as-sintered samples prepared under condition 3 showed the highest amount of elongation to fracture, as their porosity volume level was the lowest amongst the samples.

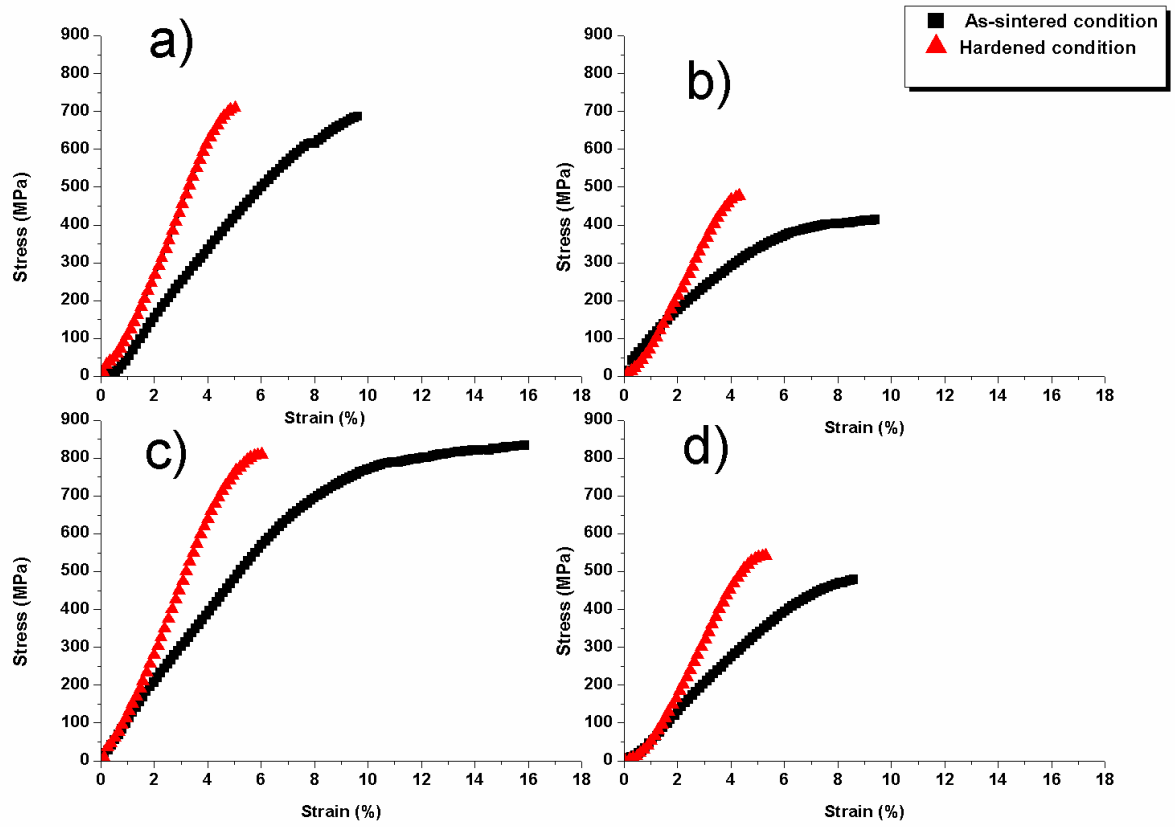

Figure 7-9: Compressive strengths of as-sintered and hardened samples prepared under different processing conditions of a) 1, b) 2, c) 3, and d) 4 (see table 7-1).

Figure 7-10 shows the stiffness of as-sintered and hardened samples at 4% strain (4E). 4% strain was chosen to calculate the stiffness in this study as all the samples processed under different conditions could exhibit this amount of deformation till fracture. For example, hardened samples processed under a fast heating rate of 10°C/min did not show much more ultimate fracture strain than 4% (figure 7-9). Note that, as explained, during mechanical testing of shape memory alloys, different types of deformation mechanisms can be active. Therefore, it is extremely difficult to isolate features related to pure elastic deformation. In addition, the existence of porosity in the samples makes the characterization of elastic properties even more complicated. Therefore, the term "material stiffness" is used in this study instead of "elastic modulus".

In most cases, a lower densification resulted in a lower stiffness. This was expected as porosity reduces stiffness [27, 35, 76]. Moreover, as with hardness and strength, the effect of heating rate was more pronounced than sintering holding time as it had more influence on density. However, hardening treatment, despite increasing the porosity, made the as-sintered samples

stiffer. This was attributed to the effect of this treatment in changing the phase composition of the samples. Irrespective of the processing conditions used, the stiffness of these porous hardened samples was less than that of bulk hardened 60NiTi alloys (~100 GPa) [4]. In fact, the level of stiffness obtained by press and sintering and then hardening is within the range recommended for bone replacement applications (10-20 GPa) [118].

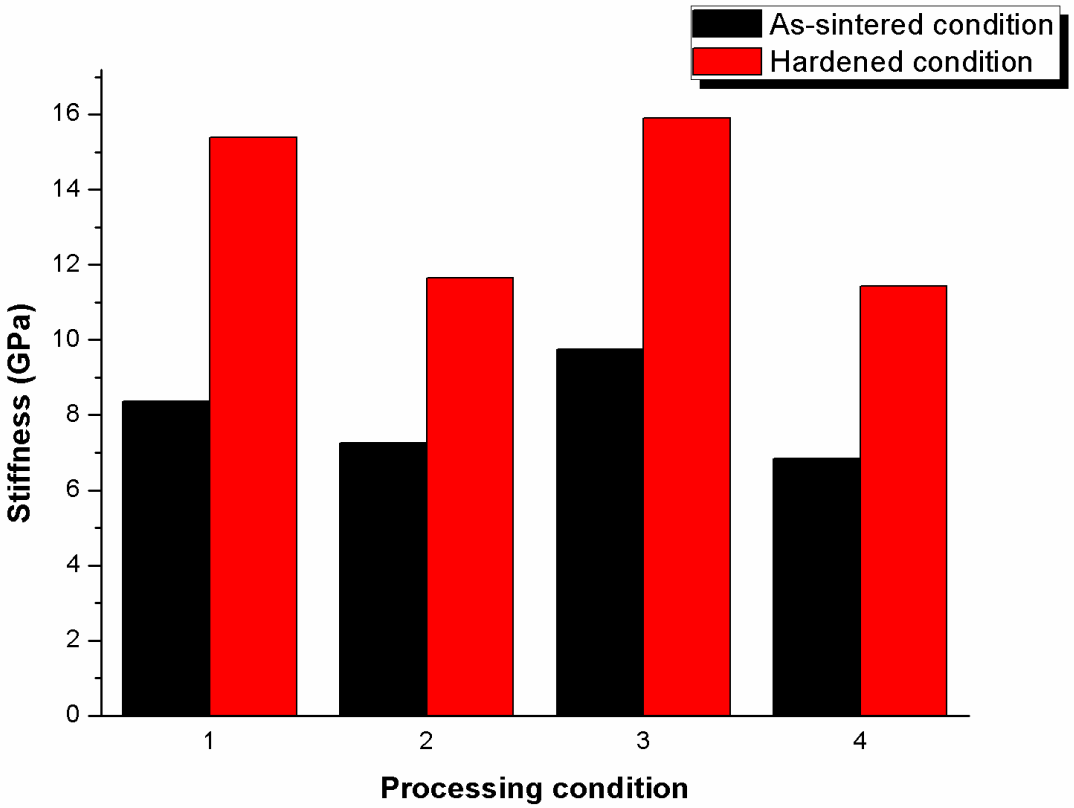

Figure 7-10: Stiffness (4E) of as-sintered and hardened samples prepared under different processing conditions of 1, 2, 3 and 4 (see table 7-1).

To better understand the effect of hardening treatment on the mechanical properties of as-sintered samples, cyclic mechanical tests [38] were conducted on both types of sample processed under condition 3. The resulting stress-strain and strain-time curves are shown in figure 7-11.

In as-sintered conditions, irrespective of applied stress, unloading does not follow the same path as loading/reloading and results in hysteresis. This is an indication of the reversible austenite-to-martensite phase transformation under stress [83, 105, 128]. This superelastic effect is not observed in hardened samples. This leads to the occurrence of less deformation and recoverable strain in hardened samples than as-sintered ones under each specific stress. In addition, in both types of sample, the strain can recover completely while the stress is below

200 MPa (figure 7-11-a, c). This stress corresponds to ~2.1 % strain in as-sintered samples and ~1.5 % strain in hardened ones. An increase in the level of stress to 400 MPa results in the generation of residual strain in both types of sample. Porosities are a possible source of residual strain in both hardened and as-sintered samples. Porosities lead to stress concentrations that result in local deformations. However, in as-sintered samples, due to the simultaneous existence of martensitic NiTi and austenitic NiTi at room temperature, it is expected that part of this residual strain is due to the detwinning of martensitic NiTi. The amount of residual strain, ~1.2 % in as-sintered samples and 0.2 % in hardened samples, does not increase appreciably in subsequent cycles under 400 MPa stress and levels off at a constant value. This might be because of the generation of interlocked dislocations due to compression. This enhances the matrix strength and makes further plastic deformation and martensitic detwinning (specific to as-sintered samples) difficult [83, 105, 128]. A subsequent increase of stress to 600 MPa increases the amount of plastic deformation in both types of sample and recoverable martensite detwinning in as-sintered ones. The residual strains follow the same trend as for 400 MPa. The amount of residual strain was ~0.4 for hardened samples and ~5.0% in as-sintered ones. Furthermore, both types of sample could complete the 5-cycle set at this stress level and fractured under the first loading cycle approaching 800 MPa.

The outcomes of these tests are in accordance with the results obtained from monotonic compressive tests. Hardening treatment resulted in embrittlement of as-sintered samples as they showed less fracture elongation than as-sintered ones (figure 7-11.b, d). Moreover, superelasticity effect was absent in hardened samples as the M_s temperature dropped well below room temperature due to Ni enrichment of the matrix after conducting hardening treatment. This led to a higher critical stress required to induce the austenite-to-martensite phase transformation than the stress required to fracture the samples.

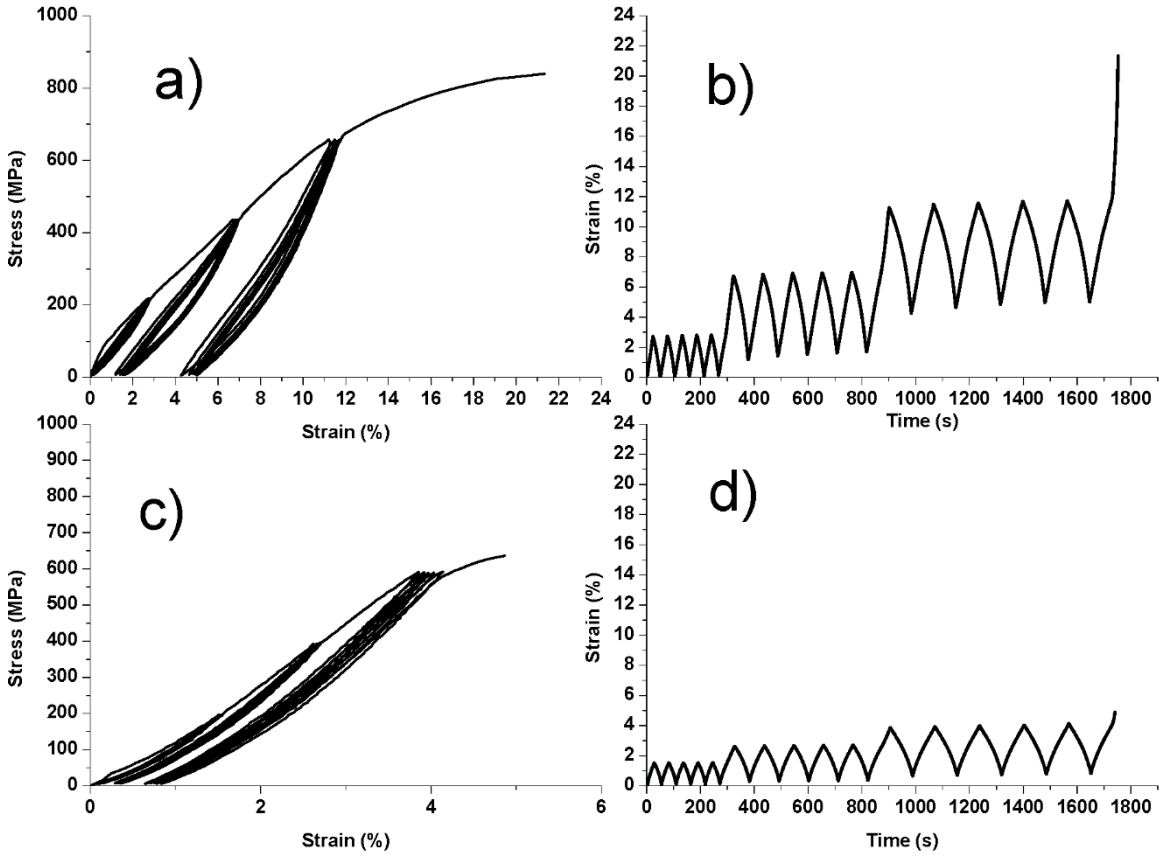

Figure 7-11: Cyclic compressive properties of as-sintered (a, b) and hardened (c, d) samples processed under condition 3 (see table 7-1). Note that the samples were cycled until fracture, which was reached at the end of this curve.

Hardened 60NiTi samples, despite showing inferior monotonic and cyclic compressive properties than as-sintered samples, are biocompatible as they do not contain Ni_3Ti and Ni_3Ti_2 phases in their compositions; these phases act as localized corrosion sites in NiTi matrix leading to the release of carcinogenic Ni to the body [9, 38]. This makes hardened 60NiTi suitable for use in general bone replacement applications. Further cyclic compressive tests (figure 7-12) carried out on these hardened samples processed under different conditions show that heating rate played a more significant role than final sintering holding time on the enhancement of cyclic mechanical properties. Hardened samples prepared under the slower heating rate fractured at a higher stress level and more loading-unloading cycles (figure 17-12.a, c) than specimens processed under the faster heating rate (figure 7-12.b, d). These samples could successfully pass all 5 cycles at 600MPa stress but failed during the first loading cycle at 800 MPa. Sintering holding time merely insignificantly increased the fracture strength of samples prepared under the same heating rate.

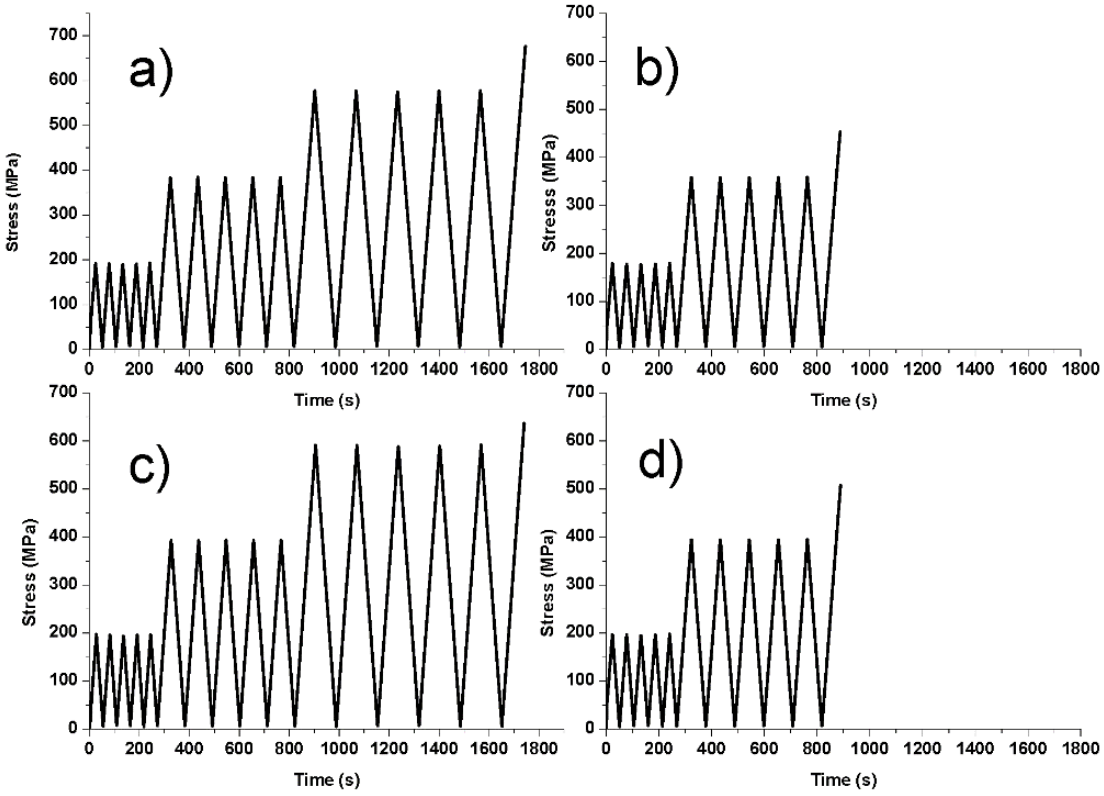

Figure 7-12: Cyclic compressive stress-time curves of solutionized samples processed under different conditions of a) 1, b) 2, c) 3, and d) 4 (see table 7-1). Note that the samples were cycled until fracture, which was reached at the end of this curve.

According to the results obtained from compressive testing, the hardened samples fulfil the strength prerequisite for biomedical applications. This is because they show higher strength than 100 MPa at 2% strain (figure 7-9). Nevertheless, none of these samples showed adequate fracture elongation, which is recommended to be at least 8% fracture strain [118].

7.3 Conclusions

The conventional press-and-sinter method has the potential to produce porous 60NiTi samples using elemental Ni and Ti materials. In this chapter, final sintering holding time and heating rate, as critical parameters affecting the porosity content of samples, were altered to obtain porous parts with different levels of open porosity. The final sintering temperature was kept constant at 1050°C as this temperature is above the temperature where a eutectic liquid, causing the generation of interconnected open porosities, is produced between Ti and Ti_2Ni phases. Applying a fast heating rate of 10°C/min resulted in decreased density, a consequent increased porosity and open porosity, as it caused the generation of more liquid as compared to that produced with slower heating rates. On the other hand, applying a long sintering holding time

of 4 hours resulted in more densification in samples than a short holding time of 30 minutes. Irrespective of the heating rate used and even under a short final sintering time of 30 minutes, all elemental Ni and Ti materials were consumed and intermetallic phases were generated. Based on the microstructural and phase analysis results, NiTi, Ni_3Ti, Ni_3Ti_2, Ni_4Ti_3 and Ti_2Ni phases were identified in these as-sintered samples. Even though NiTi existed mainly in its austenitic B2 structure, a small peak correlating to martensitic B19' NiTi was also detected in the XRD patterns. Existence of martensitic NiTi was confirmed by further low temperature DSC analysis tests. Hardening could prevent the precipitation of soft Ni_3Ti and Ni_3Ti_2 phases but not hard Ni_4Ti_3. In addition, due to the enrichment of the NiTi matrix from solved Ni, the austenite-to-martensite phase transformation shifted to well below room temperature, so that no martensitic NiTi was present at room temperature in solutionized samples.

The effect of heating rate on the densification and subsequent porosity in samples was more pronounced than sintering holding time. As a result, samples processed under the faster heating rate exhibited lower hardness and fracture strength as compared to the parts processed with the slower heating rate. Sintering holding time could improve slightly the mechanical properties of the samples but the amount of open porosity volume was reduced. Hardening treatment, despite increasing the amount of porosity and open porosity volumes, improved the hardness of as-sintered porous samples. This is because hardening treatment solved soft Ni_3Ti, Ni_3Ti_2 phases and increased the amount of hard Ni_4Ti_3 phase than what precipitated in as-sintered samples. However, hardening treatment did not improve the fracture strength of as-sintered samples and also made them more brittle. This is considered to be the result of a combinations of factors, such as increased porosity volume, oxide content and lack of martensitic NiTi which detwins under stress. In addition, since the M_s temperature is shifted to low temperatures in hardened samples, consequently more stress is needed to induce superelasticity as compared to as-sintered samples. Therefore, the austenitic structure did not have the opportunity to fully transform to recoverable martensitic NiTi, resulting in generation of strain, before the fracture of samples.

These results were also confirmed by cyclic compression testing. Even when both hardened and as-sintered samples could successfully pass 5 cycles of loading to 600 MPa stress, the final fracture elongation and recoverable strain under each stress level was much higher in as-sintered samples than hardened one.

As an outcome, biocompatible corrosion resistant homogenized 60NiTi parts with different amounts of open porosity were generated in this research. All these samples fulfilled the strength and stiffness prerequisites for biomedical applications. However, the samples did not show adequate fracture elongation. Further, only hardened samples processed under one particular set of conditions considered in this work achieved the ~30 Vol.% open porosity suitable for biomedical applications: a compaction pressure of 400MPa to press the powder mixtures, a sintering final temperature of 1050°C (which is above the temperature required to generate eutectic liquid), a fast heating-rate of 10°C/min during sintering, and a short sintering holding time of 30 min.

Chapter 8 Conclusions and suggestion of future work

This work investigated the possibility of employing hardened 60NiTi in two novel and distinct areas of interest.

In the first area of interest, research focused on the sliding wear properties of 60NiTi, an emerging superelastic material, in particular as compared to conventional wear resistant alloys such as 440C steel. 60NiTi had already been used in some rolling and ball bearing applications due to its excellent corrosion resistance and relatively high resilience. This research investigated whether 60NiTi could be a proper substitute for conventional load bearing materials such as 440C steel in other application areas, like in gears, or other contact sliding conditions.

Results of sliding wear tests carried out under different loads show that 60NiTi, exhibited an unusual and unexpected characteristic: it displays a significantly inferior wear behaviour under dry conditions in comparison to 440C steel, yet similarly to 440C steel, 60NiTi did not wear under good lubricated conditions and selected loads, making it suitable for sliding applications. The mechanisms behind these results were investigated through comprehensive scratch, indentation and microscopy tests.

At the microscopic length scale, these material classes are very different. 440C steel is a composite consisting of hard carbides and a soft ductile steel matrix, much like tungsten carbide-Co cutting tools, whereas NiTi alloys are more monolithic. This was understood to be the essence of the explanation why NiTi sliding wear differs from 440C. It was found that the matrix of 60NiTi has no soft ductile component to halt the propagation of formed microcracks. As long as the stresses are below damage thresholds for NiTi through the use of good lubrication they perform well, as shear bands and cracks are not formed. In contrast, 440C has large hard carbides to promote wear resistance and a soft ductile matrix material to halt microcracks from getting large enough to liberate wear particles.

The addition of small amounts of Hf, as well as providing benefits in terms of hardening treatment and phase stability, also prevents or reduces the formation of detrimental contaminations and inclusions in products. These have caused an interest in considering a NiTi-Hf alloy (54 at.% Ni- 45 at.%Ti-1 at.% Hf) as a substitute or alternative for the 60NiTi alloy. Results of other experiments conducted in this research showed that, in general, 58Ni39Ti-3Hf

exhibits similar sliding wear properties to 60NiTi. These results emphasize the possibility of substituting 60NiTi with the 58Ni39Ti-3Hf alloy in sliding applications.

However, 58Ni39Ti-3Hf shows relatively enhanced fatigue wear properties as compared to 60NiTi. Benafan et al. [38] speculates that 60NiTi undergoes a transient phase transformation under tension from NiTi to Ni_3Ti. The weaker Ni_3Ti allows a crack to grow under cyclic motions and causes a flake. In contrast, Benefan's work suggests that 58Ni39Ti-3Hf is immune to the formation of Ni_3Ti and thus crack growth is slower. Proving this theory is one worth further investigation in the future.

The second area of research in this work focused on processing 60NiTi to a porous structure suitable for general bone replacement applications using the conventional press-and-sinter method. This research, other than investigating the effects of different critical process parameters such as compaction pressure, sintering heating rate, final sintering temperature and sintering holding time on the dimensional stability, density, porosity characteristics, microstructural properties and phase structure of the as-sintered samples, evaluated the possibility of obtaining homogeneous porous 60NiTi with different cost-effective hardening methods. It was found that hardened samples, solutionized in electrically heated open-atmosphere furnaces, which were tube sealed could successfully form a phase structure dominated by the biocompatible Ni-rich austenitic B2 NiTi phase.

In the final stage, these findings were used to obtain homogeneous 60NiTi parts with different amounts of open porosity. Due to the absence of Ni_3Ti and Ni_3Ti_2 phases in these homogenized 60NiTi parts, these samples are also corrosion resistant and biocompatible and as a result chemically appropriate for use in general bone replacement applications. In addition, under a specific set of processing parameters, hardened 60NiTi parts containing ~30 Vol.% open porosity and porosities with an average size of 254 μm were obtained, being microstructurally appropriate for biomedical applications. Moreover, it was found that irrespective of the amount of porosity in the hardened 60NiT parts (~22%-~30%), all the samples fulfilled the strength and stiffness prerequisites for biomedical applications as they showed a higher strength than 100 MPa at 2% strain and their stiffness were between 10-20 GPa. Nevertheless, none of these samples showed adequate fracture elongation, which is recommended to be at least 8% fracture strain.

The results were correlated to the absence of a superelasticity effect in these 60NiTi parts. It can realated to the drop of the M_s temperature well below room temperature due to Ni enrichment of the matrix after conducting hardening treatment and also the existence of high amounts of porosity in the produced parts. This led to a higher critical stress required to induce the austenite-to-martensite phase transformation, resulting in the generation of strain, than the stress required to fracture the porous samples, as porosity acts as a stress raiser.

More researches are needed to be done so to fully evaluate the biocompatibility of porous 60NiTi structures when used as an implant inside the body. The importance of this topic is more when these parts are hardened using the methods explained in this thesis. This is because some impurities, such as oxides, are generated using these methods which might have detrimental effects on the biocompatibility of this alloy.

References

1. DellaCorte C. Nickel-Titanium Alloys: Corrosion" Proof" Alloys for Space Bearing, Components and Mechanism Applications. *Proceedings of the 40th Aerospace Mechanisms Symposium; Cocoa Beach, FL; United States*, 2010.
2. Della Corte C. Novel Super-Elastic Materials for Advanced Bearing Applications. *Advances in Science and Technology*, 2014; **89**:1-9.
3. Ingole S. 60NiTi alloy for tribological and biomedical surface engineering applications. *The Journal of The Minerals, Metals & Materials Society (TMS)*, 2013; **65**(6):792-8.
4. DellaCorte C, Noebe R, Stanford M, Padula S. Resilient and corrosion-proof rolling element bearings made from superelastic Ni-Ti alloys for aerospace mechanism applications. *Rolling element bearings symposium; Anaheim, CA; United Statae*s, 2011.
5. Dellacorte C, Pepper S, Noebe R, Hull D, Glennon G. Intermetallic nickel-titanium alloys for oil-lubricated bearing applications. *NASA/TM-2009-215646*, 2009.
6. Wojcik C. Methods of processing nickel-titanium alloys. *US Patent #7192496*, 2007.
7. Mosley MJ, Mavroidis C. Experimental Nonlinear Dynamics of a Shape Memory Alloy Wire Bundle Actuator. *Journal of Dynamic Systems, Measurement, and Control*, 2001; **123**(1):103.
8. Buehler WJ, Wang FE. A summary of recent research on the Nitinol alloys and their potential application in ocean engineering. *Ocean Engineering*, 1968; **1**(1):105-20.
9. Julien GJ. Manufacturing of Nitinol parts and forms. *US Patent #6422010*, 2002.
10. Neupane R, Farhat Z. Wear Resistance and Indentation Behavior of Equiatomic Superelastic TiNi and 60NiTi. *Materials Sciences and Applications*, 2015; **6**(07):694.
11. Clayton P. Tribological behavior of a Titanium-nickel alloy. *Wear*,1993; **162-164**:202-10.
12. Qian L, Xiao X, Sun Q, Yu T. Anomalous relationship between hardness and wear properties of a superelastic nickel–titanium alloy. *Appl Phys Lett*, 2004; **84**(7):1076-8.
13. Liu R, Li DI. Experimental studies on tribological properties of pseudoelastic TiNi alloy with comparison to stainless steel 304. *Metallurgical and Materials Transactions A*, 2000; **31A**:2773-83.
14. Lin HC, Wu SK, Yeh C. A comparison of slurry erosion characteristics of TiNi shape memory alloys and SUS304 stainless steel. *Wear*, 2001; **249**:557-65.
15. Li DY. Development of novel tribo composites with TiNi shape memory alloy matrix. *Wear*, 2003; **255**(1-6):617-28.
16. Otsuka K, Ren X. Physical metallurgy of Ti–Ni-based shape memory alloys. *Prog Mater Sci*, 2005; **50**(5):511-678.
17. Weafer FM, Bruzzi MS. Micromechanical investigation into the effect of texture on the fatigue behaviour of superelastic nitinol. *Int J Fatigue*, 2016; **93**:148-55.
18. Hornbuckle BC, Xiao XY, Noebe RD, Martens R, Weaver ML, Thompson GB. Hardening behavior and phase decomposition in very Ni-rich Nitinol alloys. *Materials Science and Engineering: A*, 2015; **639**:336-44.
19. DellaCorte C, Moore III LE, Clifton JS. The effect of pre-stressing on the static indentation load capacity of the superelastic 60NiTi. *NASA/TM-2013-216479*, 2013.
20. Stanford MK, Thomas F, DellaCorte C. Processing issues for preliminary melts of the intermetallic compound 60-NiTiNOL. *NASA/TM-2012-216044*, 2012.
21. Stanford MK. Hardness and Microstructure of Binary and Ternary Nitinol Compounds. *NASA/TM-2016-218946*, 2016.

22. Hornbuckle BC. Investigation in phase stability and mechanical attributes in Nickel-Rich Nitinol with and without hafnium additions. *PhD dissertation, The University of Alabama: Alabama; United States, 2014*
23. Kim J, Miyazaki S. Effect of nano-scaled precipitates on shape memory behavior of Ti-50.9at.%Ni alloy. *Acta Materialia*, 2005; **53**(17):4545-54.
24. Stanford M, Wozniak WA, McCue T. Addressing Machining Issues for the Intermetallic Compound 60-NITINOL. *NASA/TM-2012-216027*, 2012.
25. DellaCorte C, Wozniak WA. Design and Manufacturing Considerations for Shockproof and Corrosion-Immune Superelastic Nickel-Titanium Bearings for a Space Station Application. *NASA/TM-2012-216015*, 2012.
26. Stanford M. Preliminary Investigation of Surface Treatments to Enhance the Wear Resistance of 60-NiTinol. *NASA-2016-219121*, 2016.
27. Della Corte C. The Effect of Indenter Ball Radius on the Static Load Capacity of the Superelasic 60NiTi for Rolling Element Bearings. *NASA/TM-2014-216627*, 201 4.
28. Stanford MK. Thermophysical Properties of 60-NITINOL for Mechanical Component Applications. *NASA/TM-2012-216056*, 2012.
29. DellaCorte C, Moore III LE, Clifton JS. Static indentation load capacity of the superelastic 60NiTi for rolling element bearings. *NASA/TM-2012-216016*, 2012.
30. Julien GJ. NiTinol Ball Bearing Element and Process for Making. *US Patent #6886986*, 2005.
31. Dehghani K, Khamei A. Hot deformation behavior of 60Nitinol (Ni 60 wt%–Ti 40 wt%) alloy: Experimental and computational studies. *Materials Science and Engineering: A*, 2010; **527**(3):684-90.
32. Stanford MK. Hot Isostatic Pressing of 60-Nitinol. *NASA/TM-2015-218884*, 2015.
33. Stanford MK. Charpy Impact Energy and Microindentation Hardness of 60-NITINOL. *NASA/TM-2012-216029*, 2012.
34. Della Corte C, Stanford MK, Jett TR. Rolling Contact Fatigue of Superelastic Intermetallic Materials (SIM) for Use as Resilient Corrosion Resistant Bearings. *Tribology Letters*, 2015; **57**(3).
35. Della Corte C, Glennon G. Ball Bearings Comprising Nickel-Titanium and Methods of Manufacturing Thereof. *US Patent #8182741*, 2012.
36. Della Corte C, Howard A, Thomas F, Stanford M. Microstructural and Material Quality Effects on Rolling Contact Fatigue of Highly Elastic Intermetallic NiTi Ball Bearings. *NASA/TM-2017-219466*, 2017.
37. Adharapurapu RR, Jiang F, Vecchio KS. Aging effects on hardness and dynamic compressive behavior of Ti–55Ni (at.%) alloy. *Materials Science and Engineering: A*, 2010; **527**(7):1665-76.
38. Benafan O, Garg A, Noebe RD, Skorpenske HD, An K, Schell N. Deformation characteristics of the intermetallic alloy 60NiTi. *Intermetallics*, 2017; **82**:40-52.
39. Hornbuckle BC, Noebe RD, Thompson GB. Influence of Hf solute additions on the precipitation and hardenability in Ni-rich NiTi alloys. *J Alloys Compd*, 2015; **640**:449-54.
40. Adharapurapu RR. Phase transformations in nickel-rich nickel-titanium alloys: influenece of strain-rate, temperature, thermomechanical treatment and nickel composition on the shape memory and superelastic characteristics. *PhD dissertation, University of California: UC San Diego; United States, 2007*.
41. Thomas F. The Effect of Various Quenchants on the Hardness and Microstructure of 60-NITINOL. *NASA/TM-2015-218463*, 2015.
42. Li DY. A new type of wear-resistant material: pseudo-elastic TiNi alloy. *Wear*, 1998; **221**:116-23.

43. Stanford M. Hardness and Second Phase Percentage ofNi-Ti-Hf Compounds After Heat Treatment at 700 0C *NASA/TM-2017-219453*.
44. Adharapurapu R, Vecchio K. Superelasticity in a new Bioimplant material: Ni-rich 55NiTi alloy. *Experimental mechanics*, 2007; **47**(3):365-71.
45. Della Corte C, Moore III LE. Launch Load Resistant Spacecraft Mechanism Bearings Made From NiTi Superelastic Intermetallic Materials. *Proceedings of the 40th Aerosspace Mechanisms Symposium; Cocoa Beach, FL; United States*, 2010.
46. Patil D, Marinack MC, DellaCorte C, Higgs CF. Experimental Investigations of the Superelastic Impact Performance of Nitinol 60. *Tribology Transactions*, 2016; **60**(4):615-20.
47. Qin Q, Wen Y, Wang G, Zhang L. Effects of Solution and Aging Treatments on Corrosion Resistance of As-cast 60NiTi Alloy. *J Mater Eng Perform*, 2016; **25**(12):5167-72.
48. Stanford M. Friction and Wera of Unlubricated NiTiHf With Nitriding Surface Treatments. *NASA/TM-2018-219740*, 2018.
49. Liu R, Li D. Modification of Archard's equation by taking account of elastic/pseudoelastic properties of materials. *Wear*, 2001; **251**(1):956-64.
50. Lin H, He J, Chen K, Liao H, Lin K. Wear characteristics of TiNi shape memory alloys. *Metallurgical and Materials Transactions A*, 1997; **28**(9):1871-7.
51. Miyoshi K, Lukco D, Cytron SJ. Oxide Ceramic Films Grown on 55Ni-45Ti for NASA and Department of Defense Applications: Unidirectional Sliding Friction and Wear Evaluation. *NASA/TM-2004-212979*, 2004.
52. Zeng Q-f, Dong G-n. Superlubricity behaviors of Nitinol 60 alloy under oil lubrication. *Transactions of Nonferrous Metals Society of China*, 2014; **24**(2):354-9.
53. Nasehi J, Ghasemi HM, Abedini M. Effects of Aging Treatments on the High-Temperature Wear Behavior of 60Nitinol Alloy. *Tribology Transactions*, 2016; **59**(2):286-91.
54. Della Corte C, Thomas F, Leak O. Tribological Evaluation of Candidate Gear Materials Operating Under Light Loads in Highly Humid Conditions. *NASA/TM-2015-218896*, 2015.
55. Pepper SV, DellaCorte C, Noebe RD, Hall DR, Glennon G. Nitinol 60 as a material for spacecraft triboelements. *Presented at the ESMATS 13 Conference, Vienna, Austria*, 2009.
56. Pepper SV, DellaCorte C, Glennon G. Lubrication of Nitinol 60. *NASA/TM-2010-216331*, 2010.
57. DellaCorte C. Nickel-Titanium Alloys for Oil-Lubricated Bearing and Mechanical Component Applications. *Proceedings of the ASME/STLE 2009 International Joint Tribology Conference; Memphis, Tennessee; USA*, 2009:293-300.
58. Zeng Q-f, Zhao X-m, Dong G-n, Wu H-x. Lubrication properties of Nitinol 60 alloy used as high-speed rolling bearing and numerical simulation of flow pattern of oil-air lubrication. *Transactions of Nonferrous Metals Society of China*, 2012; **22**(10):2431-8.
59. Stott AC, Brauer JI, Garg A, Pepper SV, Abel PB, DellaCorte C, et al. Bonding and Microstructural Stability in Ni55Ti45 Studied by Experimental and Theoretical Methods. *The Journal of Physical Chemistry C*, 2010; **114**(46):19704-13.
60. Zeng Q, Dong G, Martin JM. Green superlubricity of Nitinol 60 alloy against steel in presence of castor oil. *Sci Rep*, 2016; **6**:29992.
61. Zeng Q, Dong G. Influence of load and sliding speed on super-low friction of nitinol 60 alloy under castor oil lubrication. *Tribology Letters*, 2013; **52**(1):47-55.
62. Tang W. Thermodynamic study of the low-temperature phase B19′ and the martensitic transformation in near-equiatomic Ti-Ni shape memory alloys. *Metallurgical and Materials Transactions A*, 1997; **28**:537-44.
63. Kaya I. Shape memory and transformation behavior of high strength 60NiTi in compression. *Smart Mater Struct*, 2016; **25**.

64. White EV, Calkins FT, Mabe JH, Butler GW. Boeing's variable geometry chevron: morphing aerospace structures for jet noise reduction. 2006; **6171**:61710O.
65. Tan L. Corrosion and wear-corrosion behavior of NiTi modified by plasma source ion implantation. *Biomaterials*, 2003; **24**(22):3931-9.
66. Ryhanen J. Biocompatibility Evaluation of Nickel-Titanium Shape Memory Metal Alloy. *PhD dissertation, University of Oulu: Oulu; Finland*, 1999.
67. Khanlari K, Ramezani M, Hayat M, Kelly P, Cao P, Neitzert T. Microstructural and Mechanical Properties of Porous 60NiTi Prepared by Conventional Press-and-sinter Method. *MATEC Web of Conferences*, 2017; **109**:01002.
68. Bolelli G, Bonferroni B, Laurila J, Lusvarghi L, Milanti A, Niemi K, et al. Micromechanical properties and sliding wear behaviour of HVOF-sprayed Fe-based alloy coatings. *Wear*, 2012; **276**:29-47.
69. Gialanella S, Ischia G, Straffelini G. Phase composition and wear behavior of NiTi alloys. *Journal of Materials Science*, 2008; **43**(5):1701-10.
70. Smialek JL, Garg A, Rogers RB, Noebe RD. Oxide Scales Formed on NiTi and NiPtTi Shape Memory Alloys. *Metallurgical and Materials Transactions A*, 2012; **43**(7):2325-41.
71. Firstov G, Vitchev R, Kumar H, Blanpain B, Van Humbeeck J. Surface oxidation of NiTi shape memory alloy. *Biomaterials*, 2002; **23**(24):4863-71.
72. Wu SK, Chu CL, Lin HC. Ion nitriding of equiatomic TiNi shape memory alloys II. Corrosion properties and wear characteristics. *Surf Coat Technol*, 1997; **92**:206-11.
73. Julien GJ. NiTinol Horseshoes. *US Patent #6454016*, 2002.
74. Julien GJ. NiTinol Ski Structures. *US Patent #6267402*, 2001.
75. Della Corte C. Failure Analysis and Recovery of a 50-mm Highly Elastic Intermetallic NiTi Ball Bearing for an ISS Application. *43rd Aerospace Mechanisms Symposium; 91-106; (NASA/CP-2016-219090)*, 2016.
76. Bahraminasab M, Jahan A. Material selection for femoral component of total knee replacement using comprehensive VIKOR. *Materials & Design*, 2011; **32**(8-9):4471-7.
77. Elloy MA, Wright JTM, Cavendish ME. The Basic Requirements and Design Criteria for Total Joint Prostheses. *Acta Orthopaedica Scandinavica*, 2009; **47**(2):193-202.
78. Shwartsmann C, Boschi L, Boschi L, Ramiro G, Yepez A. New Bearing Surfaces in Total HIP Replacement. *Rev Bras Ortop*, 2012; **47(2)**:154-9.
79. Hermawa H, Ramdan D, Djuansjah J. Metals for Biomedical Applications. *In Biomedical Engineering-From Theory to Applications, CHPT 17*, 2011.
80. Matassi F, Botti A, Sirleo L, Carulli C, Innocenti M. Porous metal for orthopedic implants. *Clinical Cases in Mineral and Bone Metabolism* 2013; **10(2)**:111-5.
81. Ni W, Cheng Y-T, Lukitsch M, Weiner AM, Lev LC, Grummon DS. Novel layered tribological coatings using a superelastic NiTi interlayer. *Wear*, 2005; **259**(7-12):842-8.
82. Alcala J, Barone A, Anglada M. The Influenec of Plastic Hardening on Surface Deformation Modes Around Vickers and Spherical Indents. *Acta Materrialia*, 2000; **48**(3451-3464).
83. Chen G, Liss K-D, Cao P. In situ observation and neutron diffraction of NiTi powder sintering. *Acta Mater*, 2014; **67**:32-44.
84. Li B-Y, Rong L-J, Li Y-Y. Porous NiTi alloy prepared from elemental powder sintering. *J Mater Res*, 1998; **13**(10):2847-51.
85. Stanford MK. Hot Isostatic Pressing of 60-Nitinol. 2015.
86. Sliney HE, Spalvins T. The Effect of Ion Plated Silver and Sliding Friction on Tensile Stress-Induced Cracking in Alumunium Oxide. *Annual Meeting of the Society of Tribologists and Lubrication Engineeris, Philadelphia, Pennsylvania, May 4-7*, 1992.

87. Salleh SH, Omar MZ, Syarif J, Ghazali MJ, Abdullah S, Sajuri Z. Investigation of Microstructures and Properties of 440C Martensitic Stainless Steel. *International Journal of Mechanical and Materials Engineering*, 2009; **4**:123-6.
88. Samal PK, Valko JC, Pannell JD. Processing and Properties of PM 440C Stainless Steel, USA. *Presented at PowderMet*, 2009.
89. Zhang C, Farhat ZN. Sliding wear of superelastic TiNi alloy. *Wear*, 2009; **267**(1-4):394-400.
90. Abedini M, Ghasemi HM, Ahmadabadi MN. Tribological behavior of NiTi alloy against 52100 steel and WC at elevated temperatures. *Mater Charact*, 2010; **61**(7):689-95.
91. Tuker Oktay S, Suh NP. Wear debris formation and agglomaration. *Journal of Tribology*, 1992; **114**:379-93.
92. khanlari K, Ramezani M, Kelly P, Cao P, Neitzert T. Reciprocating sliding wear behavior of 60NiTi as compared to 440C steel under lubricated and unlubricated conditions. *Tribology Transactions*, 2018.
93. Woldman M, Van Der Heide E, Tinga T, Masen MA. A Finite Element Approach to Modeling Abrasive Wear Modes. *Tribology Transactions*, 2016; **60**(4):711-8.
94. Swain MV, Mencik J. Mechanical property characterization of thin films using spherical tipped indenters. *TSF*, 1994; **253**:204-11.
95. Chaudhri MM. Subsurface strain distribution around vickers hardness indetations in annealed polycrystalline copper. *Acta Materialia*, 1998; **46**:3047-56.
96. Ni W, Cheng Y-T, Grummon DS. Microscopic superelastic behavior of a nickel-titanium alloy under complex loading conditions. *Applied Physics Letters*, 2003; **82**(17):2811-3.
97. Holmberg K, Laukkanen A, Ronkainen H, Wallin K, Varjus S, Koskinen J. Tribological contact analysis of a rigid ball sliding on a hard coated surface. *Surf Coat Technol*, 2006; **200**(12-13):3793-809.
98. Richardson DW, Lindberg LJ, W.D. C, Dahn J. Contact Stress Effects on Si3N4 and SiC Interfaces. *Ceramic Engineering and Science Proceedings*, 1981.
99. Farhat ZN, Zhang CAN. The Role of Reversible Martensitic Transformation in the Wear Process of TiNi Shape Memory Alloy. *Tribology Transactions*, 2010; **53**(6):917-26.
100. Khanlari K, Ramezani M, Kelly P. 60NiTi: A Review of Recent Research Findings, Potential for Structural and Mechanical Applications, and Areas of Continued Investigations. *Transactions of the Indian Institute of Metals*, 2017:1-19.
101. Cluff D, Corbin S. The influence of Ni powder size, compact composition and sintering profile on the shape memory transformation and tensile behaviour of NiTi. *Intermetallics*, 2010; **18**(8):1480-90.
102. Chen G. Powder metallurgical titanium alloys (TiNi and Ti-6Al-4V): injection moulding, press-and-sinter, and hot pressing [Doctor of Philosophy]: The University of Auckland; 2014.
103. Whitney M, Corbin S, Gorbet R. Investigation of the influence of Ni powder size on microstructural evolution and the thermal explosion combustion synthesis of NiTi. *Intermetallics*, 2009; **17**(11):894-906.
104. Chen G. Powder metallurgical titanium alloys (TiNi and Ti-6Al-4V): injection moulding, press-and-sinter, and hot pressing. *PhD dissertation, the University of Auckland, Auckland, New Zealand*, 2014.
105. Chen G, Liss K-D, Cao P. An in situ Study of NiTi Powder Sintering Using Neutron Diffraction. *Metals*, 2015; **5**(2):530-46.
106. Igharo M, Wood J. Compaction and Sintering Phenomena in Titanium—Nickel Shape Memory Alloys. *Powder Metall*, 1985; **28**(3):131-9.

107. ASTM B962-08, Standard Test Methods for Density of Compacted or Sintered Powder Metallurgy (PM) Products Using Archimedes' Principle, ASTM International, West Conshohocken, PA, 2008, www.astm.org.
108. Bansiddhi A, Dunand D. Shape-memory NiTi foams produced by replication of NaCl space-holders. *Acta biomaterialia*, 2008; **4**(6):1996-2007.
109. Yu J, Hu X, Huang Y. A modification of the bubble-point method to determine the pore-mouth size distribution of porous materials. *Sep Purif Technol*, 2010; **70**(3):314-9.
110. Yan H, Jian Y. Method of determining surface pore mouth diameter distribution of porous material. *US patent #2011/0167897 A1*, 2011.
111. Bertheville B, Neudenberger M, Bidaux J-E. Powder sintering and shape-memory behaviour of NiTi compacts synthesized from Ni and TiH 2. *Materials Science and Engineering: A*, 2004; **384**(1):143-50.
112. Green S, Grant D, Kelly N. Powder metallurgical processing of Ni–Ti shape memory alloy. *Powder Metall*, 1997; **40**:43-7.
113. Hey J, Jardine A. Shape memory TiNi synthesis from elemental powders. *Materials Science and Engineering: A*, 1994; **188**(1-2):291-300.
114. Undisz A, Reuther K, Reuther H, Rettenmayr M. Occurrence and origin of non-martensitic acicular artifacts on NiTi. *Acta Mater*, 2011; **59**(1):216-24.
115. Chen G, Liss KD, Cao P. In situ observation of phase transformation of powder sintering from Ni/TiH2 using neutron diffraction. *TMS 2014 Supplemental Proceedings*, 2014:967-73.
116. Zhu SL, Yang XJ, Fu DH, Zhang LY, Li CY, Cui ZD. Stress–strain behavior of porous NiTi alloys prepared by powders sintering. *Materials Science and Engineering: A*, 2005; **408**(1-2):264-8.
117. Bertheville B, Bidaux J-E. Alternative powder metallurgical processing of Ti-rich NiTi shape-memory alloys. *Scripta Mater*, 2005; **52**(6):507-12.
118. Bansiddhi A, Sargeant TD, Stupp SI, Dunand DC. Porous NiTi for bone implants: a review. *Acta Biomater*, 2008; **4**(4):773-82.
119. E9-09 AD. Standar Test Methods of Compression Testing of Metallic Materials at Room Temperature. *West Conshohocken, PA: ASTM International*, 2009.
120. Bertheville B, Bidaux J-E. Enhanced powder sintering of near-equiatomic NiTi shape-memory alloys using Ca reductant vapor. *J Alloys Compd*, 2005; **387**(1):211-6.
121. Li B-Y, Rong L-J, Luo X-H, Li Y-Y. Transformation behavior of sintered porous NiTi alloys. *Metallurgical and Materials Transactions A*, 1999; **30**(11):2753-6.
122. S.M. Green DMG, N.R. Kelly. Powder metallurgical processing of Ni-Ti shape memory alloy. *Powder Metall*, 1997; **40**.
123. Ramezani M, Pasang T, Chen Z, Neitzert T, Au D. Evaluation of carbon diffusion in heat treatment of H13 tool steel under different atmospheric conditions. *Journal of Materials Research and Technology*, 2015; **4**(2):114-25.
124. Whitney M, Corbin S, Gorbet R. Investigation of the mechanisms of reactive sintering and combustion synthesis of NiTi using differential scanning calorimetry and microstructural analysis. *Acta Mater*, 2008; **56**(3):559-70.
125. Zhang N, Babayan Khosrovabadi P, Lindenhovius JH, Kolster BH. ASSESSMENT OF THE DURATION OF TIME REQUIRED FOR CONVENTIONAL Ti-Ni SINTERING. *Le Journal de Physique IV*, 1991; **01**(C4):C4-163-C4-8.
126. Li B-Y, Rong L-J, Li Y-Y, GJUNTER VE. An Investigation of the Synthesis of Ti-50 At. Pct Ni Alloys through Combustion Synthesis and Conventional Powder Sintering. *Metallurgical and Materials Transactions A*, 2000; **31a**.
127. Sadrnezhaad SK, Lashkari O. Property Change During Fixtured Sintering of NiTi Memory Alloy. *Mater Manuf Processes*, 2006; **21**(1):87-96.

128. Chen G, Cao P, Edmonds N. Porous NiTi alloys produced by press-and-sinter from Ni/Ti and Ni/TiH 2 mixtures. *Materials Science and Engineering: A*, 2013; **582**:117-25.
129. Li H, Yuan B, Gao Y, Chung CY, Zhu M. High-porosity NiTi superelastic alloys fabricated by low-pressure sintering using titanium hydride as pore-forming agent. *Journal of Materials Science*, 2008; **44**(3):875-81.